Développement et application d'un nanoindenteur in situ MEB couplé à des mesures électriques

Solène Comby Dassonneville

Communauté
UNIVERSITÉ Grenoble Alpes

THÈSE

Pour obtenir le grade de

DOCTEUR DE LA COMMUNAUTE UNIVERSITE GRENOBLE ALPES

Spécialité: **2MGE : Matériaux, Mécanique, Génie civil, Electrochimie**
Arrêté ministériel : 25 mai 2016

Présentée par

Solène COMBY DASSONNEVILLE

Thèse dirigée par **Marc VERDIER**, Directeur de recherche CNRS
et codirigée par **Fabien VOLPI**, Maître de Conférences, Grenoble INP

préparée au sein du **Laboratoire Science et Ingénierie des Matériaux et Procédés**
dans **l'École Doctorale I-MEP2 – Ingénierie – Matériaux, Mécanique, Environnement, Energétique, Procédés, Production**

Développement et application d'un nanoindenteur in situ MEB couplé à des mesures électriques

Development and application of an in situ SEM nanoindenter coupled with electrical measurements

Thèse soutenue publiquement le **19 juillet 2018**
devant le jury composé de :

M. Jean-Luc LOUBET
Directeur de Recherche, LTDS, Ecole Centrale Lyon, Rapporteur
M. François BERTIN
Ingénieur de Recherche, LETI, CEA, Rapporteur
M. Roland FORTUNIER
Professeur des Universités, ISAE-ENSMA, Président du Jury
M. Frédéric HOUZÉ
Chargé de Recherche, GeePs, Supelec, Examinateur
M. Marc VERDIER
Directeur de Recherche, SIMaP, Grenoble INP, Directeur de thèse
M. Fabien VOLPI
Maître de Conférences, SIMaP, Grenoble INP, Co-directeur de thèse
M. Guillaume PARRY
Maître de Conférences, SIMaP, Grenoble INP, Invité
M. Didier PELLERIN
Directeur Général de ScienTec / CSInstruments, Invité

"Je fais des trous, des petits trous, encore des petits trous
Des petits trous, des petits trous, toujours des petits trous
Des trous de seconde classe
Des trous de première classe..."
- Serge Gainsbourg, Le poinçonneur des Lilas, 1958 -

Remerciements

Avant toute chose, je tiens à remercier M. Chatterton et M. Smith, ingénieurs de la Gutta-Percha Company, qui à eux deux inventèrent le grandiose "chatterton" sans lequel cette thèse n'aurait *jamais* pu voir le jour.

Je remercie ensuite le Centre d'Excellence sur les Matériaux Architecturés Multifonctionnels (CEMAM) qui m'a donné l'opportunité de réaliser cette thèse en finançant ce projet.

Merci aussi à tout le laboratoire Science et Ingénierie des Matériaux et Procédés (SIMaP) de m'avoir accueillie pour cette thèse, et plus particulièrement au groupe Physique du Métal (PM), au sein duquel j'ai adoré travailler. Je garderai un souvenir immuable des débats en salle café!

Ensuite, pour commencer les choses de façon chronologique, je remercie Alexis Deschamps, qui m'a le premier parlé de ce sujet de thèse et orienté vers Marc et Fabien, lorsque j'ai décidé - un peu sur un coup de tête - de me lancer dans l'aventure du doctorat.

A propos de Marc et Fabien, *justement*, que je qualifierais de façon très objective de meilleurs directeur et co-directeur de thèse du monde: Merci à vous deux, j'ai vraiment beaucoup *beaucoup* aimé travailler avec vous. Ce qui est super avec vous, c'est que vous êtes *totalement* complémentaires, et à vous deux la magie opère: les pieds sur terre et la tête dans les étoiles, la rigueur, le détail, et les idées qui clignotent. J'ai bien cru à un moment qu'on irait tester le nanoindenteur sur la lune! Bref, deux supers scientifiques, mais aussi deux (pardon, quatre!) oreilles attentives. Et vraiment, je vous souhaite tout le meilleur.

Toujours chronologiquement, je remercie Frédéric de Geuser, avec qui j'ai partagé le bureau pendant ma première année de thèse, et qui a pris le temps de tout bien m'expliquer comment ça marchait le bureau des fournitures, la loge, le bouton magique Gael, la machine café, et comment avoir un rendez-vous rapidement chez un ophtalmo à Grenoble...

Ensuite, tout le travail accompli pendant ma thèse n'aurait certainement pas été possible sans l'équipe technique du SIMaP qui s'est relayée au chevet de mon nanoindenteur et que

je tiens vraiment beaucoup à remercier, et en particulier Nadine Vidal, Stéphane Massucci et Bruno Mallery. Vous faites vraiment un travail remarquable!

Il y a aussi toutes les personnes avec qui j'ai eu le plaisir de travailler: Audrey et Hasan et leurs échantillons duplex; Catherine Tassin et Vicky dont j'ai mitraillé les soudures; Frédéric Mercier et Hardik dont j'ai explosé les structures architecturées... Merci également à Raphaël Pesci et Célia Caër de Metz avec qui j'ai eu le plaisir d'échanger et qui m'ont donné l'échantillon ferrite + cementite sur lequel j'ai fait mes mesures de nanoindentation résistive *in situ* MEB. Et surtout un merci vraiment spécial aux deux Guillaume: Guillaume Parry, le maître d'ABAQUS, et Guillaume Beutier, le maître de la Cohérence. Merci à vous deux, ainsi qu'à Alvaro pour le sprint final avant la remise de mon manuscrit.

Je veux aussi remercier toutes les personnes du Consortium des Moyens Technologiques Communs de Grenoble INP (CMTC), avec qui j'ai étroitement collaboré lors de l'implémentation *in situ* MEB du nanoindenteur, et surtout *surtout* Frédéric Charlot, qui en plus de son aide précieuse, venait régulièrement vérifier que je ne dépérissais pas devant le MEB et que je m'alimentais toujours de temps en temps. Du CMTC, merci aussi à Laurent Maniguet, Rachel, Francine, Stéphane (merci pour les RX!), Thierry, Joëlle (merci pour le Nutella lors des crêpes party!),... pour leur bonne humeur et leur aide précieuse.

Pour ce qui est des collaborations, je tiens aussi à remercier toute l'équipe de Scientec / CSInstruments: Didier Pellerin, Louis Pacheco, Sylvain Poulet, Alan Lecoguiec... Pour tous les échanges que l'on a eus et qui ont vraiment contribué à porter ce projet.

Merci également à Nanomechanics Inc. pour leur réactivité face à mes mails *parfois* angoissés.

Je veux aussi remercier les électrochimistes Yves Wouters, Elisabeth Siebert et Jacques Fouletier; merci pour les discussions passionnantes et vraiment terrifiantes que j'ai eues avec vous... Merci aussi à Grégory Berthomé pour les mesures XPS.

Un spécial merci aussi à Guilhem Martin, avec qui j'ai beaucoup aimé donner des TPs, et qui a eu la gentillesse de bien vouloir relire mon compte-rendu pour le label Recherche et Enseignement Supérieure (RES) de l'école doctorale.

Je tiens aussi particulièrement à remercier Muriel Braccini parce qu'elle vient systématiquement voir les posters de nous autres, thésards, lors des sessions posters, et discuter de nos travaux. Et pour nous c'est vraiment super que tu prennes le temps pour ça!

Merci aussi à Florence Robault pour son apport régulier de chocolats. Je ne suis pas certaine que je serais venue à bout de mon manuscrit sans eux...

Comme j'ai adoré aussi l'expérience ESRF (la nourriture y est sans doute pour beaucoup, et surtout le fromage), je tenais aussi à remercier toute l'équipe de l'ESRF, et en particulier Steven Leake, notre interlocuteur lors de la manip sur ID01.

Je remercie aussi tous les thésards et post-docs du groupe PM: Laurent - qui m'a si bien accueillie lors de mon arrivée -, Fanny, Nicolas, Dan, Eva, Maxime, Olivier, Audrey, Simon, Pierre-François, Hasan, Mahmoud, Kitty, Romain, Azzam, Rosen, Ilhem, Nadia - les balades près de l'Isère vont me manquer! - Mike, Ali, Charline, Amandine, Imad, Lorenzo, Aseem, Damien, Zélie - à quand le prochain salon de thé? -... Je n'oublie pas les thésards et post-docs rapportés des autres groupes ou laboratoires: Mano, Solène, Alexis, Thibault, Charles, Victor, Aurélien, Gabriel... qu'on est toujours content de voir quand ils passent au bâtiment thermo!

Un tout spécial merci à Zélie quand même, avec qui j'ai partagé le bureau depuis ma deuxième année de thèse, et qui m'a supportée maugréer, soupirer, siffloter, chantonner... C'était vraiment chouette de partager le bureau avec toi, déjà parce qu'il y avait plein de trucs à grignoter du coup, ensuite parce que tu es vraiment quelqu'un de super, avec qui on peut discuter de tout, et que, en plus, ta bonne humeur est contagieuse et rend joyeux!

Et puis il y a les stagiaires qui gonflent les effectifs l'été et avec qui il est toujours agréable de discuter: Valentin, Yohann, Sébastien...; et surtout les stagiaires qui ont partagé notre bureau: Lifu, Tanu, Alvaro et dernièrement Guillaume.

Last but not least, merci à ma famille sans laquelle je n'en serais pas là; et à mes amis - et en particulier Magatte qui a vraiment toujours été là pour moi, même dans les moments les plus difficiles, pour m'écouter babiller autour d'un chocotella / chococookies au french coffee.

Merci enfin à Rémy qui m'a supportée, aidée, écoutée, qui a tout donné pour me faciliter la vie cette année, et me permettre malgré tout de mener à bien ma rédaction et de pouvoir défendre mon travail. T'avoir épousé est sans aucun doute la meilleure décision que j'ai prise de ma vie.

Contents

Introduction

The increasing demand for multifunctional materials has become a recurring challenge for a wide panel of application fields such as microelectronics and structural applications. Within the framework of this project, a multifunctional characterisation set-up has been developed at SIMaP lab, mainly based on electrical and mechanical coupling. The heart of this device is an *in situ* Scanning Electron Microscope (SEM) nanoindenter coupled with a fine electrical measurement apparatus, which allows electrical measurements during indentation.
The motivations for this work is based on three points:

1. **The investigation of the mechanical behavior of small scale objects,** which requires high spatial imaging resolution, as provided by the SEM, and high resolution in displacement and force, as provided by the nanoindenter.

2. **The enrichment of mechanical characterisation by electrical measurements,** with the input of electrical data to the quantitative analysis of mechanical behavior by indentation. This can improve the knowledge of the contact area between the indenter tip and the sample. The electrical coupling can also provide additional information to fast mechanical events (oxide layer fracture, thin film delamination, dislocation bursts...). This requires an electrical characterisation apparatus able to measure sharp resistance changes over several decades with a high acquisition rate.

3. **The study of electronic properties within a structure** (such as an oxide + metal assembly), thanks to resistive measurements. This topic is extended to the investigation of dielectric properties, thanks to capacitive measurements.

The first step of this project has been the instrumental development of the experimental set-up. Then, the nanoindenter has been applied to various case studies in order to investigate these three key points.
This thesis is divided into four main parts:

- Chapters 1 and 2 are literature reviews on both contact mechanics (including nanoindentation) and electrical contacts. A brief review on the devices allowing either nanoindentation / electronic microscope coupling or nanoindentation / electrical measurements coupling is given.

- Chapter 3 focuses on the experimental development of the *in situ* SEM set-up coupled with electrical measurements. The issues raised by the *in situ* SEM integration and by the electrical coupling are successively discussed. Both mechanical and electrical validations are performed. An example of experiments with electrical measurements during *in situ* SEM nanoindentation is finally given.

- Chapters 4 and 5 are based on the application of the *in situ* SEM nanoindenter, without the electrical coupling.

  Chapter 4 is constituted of various case studies where the use of *in situ* SEM nanoindentation is required. In particular, multiphase alloys with micrometric phases, dissimilar weld, and AlN-coated polymer scaffolds are studied.

  Chapter 5 concentrates on the particular behavior of small scale objects, with the case of submicrometric gold individual crystals on sapphire substrate.

  All these case studies are related to pre-existing research topics of our research group.

- Chapters 6 and 7 focuses on electrical measurements, without the *in situ* SEM integration.

  Chapter 6 focuses on the resistive measurement during nanoindentation of model specimens, such as noble metal (gold) or natively oxidised metals (copper and aluminum), either as bulk single crystals or as polycrystalline thin films. The monitoring of the mechanical contact area is discussed, as well as the tracking of fast mechanical events. The effect of local environment on electrical measurements is also discussed.

  In chapter 7 electrical measurements are no more based on resistance monitoring, but on capacitive measurements. The particularity of this chapter is that the nanoindenter is no more used as an apparatus for mechanical testing, but as a surface probe for capacitive measurements. Several dielectric films thicknesses are investigated.

Within the frame of this Ph.D, main efforts have been made to apply to various systems the nanoindenter *in situ* SEM on one side and with the electrical coupling on the other. Thus, the difficulties arising from both aspects could be decorrelated. However, one example of electrical

measurements during indentation *in situ* SEM is given, which validates from an instrumental point of view the performing of electrical measurements *in situ* SEM (chapter 3, page 81).

This project has been funded by the CEMAM Labex (Center of Excellence for Multifunctional and Architectured Materials ANR-10-LABX-44-01) [1].
The *in situ* SEM development has been performed in collaboration with the CMTC (Consortium des Moyens Technologiques Communs), the characterization platform of grenoble INP (France).
The development of resistive nanoindentation has been performed in collaboration with Scientec / CSI company (Concept Scientific Instrument, Les Ulis, France).

Chapter 1

Contact mechanics and nanoindentation

Instrumented nanoindentation testing allows local measurement of mechanical properties. During nanoindentation, a tip is pressed onto a sample surface. The force applied on the sample and the indentation depth are continuously recorded, leading to load-displacement curves. Mechanical properties are extracted from these curves.

Nanoindentation testing is relatively easy to perform. Contrary to other mechanical testing such as uniaxial tensile tests, the specimen to indent does not need specific preparation or shape. Indeed, the sample requires "only" to be flat and polished, although tensile specimens must have complex geometries, which can become an issue for small size samples.

Moreover, nanoindentation testing gives local mechanical properties, whereas tensile tests only bring global information. This makes nanoindentation highly relevant to assess mechanical properties of complex samples, such as architectured specimens or multiphase alloys.

However, the interpretation of nanoindentation data is rather complicated. Indeed, it deals with a 3D displacement field involving mixed boundary conditions (figure 1.1 A). As a result, the contact area (A_c) between the tip and the sample is unknown, making difficult the computation of the mean flow pressure (*i. e.* the load divided by the contact area). For comparison, this physical value can be obtained immediately in case of uniaxial tensile test, where the corresponding "contact area" (*i. e.* the transverse section) is perfectly known (figure 1.1 B).

Several analytical models have been developed in order to determine the contact area during nanoindentation testing. These models are detailed in the second section of this chapter, after a first section where nanoindentation is briefly described.

The knowledge of the contact area gives access to the mean flow pressure during indentation. To go further, some efforts have also been made in literature to reach elasto-plastic constitutive

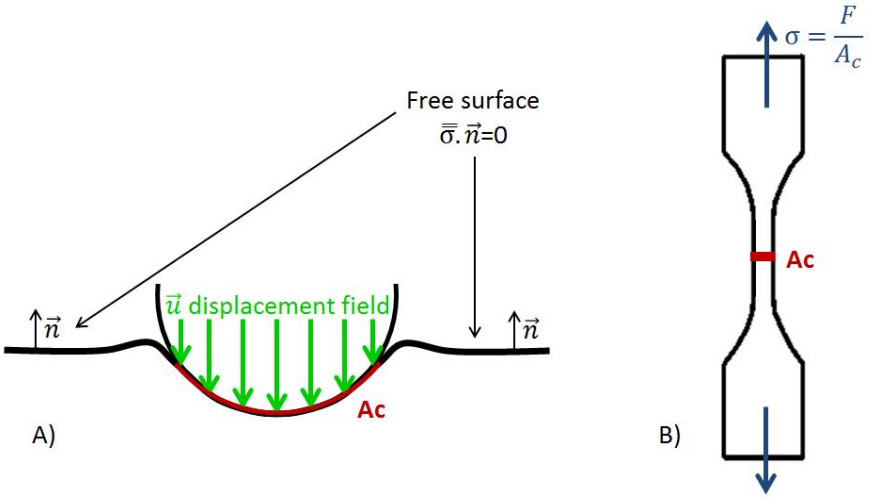

Figure 1.1: A) Mixed boundary condition and contact area in nanoindentation testing and B) corresponding contact area in uniaxial tensile tests.

law identification from nanoindentation data, which means to obtain the equivalent stress-strain curves from nanoindentation load-displacement curves. The methods developed in literature are described in the third section of this chapter.
In the last section of this chapter, a literature review on *in situ* nanoindentation in electronic microscopes is given.

1.1 Introduction to nanoindentation testing

1.1.1 Origins of depth-sensing indentation methods and nanoindentation

Historically, geologists used to compare the hardness of rocks by observing permanent scratch left on a material by another one. The Mohs's scale of 1822 classifies materials according to their hardness, giving the maximum value of 10 for the diamond.
Between 1900 and 1950, the method evolves by using normalized tips with specific geometries to penetrate the material, so that more comparable and repeatable results are obtained. This leads to conventional hardness tests, also called "static" indentation methods, which consist in measuring the size of the imprint left in a material by a tip with a known geometry:

- Brinell hardness testing was first elaborated in 1900. During Brinell tests, a hard sphere

is pressed onto a sample under a constant load. The Brinell hardness is then defined as the load divided by the surface area of the imprint.

- Following Brinell hardness, the Meyer hardness was first described in 1908. It is similar to Brinell hardness, except that Meyer used no more the real surface area of the imprint to compute the hardness, but the projected surface area, *i. e.* the area of the imprint projected on the sample surface.

- Vickers hardness was then introduced in 1922. It is based on the penetration of a four-sided pyramidal indenter into the sample. As for Brinell hardness, Vickers hardness is defined as the load applied on the sample divided by the real surface area of the imprint.

The main interest of hardness tests is that they provide local and "non destructive" information about mechanical properties of materials, without the need of complicated geometries for tested samples, unlike the dedicated geometries required for uniaxial loading. Any sample can be used, provided that their dimensions are large enough to avoid edge effects, and that the tested surface is flat.
Nevertheless these methods involves some microscopy to determine the imprint size in the material, which is time consuming, and which can be an issue for small imprint size. That is why Rockwell hardness was elaborated in 1914, where the depth of penetration is used instead of the imprint size for hardness computation. Penetration depth under load is recorded and compared with penetration depth under a pre-load. Several tip shapes can be used, either conical or spherical, as well as several tip materials, such as diamond or steel.
Rockwell hardness can probably be seen as the closest ancestor of depth sensing indentation methods, as the difference that for Rockwell tests the load is not monitored versus time and both depth and load are not continuously measured during testing.

Originally, the development of nanoindentation testing has been motivated by the need of mechanical characterization of small material volumes, such as thin films, where the penetration depth cannot exceed several tens of nanometers. For such samples, conventional hardness tests probe a too large volume of material. Therefore, nanoindentation is first no more than indentation with penetration depths of several nanometers, and so with a sub-micrometric or micrometric imprint size. However, these tests bring two main issues:

- The indenter monitoring must allow indentation at depths as small as tens of nanometers

- and sometimes even less -, with a nanometer sensitivity.

- Due to the small residual imprint, it becomes difficult to determine with enough precision the imprint size using usual optical microscope.

Thus, nanoindentation testing is based on depth-sensing indentation, developed around 1980 by Loubet and Pethica [2, 3, 4]. During depth-sensing indentation, load on sample and penetration depth are continuously measured. Provided the use of elastic contact models, the knowledge of the penetration depth allows the projected contact area computation - without using optical microscopy - from which the hardness can be determined, but also other mechanical properties such as the Young's modulus.
The main issue in nanoindentation is then the knowledge of the projected contact area from the penetration depth. Note that in nanoindentation, as for Meyer hardness, the projected contact area is used instead of the real contact area. It will be noted as A_c and most often simply called "contact area" in what follows.
The contact area depends on two factors: i/ the tip geometry and ii/ the sample rheology, which leads to different contact topologies. These factors are described in the two next paragraphs.

1.1.2 Indenter tips geometry

Several indentation tips can be used for indentation testing. The material chosen for the tip must be harder as possible, so that the indenter deformation would be neglected during the test. It also must have high Young's modulus to stay elastic during the test. Thus, diamond or sapphire tips are most commonly used, with hardness around 40 GPa and 30 GPa respectively, and Young's modulus around 1100 GPa and 400 GPa respectively.
Various tip geometries can be used, as shown in figure 1.2. Usually indenter tips are either spherical, conical or pyramidal. The choice of the tip geometry clearly depends on the nature of the investigated sample, its constitutive material and its properties.

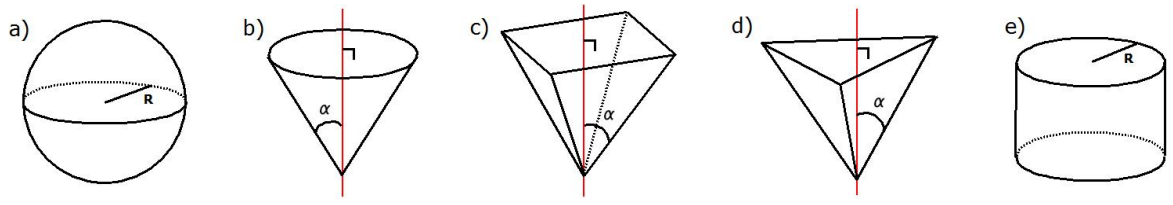

Figure 1.2: Several tip geometries: spherical tip (a), conical tip (b), Vickers tip (c), Berkovich or cube corner tip (d), flat cylinder punch (e).

Historically, pyramidal tips were mainly used, as the four-sided Vickers tips. For Vickers tips, the opposed faces make a semi-angle $\alpha = 68^o$ and each of the four faces makes an angle $\beta = 22^o$ with the flat surface. If we consider a fictive spherical tip of radius R, tangent to the contact point and with a contact radius a which corresponds to the semi diagonal of the contact area, the indentation strain a/R with this spherical indenter is equal to $\sin(\beta) = 0.375$. This corresponds to the strain values at which Brinell hardness tests with spherical indenters are usually performed.

Knoop tips are also four-sided pyramidal tips but with one diagonal higher than the other. Knoop tips were developed in order to measure hardness of very hard material, in which only small residual imprint are left. In such materials, it is easier to measure the length of a longer diagonal.

The main issue of the four sided pyramidal tips is that in practice it is impossible to realise a tip with four faces that ends with a perfect single point. There is always a line between the four faces, which is a non negligible tip defect for small scale investigations. Thus, Berkovich tip was developed, with only three faces which meet at a single point. The face angle of Berkovich tip is $\alpha = 65.27^o$. This leads to the same ratio between the projected contact area and the contact depth as for Vickers tips.

Cube corner tips are also increasingly used for indentation tests. They correspond to the same geometry as Berkovich tips, but they are much sharper, with a face angle $\alpha = 35.26^o$. It allows to reach higher material strain than with a Berkovich tip for equivalent indentation depth.

Conical tips are also used, but in practice it is more difficult to polish diamond tips as cone than as pyramidal tips. Nevertheless conical tips are of considerable interest for probing anisotropic material response, since those tips have an axial symmetry. Usually, the semi angle used for a conical tip is chosen to be 70.3^o, which corresponds to the Berkovich or Vicker equivalent conical tip, *i. e.* which leads to the same ratio between the projected contact area and the contact depth.

The main interest of conical and pyramidal tips is that those tips are self similar. It means that for a semi-infinite isotropic material, whatever the penetration depth into the sample, both deformations and constraints fields are geometrically similar.

Spherical tips are used due to the possibility to first deform elastically. They also allow to detect the smooth transition between elastic deformation and plastic deformation during indentation. Indeed, there is no singularity at the end of the tip, and consequently no immediate plastic deformation.

Literature also describes flat cylinder punch, which are essentially used for modelling and for mathematical derivations or to perform nanocompression.

Flat punch	**Conical tip of semi angle ϕ**	**Pyramidal tip of leading term LT**	**Spherical tip of radius R**
$A_c = constant$	$A_c = \pi(h_c.\tan(\phi))^2$	$A_c = LT.h_c^2$	$A_c = \pi R.h_c$

Table 1.1: Contact depth to contact area relations. $LT = 24.5$ for a Vickers or Berkovich indenter tip and $LT = 2.6$ for a cube corner tip.

As mentioned earlier, the projected contact area A_c is used rather than the real contact area to analyse depth sensing indentation data. Knowing the contact depth h_c, the projected contact area can be computed using expressions given in table 1.1 for ideal tip geometries. The expressions between the projected contact area and the contact depths are known as the "shape functions". These relations must be adjusted for real tip, which exhibit geometrical defects (see paragraph 1.2.6, page 37).

1.1.3 Contact topology

The knowledge of the shape function of the tip and the contact depth ensure the computation of the projected contact area A_c. The main issue is then the determination of the contact depth h_c, which means the depth along which both the tip and the material are in contact. This depth depends on the material rheology, which can lead to different contact topologies.
Indeed, when a tip penetrate into a material, several behaviours can occur, as shown in figure 1.3. If deformation induced during indentation is purely elastic, the material sinks in around the indenter, as shown in figure 1.3 a. On the contrary, if the deformation is perfectly plastic, the material piles up around the indenter (figure 1.3 b). For the intermediate elasto-plastic case, material can either sink-in or pile-up around the indenter, depending on its rheology.
In both cases, the penetration depth h corresponds to the distance between the sample surface before indentation and the extremity of the tip. The contact depth h_c corresponds to the distance along which the indenter and the surface are in contact. Typically, if there is sink-in $h_c < h$ and if there is pile-up $h_c > h$. For notations, when the indenter reaches its maximal depth $h = h_{max}$ and $h_c = h_{c,max}$.
The projected contact area A_c corresponds to the horizontal section of the indenter at the

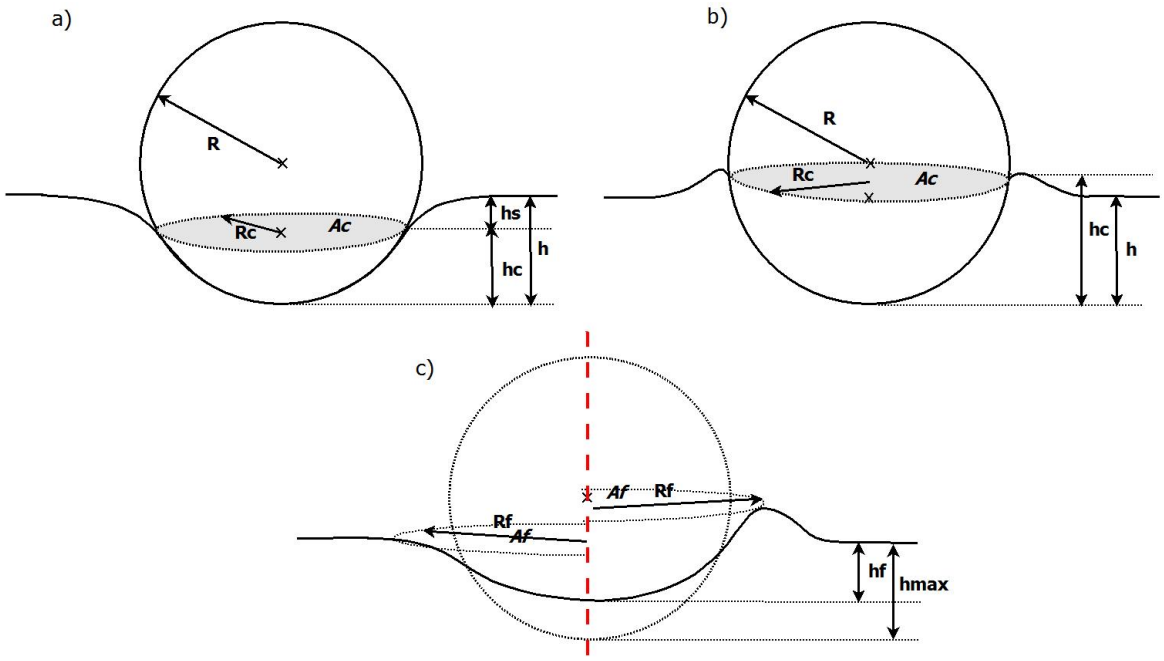

Figure 1.3: Contact topology during indentation with a spherical tip showing: a) sink-in behaviour during loading, b) pile-up behaviour during loading, c) pile-up and sink-in behaviour after unloading (with the tip position at maximal depth in dotted line).

contact depth h_c, shown in grey on figure 1.3 a and b. The contact radius r_c is defined as $\sqrt{A_c/\pi}$.

After unloading, material can either exhibit pile-up or sink-in, as shown in figure 1.3 c.

Since there is an elastic spring-back during unloading, the final depth h_f after complete unloading is always smaller than the maximal depth h_{max}. This highlights the interest of using the contact area A_c under loading to determine the hardness, instead of using the residual imprint A_f as for Brinell hardness. Indeed, with the Brinell convention for hardness computation, perfectly elastic material, which exhibits an entire spring-back, would have an infinite hardness. This is obviously not the case when using the contact area A_c under loading.

1.1.4 Nanoindentation data analysis

During depth sensing indentation methods, the load applied onto the sample and the displacement of the indenter are continuously recorded. This leads to load-displacement curves, as illustrated in figure 1.4: during loading, the load onto the sample surface increases from 0 to a maximal value L_{max} reached at the maximal depth h_{max}. During unloading, the load decreases from its highest value to 0, corresponding to the final depth h_f. The maximal load is often

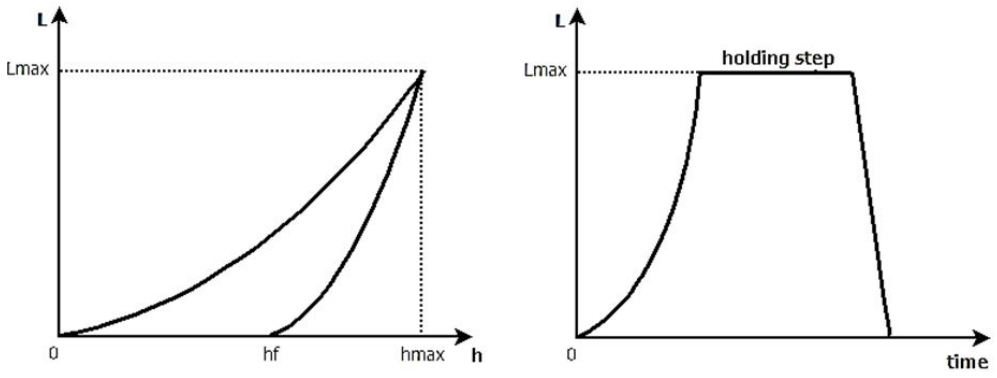

Figure 1.4: Load-displacement curve and corresponding load-versus-time curve after one loading and unloading cycle.

kept constant for a given time before unloading. This corresponds to the holding step. Nanoindentation data can then be analysed at different levels:

- **Level 0: Qualitative approach.** The shape of the load-displacement curves are qualitatively studied. This gives information about:

  – *The material rheology:* Oyen and Cook [5] have proposed a guide to discriminate the material rheology thanks to the shape of the curve. Purely elastic behavior leads to curve with no hysteresis (figure 1.5 A); if the hysteresis does no change with rate the behavior is elasto-plastic (figures 1.5 B1 and B2); otherwise the behavior is viscous-elastic for entire recovery after unloading (figure 1.5 C) or viscous-elasto-plastic (figure 1.5 D).

  In some cases unloading part of the curves can also qualitatively provide evidence of sink-in ($h_f << h_{max}$, figure 1.5 B1); or pile-up (h_f close to h_{max}, figure 1.5 B2).

  – *Mechanical events or phase transformations occurring in the material:* A change in the slope of the initial loading curve generally occurs at the transition between elastic and irreversible stages. Some events can also happen, such as pop-in events, which appear on the loading curve, or pop-out events, which appear on unloading curve (figure 1.6). They are generally due to dislocation bursts, cracking, film delamination or even pressure induced phase transformations.

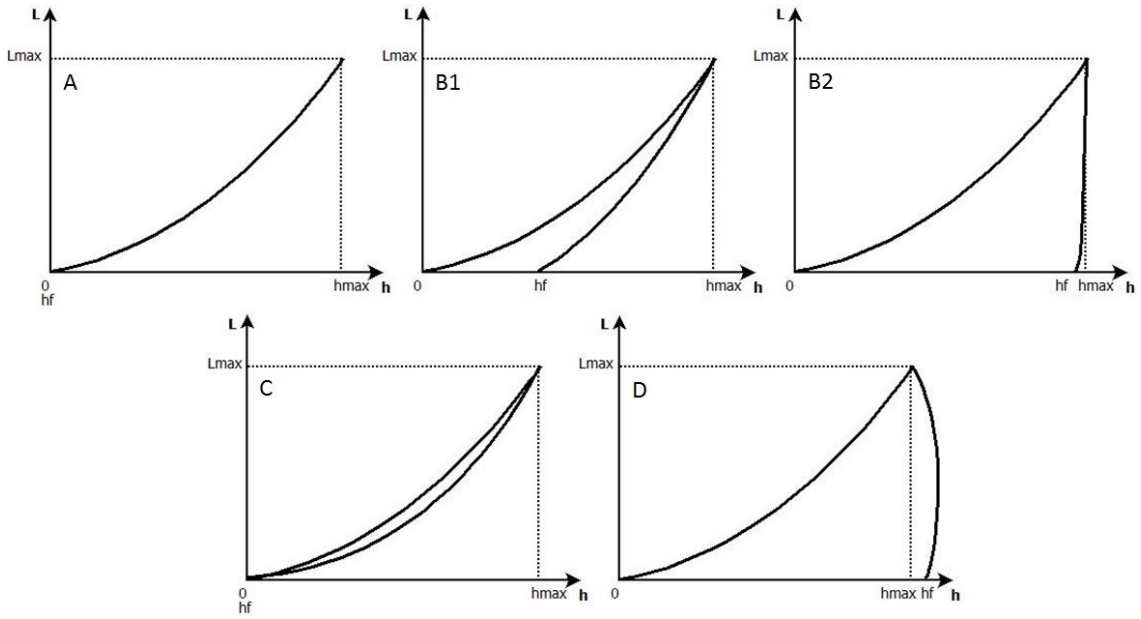

Figure 1.5: Load-displacement curves and material rheology.

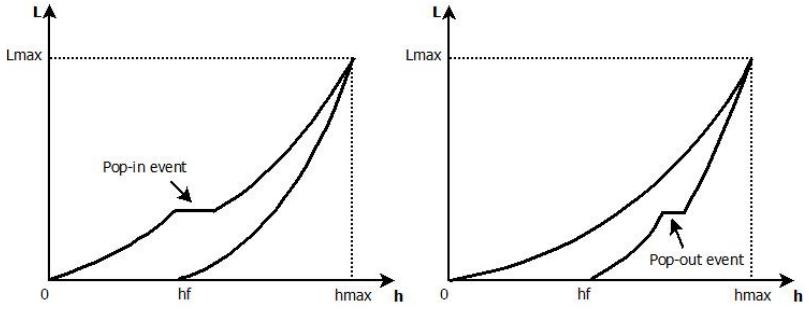

Figure 1.6: Pop-in and pop-out events on load-displacement curves.

- **Level 1: Cinematic approach.** The penetration depth is studied versus time during the holding step at maximal load (at room temperature or at high temperature). This gives information about viscoplasticity properties [6, 7, 8].

- **Level 2: Modulus and hardness computation.** The contact depth is computed, giving access to the contact area A_c, which allows the calculation of the Young's modulus and the hardness. The main issue at this level is the computation of the contact depth. This is performed by using elastic contact models described in section 1.2 (page 28).

- **Level 3: Constitutive law identification.** The aim of this level is to access to the entire strain-stress curve of the material. Several methods (analytical, numerical, parametric and direct methods) have been described in the literature. They are briefly detailed in section 1.3 (page 39).

1.2 Elastic contact models for hardness and modulus computation

1.2.1 Elastic contact between smooth surfaces

Since the end of the nineteenth century, several elastic models, based on contact mechanics have been derived for nanoindentation data analysis. In particular, they allow hardness and modulus determination.

The first model used for data interpretation is the Hertz's model [9, 10], which deals with elastic contact between the smooth surfaces of two isotropic bodies.

Hertz discussed the problem of elastic deformation during contact between two spheres, two parallel cylinders or two perpendicular cylinders or even between a sphere and a plane. The latter case can be applied to indentation with a spherical tip, in the elastic range, so either at the very beginning of the indentation, or during unloading (provided that unloading kinematic is considered to be purely elastic).

The problem resolution is mostly based on the solution of a semi infinite plane loaded by a point force: the problem is considered as an elastic isotropic half-space loaded over a small elliptic area. The contact is supposed to be frictionless, and the strain to be small, in order to stay in the range of small strain approximation.

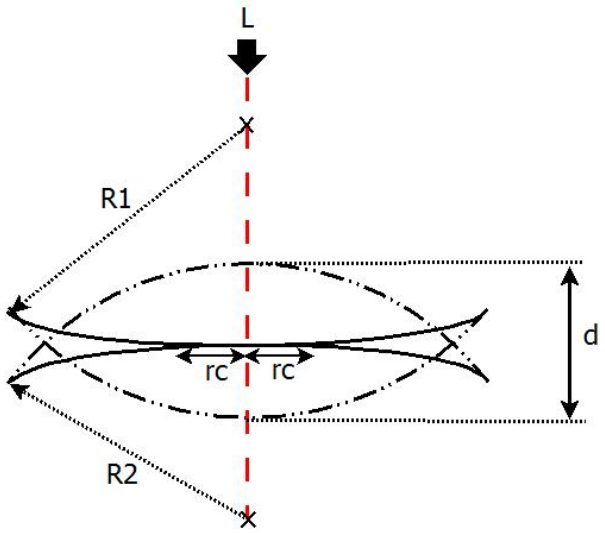

Figure 1.7: Elastic contact between two spheres, according to Hertz model.

For contact between two spheres, Hertz gives relations between the contact area A_c, the applied load L, the mutual distance between points on tip and specimen d, the spheres radii and moduli

R_1, R_2 (in the case of the contact between a sphere and a plane R_2 is taken as the infinity), E_1, E_2, and the Hertz contact stiffness S_h. The equations obtained are given below and are based on notation given in figure 1.7.

$$d \cdot R = r_c^2 \tag{1.1}$$

$$L = \frac{4}{3} \cdot E^* \cdot \sqrt{R} \cdot d^{3/2} \tag{1.2}$$

$$r_c = \frac{3}{4} \cdot \frac{L}{d \cdot E^*} \tag{1.3}$$

For the computation of the load applied on the surface, the Hertz pressure is used, which is a pressure profile given by equation 1.4, and with the maximal pressure given by equation 1.5. For this profile, the mean pressure is found to be the two third of the maximal pressure.

$$p(r) = p_{r,max} \cdot (1 - (\frac{r}{r_c})^2)^{1/2} \tag{1.4}$$

$$p(r, max) = \frac{2 \cdot E^*}{\pi} \cdot \sqrt{\frac{h_c}{R}} \tag{1.5}$$

The indentation between a non rigid indenter of radius R_1, modulus E_1 and Poisson coefficient ν_1 in a material of radius R_2, modulus E_2 and Poisson coefficient ν_2 corresponds in term of mutual distance d to the indentation between a rigid indenter of radius R and a material with a smooth surface and a modulus E^*, with R and E^* the radius and the reduced modulus of the system, *i. e.* $R^{-1} = R_1^{-1} + R_2^{-1}$ and $E^* = (\frac{1-\nu_1^2}{E_1} + \frac{1-\nu_2^2}{E_2})^{-1}$. In this case the mutual distance d corresponds to the contact depth h_c.

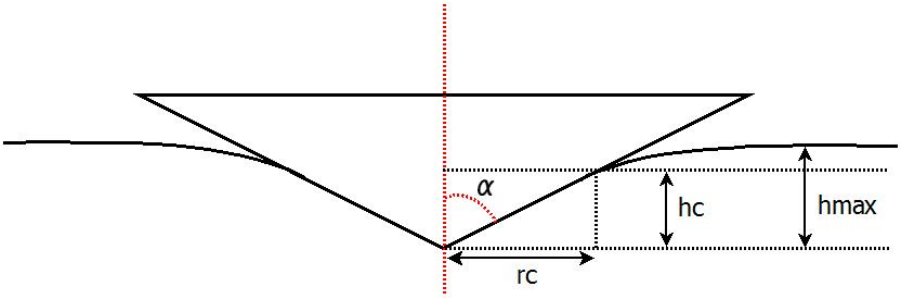

Figure 1.8: Love contact topology for a conical indenter.

1.2.2 Elastic contact with singularities

In the Hertz model, solids surfaces are supposed to be perfectly smooth. There is no contact discontinuity. Thus, this model cannot be used to describe the contact between a solid and conical or pyramidal tips. Problem of a mechanical contact with a tip singularity was first discussed by Love [11]. His work is mostly based on the work of Boussinesq [12, 13], who developed a theory based on the use of potentials to describe mechanical contacts for a plane loaded by a force point.

Love discussed the indentation of an isotropic material by a conical indenter, with contact topology shown in figure 1.8. He described the pressure distribution by equation (1.6) and found the relation between the applied load and the penetration depth (equation 1.7), with r the tip radius at depth between h_{max} and h_c. As shown by (1.6) the contact pressure diverge when r tends to zero , *i. e.* at the end of the tip.

$$p(r) = \frac{E^*}{2} \cdot \cot(\alpha) \cdot \cosh^{-1}(\frac{r_c}{r}) \tag{1.6}$$

$$L = \frac{2}{\pi} \cdot E^* \cdot \tan(\alpha) \cdot h^2 \tag{1.7}$$

The penetration depth h_c is simply related to the contact radius by the geometrical relation $h_c = r_c \cdot \cot(\alpha)$. As the result and as shown in equation (1.8) the hardness is found to be a constant which does not depends on the penetration depth and which depends only on the semi angle of the conical tip α and on elastic properties of the material. This is a general property found for self similar tips in case of isotropic materials.

$$H = \frac{1}{2} \cdot E^* \cdot \cot(\alpha) \tag{1.8}$$

Same results were also found by Sneddon [14, 15] using Fourier transforms.

This model was also extended by Willis [16] in the case of an hertzian contact between two anisotropic bodies.

Some authors also studied the indentation of an elastic semi infinite plane by a flat ended punch [13, 14, 15, 17], where there is a discontinuity at the edges of the tip. The relation between applied load and depth for a flat ended cylindrical punch of radius R are given in equation (1.9).

$$L = 2E^* R h_c \tag{1.9}$$

1.2.3 The so-called "Sneddon's equation"

In a paper of 1965, Sneddon [14] refound the load to depth relations previously discussed for elastic rheology, using Hankel's transform. He also found load to depth relations for various tip geometries, included tip shapes based on the revolution of any smooth function. For all these geometries Sneddon showed that the indenter load L is related to the indentation depth h by a power law, as suggested by equation (1.10), with α and m constants.

$$L = \alpha \cdot h^m \tag{1.10}$$

The value of the power law exponent m depends on tip geometry. Thus, m was found to be 1 for cylinder punch, 2 for cones and 3/2 for paraboloids of revolution or spheres in the case of small displacements. The corresponding expressions are given in table 1.2.

Nevertheless, despite the strong effect of tip geometry on power law equations, the contact stiffness S_c (*i. e.* the derivation of the load by the contact depth) is simply related to the contact area A_c by equation 1.11, also known as Sneddon's equation [3, 18]. This relation is obtained for any tip geometry (spherical, conical, pyramidal or flat ended punch). Using the contact radius r_c, the Sneddon's equation is simply given by 1.12. In 1992, Pharr et al. [19] have extended Sneddon's equation to tip shapes based on the revolution of any smooth function.

$$S_c = \frac{dL}{dh_c} = \frac{2}{\sqrt{\pi}} \cdot E^* \cdot \sqrt{A_c} \tag{1.11}$$

$$S_c = \frac{dL}{dh_c} = 2 \cdot E^* \cdot r_c \tag{1.12}$$

	Flat punch of radius R	**Conical tip of semi angle ϕ**	**Pyramidal tip of leading term LT**	**Spherical tip of radius R**
Contact area	$A_c = \pi \cdot R^2$	$A_c = \pi \cdot (h_c \cdot \tan(\phi))^2$	$A_c = LT \cdot h_c^2$	$A_c = \pi \cdot R \cdot h_c$
Load	$L(h) = 2E^* Rh$	$L(h) = \frac{2}{\pi} E^* \tan(\phi) h^2$	$L(h) = \frac{2\sqrt{LT}}{\pi\sqrt{\pi}} E^* h^2$	$L(h) = \frac{4}{3} E^* \sqrt{R} h^{\frac{3}{2}}$
Stiffness	$S(h) = 2E^* R$	$S(h) = \frac{4}{\pi} E^* \tan(\phi) h$	$S(h) = \frac{\sqrt{2LT}}{\pi\sqrt{\pi}} E^* h$	$S(h) = 2E^* \sqrt{Rh}$
Contact stiffness	$S(r_c) = 2E^* r_c$	$S(r_c) = 2E^* r_c$	$S(r_c) = 2E^* r_c$	$S(r_c) = 2E^* r_c$
Hardness	$H(h) = \frac{2E^* h}{\pi R}$	$H(h) = \frac{1}{2} E^* \cot(\phi)$	$H(h) = \frac{\sqrt{\pi}}{2\sqrt{LT}} E^*$	$H(h) = \frac{4}{3\pi} E^* \sqrt{\frac{h}{R}}$

Table 1.2: Elastic solutions for several ideal tip geometries. $LT = 24.5$ for Vickers or Berkovich tip and $LT = 2.6$ for cube corner tip.

Most of indentation data interpretation methods are now based on Sneddon's equation. Experimentally, the contact stiffness can simply be measured on load-displacement curve as the slope at the beginning of the unloading part of the curve, where the purely elastic regime condition is satisfied (figure 1.9). This means that unloading data can by analysed using the model of an elastic deformation between an elastic half space and an elastic tip, which are the assumptions used in Sneddon's equation. The hidden assumption here, is that Sneddon's equation which describes a half space indented by a tip, also applies to a residual imprint indented by a tip.
Once the contact stiffness is measured, the Sneddon's equation is crucial because it gives access to two types of information:

- If the Young's modulus of the material is already known, the contact radius can be determined using Sneddon's equation, and thus the hardness can be computed.
- If the Young's modulus of the material is unknown, the knowledge of the contact area gives access to both hardness (immediately) and Young's modulus (using Sneddon's equation).

In practice, however, the material modulus is often unknown, and the contact area must be determined independently of Sneddon's equation.

1.2.4 Indentation data analysis based on elastic contact models

With depth sensing indentation techniques, indenter displacement and applied load are continuously recorded. Since the 80's, efforts have been made to use elastic contact models developed in literature to analyse load-displacement curves, especially in order to determine the contact depth from some assumptions concerning the partitioning between elastic and plastic deformations.

In 1986, Doerner and Nix [18] proposed a method to determine hardness and Young's modulus from indentation data. The main idea of their work is to decorrelate elastic and plastic contributions from total displacement. Indeed, nanoindentation data involves both elastic and plastic deformations, contrary to conventional hardness tests where the hardness is computed from residual imprint, and thus is only due to the plastic deformation (even if some errors can occur due to imprint contractions caused by the elastic spring-back during unloading).

In order to decorrelate plastic and elastic contributions to the total indenter displacement, Doerner and Nix assumed that plastic depth is the intersection between the tangent to the unloading curve at maximal depth and the x-axis (figure 1.9).

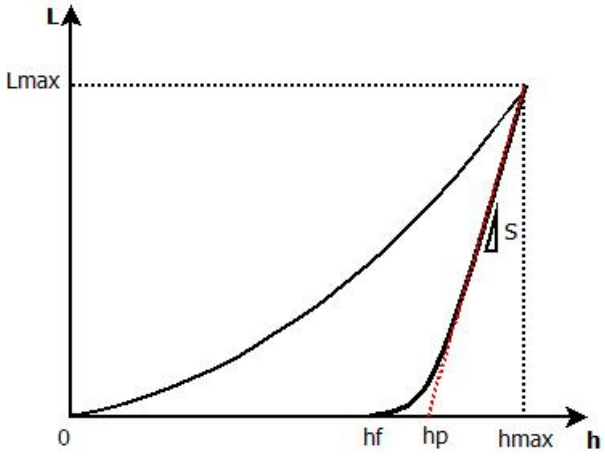

Figure 1.9: Plastic depth computation in Doerner and Nix model.

Doerner and Nix computed the hardness as the ratio between the maximal applied load L_{max} and the tip shape function $A(h)$ at plastic depth h_p. Young's modulus is determined by using Sneddon's equation (1.11), providing that the tip modulus and Poisson's ratio and the material Poisson's ratio are known. In Sneddon's equation, the shape function $A(h)$ is determined for the plastic depth h_p, as for hardness. As mentioned previously the contact stiffness corresponds to the slope of the unloading curve.

In this model, Doerner and Nix assumed that the unloading part of the curve is mostly linear,

as it was previously shown in literature for flat cylinder punch [3]. The change in curvature of the unloading curve is mainly due to a loss of contact of the indenter. This essentially comes from elastic recovery and leads to a change in residual imprint. But Doerner and Nix explained that even for silicon where there is a lot of elastic recovery, a linear unloading occurs at least for the first third of the unloading curve. Nevertheless Oliver and Pharr [20] showed later that this was inexact. Indeed Oliver and Pharr explained that even if the unloading curve seems to be linear, in metal for instance, it is clearly not when drawing it in expanded or logarithmic axes. This basically leads to an under estimation of the hardness in Doerner and Nix model.
Thus, Oliver and Pharr [20] proposed a new method to analyse depth sensing indentation curve. In this model, the total depth h is the sum between the contact depth h_c, which is the depth along with the contact is made, and the contact parameter h_s which is the vertical distance between the initial position of the material surface and the projected contact area (figure 1.10). This parameter can be seen as the degree of sink-in.

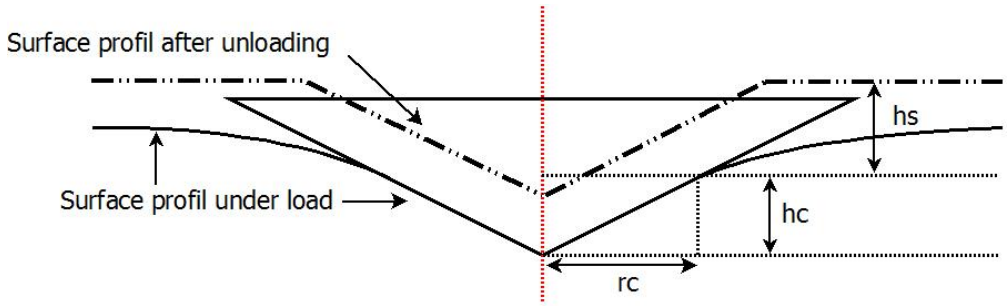

Figure 1.10: Contact topology according to Oliver and Pharr model.

At maximum load, the contact depth can be described by equation (1.13). Then, the contact parameter h_s can be expressed by considering the surface shape outside the contact area, given by Sneddon [14] for a conical indenter. As a result, the contact parameter is found to be proportional to the ratio between the maximum load L_{max} and the contact stiffness S_c (equation 1.14). The proportional coefficient ϵ depends on the tip geometry. The values of ϵ for several tip shapes are given in table 1.3.
Note that for the flat punch, $h_s = L_{max}/S_c$ and the contact depth is precisely the interception between the displacement axis and the initial unloading slope, as given by Doerner and Nix model.

$$h_c = h_{max} - h_s \tag{1.13}$$

$$h_s = \epsilon \cdot \frac{L_{max}}{S_c} \tag{1.14}$$

Flat punch	**Conical indenter**	**Paraboloid of revolution**	**Sphere**	**Pyramidal indenter**
$\epsilon = 1$	$\epsilon = 0.72$	$\epsilon = 0.75$	$\epsilon = 0.72$	$\epsilon = 0.75$

Table 1.3: Value of the proportional coefficient ϵ for several tip geometries.

Even if Oliver and Pharr model is now the most commonly used model to determine the contact depth in nanoindentation, this model fails to take into account pile-up. Indeed, the contact depth h_c is always lower than the total displacement h (or h_{max} at maximum load) (1.13). Thus, only sink-in behaviour can be modelled, and errors are obviously made when material piles-up.

In order to take into account pile-up, an alternative model to determine the contact depth was proposed by Loubet et al. [21] and validate by finite element simulations [22, 23].

As in Doerner and Nix model, Loubet considers the plastic depth h_p as the intersection between the slope of the initial unloading curve and the displacement axis. Then, the idea of Loubet is to obtain the contact depth h_c by multiplying the plastic depth by a factor α_{loubet} found to be equal to 1.2 (equation 1.15). For perfectly plastic materials, where typically pile-up occurs, the total displacement h is equal to the total plastic depth h_p, and the ratio $h_c/h = 1.2$. The contact depth is then higher than the total displacement, which accounts for pile-up. This model obviously fails to take into account sink-in.

In literature, deviations between modulus values obtained using Oliver and Pharr model and Loubet model were found to be from 10 to 20 % [23].

$$h_c = \alpha_{loubet} \cdot h_p \tag{1.15}$$

For both Oliver and Pharr and Loubet models, the contact area is calculated by using the tip shape function $A_c(h)$ at the contact depth h_c. Both hardness and modulus can then be computed thanks to Sneddon's equation. Hardness and modulus depends then deeply on the tip shape function, which must be precisely known. Some calibration procedure have been proposed in literature to measure the indentation tip profile. They are described in paragraph 1.2.6 (page 37) .

The computation of the Young's modulus of the sample also depends on the modulus and Poisson's ratio of the tip, and on the Poisson's ratio of the material. Nevertheless, Doerner and Nix have shown that the values of both Poisson's ratios do not need to be known with great precision to obtain an accurate value of the Young's modulus [18].

1.2.5 Continuous Stiffness Measurements mode

As previously detailed, elastic contact models extract the mechanical properties from contact stiffness. However, in static nanoindentation, contact stiffness can only be determined from the beginning of the unloading of indentation curves. This allows Young's modulus and hardness computation only at the maximal indentation depth. In order to measure mechanical properties during the whole nanoindentation test, a technique based on continuous stiffness measurements (CSM) has been developed around the 90's [20, 24, 25].

In CSM mode, an harmonic force is superimposed to the increasing nominal force, leading to small oscillations in indentation curves, as shown in figure 1.12. The ratio $(\frac{\partial L}{\partial h})_{elastic}$ is measured by a lock-in technique. Typically dynamic displacement amplitude is around 1-2 nm and dynamic force amplitude around fractions of μN. Thus, devices operating in CSM mode must have a subnanometer resolution in displacement and a resolution in force around the nano-Newton.

As described in a review by Li and Bhushan [26], system operating in CSM mode can be schematised by figure 1.12, with K_f the frame stiffness, K_s the stiffness of lateral springs that maintain the nanoindenter verticality, S the contact stiffness, C a damping coefficient due to the air in the capacitor displacement sensing system and m the indenter mass. The response of the system to an excitation of frequency $f = 2\pi\omega$ will lead to dynamic equations (1.16) and (1.17). These equations have to be adapted in the case of viscoelastic materials, where a dumping coefficient at the contact must be added [27].

$$\frac{L}{h(\omega)} = \sqrt{((S^{-1} + K_f^{-1})^{-1} + K_s - m\omega^2)^2 + \omega^2 C^2} \tag{1.16}$$

$$\tan(\Phi) = \frac{\omega C}{(S^{-1} + K_f^{-1})^{-1} + K_s - m\omega^2} \tag{1.17}$$

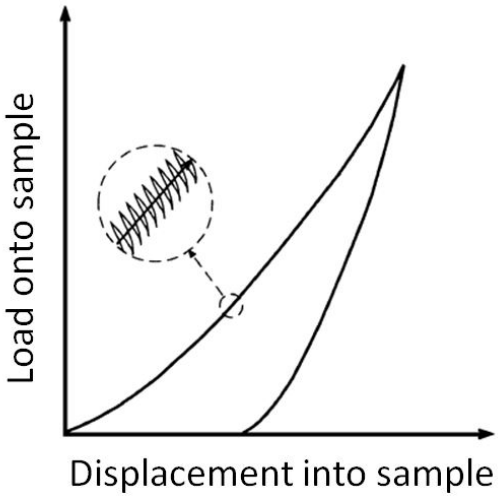

Figure 1.11: Load-displacement curve in CSM mode, from Li *et al.* [26]

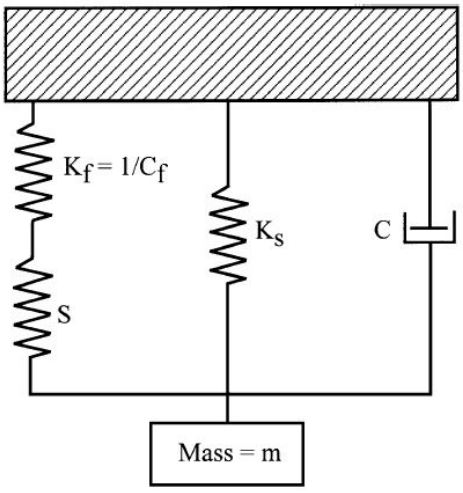

Figure 1.12: Schematic of the system in CSM mode, from Li *et al.* [26]

Thus, stiffness can be continuously computed during loading. Hardness and Young's modulus can then be determined versus the indentation depth. Thanks to CSM mode, nanoscale fatigue tests can also be performed, which is of great interest for magnetic storage and MEMS (Micro-Electro-Mechanical Systems) devices [26].

1.2.6 Calibration procedures

As mentioned in paragraph 1.2.4 (page 33), the tip shape function $A(h)$ is crucial for hardness and modulus computation. Moreover, during indentation, the measured displacement is due to the deformation field inside the sample but also the deformation field of the measurement chain, which brings an additional stiffness. This "frame stiffness" must also be known to substrate its effect from the measured displacement.

Historically, the shape function was determined by imaging nanoindentation residual imprints made at several contact depths. Nevertheless, numerous indent were necessary, and the imaging of contact areas by scanning electron microscopy [28] or atomic force microscopy as well as by using TEM replica [18] was time consuming.

In 1992, Oliver and Pharr [20] proposed a way to determine both the frame stiffness and the area function, without any imaging, following this procedure:

1. **Computation of the frame stiffness:** Indentation with several large penetration depths are performed on a material with a known modulus.

According to Sneddon's equation, the contact compliance $C_c = 1/S_c$ can be written by equation 1.18, with C_f the frame compliance.

$$C_c = C_f + \frac{\sqrt{\pi}}{2E^*} \cdot \frac{1}{\sqrt{A_c}} \tag{1.18}$$

The weight of the frame compliance is more important for large indentation, where the tip defect of the indenter is also negligible, and thus the tip can be considered as ideal.

For pyramidal indenter, the contact area can simply be related to the contact depth by equation 1.19, where LT is the leading term of the tip (LT can easily be computed by knowing the angles between the tip faces and the angle between the faces and the tip axis).

$$A_c = LT \cdot h_c^2 \tag{1.19}$$

By drawing C_c versus $1/\sqrt{A_c}$ at large indentation depths the frame compliance C_f can be determined.

2. **Shape function computation:** Indents are performed at several indentation depths on a material with a known modulus. Originally, Oliver and Pharr proposed the method with only 6 different depths. The contact depth is determined by Oliver and Pharr method, using Sneddon's equation with the frame compliance found in the previous step.

   The imprint size-versus-contact depth curves are fitted according to the relation given in equation (1.20), where $c_1, c_2 ... c_8$ are the fit coefficients. This relation corresponds to the shape function.

$$A(h_c) = LT \cdot h_c^2 + c_1 \cdot h_c + c_2 \cdot h_c^{1/2} + ... + c_8 \cdot h_c^{1/128} \tag{1.20}$$

This procedure can be done iteratively by using the obtained shape function to compute the frame stiffness, and so forth. This method is still used when using static nanoindentation.

For CSM mode, Oliver and Pharr [28] proposed in 2004 another calibration method, mainly based on the calibration method for static indentation. In this case the contact stiffness is known continuously with the contact depth. As a result only one test can be used for calibration. Moreover, there is much more available data, and a unique fit of the contact stiffness versus the contact depth can be done, giving the shape function coefficients $c_1, c_2 ... c_8$ as well as the frame stiffness S_c.

The Oliver and Pharr method is probably the most used calibration method. Nevertheless, this is no more than a mathematical fit of data, with no physical meanings behinds.

Thus, Hochstetter et al. [22] also proposed another way to calibrate the shape area of an indenter, but by taking into account the real meanings of the indenter shape deviation from the ideal shape, *i. e.* by clarifying the tip defect height.

In its model, Loubet [21] also proposed to use the real tip defect height of the indenter. According to Sneddon's equation, the contact stiffness S_c is directly proportional to the contact radius r_c, which is also proportional the to contact depth h_c for an ideal auto similar tip. As a consequence, the contact depth is proportional to the contact stiffness for ideal pyramidal and conical tips. However, when the tip exhibits a tip defect, the contact depth is proportional to the contact stiffness only over a given value of the contact depth. By extrapolating the linear part of the stiffness-versus-depth curve, a negative plastic depth $h_{p,0}$ is obtained at zero stiffness (figure 1.13). This corresponds to the tip defect height value. Loubet proposed to add this value to the measured plastic depth to obtain the contact depth, leading to equation 1.21.

$$h_c = \alpha_{loubet} \cdot (h_p + h_{p,0}) \tag{1.21}$$

1.3 Towards elasto-plastic constitutive law identification

Previously described models are elastic contact models, which means that material plasticity is not exploited, even if plasticity occurs during indentation. The aim of the models described in this section is to take into account plasticity in order to get more accurate results, but also to determine plastic properties of material, such as hardening coefficient or elastic limit. The final purpose of these models is to find a way to relate indentation curves to stress-strain curves from conventional tensile or compressive tests.

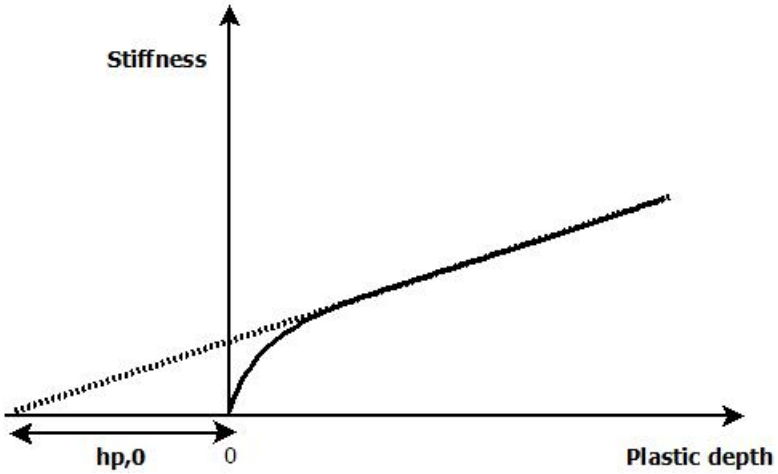

Figure 1.13: Linear extrapolation of the stiffness-versus-plastic depth curve, according to the Loubet's model.

1.3.1 Analytical models

Contact model for plastic material with low elastic deformation

Tabor [29, 30] was one of the first to study contact mechanic between a tip and a material from the point of view of the plasticity. In a paper of 1948 [29] he tried to relate hardness properties to the well known stress-strain curves of a steel material. Since depth sensing indentation methods were not fully developed at this time, its work is based on static hardness measurement, and so related to conventional Brinell, Meyer or Vickers hardness tests.

Tabor showed that the hardness of a material could be linearly related to the elastic limit or yield stress Y of a tensile test (equation 1.22), with c the proportional constant. For a frictionless spherical tip and an ideal plastic material, Tabor found that c could be approximated by 3 in the case where the plasticity domain is located all around the indenter. This is mostly the case for conventional static hardness measurements with high applied load, as performed before the 50's. The value of 3 is in good agreement with other results found in the literature for either spherical tips or conical tips [31, 32] in the plastic regime.

Nevertheless, according to Tabor, in the case where the load applied is small, the plastic domain is confined beneath the tip and the value of c is around 1.1.

$$H = c \cdot Y \tag{1.22}$$

In Tabor's work, the c values were found for highly pre-deformed materials, so that they are not able to work harden anymore. Thus, materials behave as perfectly plastic materials. In

that case, the elasticity limit Y does not depends on the amount of deformation. The elasticity limit is then constant in the deformation area of the material, *i. e.* around the tip.

In materials which are able to work harden, things are less obvious since the amount of work hardening is not the same everywhere around the tip. Since the elasticity limit depends on the amount of deformation, it is not uniform in the deformation area beneath the tip. In that case, only a representative value of the elasticity limit Y_r can be used.

According to Tabor, deformation in the case of a spherical punch is fully determined by the ratio $\frac{d}{r'}$ where d and r' are respectively the diameter and the curvature radius of the imprint. Usually, the curvature radius of the imprint r' can be approximated by the indenter radius $r = D/2$, and deformation is a function of $\frac{d}{D}$. Thus, the elasticity limit, which depends on the deformation for material which work harden, is a function of $\frac{d}{D}$.

In order to determine the linear relation between the deformation and the ratio $\frac{d}{D}$ Tabor measured the hardness of materials by using the size of the imprint left by an indenter. From the residual imprint, he derived the ratio $\frac{d}{D}$. From the hardness, he computed the value of the representative elasticity limit Y_r. Then, the strain ϵ corresponding to this elasticity limit was determined by using tensile test, and compared to the ratio $\frac{d}{D}$. Tabor showed that the ratio between the two values was about 0.2.

Thus, Tabor introduced the idea of a representative strain ϵ_r, which, for a spherical indenter, can be expressed by equation (1.23).

$$\epsilon_r = 0.2\frac{d}{D} \tag{1.23}$$

If the same work is done with a four-sided pyramidal indenter, Tabor showed that the representative strain is related to the semi angle ϕ of the equivalent conical tip by equation (1.24). The representative strain is constant during indentation ($\sim$ 7 % for a Berkovich indenter and $\sim$ 22 % for a cube corner tip), which is a property of self similar tips.

$$\epsilon_r = 0.2\cot\phi \tag{1.24}$$

Tabor was then able to relate the hardness measurements to the stress-strain curves of tensile tests, provided the use of several several imprint sizes in the case of a spherical tip, or several angles in the case of pyramidal tip. Nevertheless, some authors showed in the next the limits of

the Tabor model. Thus, Herbert *et al.* [33] have shown an error up to 50 % for the determination of the yield stress of aluminium alloys using Tabor model.

Contact model for elasto-plastic material

The limit of Tabor model is that it applies only for plastic material with no or low elastic deformations. In the case where elastic deformations cannot be neglected, the value of $c = 3$ announced by Tabor leads to pressures overestimations. Thus, following Tabor, Jonhson [34] also tried to relate hardness measurements to stress-strain properties for elasto-plastic materials. His work is based on the assumption of a spherical expanding cavity in an elasto-plastic material, as derived by Bishop et al. [35], Marsh [36] and Hill [37]. In this model, the hardness - expressed as the mean pressure p_m of the indenter on material - is related to Young's modulus E and elasticity limit Y for a tensile test, according to equation (1.25). A and B are constants which depend on the inclination angle β between the faces of the tip and the solid surface (for instance for pyramidal indenters $\beta = 90^o - \phi$, with ϕ the semi-angle of the equivalent conical tip).

$$\frac{p_m}{Y} = A + B \cdot \ln(\frac{E}{Y}) \tag{1.25}$$

For blunt indenters, where β is small, Johnson proposed that the indentation mean pressure p_m over the elasticity limit Y is simply a function of the inclination angle β and the material parameter $\frac{E}{Y}$. He proposed then to relate the mean pressure to the parameter $\tan(\beta) \cdot \frac{E}{Y}$. This parameter can be seen as the ratio between the strain imposed by the indenter, $\tan(\beta)$, and the yield strain $\frac{Y}{E}$, which is no more than the maximal strain that the material can accommodate before yielding. For strain-hardening materials and following Tabor's model [29, 30], Johnson also chose a representative value of the elasticity limit Y_r corresponding to a strain of $0.2 \cdot \cot(\alpha) = 0.2 \cdot \tan(\beta)$.

By drawing the ratio $\frac{p_m}{Y}$ versus the parameter $\tan(\beta) \cdot \frac{E}{Y}$ for a set of data given in literature, Johnson showed that when the parameter $\tan(\beta) \cdot \frac{E}{Y}$ is below 2, which typically corresponds to $p_m < Y$, the material deforms mainly elastically and equations for the mean pressure are given by equations of elastic contact models. The limit $\tan(\beta) \cdot \frac{E}{Y} = 2$ corresponds to the limit $c = 1.1$ given in Tabor model.

When $\tan(\beta) \cdot \frac{E}{Y}$ becomes higher than 100, which corresponds to $p_m > 2.8 \cdot Y$ the deformation mode becomes fully plastic, as in Tabor model for $c = 3$. This leads to pile-ups of the material around the indenter, as suggested by the rigid plastic theory of Lockett [38].

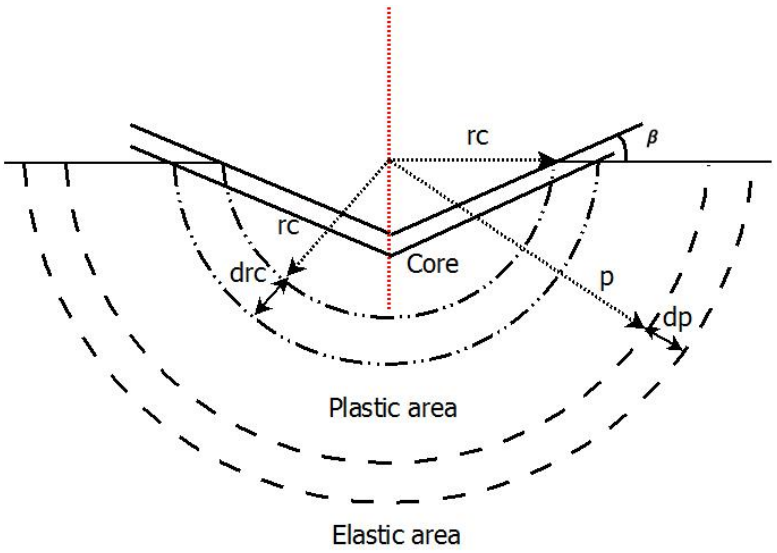

Figure 1.14: Hill's model of cavity adapted to Johnson's model.

Between the fully elastic regime and the fully plastic regime, plastic deformations were found to start beneath the indenter and to extend with increasing values of $\tan(\beta) \cdot \frac{E}{Y}$. In this stage, Johnson used expanding cavity model of Hill [37] to predict the relation between the ratio $\frac{p_m}{Y}$ and the parameter $\tan(\beta) \cdot \frac{E}{Y}$, except that instead of the cavity, Johnson introduced a hemispherical "core" around the indenter, with radius r_c.

The inclination angle β was introduced by the analogy between the expansion of the volume of the "cavity" and the volume displaced by the indenter. In the core, a hydrostatic mean pressure p_m was assumed. Outside the core, radial symmetries were assumed for stresses and displacements. Stresses and displacements were assumed to be the same as in Hill model with a cylindrical or spherical cavity expending in an elastic perfectly-plastic body. Then, since the mean pressure p_m inside the core has to be equal with the radial pressure at the boundary of the core, the Hill's model is able to determine $\frac{p_m}{Y}$.

Johnson found relatively good agreement between model and experiments, with a linear dependency between $\frac{p_m}{Y}$ and $\tan(\beta) \cdot \frac{E}{Y}$, provided that indentation tips are blunt enough to avoid friction (typically $\beta < 30^o$) and provided small strains.

Following Johnson's work, Kermouche [39, 40] proposed an analytical solution to relate the couple $(p_m;E)$ to the representative stress and the representative strain $(\sigma_r;\ \epsilon_r)$. This model has been successively validated with finite element simulation. However, the couple $(\sigma_r;\ \epsilon_r)$ extracted from nanoindentation measurements on various materials were found to differs from experimental tensile curves. According to Kermouche, this highlights the differences between the macroscopic mechanical properties (tensile tests) and the local mechanical properties (nanoin-

dentation), which are subjected to material inhomogeneities or surface hardening effects.

1.3.2 Numerical approach

Dimensional analysis model of Cheng and Cheng

Cheng and Cheng [41, 42, 43] were the first to apply dimensional analysis based on the Π theorem to derive relations between material properties, hardness, contact area, applied load and initial unloading slope. They considered a 3D frictionless ideal sharp rigid conical indenter. Elasto-plastic properties of the materials were defined as suggested by equation (1.26), with σ_u the stress, ϵ the strain, E the Young's modulus, Y the yield stress, K the strength coefficient and n the work hardening coefficient. By continuity the strength coefficient K is equal to $Y(\frac{E}{Y})^n$.

$$\sigma_u = E \cdot \epsilon \quad if \quad \epsilon < \frac{Y}{E} \qquad \sigma_u = K \cdot \epsilon^n \quad if \quad \epsilon > \frac{Y}{E} \tag{1.26}$$

Cheng and Cheng divided the dimensional analysis into two parts, corresponding to the loading and the unloading of nanoindentation testing. In both cases the quantities of interests are the load L and the contact depth h_c, from which the projected contact area A_c and the hardness H can be computed.

- **For loading**, the two quantities of interest L and h_c depend on six different parameters, respectively the Young's modulus E, the Poisson's ratio ν, the elasticity limit Y, the work hardening exponent n, the indenter displacement h and the semi angle of the cone α. Among these six quantities, there is only two independent units. Thus, according to the Π theorem, the quantities of interest can be written as a function of four dimensionless quantities. As a result, Cheng and Cheng obtained equations (1.27) and (1.28), with $\Pi_{L,l}$ and $\Pi_{h_c,l}$ two dimensionless functions.

$$L = Eh^2\Pi_{L,l}(Y/E, \nu, n, \alpha) \tag{1.27}$$

$$h_c = h\Pi_{h_c,l}(Y/E, \nu, n, \alpha) \tag{1.28}$$

- **For unloading**, the quantities of interest depend also on the maximal depth h_m for a same number of independent units. Thus, the quantities of interest depend on five dimensionless quantities. In particular, this time the load can be expressed by equation (1.29), with $\Pi_{L,u}$ a dimensionless function. By derivation, the initial slope of unloading curve $\frac{dL}{dh}|_{h=h_{max}}$, which corresponds to the contact stiffness S_c can be expressed and is given by equation (1.30), with $\Pi_{S,u}$ a dimensionless function.

$$L = Eh^2\Pi_{L,u}(h/h_m, Y/E, \nu, n, \alpha) \tag{1.29}$$

$$S_c = Eh_m\Pi_{S,u}(Y/E, \nu, n, \alpha) \tag{1.30}$$

Coming from these equations Cheng and Cheng showed that during loading, the load L is proportional to the square of the indenter displacement h, what was found by Love in the particular elastic case. The ratio h_c/h is also found to be independent of the indenter displacement. Consequently, the hardness is shown to be independent of the load L or of the indenter displacement h. This, again, was shown by Love in the particular case of elastic contact, and this is property of auto similar tips.
Nevertheless, during unloading, the load L is no more dependent on the square of the indenter displacement, since in this case the load also depends on the ratio $\frac{h_m}{h}$.
Cheng and Cheng also did a finite element analysis in order to examine the behaviour of each dimensionless quantities. They found four crucial points.

1. The loading curve alone do not allow the determination of both the elasticity limit Y and the work harden coefficient n. Indeed, according to finite element simulations, the dimensionless ratio F/Eh^2 clearly depends both on the dimensionless ratio Y/E and the dimensionless work hardening coefficient n. Thus, only an effective yield stress $Y^* = (YK)^{1/2}$ can be determined, provided that the Young's modulus E is known. Conversely, the Young's modulus can be obtained if the effective yield stress is known.

2. The dimensionless ratio $(1-\nu^2)\cdot S_c/(E\cdot r_c)$ is independent from both the ratio Y/E and the work hardening coefficient n. For a common semi angle α of 68^o and a Poisson's ratio of 0.3, the ratio $(1-\nu^2)\cdot S_c/(E\cdot r_c)$ was found to be around 2.17, which is really close

to the value of 2 given in elastic contact models by the Sneddon's equation (1.12). Thus Cheng and Cheng showed that Sneddon's equation is still valid for material with work hardening and residual stress.

3. The ratio between hardness and initial yield stress H/Y is a function of the ratio of initial yield stress over Young's modulus Y/E and of the work harden exponent n. For large value of Y/E, the ratio H/Y was found to be roughly independent of n. Only in this case the yield stress can be determined from hardness measurements. Nevertheless, for small value of Y/E, the ratio H/Y was found to depends on the work hardening coefficient n. By using a value of 0.1 for the strain, which is the value corresponding to the representative yield stress of Tabor model, Cheng and Cheng also validated the concept of representative yield stress Y_r, by showing that in this case, the ratio H/Y_r is independent of n and only depends on the ratio Y_r/E. In the case of low Y_r/E ratio, Cheng and Cheng found the value of 3 given for the coefficient c in Tabor model. Cheng and Cheng also showed that the value of H/Y_r is a function of Y^r/E, what did not appear in Tabor's model.

4. Cheng and Cheng also studied the evolution of h_c/h (*i. e.* the amount of sink-in or pile-up) versus both Y/E and n:

   - For high Y/E ratio ($Y/E > 0.2$), Cheng and Cheng found values of h_c/h lower than 1, evidence of sink-in, whatever the value of the n coefficient.
   - For low values of Y/E ratio and high work hardening coefficient($n > 0.3$), h_c/h was also found to be lower than 1. This corresponds to elastic solids of Sneddon's model.
   - For low values of Y/E ratio and low values of n, the ratio h_c/h is found to be higher than 1, which is the evidence of pile-up. In particular, this is the behavior expected for perfectly plastic material ($n = 0$).

Cheng and Cheng also studied the difference between their model and the Oliver and Pharr model [41], where pile-up is not described. They found that for high values of Y/E ($Y/E > 0.5$), where their is only sink-in, both models give similar result for h_c/h versus Y/E. But for low value of Y/E and n exponent Oliver and Pharr model leads to an underestimation of the ratio h_c/h. This corresponds to an underestimation of the projected contact area, and then an overestimation of the hardness. For low value of Y/E and high value of the n exponent, the

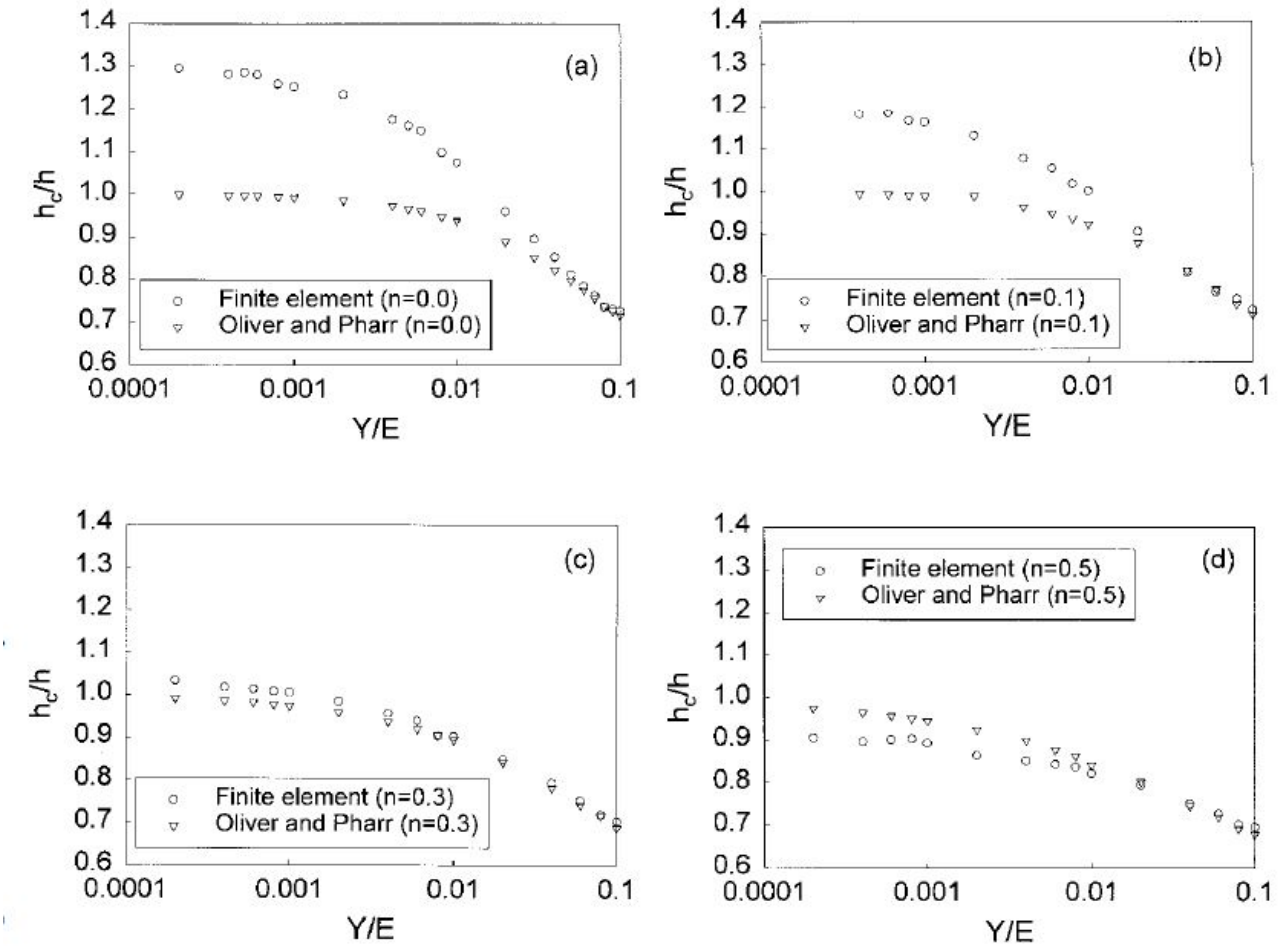

Figure 1.15: h_c/h versus Y/E from Oliver and Pharr model and numerical computation, from Cheng and Cheng [41].

Oliver and Pharr model also give incorrect results, leading this time to an overestimation of the h_c/h ratio, and then to an underestimation of the hardness. The transition points seems to be for a n exponent around 0.3 where both models give similar results (figure 1.15).

The inverse method

Following Cheng and Cheng, some authors tried to use the dimensional analysis to extract the stress-strain properties of a material from indentation curves.

Thus, Dao *et al.* [44] tried the first to use dimensional analysis approach to determine a stress-strain curve from an indentation curve. The work of Dao *et al.* is based on the inverse methods previously proposed by Giannakopoulos *et al.* [45]. The inverse methods proposes to simulate with the finite element method the indentation of a set of mechanical behavior representative of the indented material. The experimental load-displacement curve is then compared to the

simulated curves and the properties of the material is deduced from the closest simulated mechanical behaviors.

Using dimensional analysis, Dao *et al.* reduced the problem and were able to obtain three independant parameters of a stress-strain curve, allowing the drawing of the entire curve. Typically the output parameters were the yield stress Y, the stress at 3.3 % of representative strain $\sigma_{0.033}$, the equivalent modulus E^* or the work hardening parameter n.

Nevertheless, even if the method gives reasonable values for the output parameters, it also gave some incoherency, and even sometimes two sets of solutions for the same input. In particular, even if Dao *et al.* found good results for the determination of equivalent modulus E^* and representative stress $\sigma_{0.033}$, the determination of strain hardening coefficient n was less precise. Conversely, Dao also gave a direct method to determine indentation curves from stress-strain data, and results obtained were quite reliable.

Following the work of Dao et al., Casals and Alcala [46] showed that even if it is possible to determine the indentation parameters from a stress-strain curve, the problem is not bijective. He finally proposed a way to determine which is the correct set of parameters, by checking if the residual imprint exhibits sink-in or pile-up. Indeed, the two solutions obtained are far enough to exhibit completely different contact topology.

Bucaille [47, 23] proposed an other way based on dimensional analysis to determine the stress-strain parameters from indentation curves. Bucaille used Dao's method for the determination of the stress-strain curve parameters, but using two tips with different angles (usually a cube corner tip and a Berkovich tip), as previously proposed by Tabor [30]. Bucaille also improved the Dao's method by taken into account the friction between the tip and the material, as well as indenter geometry. This method is now the most commonly used inverse method in literature. However, the use of a Berkovich tip and a Cube corner tip to determine the yield stress is questionably, since with a Berkovich tip the deformation starts at 7 % of plastic strain, which is far from the elastic limit. This issue is overcome by using a spherical tip, as proposed by Kalidindi and Pathak [48], where their is a smooth transition between elastic and plastic deformations.

The direct method

The main default of inverse method is that the work hardening is simulated using Hollomon-like laws, which are not based on physical mechanisms such as dislocations movements in material. Some authors [49, 50, 51, 52] have proposed direct method to model indentation of

FCC materials. They are based on crystalline plasticity, which implements a finite element model. The first, Chang *et al.* [53, 54] have reported comparison between direct method simulations and experimental measurements on copper single crystal (figure 1.16). The only adjustable parameter was the dislocation density, which was validated by X-Ray diffraction measurements [55].

Vu Hoang *et al.* [56, 57] have improved the model of Chang by using an implicit formulation instead of an explicit formulation in the finite element model, and by adapting it to several tips geometries and thin film.

Direct methods give robust results, however so far they only apply on ideal samples (FCC structure and single crystals). All the modelling are also based on continuous mechanics and they do not include the issues of sample size effects or nucleation of plasticity.

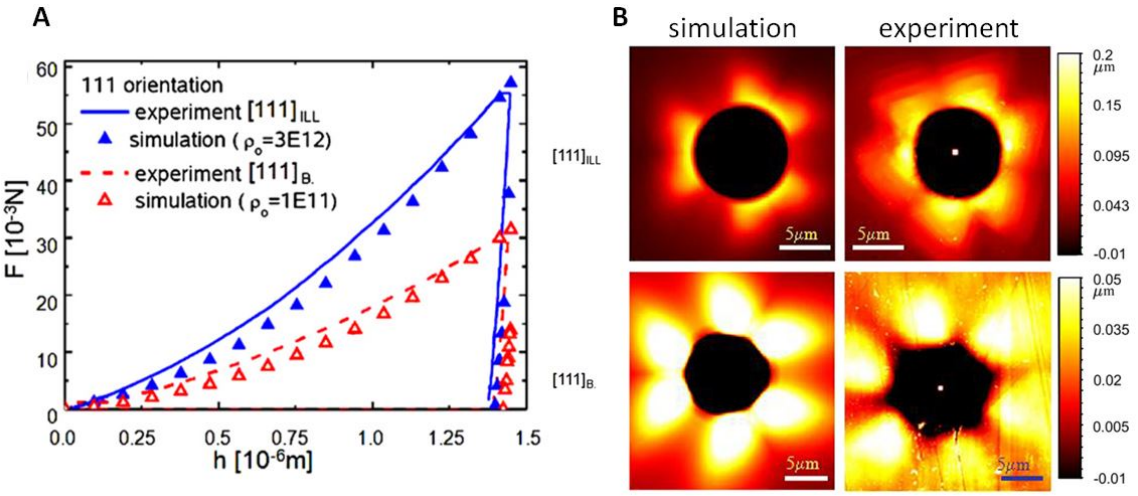

Figure 1.16: a: Experimental and simulated load-displacement curves for two copper single crystal, and b: corresponding simulated and experimental AFM pattern, from Chang *et al.* [55]

1.4 *In situ* mechanical testing in electronic microscopes

Nanoindentation is a powerful technique to assess local mechanical properties of a material. Conventional nanoindenter are used to measure Young's modulus or material hardness. The discrete events on the loading curves, the so-called "pop-in" are related to fast events occurring in the material. However, in conventional ex-situ nanoindenter, there is no simultaneous imaging during nanoindentation. Only residual imprints are observed by optical microscopy or

atomic force microscopy (AFM). Thus, the nature of mechanical discontinuities is not always known.

As discussed in [58], this issue was the driving force for the development of *in situ* nanoindenter in electronic microscope, *i. e.* either scanning electron microscope (SEM) or transmission electron microscope (TEM).

One of the first examples of an *in situ* SEM nanoindentation system was reported by Rabe *et al.* [59]. Electron micrographs have been collected at various points of the indentation process. Each point of the load-displacement curve was correlated to microstructural changes such as cracks or pile-ups.

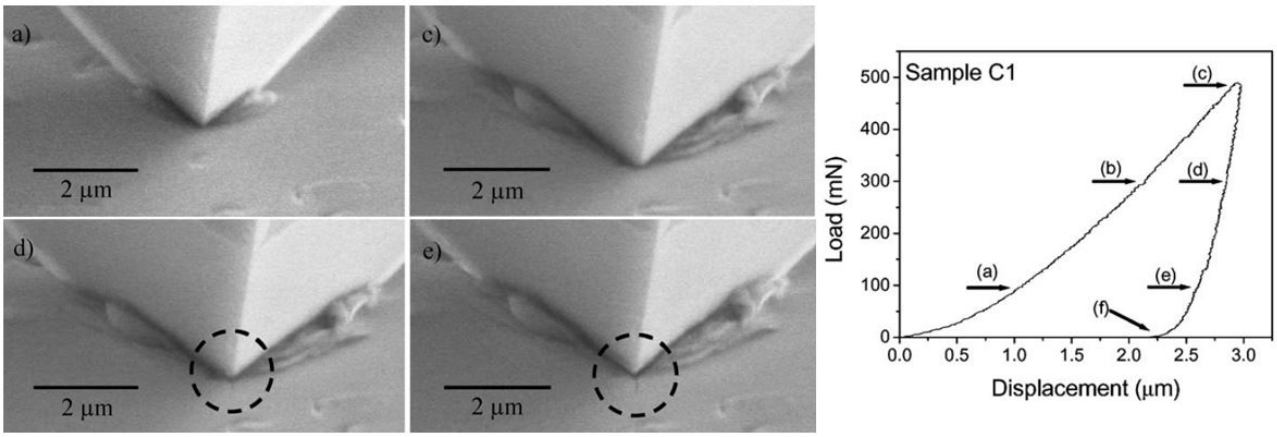

Figure 1.17: *In situ* SEM indentation TiN/SiN stacks. Adapted from [59].

Similar observations have been reported on aluminum and gold thin films, but with much smaller vertical displacements ($\sim$ 200 nm) [60]. Moser *et al.* [61, 62] have studied the correlation between mechanical bursts and shear bands activity on zirconium based metallic glasses. Deformation and sink-in of an elastomer during nanoindentation was also investigated [63]. Rzepiejewska-Malyska *et al.* [64, 65] also observed adhesive and cohesive failure for high loads on multilayers of TiN and CrN. In [65] the team has reported a direct calculation of the contact area from SEM images. Data differed significantly from the theoretical prediction of the standard Oliver and Pharr approach [20]. Study from Vecchione *et al.* [66] on yttrium-stabilized zirconia thin film also concluded to an underestimation of the Young's modulus obtained by Oliver and Pharr model, due to significant elastic structural deformation during nanoindentation. This highlights the need to refine theoretical understanding of tip-to-surface interaction, and reinforces the benefits of *in situ* imaging during indentation.

Although nanoindentation *in situ* SEM improve understanding of micron and sub-micron effects during indentation, it fails to follow crack propagation through thin films. For that purpose,

nanoindentation *in situ* TEM was widely developed. Stach *et al.* [67] have first conducted *in situ* TEM measurements on bulk aluminium, titanium carbide, silicon and aluminium thin films. Nucleation, propagation and interaction of fractures and dislocations has been successively followed during indentation (figure 1.18). Several metals have been investigated by *in situ* TEM nanoindentation, from aluminum [68, 69], which is ideal due to its ductile properties, to iron based system [70, 71, 72] and more complex alloys [73].

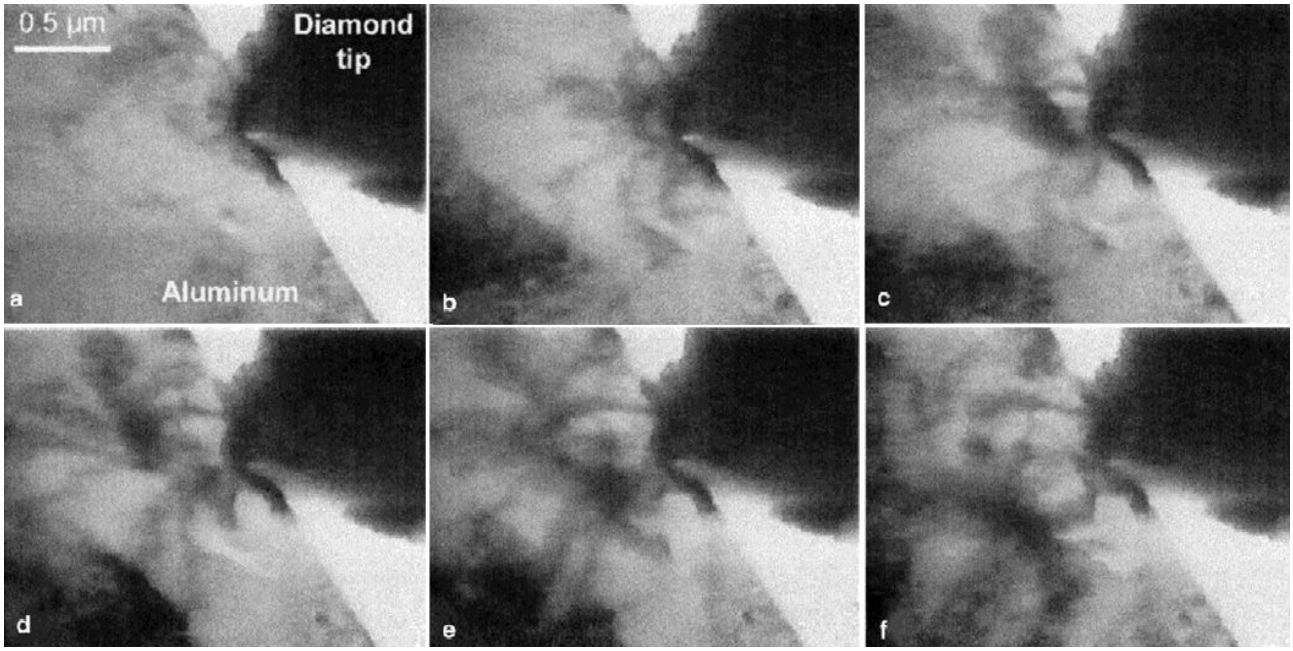

Figure 1.18: *In situ* TEM indentation of an aluminium FIB sample. Adapted from [67].

Chapter 2

Electrical contacts

This second chapter reports a literature review on electric contacts. The first section focuses on current transfer across a contact interface. The electrical contact topology is first described. Resistance models across the so-called "a-spots" are given and the effect of the oxide layer at the contact interface is discussed. Finally, heat generation due to current flow through the contact is detailed.

The second section focuses on electrical measurement techniques through a mechanical contact. Both electrically coupled scanning probe microscopy and nanoindentation are detailed. The contribution of electrical measurements to the understanding of mechanical behavior during indentation is discussed.

2.1 Current transfer across the contact interface

2.1.1 Electrical contact topology

The contact interface between two solids is never smooth, and since solid surfaces are always rough, contact occurs at several contact spots. The real contact area is then different from the apparent contact area (figure 2.1). The number and size of these contact spots depend on the roughness of both solids, but also on the load L at which the two solids are pressed. Indeed, if the two solids are not perfectly rigid, they can deform elastically and plastically under load, leading to an increase of the real contact area.

When an electric current passes through two solids, from the anode solid to the cathode solid, the electrical contact area is reduced to "a-spots" [74, 75, 76] (figure 2.1). These "a-spots" correspond to the electrical contact area. They are even smaller than the real contact area,

which corresponds to the mechanical contact area. Indeed, the contact behavior is affected by the presence of insulating layers due to contaminants or oxides. This reduces the effective electrical contact area compared to the mechanical contact area.

The contact resistance is governed by the size, the shape and the density of these "a-spots", at which distortion of current lines occurs (figure 2.2), leading to an increase of the total resistance. In case of isotropic roughness, the a-spots can first be approximated as circular spots of radius a. This approximation will be used in what follows.

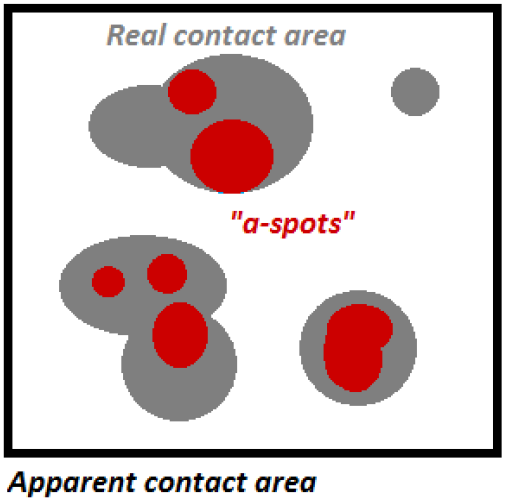

Figure 2.1: Difference between apparent contact area, real contact area and the so-called "a-spots", with mechanical contact area in grey and electrical contact area in red.

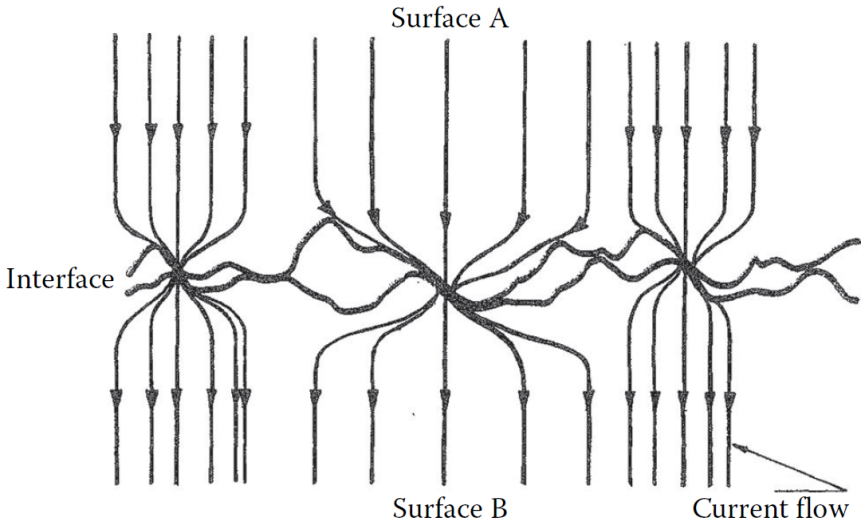

Figure 2.2: Schematic diagram of a bulk electrical interface, according to Timsit [75].

2.1.2 Influence of the a-spot size on the contact resistance

Maxwell's model and the diffusive regime

In classical electrical contact theory, electrical currents are supposed to be continuous and smoothly varying through a geometrical constriction. This is the diffusive regime, were electronic transport is represented as continuous. This assumption can be made if the a-spot size is much larger than the electronic mean free path ($a >> \lambda$). In this regime, the contact resistance is then equal to the spreading resistance $R_{spreading}$, which accounts for the constriction of the current lines at the asperity. Assuming a-spots to be circular and the two solids to be semi-infinite and parallel to the average plane of the electrical interface, the spreading resistance can be described by Maxwell equation (2.1), with ρ the solids resistivity (ρ=($\rho_1 + \rho_2$)/2 for solids with different resistivity), and a the radius of the circular a-spots.

$$R_c = R_{spreading} = \frac{\rho}{2a} \tag{2.1}$$

a-Spot shape	Spreading resistance	Comments
Circular	$\rho/2a$	
Elliptical	$\rho/2a \cdot f(\gamma)$	$f(\gamma)$ is a form factor depending on $\gamma = \sqrt{a/b}$, with a/b the aspect ratio of the elliptical constriction [74, 76]
Rectangular	$2k\rho/S^{0.63}$	S is the constriction area and k varies from 0.36 to 1 (with ρ in Ω.mm and S in mm) while the constriction width varies from 1 to 10 mm [76, 77]
Square or Circular ring	$R_0 \cdot F(\xi)^{-1}$	R_0 is the full circular or square resistance, $F(\xi)$ is a conductance form factor depending on $\xi = t/a$ or with t the ring thickness. For rectangular ring $a = \sqrt{(Lw)}$, with L and w the rectangular dimensions [76, 78]

Table 2.1: Spreading resistance for different a-spot shapes.

If a-spots are elliptic, squared spots, or rings, the spreading resistance is adjusted as summarized by table 2.1.

The model must be modified if the thickness of the constriction cannot be neglected, as for a metallic contact along a crack in an insulating film [75].

In the case where both solids exhibit specific shape, the previous model also has to be ajusted: for cylinder of radius R of the same order of magnitude of the constriction size (typically $R < 20a$), the formula turns to equation (2.2), as proposed by Cooper *et al.* [79].

$$R_c = \frac{\rho}{2a}(1 - \frac{a}{R})^{3/2} \tag{2.2}$$

Most commonly, if both solid surfaces are not parallel to the average plane of the electrical interface, but make a θ angle with the interface plane (figure 2.3), the contact resistance is modified as proposed by Sano [80] in equation (2.3). For $\theta = 0$, the equation is equivalent to Maxwell equation (2.1). Sano have also shown that this modification could not be neglected for θ angle higher than 10°, which can be the case for rough surfaces, or, obviously, during indentation. Surprisingly, this adaptation of Maxwell model is only rarely taken into account in the literature.

$$R_c = \frac{\rho}{4a}\tan(\frac{\pi + 2\theta}{4}) \tag{2.3}$$

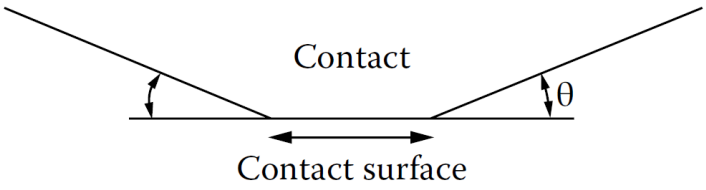

Figure 2.3: Schematic of the a-spot vicinity, with the solids in contact making a θ angle with the interface plane, according to Sano [80].

Sharvin's model and the ballistic regime

If the contact size is much smaller than electron mean free path ($a << \lambda$), the assumption of continuous electrical current fails, and the electronic transport becomes ballistic. The resistance

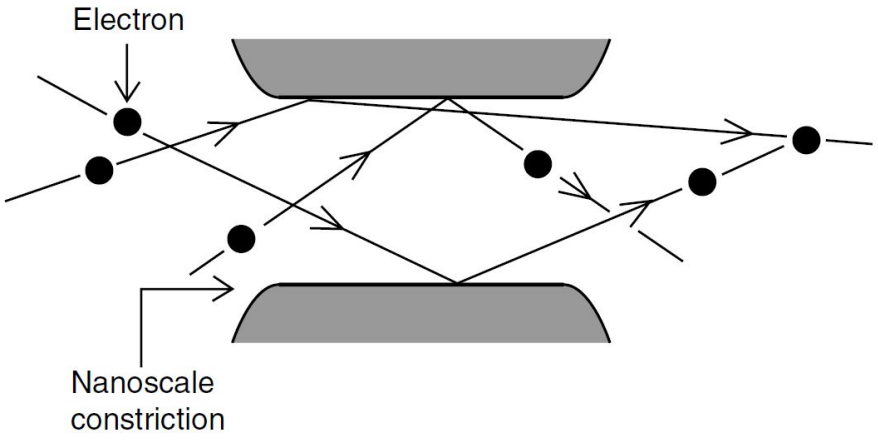

Figure 2.4: Ballistic motion of the electrons through a small constriction, from Brauvonic *et al.* [76]

is due to irregular motion of electrons and their collisions with the "a-spots" walls (figure 2.4). Then the contact resistance is equal to the Sharvin resistance $R_{Sharvin}$ [81] (equation 2.4), also called Knudsen resistance elsewhere [82, 83].

$$R_c = R_{Sharvin} = \frac{4\rho\lambda}{3\pi a^2} \tag{2.4}$$

Mixed models for the transition regime

In the intermediate case where the contact size and the electron mean free path are of the same order of magnitude ($a \sim \lambda$), some authors have proposed a combination of both ballistic and diffusive components.

Wexler [82] has first derived a function (equation 2.5), as the sum of Sharvin and Maxwell resistances, weighted by a $\gamma(K)$ function, where $K = \lambda/a$ is the Knudsen number.

The $\gamma(K)$ function tends to 1 when K tends to zero ($a >> \lambda$), and in this case the contact resistance is equivalent to the Maxwell resistance; and it tends to $9\pi^2/128 \simeq 0.694$ when K tends to the infinity ($a << \lambda$).

Mikrajuddin *et al.* [84] have shown that the $\gamma(K)$ function could be approximated by equation (2.6), but in this case, $\gamma(K)$ tends to zero when K tends to the infinite.

Nikolic and Allen [85] were able to approximate the $\gamma(K)$ function to a simple expression (equation 2.7), which differs only by 1 % from their most accurate numerical calculation, and which thus can be used for practical purpose. Figure 2.5 shows the Nikolic and Allen approximation

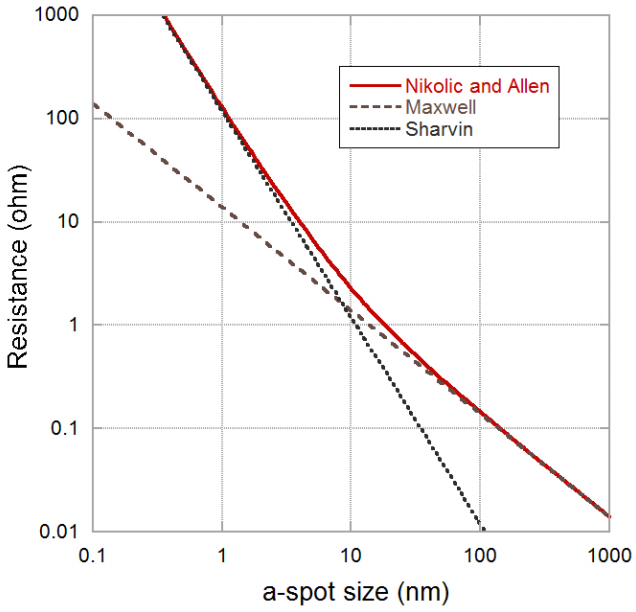

Figure 2.5: Nikolic and Allen approximation for contact resistance, compared to Maxwell and Sharvin models, $\lambda = 10$ nm.

of the resistance, compared to Sharvin and Maxwell models, for a mean free path λ of 10 nm. In this approximation, the $\gamma(K)$ function tends to 0.624 when K tends to the infinity, which is closer to the asymptote in the case of Wexler model. They have also shown that the naive approximation of the contact resistance as the sum of the Sharvin components and the Maxwell component (*i. e.* $\gamma(K) = 1$) only differs from 11 % when K tends to 1.

$$R_c = R_{Wexler} = \frac{\rho}{2a} \cdot \gamma(K) + \frac{4\rho K}{3\pi a} \tag{2.5}$$

$$\gamma_{Mikrajuddin}(K) = \frac{2}{\pi} \int_0^\infty \exp^{-Kx} \operatorname{sinc}(x) dx \tag{2.6}$$

$$\gamma_{Nikolic}(K) = \frac{1 + 0.83K}{1 + 1.33K} \tag{2.7}$$

For materials with an electronic mean free path of $\sim$ 10 nm (typical order of magnitude for metals), simple derivations using equation (2.7) show that Maxwell contribution to the contact resistance becomes higher than 90 % for a contact size larger than 100 nm ($a = 10\lambda$). Thus, below a contact size of 10λ, Sharvin contribution to the contact resistance cannot be neglected

and a mixed representation must be adopted. Inversely, Sharvin contribution to the contact resistance becomes higher than 90 % for contact size smaller than 1 nm ($a = 0.1\lambda$).
This was also seen experimentally by some authors [83, 86]. By measuring the voltage drop when passing an electrical current through an aluminum/aluminum contact, and by comparing it to the calculated voltage drop using the continuous Maxwell model, Timsit [83] have shown that Sharvin contributions became noticeable for a contact size below 30 nm. Using a scanning tunelling microscope (STM) inside a transmission electron microscope (TEM) Erts *et al.* were able to measure conductance of gold point contacts as a function of contact size, from a single atom to 20 nm. They have shown that the data fit well the Wexler model (figure2.6), for a mean free path of ~ 3.8 nm, which is 10 times shorter that the mean free path of gold at room temperature. Similar results were also reported elsewhere [87, 88]. According to Erts *et al.* this low mean free path could be due to the large number of scattering centers due to contact formation, and not from an increase in temperature at the interface, which was estimated to be of only 2K.

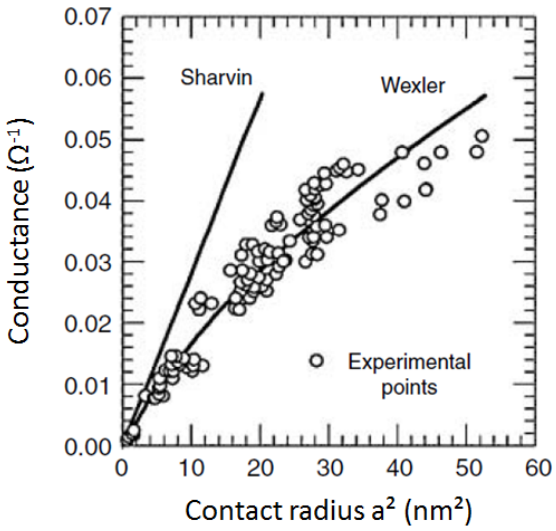

Figure 2.6: Erts *et al.* [86] measurements and Wexler interpolation using $\lambda = 3.8$ nm.

2.1.3 Multi a-spot models

Paragraph 2.1.2 deals with a unique contact spot, but in practice the contact is made of a large number of micro-contacts (figure 2.1), also called clusters of a-spots. Holm [74] have shown that for a large number of small equal spots distributed uniformly over a circular area, the conductance was the sum of all the parallel conductances corresponding to each individual

spots and an additional term, which accounts for interaction between the different spots, as described by equation (2.8). This interaction terms is due to additional potential created at a contact spot by current passing through the other contact spots. This additional resistance disappears if a-spots are far enough from each others.

$$R_c = \rho(\frac{1}{2na} + \frac{1}{2\alpha}) \tag{2.8}$$

where n is the number of a-spots, a the radius of a spot and α is the cluster radius, or Holm radius

Greenwood [89] extended this model for a-spots of different sizes, introducing the mean a-spot size $\bar{a}$. He also approximates the Holm radius as $(\frac{3\pi}{16n^2}\sum_{i\neq j}\frac{1}{s_{ij}})^{-1}$, where s_{ij} is the distance between two a-spots). This leads to equation (2.9). The error between this approximation and the exact formula (which involves individual a-spots sizes) is small in case where there is no correlation between the size of a contact spot and its position in the cluster.

$$R_c = \rho(\frac{1}{2n\bar{a}} + \frac{3\pi}{32n^2}\sum_{i\neq j}\frac{1}{s_{ij}}) \tag{2.9}$$

where n is the number of a-spots, a the radius of a spot and α is the cluster radius, or Holm radius

Figure 2.7 shows several a-spot distributions calculated by Greenwood for the same Holm radius and for different equivalent single circular a-spot area.

Greenwood also pointed out a crucial point. Taking the example of the uniform a-spot distribution of figure 2.7 a, Greenwood showed that the contact size could not be easily determined from contact resistance by assuming a single circular a-spot with the same resistance. This is due to the two contributions to the contact resistance, *i. e.* the parallel resistance contribution and the interaction term.

Indeed, Greenwood calculated the different resistance contributions for increasing a-spot size of the configuration of figure 2.7 a. This is typically what happens during mechanical loading. Results are shown in table 2.2. By increasing a-spot size, parallel resistances contributions deeply decrease. However, the cluster size does not increase a lot, and thus the interaction term only slowly decreases. Consequently, the total resistance decreases much less than in the

hypothesis of a single contact. Here, as the total resistance decreases by a factor 4, the contact area in the assumption of a single circular contact should increase by a factor 16. But in this case, considering the mean a-spot radius increase, the total electrical contact area is multiplied by a factor 625. Thus, the electrical contact area can only be deduced from the resistance in the upper limit where we have a reasonably large number of contacts, which are not to small.

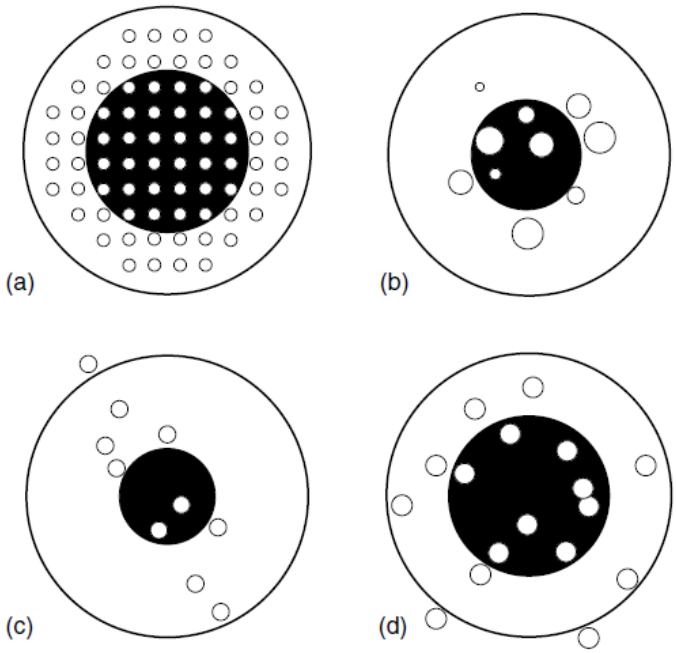

Figure 2.7: (a) Regular array of a spots as used in Holm's model [74] (b, c, d) Clusters of a-spots as used in Greenwood's model [89]. The black area is the single continuous contact corresponding to the same resistance; the outer circle is the Holm radius [76].

a-spot radius	**Total resistance**	**Parallel resistance**	**Holm radius**	**Interaction term**	**Radius of single spot of same resistance**
0.02	0.4226	0.3289	5.34	0.0937	1.18
0.04	0.2577	0.1645	5.36	0.0932	1.94
0.1	0.1581	0.0658	5.42	0.0923	3.16
0.2	0.1238	0.0329	5.50	0.0909	4.04
0.5	0.1012	0.0132	5.68	0.0880	4.94

Table 2.2: Greenwood [89] values for an uniform a-spot distribution.

2.1.4 Effect of an oxide film at the interface

Influence of an oxide film on contact resistance

As mentioned earlier, the electrical contact behavior is deeply affected by the presence of insulating layers, such as contaminants or oxide layers. In literature, the problem of insulating thin film on conductive substrate has been extensively studied, especially for native aluminium oxide in aluminum-aluminum contact [90, 91, 92, 93, 94, 95]. Different cases can be considered, depending on the hardness of the oxide film.

As described by Mohamed and Washburn [96], when two metals covered with their oxides are pressed together, plastic deformation occurs in the metal, and dislocation loops approach the surface, where they are blocked by the oxide, which acts as a barrier. If the oxide film is deformable, it means that the ratio of the film hardness over the metal hardness is low enough, and in this case dislocations multiply in the oxide, and both metal and oxide accommodate plastic deformation together. Thus, no fracture is expected in the insulated layer. This also occurs for low loading contacts. In this case the resistance of the film R_{film} is added to the total resistance, as given by equation (2.10), with $\rho_{1/2}$ and $d_{1/2}$ the resistivity and the thickness of both oxides.

Most often the electrical resistivity of the film is really high, and the electrical behavior is in fact dominated by tunnelling effect, provided that the oxide layer is small enough (typically few nanometres, as for aluminium native oxide). Then the film resistance can be expressed by equation (2.11) [97], provided that both conductive solids are the same.

$$R_{film} = \frac{\rho_1 d_1 + \rho_2 d_2}{A} \tag{2.10}$$

$$R_{tunnelling} = \frac{t_{film}}{A}\left(\frac{h}{e}\right)^2\left(\frac{2}{3\sqrt{2m_e\Phi}}\right)\exp\left(\frac{4\pi t_{film}}{h}\sqrt{2m_e\Phi}\right) \tag{2.11}$$

with h, m_e and e the Planck constant, the electron masse and the electron charge, and Φ the tunnelling barrier energy for the considered metal-oxide-metal assembly

On the contrary, if the oxide film is harder than the metal, or if the mechanical loading is large, Mohamed and Washburn [96] explained that dislocation pile-ups at the metal-oxide interface is most often relieved by a crack opening in the oxide, normal to the interface.

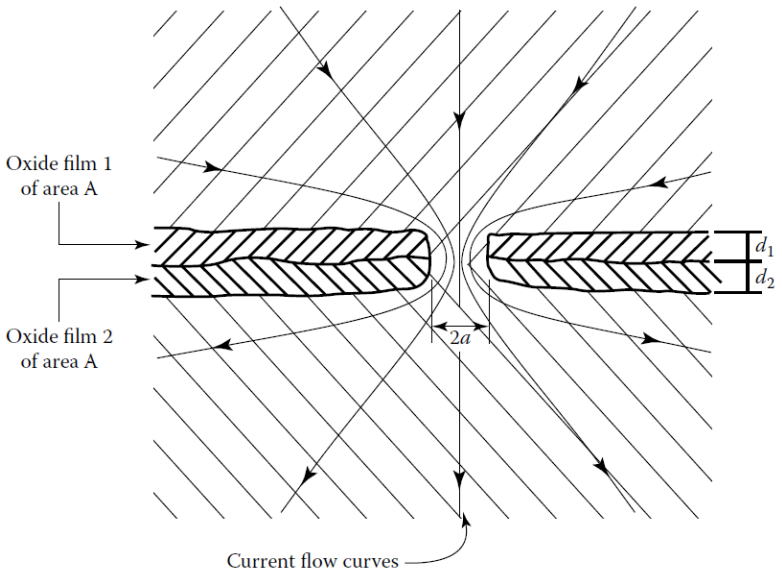

Figure 2.8: Schematic view of an a-spot surrounded by oxide films [75].

In this case, free metallic areas can overlap one above the other, provided two conditions: i) a crack in one oxide coincides with a crack in the other, creating a gap ii) the loading is sufficient for metal extrusion to occur through the created gap. This was experimentally verified by Le *et al.* [94, 95]. Usual contact resistance expressions can then be used, as those given in sections 2.1.2 (page 55) and 2.1.3 (page 59). However the new topology involving cracks within the oxide must be taken into account (figure 2.8).

The oxide fracture mechanism can be affected by many variables, such as the surface roughness, which was shown to facilitate the oxide fracture [91] or the boundary lubrication [94, 95], which affects the contact resistance by being trapped in the oxide gaps.

Electrical breakdown of oxide films

When the electric field applied through an insulator exceeds a critical value E_c, the resistance of this dielectric suddenly drops and the insulator becomes conductive: this is the electrical breakdown. In the case of oxides, this electrical breakdown was shown to be caused by the formation of defects, leading to a conductive path within the oxide [98, 99]. Gloos *et al.* [99] have experimentally studied the electrical breakdown of aluminum oxide, and they have found a strong dependency between E_c, the critical electrical field, and t, the aluminium oxide thickness, as shown in equation (2.12). This dependency could be explained by positive or negative excess of charges in the oxide.

$$E_c = \frac{1.6}{t^2} \tag{2.12}$$

with E_c the critical electrical field, in $GV.m^{-1}$, and t the oxide thickness, in nm

Oxide growth during contact

Another point has to be taken into consideration: oxide growth during mechanical contact. In all the studies mentioned above, the oxide layer was supposed to remain unchanged, but this is not uncommon that it grows with time during the contact. Indeed, if metals are polarized at different voltages, the two electrodes respond like a battery, provided that the atmosphere acts as an electrolyte. This basically leads to anodic oxidation. This was experimentally shown by Bouchoucha *et al.* [100] in the case of a cooper-steel contact, under different atmospheres (figure 2.9). The oxide growth was shown to accelerate for higher electric field, and to be more important under humid air or O_2 atmosphere, instead of dry air or argon atmosphere.

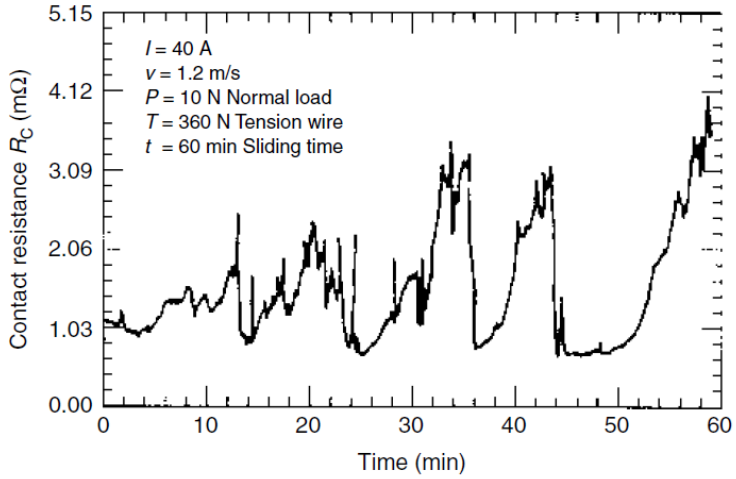

Figure 2.9: Evolution of electrical contact resistance versus time of a copper-steel contact, according to Bouchoucha *et al.* [100]

2.1.5 Heat generation at the interface

In the diffusive regime, when a large current is applied within an a-spot, the crowding of current lines generates a thermal gradient normal to the constriction, and large Joule heating is produced at the contact. Thus, the temperature increases and can disturb the mechanical contact behavior, by causing creep, or even local melting [74], or by enhancing electromigration,

as well as diffusion, which can increase the growth rate of intermetallics [101]. Thus, the knowledge of the temperature within electrically heated a-spot is a crucial point.

With the assumption that outer surfaces of the conductors are thermally insulated from the environment, the heat generated within the a-spot can only be dissipated by conduction within the solids in contact. It follows that electrical potential and isothermal surface within the conductors coincide. Under these conditions, Kohlraush [102] proposed a general equation between the voltage drop V within the contact and the maximum temperature T_m reached at the interface (equation 2.13).

$$V = (2\int_{T_1}^{T_m} \lambda_1\rho_1 dT)^{1/2} + (2\int_{T_2}^{T_m} \lambda_2\rho_2 dT)^{1/2} \tag{2.13}$$

with $\lambda_{1/2}$ and $\rho_{1/2}$ respectively the thermal conductivity and the electrical resistivity of both solids in contact, and $T_{1/2}$ the temperature of their outer surfaces

Kohlraush equation can be simplified if both thermal conductivity and electrical resistivity are roughly constant with the temperature, leading to equation (2.14), if both solids are identical. Note that these equations do not depend on the a-spot dimensions, and are valid for any contact shape.

If thermal conductivity and electrical resistivity vary with temperature, this dependence has to be taken into account in the integration of equation (2.13). Usually, thermal conductivity can be expressed as $\lambda = \lambda_0(1 - \beta T)$ and the electrical conductivity as $\rho = \rho_0(1 + \alpha T)$, where β and α are the temperature coefficients of the thermal conductivity and the electrical resistivity, respectively.

In addition, metals follow the Wiedemann-Franz law, that relates thermal conductivity and electrical resistivity to temperature as $\rho\lambda = LT$, where L is the Lorentz constant ($L = 2.45 \cdot 10^{-8} V^2K^{-2}$). Injected to Kohlraush equation, this leads to equation (2.15).

Using these equations, Timsit [75] showed that the temperature within an a-spot significantly deviates from the bulk temperature for voltage drops as small as 10 mV.

$$\frac{V^2}{8\rho\lambda} = T_m - T_0 \tag{2.14}$$

$$\frac{V^2}{2L} = T_m^2 - T_0^2 \tag{2.15}$$

All the above equations derived from Kohlraush model, which account for a diffusive and continuous electrical regime, as for Maxwell model. It applies well in the case where the a-spot size is not too small.

In the ballistic regime, which means when the a-spot size is smaller, typically below 100 nm, Timsit [103] showed experimental deviations from Kohlraush model for aluminum-aluminum contacts. Timsit proposed two explanations for these variations.

The first one is the Sharvin component of the resistance, which prevails for small contacts. However, Sharvin resistance accounts for the ballistic electrical regime, and so originates from the collisions between the charge carriers and the "a-spots" walls, and not from charge carriers scattering by impurities, defects or by the lattice of the medium. Thus, it is not responsible for Joule heating. In this case, the increase in temperature as computed by Kohlraush model is clearly overestimated. This point was extensively investigated by Timsit [83].

The other explanation could be the heat dissipation through an oxide layer. This was also investigated by Konchits and Kim [104] on steel-steel contacts. They derived an expression based on Blok and Jaeger's work [105, 106], which relates overheating $Q_m = T_m - T_0$ to the current density j (equation 2.16). Konchits and Kim studied the dependence of overheating on the current density for different a-spot sizes and specific film resistances (Figure 2.10). The heating starts for a critical current density j_{cr} at which an increase in temperature of 1K occurs. Typically, the critical current density is 4-5 orders of magnitude lower for contact with poorly conductive film than for film free contacts. Then, for all samples, an increase of current density of one order of magnitude causes an overheating of $\sim$ 200 K. Further increases in current density leads to faster temperature increases, with an overheating of $\sim$ 1000 K for a total increase of current density of two orders of magnitude.

$$j = \frac{2}{\pi}\left(\frac{2Q_m\lambda}{a(2a\rho + R_f^*)}\right)^{1/2} \tag{2.16}$$

with R_f^* the specific resistance of the film

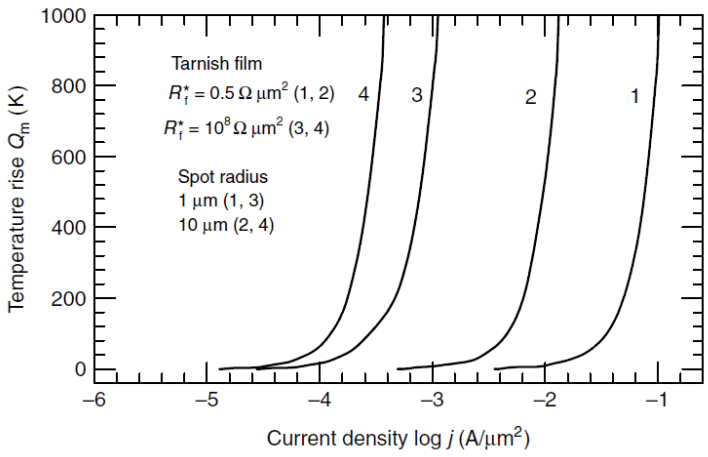

Figure 2.10: Temperature rise for contact with different a-spot size and film with different specific resistance, according to Konchits and Kim [104].

2.2 Electrical measurements during mechanical testing

In the first section of this chapter, electrical contact has been detailed. This second section focuses on electrical measurements techniques through a mechanical contact. Electrically coupled scanning probe microscopy as well as nanoindentation are reviewed. However this review is limited to technique which measure the electronic transport trough a mechanical contact. Techniques involving capacitive measurements are detailed in chapter 7 (page 239).

2.2.1 Development of scanning probe microscopy

Scanning probe microscopy (SPM) based on electrical characterisation techniques gives both topographic and electrical information. Topographic map can be simultaneously recorded with 2D current maps (scanning spreading resistance microscopy or conductive atomic force microscopy) or 2D capacitance distributions (scanning capacitance measurements). During such experiments a probe is put into contact with a sample. A voltage is applied between the probe and the sample, enabling either capacitance or current measurement at the contact. In this configuration a mechanical contact is established as well as an electrical contact. Thus, even if SPM is not a complete mechanical testing machine, it involves both mechanical and electrical contacts. Large developments have been performed in this field for the understanding of electronic transport through a mechanical contact. This paragraph deals with some of the electrical characterisations developed around SPM, especially methods involving atomic force microscopy (AFM).

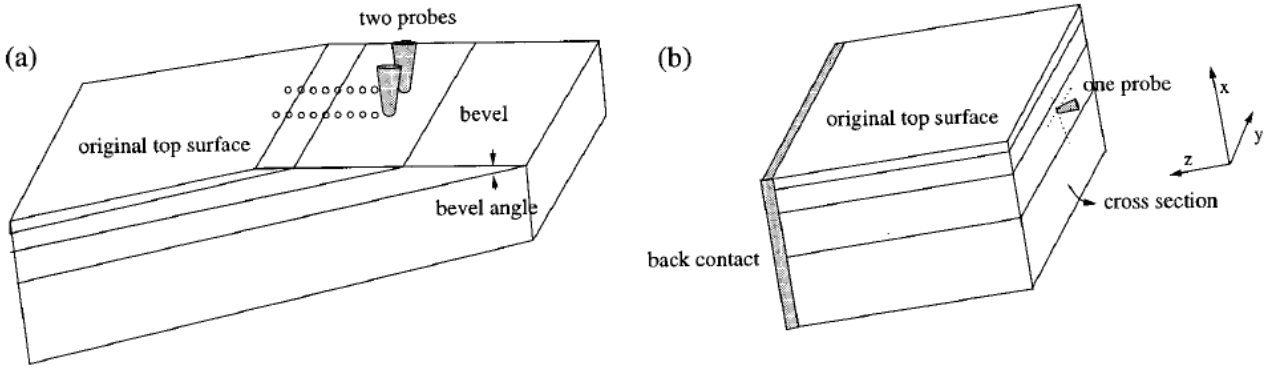

Figure 2.11: Schematic of traditional SRP (a) and SSRM (b) methods [107].

Scanning Spreading Resistance Microscopy (SSRM)

Conventional Spreading Resistance Profiling (SRP) has been developed to profile doping in semiconductors. SRP is a dual probe technique, involving two 2 µm diameter tips (usually tungsten carbides), separated by 20 µm, which are pressed on the sample surface. A controlled current is injected, while the voltage drop between the probes is measured. Due to its large probe scale, SRP can only be applied on a beveled sample, involving basic beveling steps such as bevel rounding, reverse carrier spilling, and thin layer corrections due to layer roughness. Sample preparation is then time consuming. Moreover, the large distance between both probes and the probes size hinders fine lateral resolution.

As an improvement to SRP, Scanning Spreading Resistance Microscopy (SSRM) was conceived in 1992 by Vandervorst *et al.* [108]. It was developed to measure carrier distribution with sufficient spatial resolution and accuracy on downscaling semiconductors [109]. Investigated samples are essentially silicon sample.

SSRM, sometimes called nano-SRP, is quite similar to SRP. Nevertheless it differs from few points (figure 2.11):

- SSRM is a unique probe technique. The current flowing from a conductive AFM probe to a semiconductor sample is measured for an applied DC bias. The return path is provided by a back contact on the sample. For current measurement a logarithmic current amplifier providing a typical range of 10 pA to 0.1 mA is used.

- The probe size is around 10 nm, which is much smaller than for SRP probes. Typical SSRM probes are silicon tips coated by PVD with boron-doped diamond.

- Due to its small probe scale SSRM can be conducted directly on cross sections (fig-

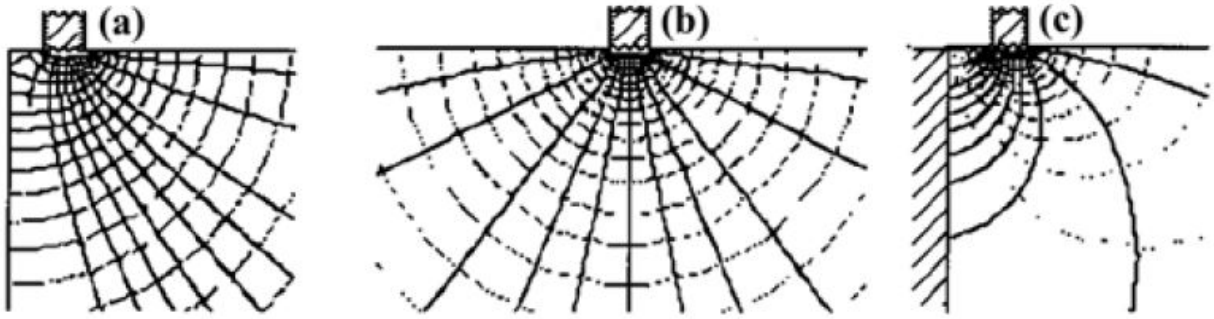

Figure 2.12: Current distributions (solid lines) and equipotential curves (dashed lines) under a SSRM probe nearby an insulating boundary (a), in a semi-infinite uniform layer (b) and nearby a perfectly conducting boundary (c) [107].

ure 2.11b). This avoids the basic beveling steps.

During SSRM measurements, the force applied on the sample is rather large (>μN, *i. e.* 1-10 GPa for a 10 nm probe size) to create an intimate contact between the probe and the sample. Consequently, the contact resistance is negligible with respect to the spreading resistance. The resistance obtained can then be analysed by Maxwell or Sharvin models, depending on the indentation depth. As for SRP, the theoretical equation relating the measured resistance to the resistivity, and thus to the carrier distribution, is given by Maxwell equation (2.1).
However, De Wolf *et al.* [107] have underlined that electrical properties of the contact depends in fact on many factors, such as the precise probe shape, the surface state concentration and energy distribution and the force applied on the probe. Equation (2.1) must then be adapted and turns to equation (2.17), where $R_{barrier}$ accounts for the above factors. CF is a correction factor due to the effect of the carrier profile in the neighbourhood of the probe. Indeed, current distribution at the probe is affected by the presence of more insulating or more conducting area in the regions surrounding the probe, as shown on figure 2.12.

$$R = CF \cdot \frac{\rho}{4a} + R_{barrier} \tag{2.17}$$

During SSRM, spectroscopy measurements are usually conducted along sample profile. This gives calibration curves, *i. e.* resistance-versus-resistivity curves at different location and for different biases, and I-V curves at different location (figure 2.13). I-V curves have either an ohmic-like shape in highly doped areas ($\rho_{sample} < 0.001$ Ωcm) or a Schottky shape on lowly-doped areas ($\rho_{sample} > 0.01$ Ωcm) [110]. The Schottky behavior is not surprising since neither

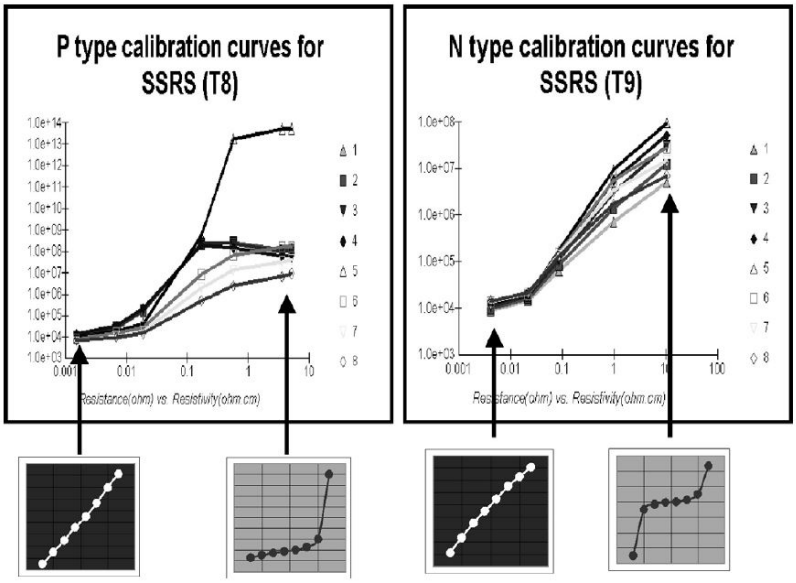

Figure 2.13: Experimental calibration and I-V curves for highly and lowly doped region of p-type and n-type samples, from Eyben *et al.* [110]

the probes (silicon coated with diamond) nor the sample (silicon) are metals. The configuration is far from a metal-metal contact. For highly doped areas, the ohmic-like shape can be explained by tunnelling current through the potential barrier of the contact.
Implementing tunnelling, Schottky-like contact [110] and surface states [111] on the contact modelling allows generation of I-V curves or calibration curves qualitatively close to the experiments (figure 2.14). For highly-doped material surface states can usually be neglected.

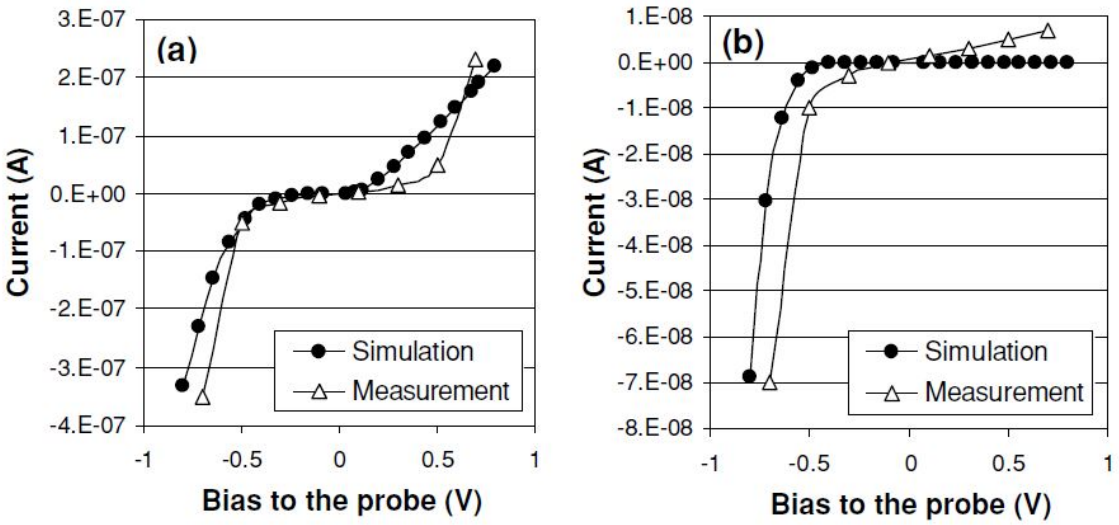

Figure 2.14: Simulated and experimental I-V curves for lowly doped n-type and p-type silicon samples, from Eyben *et al.* [109]

Conductive Atomic Force Microscopy (Conductive AFM)

Contrary to the SSRM technique, which has been developed for semiconductor characterisation, conductive atomic force microscopy (conductive AFM) has been developed for dielectric film characterisation. As for SSRM, an AFM probe scans the sample surface and current flowing from the AFM probe to a sample back contact is measured for an applied DC bias. Nevertheless, the force involved for conductive AFM are much lower than for SSRM, typically 1-100 nN, which corresponds to 1-100 MPa for a 10 nm probe size. For such forces, oxide layers are expected to stay intact, and thus they affect the electrical measurement: for conductive AFM, contact resistance is not negligible with respect to the spreading resistance.

Originally, conductive AFM was developed for dielectric film thickness measurements [112, 113, 114, 115, 116] or dielectric degradations and breakdown studies [117, 118, 119], but its applications have been expanded to other electrical characterisations such as local conductivity [120, 121], V-defect investigation [122], charge transport [119, 123] or electron emission [115].

The choice of the probe used for conductive measurements is crucial. Indeed, the tip must have a high aspect ratio, a small tip curvature, a good conductivity and be highly resistant against wear. As for SSRM measurements silicon tips coated with boron-doped diamond can be used, but they have a high electrical resistance and display non linear I-V curves [124]. Nevertheless, they provide satisfactory mapping resolution [113]. Due to their high conductivity and their acceptable tip curvature (10-40 nm), conductive metal coated tips are preferentially used. Si tips with metallic coating were found to be more brittle than Si_3N_4 tips with metallic coating [113]. The use of entire W tips [124] have also been investigated to scan a gold sample. For extremely high current density (10^8 A/cm^2), W tips were found to undergo anodic oxide growth at the apex, and eventually no more electrical conduction were observed. Highly-doped Si tips can also be used without coating, but O'Shea *et al.* [125] have found that while scanning a graphite sample, the tips were subject to strong anodic oxidation for intermediate current density (10^3 A/cm^2), which leads to unreliable results.

Some authors have also found that oxide thickness computation depends on tip material [115]. This could be due to different electron emission behaviour depending on the material, as well as electrochemical effects, presence of a water meniscus, wear effect or tip contamination.

During conductive AFM, local I-V measurements can also be performed. Depending on conduction type, I-V curves can be fitted, which allows oxide thickness computation. Some authors [119, 126] have described the different conduction mechanisms which can occur when a tip con-

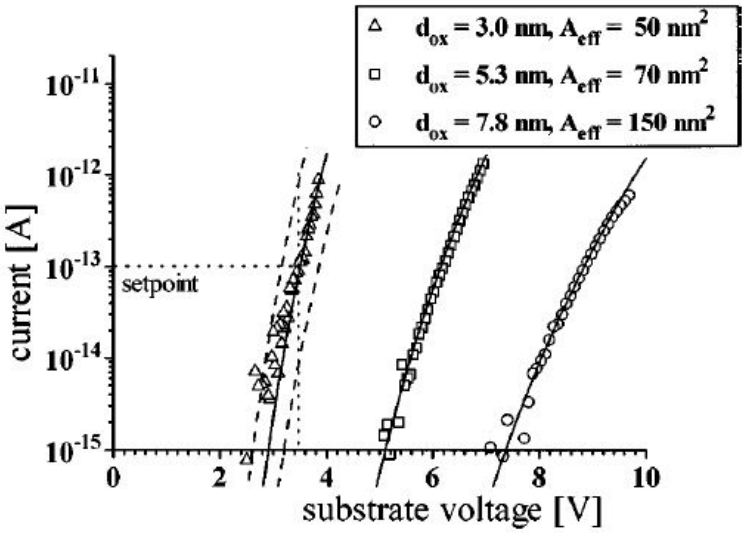

Figure 2.15: I-V characteristics measured by conductive AFM on $Si0_2$ films of different thickness (respectively 3 nm, 5.3 nm and 7.7 nm, measured by ellipsometry). The straight line represent the Fowler-Nordheim current fit to experimental data. Fit parameter are shown in the inset. According to Olbrich *et al.* [112]

tacts an oxide layer, which means for a metal-oxide-semiconductor (MOS) structure. These conduction mechanisms can be dominated by:

- Direct tunnelling, which is not voltage dependant. This essentially occurs for ultra thin insulator (<4nm). This mechanism is schematized in figure 2.16 A and occurs when charges travel through the oxide potential barrier.

- Fowler-Nordheim tunnelling, *i. e.* induced by external fields. Fowler-Nordheim mechanism (equation 2.18) is the main mechanism involved for conductive AFM [112, 112, 115, 116], where an high electric field is involved. High electric field pulls down the conduction band edge of the oxide, which enhances tunnelling, as shown on figure 2.16 B. It happens for typical oxide layer of 5-10nm. Fowler-Nordheim tunnelling leads to a linear relation between $\ln(I/V^2)$ and $1/V$.

$$I \propto V^2 \exp(-\beta \frac{t}{V}) \tag{2.18}$$

- Schottky emission (equation 2.19) [119, 121]. Schottky emissions are characterised by charges being injected into the oxide conduction band. The oxide potential barrier can

be lowered by the electric field (image-force effect), as shown on figure 2.16 C. Schottky emission mechanism is characterized by a linear relation between $\ln(I)$ and $\sqrt{V}$.

$$I \propto T^2 \exp(-\beta \frac{\sqrt{e^3 V/\epsilon}}{kT}) \tag{2.19}$$

- Poole-Frenkel emission (equation 2.20) [123]. Poole-Frenkel emission considers charges already trapped in the oxide layer (figure 2.16 D), and describes how these trapped charges are injected into the oxide conduction band. It is characterized by a linear relation between $\ln(I/V)$ and $\sqrt{V}$.

$$I \propto V \exp(-\beta \frac{\sqrt{e^3 V/\epsilon}}{kT}) \tag{2.20}$$

- Hopping conduction (equation 2.21) [126, 127]. Charge carriers can pass by tunnelling from one trap to an other trap of the insulator (figure 2.16 E). This is due to high concentration of traps within the insulator and a charge carrier energy lower than the maximal energy barrier between two traps. It is characterized by a linear relation between $\ln(I/V)$ and $1/T$.

$$I \propto V \exp(\frac{-T_0}{T}) \tag{2.21}$$

- Space charge limited conduction (equation 2.22) [126, 127]. When the charges injected by the cathode are important, the conduction is limited by the insulator ability to transport charge carriers and to evacuate them through the anode. This conduction is characterized by the Child's law where I is proportional to V^2.

$$I \propto V^2 \tag{2.22}$$

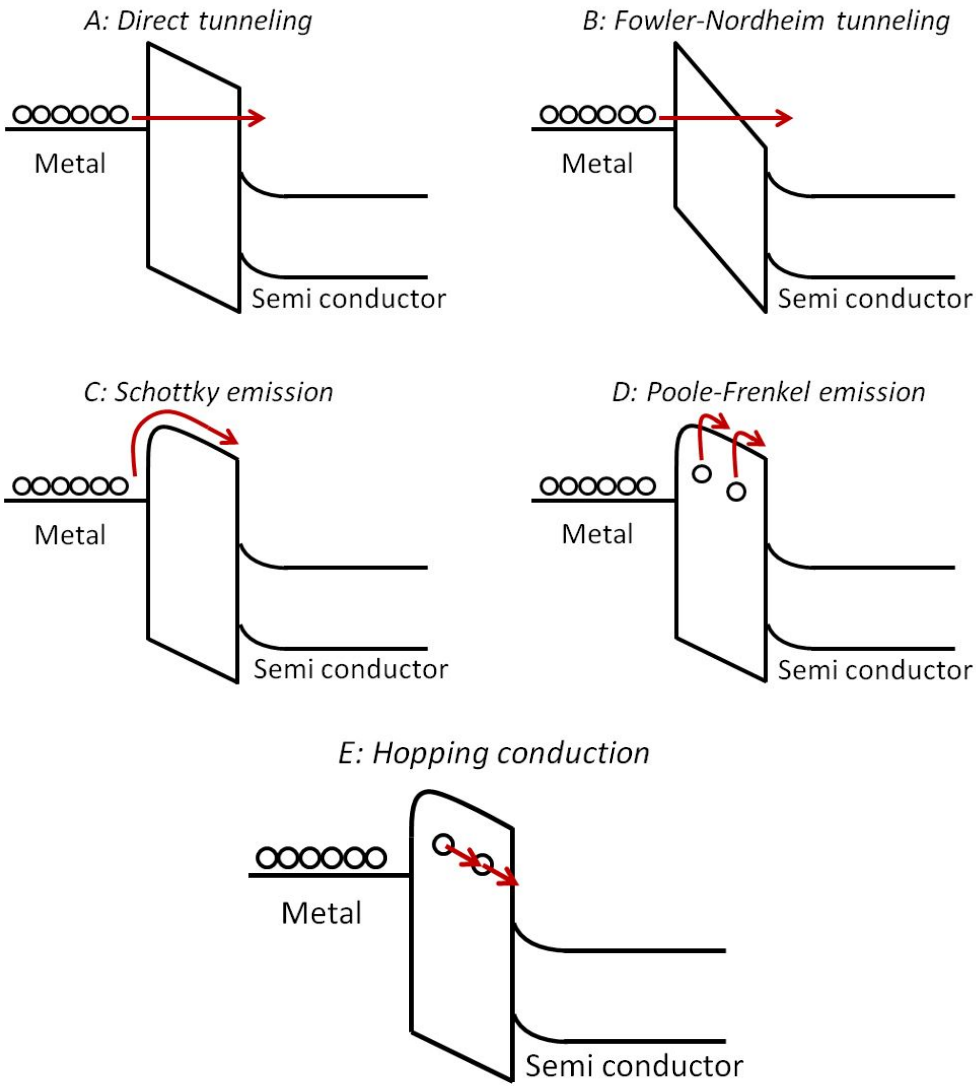

Figure 2.16: Band diagrams of different conduction mechanisms in MOS systems.

Most studies in conductive AFM are on silicon with silica oxide of tens of nanometers (2-40 nm) [112, 113, 115, 116, 117, 118, 119]. In case of $Si/Si0_2$ samples, electric field applied are around 10 $MV.cm^{-1}$, which is close to the critical electric field of silica (20-40 $MV.cm^{-1}$). Such high field enables the study of dielectric degradation and breakdown [117, 118, 119]. Lower electric field of 0.01-0.1 $MV.cm^{-1}$ are sometimes used for the investigation of weaker dielectrics, such as GaN films [121], InGaN/GaN films [122].

Nevertheless, even for high electric fields, relatively low current densities are reached ($<$10 $A.cm^{-2}$). However, some inhomogeneities on current maps are assumed to be localised area with higher current flow, and thus higher current density [119, 128]. These "dark spots" (figure 2.17) are supposed to act as breakdown precursors. Some authors have studied the effect of dislocations on current conduction [119, 122, 128]. In GaN/InGaN, GaN/GaN or

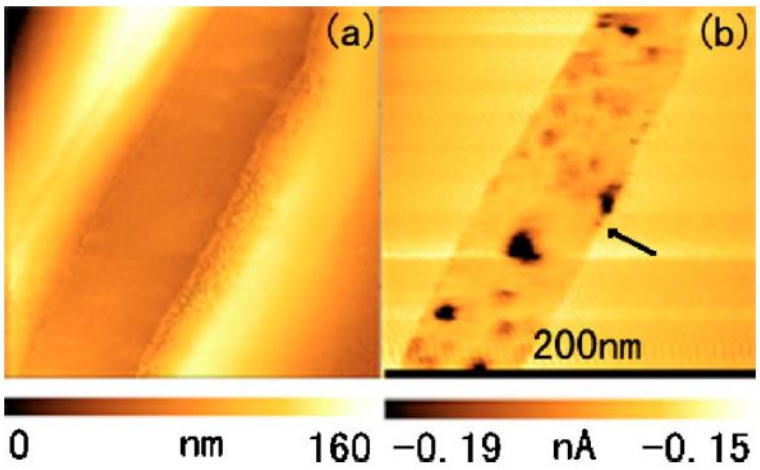

Figure 2.17: Conductive AFM topography map (a) and corresponding current map, showing the presence of "Dark spots" on a 4 nm $Si0_2$ area. From Sun *et al.* [119]

AlGaN/GaN structures, screw dislocations and at a latter extent mixed-dislocations where found to act as pathways for leakage currents and responsible for these "dark spots".
Some investigations have been conducted on the impact of the environment on conductive AFM measurements. Lanza *et al.* [129, 130] have shown that operating measurements under different atmospheres (Air, dry nitrogen or ultra high vacuum) does not change the conduction mechanisms involved. However the presence of water meniscus between the tip and the sample increases the effective electrical area, degrading the spatial resolution and increasing the current passing through the contact (figure 2.18). Only experiments conducted at ultra high vacuum shows a current increasing with increase mechanical contact area. Indeed, under air or dry nitrogen, the effective electrical area is much larger than the mechanical contact area. Consequently the variation of mechanical contact area appears negligible when compared to the effective electrical area.
Some authors have studied the anodic oxidations occurring on sample during conductive AFM-measurements [131]. On $Si/Si0_2$ sample anodic oxidation was found to occur only when a positive bias is applied to the sample with respect to the tip [131, 120]. In this configuration electric field is supposed to attract OH^- ions from the atmosphere, which reacts with the sample, leading to an oxide growth beneath the tip. The presence of a water meniscus and atmosphere oxygen seems essential for anodic oxidation. Thus, no anodic oxidation was seen by Lanza *et al.* [129] [130] when operating under ultra high vacuum condition. An electric field around 10 $MV.cm^{-1}$ is also necessary for anodic oxidation.

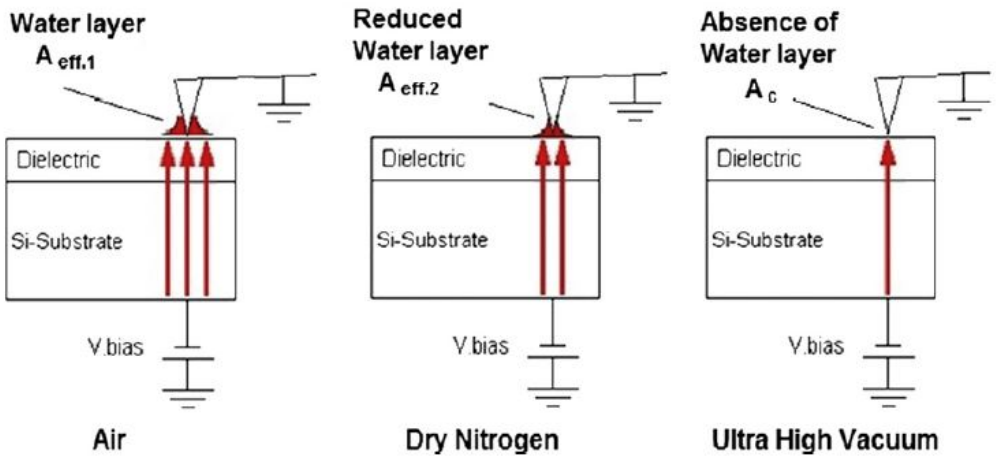

Figure 2.18: Schematic of the current flow through the tip under different atmospheres. From Lanza *et al.* [130]

2.2.2 Electrical measurements during instrumented indentation

Contrary to SPM techniques, where only the load applied to the sample is controlled, instrumented indention allows both force control and displacement monitoring. With instrumented indentation coupled with electrical measurements, mechanical behavior can then directly be correlated to electrical behavior. As discussed in a recent review from Nili *et al.* [58], since the 1990's, effort have been made to perform instrumented indentation coupled with electrical characterisation. This paragraph details the state-of-the art of electrically coupled instrumented indentation.

One of the main initial motivations for electrically coupled indentation is the local monitoring of semiconductor phase transformation. Thus, electrical monitoring of phase transformation on Si, Ge and GaAs was extensively studied in microindentation [132] as well as in nanoindentation [133, 134, 135, 136, 137, 138]. On loading, a transformation from crystalline Si-I or a-Si to a conducting metallic phase (Si-II for the case of c-Si) occurs at a critical pressure. This phase nucleation within the bulk material is sensed in real time during indentation tests. Although in earlier studies the two contacts for electrical measurements were taken on the sample [133, 136] leading to a lack of sensitivity, recent studies have performed current measurement directly from the indenter tip, with a sample back-contact [137, 138]. This considerably increases the measurement sensitivity. This configuration is now commonly used for electrically coupled indentation.

Electrically coupled indentation has also been developed for fast mechanical event monitoring. Thus, Pethica and Tabor [140] have investigated oxide layer cracks during loading of a tungsten

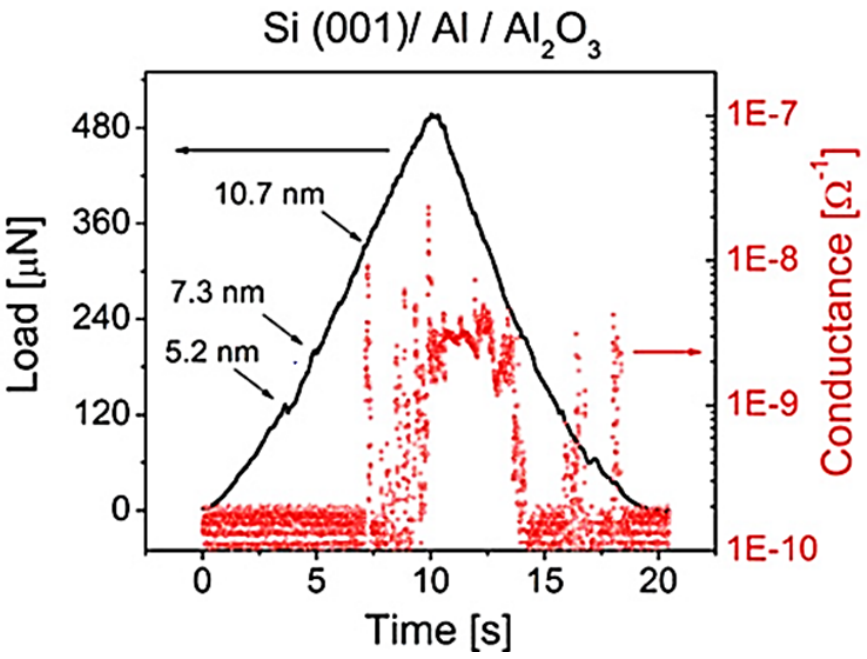

Figure 2.19: Real-time acquisition of electrical and mechanical data during indentation of oxidized Al. From Stauffer *et al.* [139]

tip on nickel. However the set-up used was not instrumented in depth and only the load was monitored. Plastic response of native oxide on thin metallic films has also been investigated by Stauffer *et al.* [139] with instrumented nanoindentation (figure 2.19). Small indenter displacement (below 20 nm) has been correlated with a current rise, showing evidence of oxide fracture. Thin film delamination was observed by Nguyen *et al.* [141] with an electrically coupled nanoindenter.

In a work from Duvivier [142] electrical monitoring during nanoindentation was also performed to study the degradation of MEMS (microelectromechanical systems) micro switches attributed to the degradation of the electrical contact.

Efforts are also made to estimate contact area from electrical measurements. Indeed, this would give additional information for mechanical equations, and would avoid the use of models for contact area computation, as Loubet or Oliver and Pharr models (see section 1.2.4, page 33). A first attempt was made by Fang *et al.* [143], by relating non linear I-V curves performed during nanoindentation to instantaneous contact area. However this study was performed with microindentation and this approach is not valid anymore for nanoindentation. More promising results were obtained by Sprouster *et al.* [144], where the resistance-versus-depth curve during indentation of Au sample by a vanadium carbide tip was successively fitted using the Maxwell spreading resistance expression (equation 2.1). This allows sample resitivity computation, or

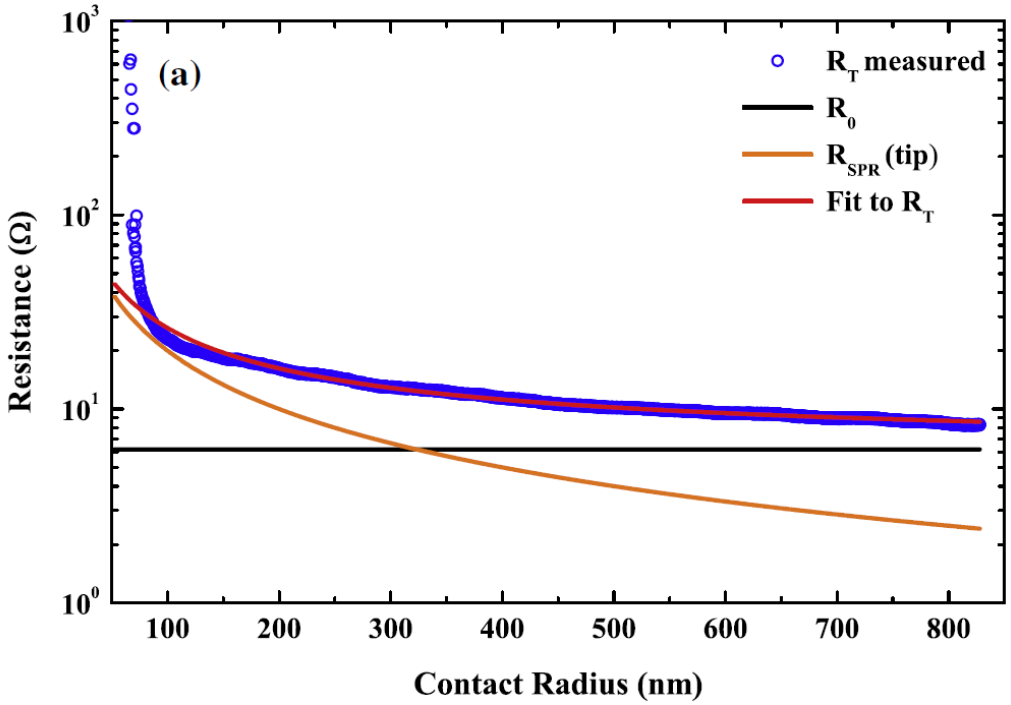

Figure 2.20: Measured resistance R_T as a function of contact radius for gold sample. The resistance fit components are in solid lines (R_{SPR} is the spreading resistance component and R_0 the constant resistance component). From Sprouster *et al.* [144]

if this resistivity is known, electrical contact area monitoring. Nevertheless this later part was not discussed by Sprouster *et al.*

A crucial point for electrically coupled indentation is the choice of the indentation tip, which has to be conductive enough. Boron-doped diamond (BDD) tips are the most commonly used in literature [137, 138, 143]. Nevertheless electrical measurements with BDD tips lead to non-linear I-V characteristics even at large indentation depths, especially for poorly doped BDD (below 10^{19} cm^{-3}) [137, 145] (figure 2.20). Sprouster *et al.* [145] have related this non linearity to dopant segregation and heterogeneities of the dopant activation at the tip surface. Some authors have conducted electrical measurements with vanadium carbide tips [134, 135, 144]. Indeed, excellent mechanical properties (high Young's modulus and hardness) and low resistivity of transition metal carbides such as vanadium carbides make them excellent choice for electrically coupled indentation.

Recently an indentation manipulator (with 10 nm resolution) coupled with electrical measurements has been integrated *in situ* SEM to study Sn extrusion across fractures of its oxide during loading [146]. This allows the direct imaging of indents after each measurements.

Electrically-coupled nanoindentation is then a promising tool for a wide panel of applications.

In particular, it brings new understanding to fast mechanical events, such as oxide cracking, pressure- induced phase transformation or thin film delamination. Moreover, electronic transport through oxide film can be studied. Experimental results are now promising for local resistivity computation or electrical contact area monitoring during indentation.

Chapter 3

Development of an *in situ* FEG-SEM nanoindenter coupled with electrical measurements

A multifunctional characterisation set-up is being developed at SIMaP laboratory, mainly based on electrical and mechanical coupling. The heart of this device is an *in situ* FEG-SEM (Field Emission Gun Scanning Electron Microscope) nanoindenter coupled with an electrical measurement apparatus. The aim of this set-up is:

1. To investigate the mechanical behavior of small scale objects. Thanks to the FEG-SEM integration, indents can be precisely positioned on submicrometric objects.

2. To generate an input to the quantitative analysis of mechanical behavior thanks to the electrical resistance monitoring during indentation. This can improve the knowledge of plastic flow, oxide fracture mechanisms or thin film delamination.

3. To study electronic transports within a structure, such as an assembly metal with its oxide, and allow phase identification through electrical transport signature.

In order to pursue these objectives, several constraints have to be taken into account:

- **Constraints due to the SEM environment**

  - The main constraint for *in situ* SEM integration is the device size limitation. The total mass of the device must also be less than 1-4 kg.

  - The nanoindenter must be optimized and compatible with high vacuum.
  - There must be the possibility of indent imaging during indentation.

- **Constraints due to precise mechanical measurements**
  - The nanoindenter head must have a high resolution in displacement and load.
  - The CSM (Continuous Stiffness Measurements) option must be available.

- **Constraints due to precise electrical measurements**
  - The electric apparatus must be able to measure sharp resistance change over several decades (typically from 1 Ω to 1 TΩ), without being blinded by a range change.
  - In order to catch fast mechanical events, the electronic apparatus must be able to register data with a high acquisition rate.

The following sections describe the set-ups developed at SIMaP laboratory in order to answer these requirements. In the first section the heart of the experimental set-up is described and mechanical validations are made. Then the *in situ* SEM integration is detailed, as well as the procedure for precise indent positioning. In a third section, the electrical coupling is detailed, with a study of electrical sensitivity. Lastly, the coupling between electrical measurements and *in situ* SEM integration is described.

3.1 Description and validation of the experimental setup

3.1.1 Set-up description

Nanoindenter head description

Within the frame of this project, two nanoindenter heads (also called actuators) were used, both provided by Nanomechanics Inc. A prototype model, the so-called "square head" (figure 3.1), was used during the first part of the project. A dedicated Labview interface has been developed for three months to monitor it. This development is detailed in appendix A (page 271). The square head has been used for preliminary tests but has been quickly replaced by the commercial version, the Inforce 50 actuator from Nanomechanics (figure 3.2).
Both nanoindenter heads are based on the same technology (figure 3.3). An electromagnetic coil controls the force imposed to the nanoindenter column. The column is supported by a

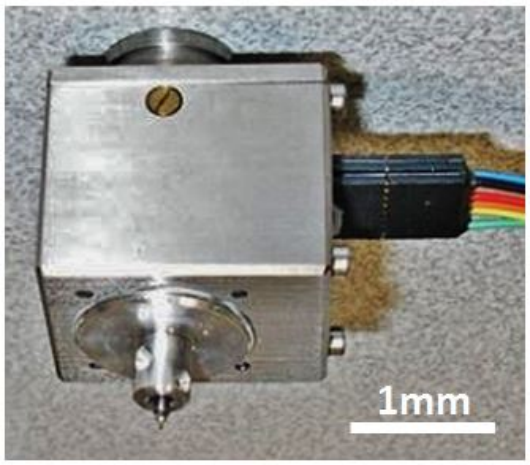

Figure 3.1: Square nanoindentation head.

Figure 3.2: Inforce nanoindentation head.

vertical spring and its displacement is measured by a capacitive gauge. High stiffness lateral springs ensure the column verticality.
The Inforce actuator has the following specifications:

- **Force:** Maximal load up to 50 mN, with load resolution of 3 nN. Typical noise below 50 nN.
- **Displacement:** Displacement range of [-25;+25] µm, with 0.02 nm of electronic displacement resolution.
- **Stiffness:** Typical spring stiffness of 180 $N.m^{-1}$, linear at ± 3 % on the displacement range.
- **Dynamic mode:** Operating in Continuous Stiffness Measurement (CSM) mode with typical resonant frequency around 140 Hz.

The actuator is monitored by a controller (so-called "InQuest" controller), which allows data acquisition at rate up to 100 kHz and dynamic excitation from 0.1 Hz to 1 kHz operating with a lock-in amplifier. More information can be found on Nanomechanics website [147].
The Inforce actuator can either be operated by home-made Labview programs or by the Inview software, provided by Nanomechanics Inc. The Inforce head monitored by Inview software was used for most of the applications detailed in this thesis, and we will focus on it in the coming sections.
Different tips can be screwed directly onto the nanoindenter column or onto an intermediary titanium extender to increase the space in the sample vicinity. As it will be seen in the next,

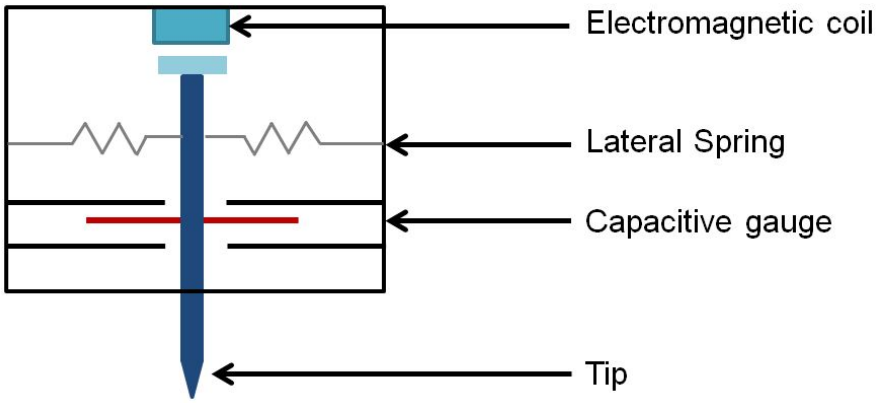

Figure 3.3: Schematic of an nanoindenter head.

this is a crucial point to avoid collisions with the SEM lens in the SEM chamber and to allow *in situ* indentation imaging.

Assembly description

Two home-made set-ups have been developed: the so-called "3-axes" and "5-axes" set-ups. The 3-axes set-up is shown in figure 3.4. It is composed of one of the actuator described above and three piezo-translators from SmarAct. SmarAct piezo-translators are based on the "Stick-Slip" drive technology, which allows macroscopic travels with subnanometer resolution [148]. In the case of closed loop control, the resolution is about 1 nm for macroscopic travels up to 25 mm for the Z-axis and 18mm for the X- and Y-axes. These SmarAct translators are also compatible for high vacuum applications.

The nanoindenter head is fixed on a first "Z-axis" translator, along the nanoindenter axis. This axis will be further called "extension axis".

Samples mounted on 10 mm diameter stubs are fixed on the two others translation stages, respectively the "X-axis" and the "Y-axis". Two samples can be put at the same time on the sample holder.

For the 5-axes set-up, two stages are added (figure 3.5). The sample is positioned on a SmarAct rotation stage, allowing the sample to face either the nanoindenter, the SEM beam or different SEM detectors in the SEM chamber. An extra stage allows an additional Z-axis translation to the samples. This stage aims at adjusting the sample position after rotations. In the current work, only the 3-axes set-up was used. Thus, 5-axes set-up will not be further discussed.

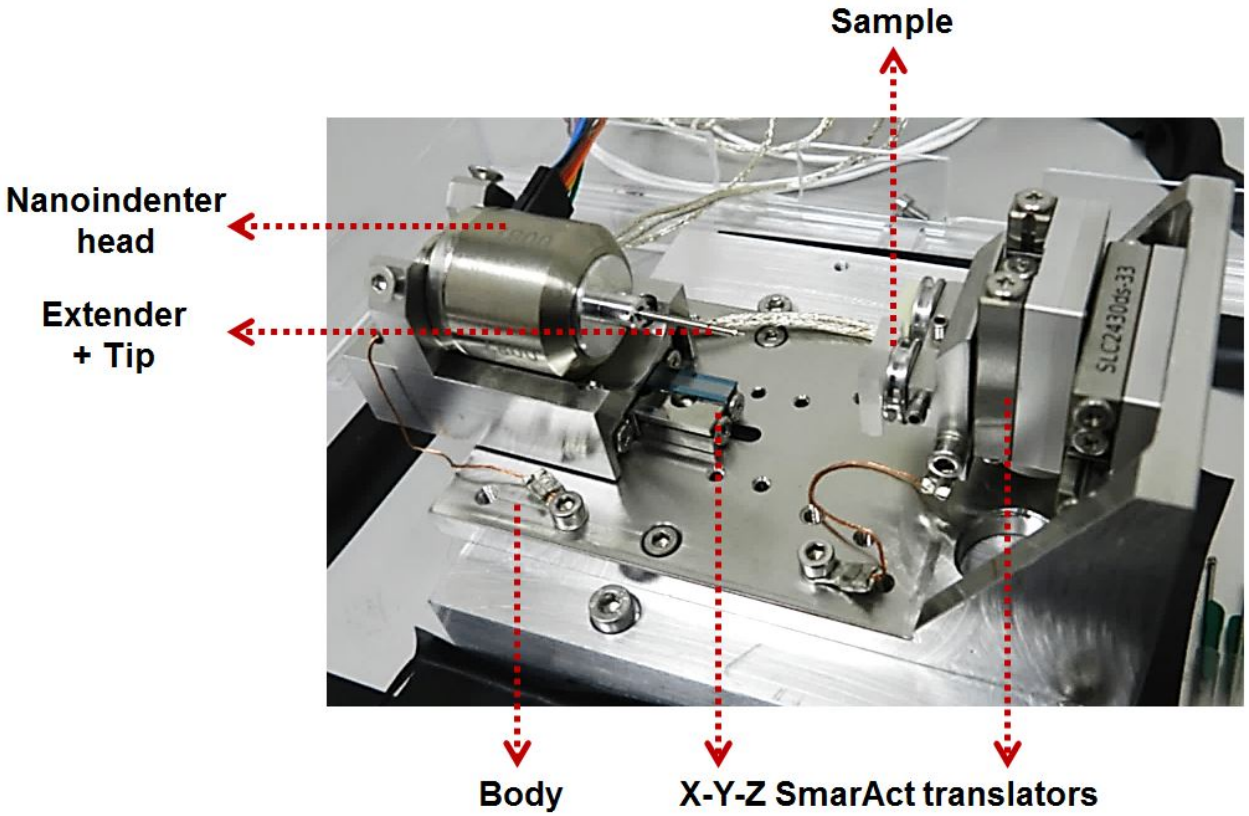

Figure 3.4: 3-axes set-up.

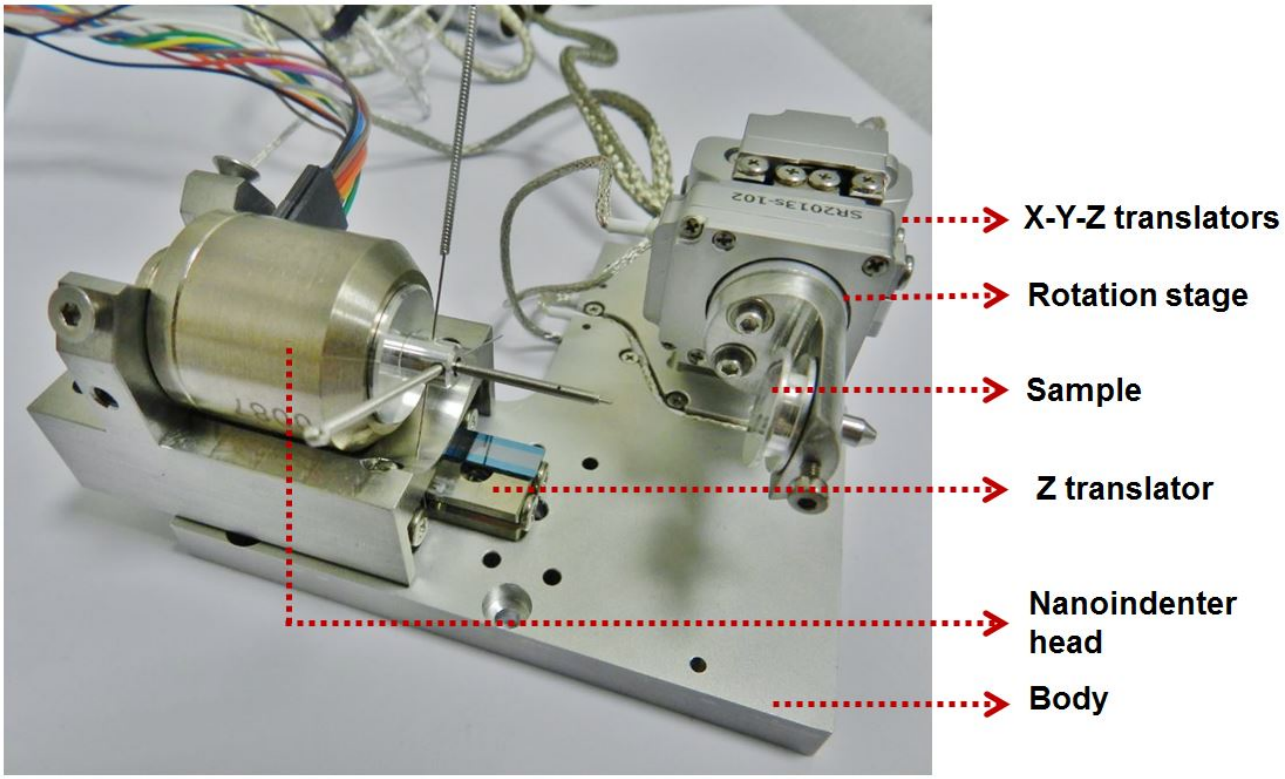

Figure 3.5: 5-axes set-up.

Set-up control monitoring

Both nanoindenter head and translators are controlled via the Inview interface, as shown in figure 3.6. All the electrical grounds of each devices are connected to the body of the set-up, which is grounded via the head controller.

Two kinds of command can be run by Inview software: manual commands and macros, also called methods.

Four different manual commands can be run:

- A macro displacement of the sample, *i. e.* the displacement of X- and Y-axes. This allows sample positioning facing the indentation tip.
- A macro displacement of the nanoindenter head, *i. e.* the displacement along the Z-axis ("extension" axis). This allows a macroscopic approach of the indentation tip, with displacement range over 25 mm. This approach is used for the initial raw surface detection.
- The displacement of the nanoindenter column. This corresponds to the 50 µm displacement of the column. This is the displacement used for nanoindentation testing. The column can be controlled either with a force set-point, or with a displacement set-point, by means of a closed-loop on force (with a 1 kHz response time).
- Dynamic displacement: dynamic oscillations can be manually adjusted.

Specific indentation methods are run using macros. Two kinds of methods can be run: "Single Mode" methods or "Multisample Mode" methods:

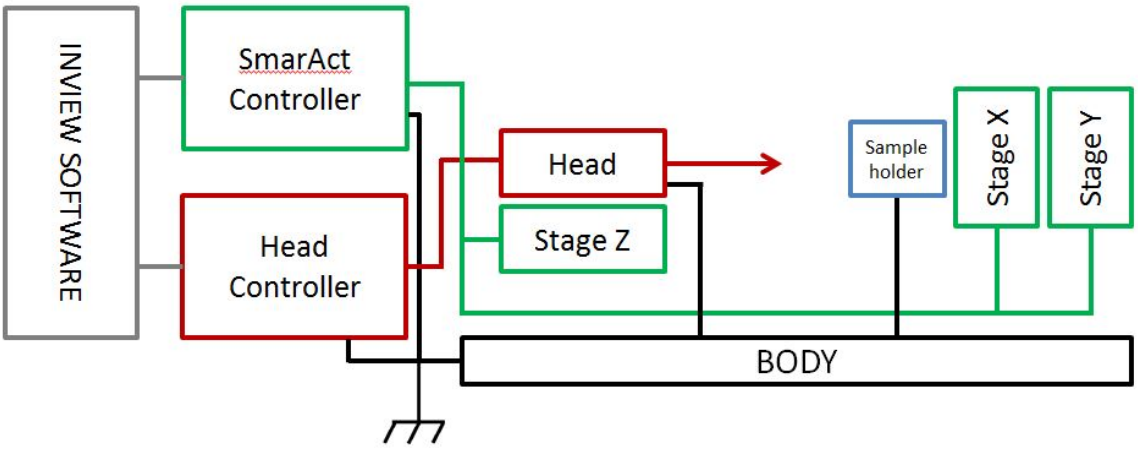

Figure 3.6: Set-up control monitoring.

- With Single Mode methods, the tip is brought close to the surface by manual commands (typically 2 µm away from the surface). Then the test is run. During the test, translators do not move. The only movements are those of the nanoindenter column, *i. e.* nanometric ones. "Single Mode" methods are preferential methods for *in situ* SEM indentation with precise positioning of indents on submicrometric objects.

- Multisample mode methods allow the creation of a matrix of indents. With this mode the Z-translator is first withdrawn to its minimum value. Then the test is conducted following several steps:

  - **First raw surface approach:** The displacement of the column is put at +20 µm and is controlled in force. The extension axis moves fast toward the surface (figure 3.7-1), until a significant backward of the column is detected (typically 2 µm, figure 3.7-2). The extension axis stops and the column goes to its park position (*i. e.* column displacement at −25 µm , figure 3.7-3).
  - **Second fine surface approach:** X- and Y-axes translates by ∼ 25 µm. The actuator column is set at +2 µm. The Z-axis moves slowly (figure 3.7-4) until a small backward of the column is detected (figure 3.7-5). The extension axis does not move anymore from this point.
  - **Thermal drift:** The actuator column moves a bit to slightly indent the sample (figure 3.7-6). The force imposed to the actuator is then kept constant, while the column displacement is recorded in order to measure the displacement drift (mechanical or thermal). This step lasts until the drift falls below a threshold value (most often 0.05 $nm.s^{-1}$).
  - **Indentation:** The column steps back to its park position (*i. e.* −25 µm, figure 3.7-7). X- and Y-axes move from ∼ 25 µm up to the position of the first indent. Indentation testing is then performed by running with the chosen method (figure 3.7-8). The column then steps back to its park position (figure 3.7-9) and X- and Y-axes go to the next location of the chosen matrix.

Several standard indentation methods can be used, either with static or dynamic indentation (CSM mode), and either with constant loading rate or with constant strain rate. A high-speed indentation method called "nanoBlitz 3D" method is also available. It allows very large indentation mapping with up to one indent per second. The pattern drawn by nanoBlitz 3D

method avoids large X and Y displacements that would lead to tip crash on non-planar samples (figure 3.8).

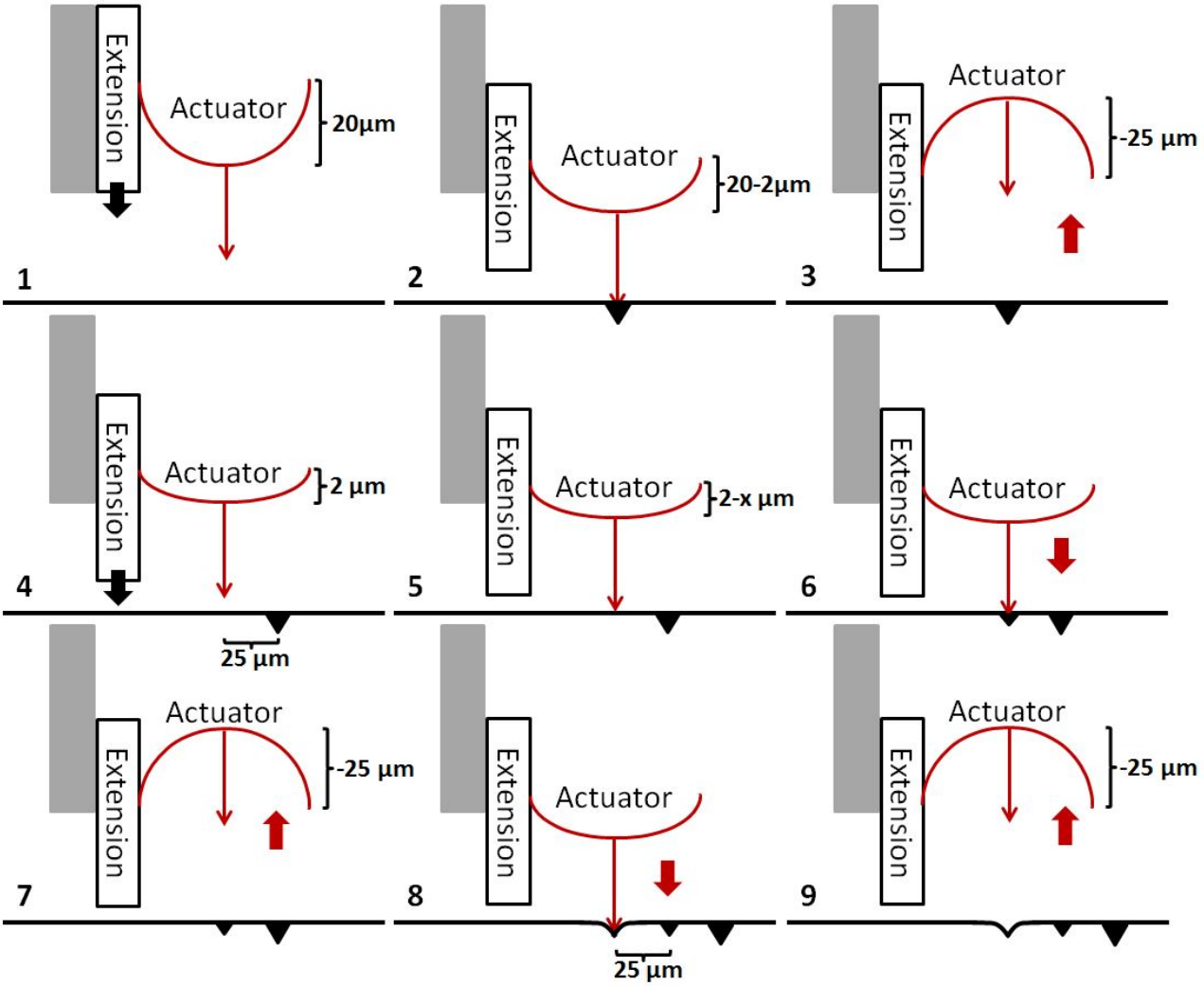

Figure 3.7: Inview procedure for Multisample mode.

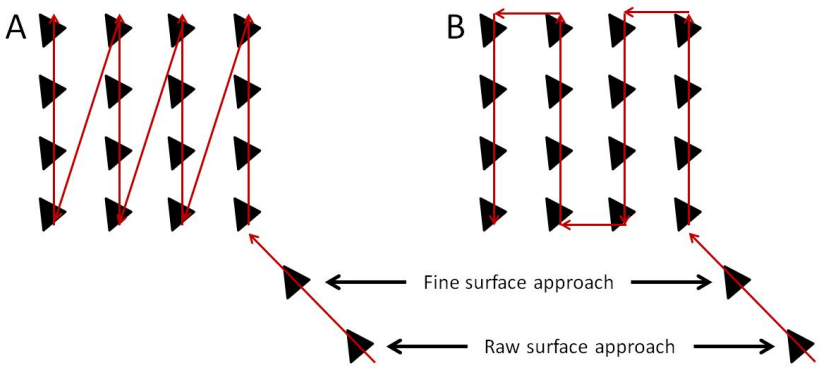

Figure 3.8: Matrix pattern for standard methods (A) and nanoBlitz 3D method (B).

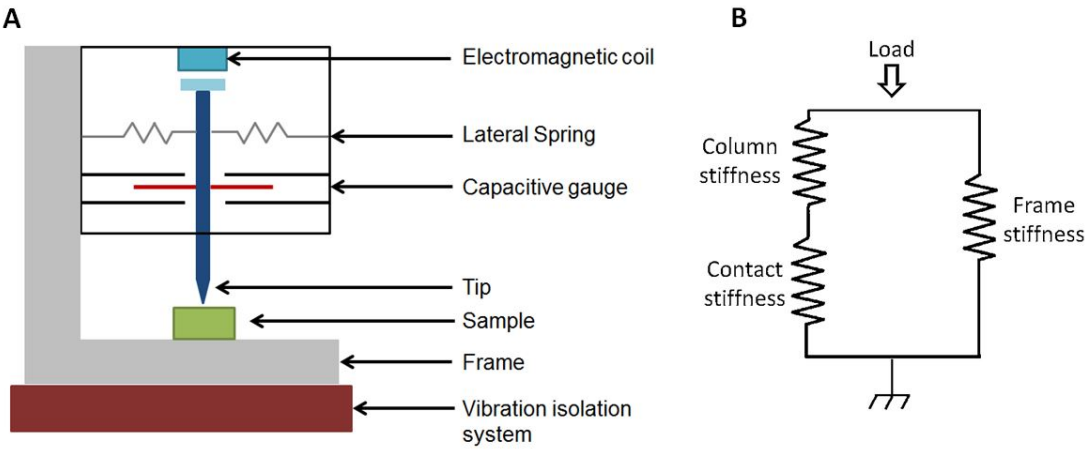

Figure 3.9: A: Schematic of a nanoindenter and B: corresponding mechanical diagram.

3.1.2 Set-up validation

Before operating sample characterisation, the experimental set-up requires to be validated. To produce reliable indentation testing, three technical points are crucial, which corresponds to a check-list procedure to ensure mechanical validity:

- The device must operate under low vibration environment
- The lateral springs (figure 3.9), which maintain the nanoindenter column, must have an high lateral stiffness to maintain the system verticality, and a small vertical stiffness.
- The frame stiffness must be high compared to the contact stiffness.

Vibration level of the set-up

As shown in figure 3.9, the set-up is positioned on a vibration isolation system (TS-150/140 LP), in order to reduce the vibration level. The mechanical noise level was measured at room atmosphere, without contact, by holding the force imposed to the head. The initial column displacement value was 0 nm. Results after removing the thermal drift baseline are shown in figure 3.10. The maximal displacement is less than 6 nm, and the standard deviation is 1.7 nm. This gives sufficiently low vibration level for nanoindentation testing.

Column stiffness

The nanoindenter head is controlled by a force exerted by an electromagnetic coil. The column displacement depends both on this force and on the total stiffness, *i. e.* the contact stiffness and

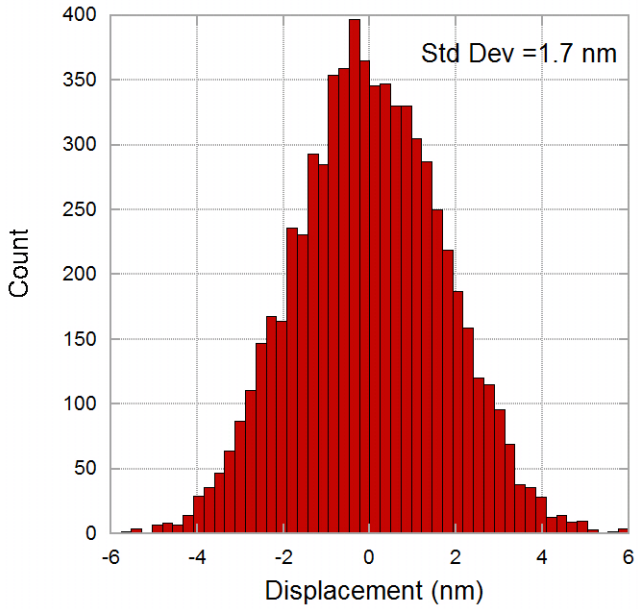

Figure 3.10: Noise level when operating the set-up at room atmosphere on an isolated table.

the vertical stiffness of lateral springs which comes in series (also called column stiffness). The column stiffness must then be perfectly known, in order to get the contact stiffness contribution. The column stiffness is simply obtained by deriving the force-versus-depth curve without contact. The obtained value depends on the column displacement, as shown in figure 3.11. These values can be compared to the constructor calibrated values. The relative errors between our data and the calibration are below 2 %, as shown in figure 3.12. Nevertheless, since the column stiffness can slightly evolve with time, it is regularly recomputed.

Frame stiffness validation

The last point to validate is the frame stiffness value (figure 3.9), which corresponds to the parallel stiffness coming from piezo-translators and work-pieces of the set-up. The frame stiffness must be high enough (typically $> 10^6$ N.m^{-1}) to limit its contribution on total stiffness.
Frame stiffness value was checked by an indirect way. Considering only the Sneddon's relation [14] and the hardness definition, the following relation between the dynamic stiffness S, the load L applied on the sample, the reduced Young's modulus E^* and the hardness H can be established (3.1):

$$\frac{S^2}{L} \propto \frac{E^{*2}}{H} \tag{3.1}$$

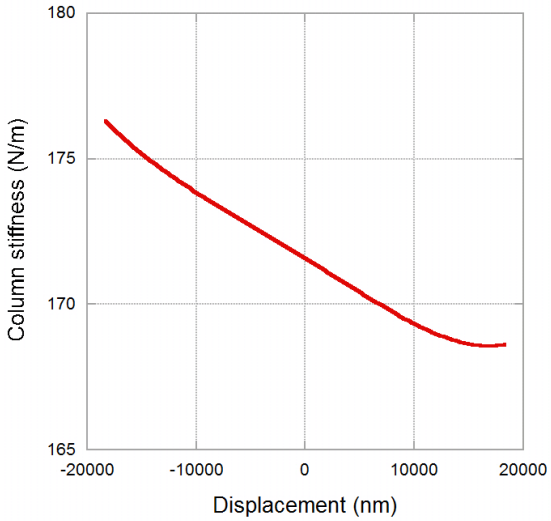

Figure 3.11: Column stiffness versus displacement.

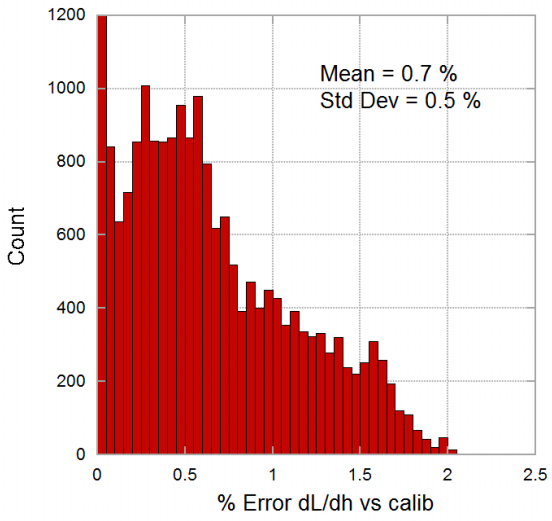

Figure 3.12: Column stiffness deviation from the calibration.

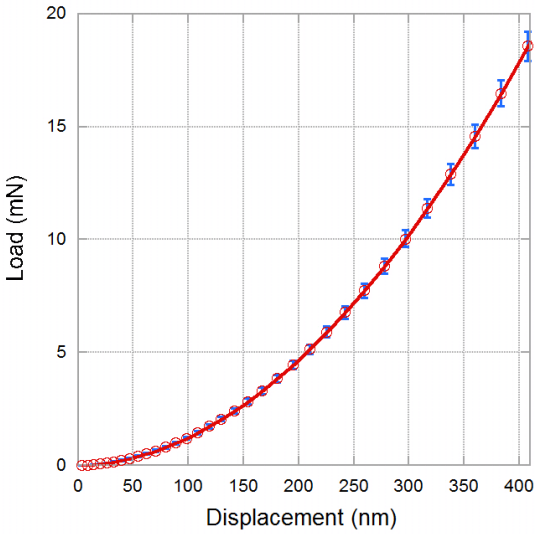

Figure 3.13: Load-versus-depth curves on fused silica.

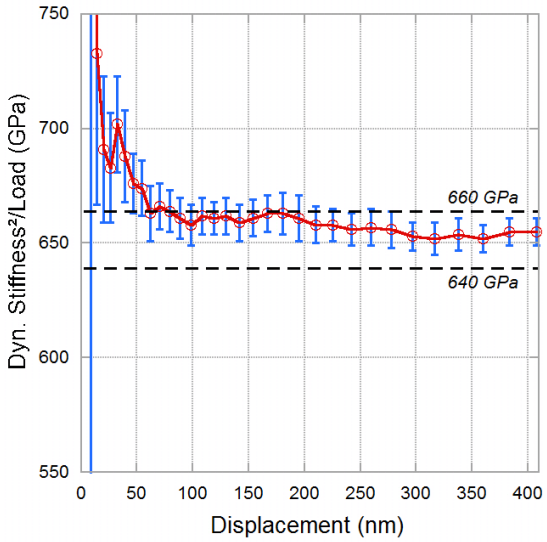

Figure 3.14: Square of dynamic stiffness over load versus indentation depth for fused silica.

Since both dynamic stiffness and load applied are direct measurements, this ratio can be computed without any assumption on material rheology. Moreover, it depends only on material constants (Young's modulus and Hardness), providing that the frame stiffness is high enough. In particular, this ratio does not depend on the shape function of the tip. For fused silica, it is well accepted that the ratio is constant with indentation depth and belongs to [640,660] GPa for acceptable values of frame stiffness.
S^2/L was determined for fused silica by running 4x4 indents with a diamond Berkovich tip. The average load-versus-depth curves are shown in figure 3.13. The corresponding S^2/L ratio is shown in figure 3.14. As expected, the ratio is found roughly constant for indentation depth higher than 100 nm, with a mean value of 655 GPa +/− 2 GPa. Similar results where obtained with a cube corner tip. This allows us to validate the frame stiffness.

As a result, the check-list procedure allows us to validate the experimental set-up. The two next paragraphs will describe respectively the set-up integration in the SEM chamber and the electrical coupling to the set-up. Since both configurations can affect the vibration level and the column stiffness, these points will be checked in the same way for each of those configurations.

3.2 *In situ* SEM integration

3.2.1 *In situ* SEM experimental set-up

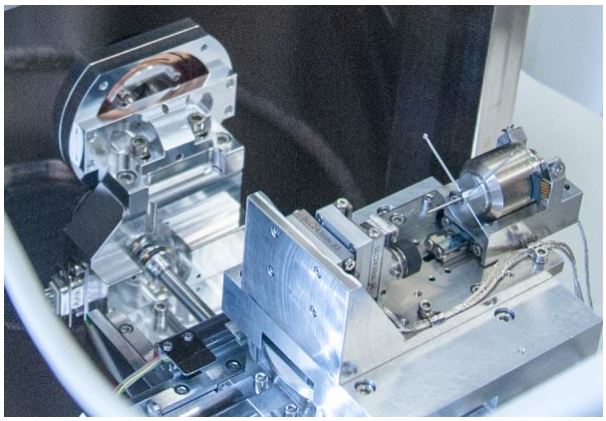

Figure 3.15: View of the set-up in the SEM chamber.

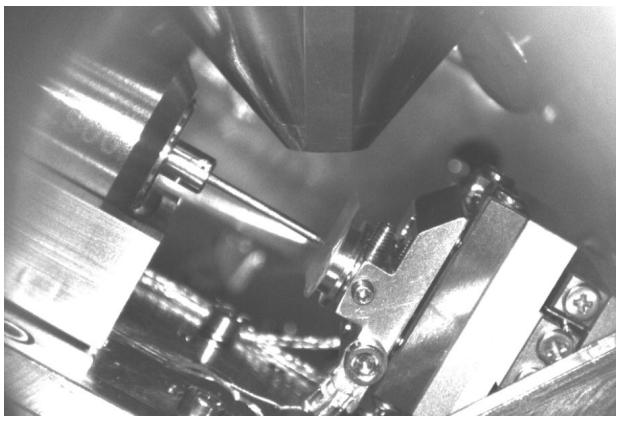

Figure 3.16: Infra-rouge image of the set-up inside the SEM chamber.

In situ SEM nanoindentation testing has been performed at CMTC (Consortium des Moyens Technologiques Communs), which is a physico-chemical characterization platform of Grenoble-

INP. The SEM used is a Field Emission Gun (FEG) GEMINI SEM 500 from Zeiss. This is a new generation of FEG-SEM with two major innovations dedicated to aberration reduction [149]:

- A high resolution mode at the Schottky FEG, to limit energetic dispersion.
- A new objective lens with an electrostatic and magnetic coupling (Nano-Twin lens).

This SEM can potentially work in low vapour pressure mode with controlled pressure from 5 Pa to 500 Pa and has an *in situ* plasma cleaner.

The experimental set-up is integrated directly into the SEM chamber, as shown in figures 3.15 and 3.16. The set-up can either be fixed on the SEM dovetail or directly screwed on the SEM tray thanks to an adaptation work-piece. This adaptation work-piece has shown to bring more stability to the set-up. In figure 3.16, the importance of the extender between the nanoindenter and the sample is highlighted: the extender length gives the required space to avoid collision with the objective lens when the tip is in contact with the sample.

A parametric work has been done to optimize the tilt angle and the vertical position of the set-up in the SEM chamber. Settings obtained for the SEM axes (tilt angle and X-Y-Z-positions) and the resulting working distance are given in table 3.1, with Y-position depending on the sample thickness.

Tilt Angle	Z_{SEM}	X_{SEM}	Y_{SEM}	Resulting Working Distance
30°	11 mm	$\sim$ 48 mm	30-40 mm	$\sim$ 13 mm

Table 3.1: Optimized settings for the SEM axes.

The position of the set-up was optimized to avoid collision with the objective lens, and to enable simultaneous imaging while indenting. The safety positions for the SEM stages while operating *in situ* SEM indentation were found to be 11 mm in height, with a tilt of 30°. Under these conditions, the indents are located around 48 mm for the X axis of the SEM stages, and in the range [30-40] mm for the Y axis, depending on the sample thickness. Then, once the position of the tip in contact with the sample is well centered below the electron beam, there is no more risk of collision while moving the SmarAct piezo-translators. Typically the working distance at this point is around 13 mm, and high resolution pictures can be done during the indentation, even for high magnifications.

As explained earlier, the nanoindenter head and the sample must be grounded. This is even more crucial for *in situ* SEM indentation to avoid charge effects during beam scanning. Both the nanoindenter head and the sample are connected to the SEM ground, which is then connected to grounds of controllers outside the microscope.

In order to image *in situ* nanoindentation, a conductive tip must be used. Within the frame of this project boron-doped diamond (BDD) tips were used, which combines the excellent mechanical properties of the diamond with enough conductivity to avoid charge effects. Cube corner tip, Berkovich tip and flat punch have been extensively used for *in situ* SEM nanoindentation, but due to the configurations in the SEM chamber, only cube corner tips were used for simultaneous imaging and indentation. Berkovich tip shadows the imaging during indentation. In that case, the SEM is only used to target the indents. A similar issue happens with flat punches for small objects compression. However, it is possible to image *in situ* compression of a plane surface (the edge between the compressed surface and the flat punch remains visible).

3.2.2 Procedures for *in situ* SEM nanoindentation

One purpose of *in situ* SEM nanoindentation is the precise positioning of indents on submicrometric objects. This section details the procedure for precise indent positioning. First, both SEM and nanoindenter axes systems are described. The method for indent location is then detailed. Finally, possible drift sources that can affect indent positioning are given and potential solutions to avoid them are proposed.

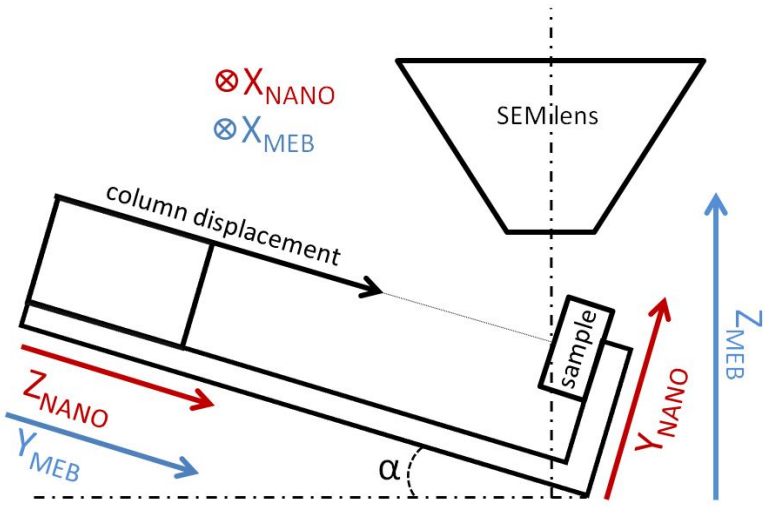

Figure 3.17: Schematic of both SEM and nanoindenter axes system.

SEM and nanoindenter system axes

In situ SEM nanoindentation deals with two different system axes, corresponding to the SEM translators on one side, and the nanoindenter translators on the other side (figure 3.17). For more clarity the stages corresponding to the nanoindenter will be followed by the suffix $NANO$ and those corresponding to the SEM by the suffix SEM. The X_{NANO}, Y_{NANO} and Z_{NANO} axes make an orthonormal coordinate system, related to the body of the nanoindenter. However, due to the tilt angle ($\alpha = 30°$), this is not the case for the SEM coordinate system.
A SEM picture projection of a displacement of x in the X-direction with the X_{NANO} translator results in a displacement of x in the X-direction of the SEM picture. However, a displacement of y of the Y_{NANO} translator leads to a displacement of $cos(\pi/2 - \alpha) \cdot y$ in the Y-direction of the SEM picture. Therefore, the distance in the SEM picture along the Y_{SEM} direction must be divided by $cos(\pi/2 - \alpha)$, *i. e.* 2 in our case, in order to have the real distance.

Procedure for indent positioning

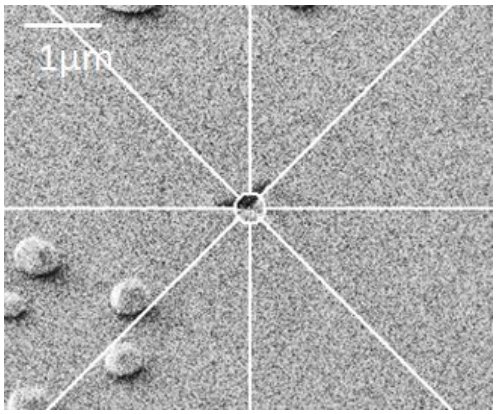

Figure 3.18: Calibration procedure for a pyramidal tip.

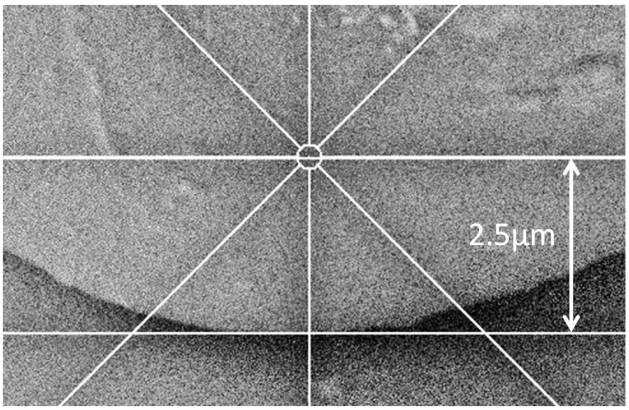

Figure 3.19: Calibration procedure for a flat punch of diameter µm.

Once the SEM axes are positioned according to the settings described in table 3.1, the procedure for indent positioning can be described in four steps:

1. The sample is roughly positioned under the indentation tip. Note that this step can also be done at air before the set-up introduction within the SEM chamber.

2. A first reference indent is done at a position (X_{NANO}, Y_{NANO}).

3. SEM translation stages are adjusted. This corresponds to the calibration phase. Only the X_{SEM} and Y_{SEM} translation stages are used. At this point there are two options:

- The indentation tip is pyramidal. The residual imprint is taken as the reference. X_{SEM} and Y_{SEM} translation stages are adjusted to bring the imprint at the center of the field of view (figure 3.18).
- The indentation tip is a circular flat punch of radius r. X_{SEM} and Y_{SEM} translation stages are moved while the flat punch is in contact with the surface. The Y_{SEM} stage is then moved so that the edge of the punch tangents a virtual horizontal line at a distance r from the center of the SEM field of view (figure 3.19). The X_{SEM} stage is moved so that a vertical line centered in the SEM field of view crosses the middle of the punch.

After this step the SEM stages are calibrated. They are then kept at this position for further steps.

4. The object to indent is selected. The sample displacement is done by moving nanoindentation stages (X_{NANO},Y_{NANO}). The object is brought to the center of the SEM image (figure 3.20). If the thickness of the object to indent is not negligible an adjustment must be done by moving the Y_{NANO} axis.

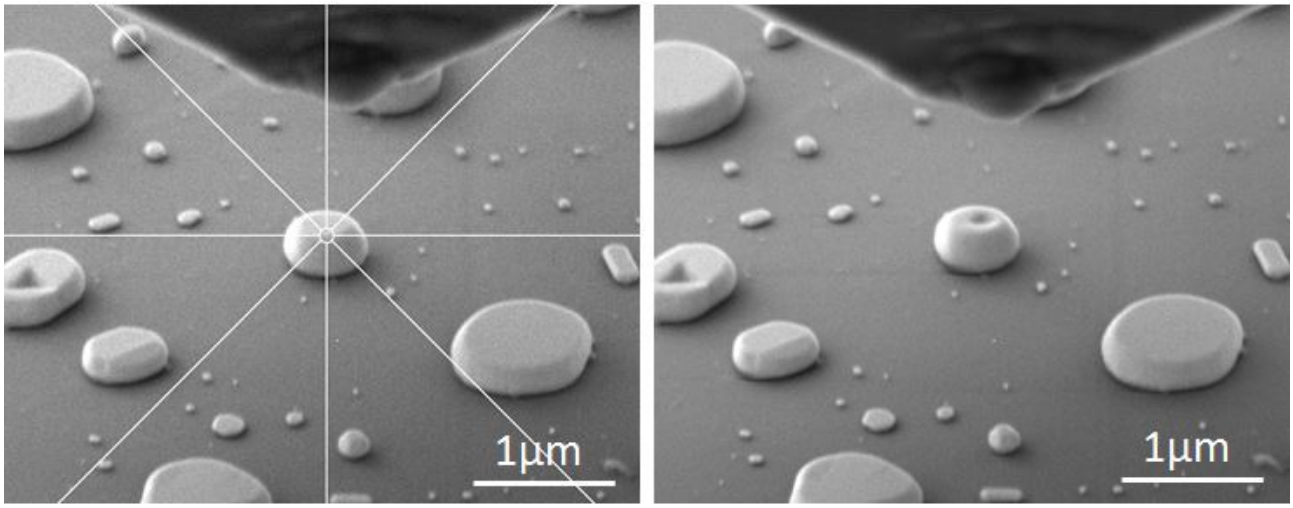

Figure 3.20: Selection of the object to indent (left: before the indent; right: after the indent).

Drift issues affecting precise indents positioning

Even with the procedure described above, many factors can disturb indents positioning, by causing a shift of SEM image during or after the calibration procedure. This SEM image shift can be related to:

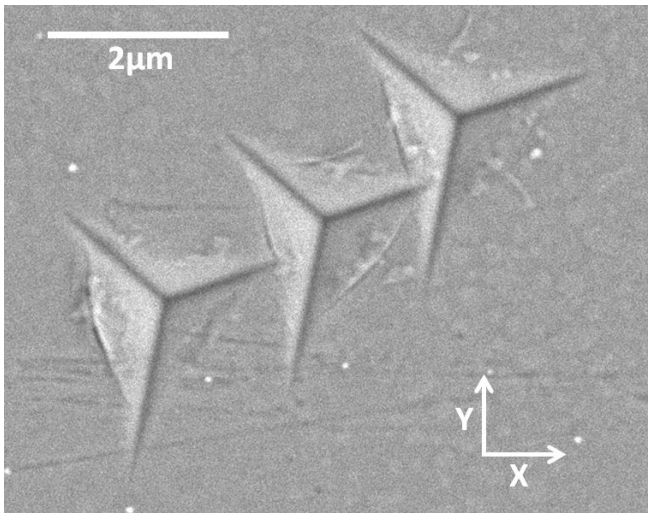

Figure 3.21: SmarAct drift after large piezo displacement (indents on fused silica, SEM picture).

- **The displacement of the metallic masses inside the SEM chamber**, which causes a deflection of the electron beam. This can be due to the movement of the actuator column or of the piezo-translators. To limit this effect, the calibration procedure and the targeting of the object to indent must be done with similar values of column displacement and Z_{NANO} coordinate.

- **The image drift in SEM imaging due to charging effect**, especially for poorly conductive samples. In that case no physical motion of the object is involved. To avoid this effect a stabilisation can potentially be obtained after a waiting time, but the best solution consists in decreasing the acceleration voltage or the beam current.

- **The mechanical drift related to the SEM stages**. Nevertheless this drift is rather slow, and can easily be corrected by starting over the calibration procedure. Typically, the drift of the SEM stages after one night was found to be no more than 20 µm.

- **The drift coming from piezo-translators**. When large displacement are performed with these translators (typically 100 µm), large drifts are observed, probably due to thermal heating. In order to investigate this effect, several tests have been done at fixed (X_{NANO},Y_{NANO}), but a large displacement of 200 µm along X-axis was performed between each indent. As it can be seen in figure 3.21, a 2 µm shift is observed. The only way to prevent this phenomenon is to avoid large displacements. In that purpose, "Single Mode" methods are preferentially chosen (see section 3.1.1, page 86). If large displacements cannot be avoided, the calibration procedure must be performed after each

indent around target location.

Finally our experience shows that to reduce drift issues, the calibration procedure must be done as often as possible, and after each indent is the best. With this approach, a precision better than 100 nm can be obtained. An example is shown in figure 3.22 for a gold island on a non conductive sapphire substrate.

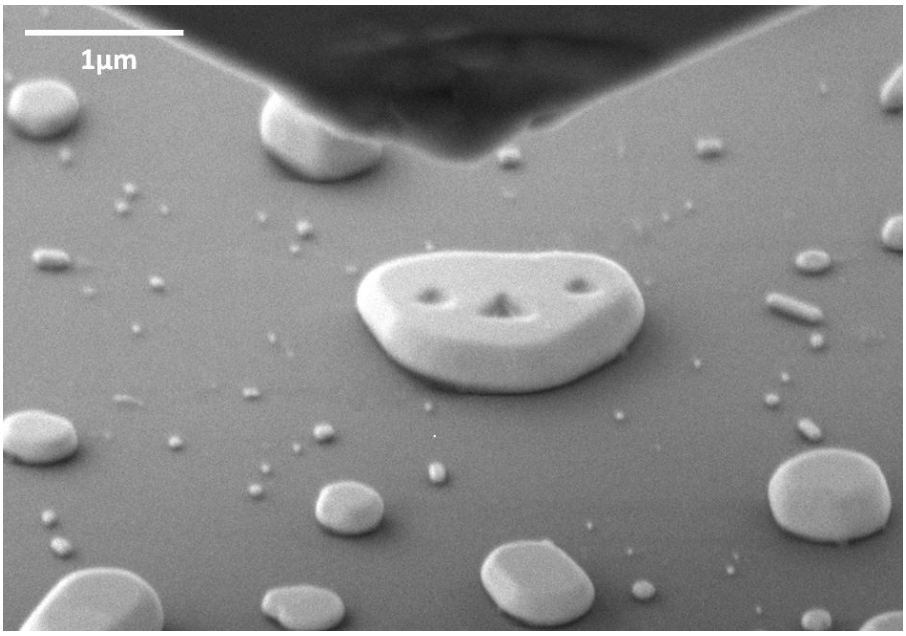

Figure 3.22: *In situ* SEM nanoindentation of a gold island on sapphire substrate (60 µm diaphragm, 3kV).

3.2.3 Set-up validation *in situ* SEM

Mechanical validations

Vibration level and column stiffness can both be affected by the SEM environment. To ensure mechanical testing validity of the *in situ* SEM set-up, both are checked with the procedure described in section 3.1.2 (page 89).

Vibrations level and column stiffness has been determined *in situ* SEM with a 30° tilt, and compared with value at room atmosphere, with no tilt.

The noise level appear to be even lower *in situ* SEM, with maximal vibrations around 4 nm (compared to 6 nm at air) and a standard deviation of 1.2 nm (compared to 1.7 nm in air).

The column stiffness is also quite comparable to the column stiffness at air, as shown in figure 3.23. The deviation between both stiffness does not exceed 1 $N.m^{-1}$.

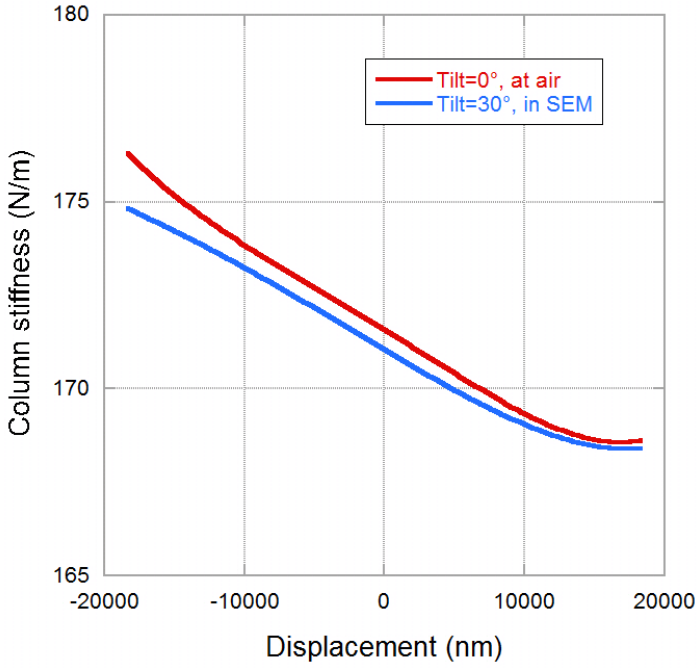

Figure 3.23: Column stiffness versus depth at air and *in situ* SEM with a 30° tilt.

Thus mechanical testing is validated for the *in situ* SEM configuration of the set-up.

Beam scanning effect on nanoindenter column displacement

In situ SEM measurements bring new issues, such as the effect of beam scanning on indenter signal acquisition. Indeed, when testing poorly conductive sample, such as fused silica, beam scanning can be sensed on indentation curves. Figure 3.24 shows nanoindentation curves on fused silica metallized with 5-7 nm of carbon under beam scanning (10 kV). Indentations were performed with a BDD tip. The oscillations on the curves come from the beam scanning and their frequency depends on the scanning speed used. These features happen even for metallized sample. Nevertheless, they were never observed on highly conductive materials.

This phenomenon has been further investigated at 10 KV on the metallized fused silica sample. The force imposed was kept constant, and the column displacement was measured for different beam scanning conditions. Results are shown in figure 3.25. When the tip and the sample are not in contact, there is no evidence of beam effect on the column displacement (figure 3.25 A). However, at indentation depth of 150 nm (figure 3.25 B), there is a high effect when scanning the sample over small area (300x500 nm^2). A slight effect also appears when scanning the tip near the contact, but no visible effect is seen when scanning it far from the contact. Other experiments have shown that scanning the sample over large area (50x40 μm^2) reduces the

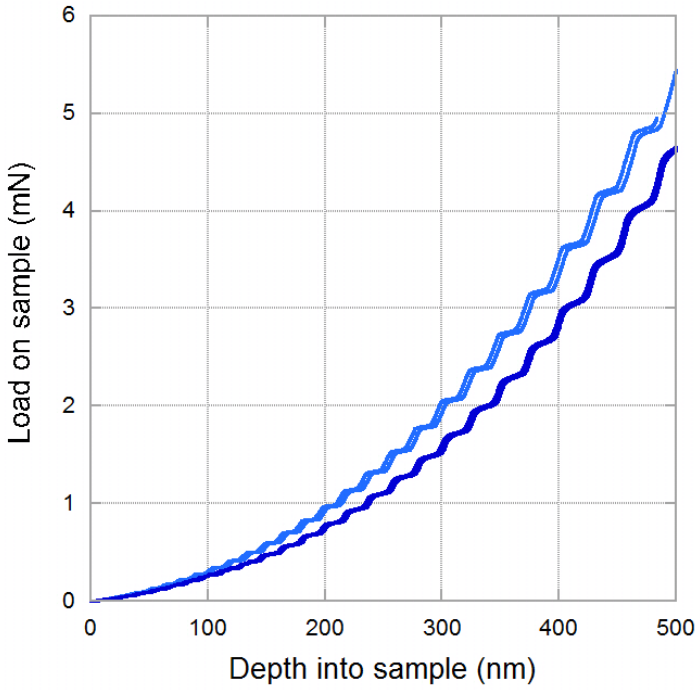

Figure 3.24: Beam effect during indentation of metallized fused silica (EHT=10 kV).

beam effect on the column displacement.

This phenomenon fits with a charge effect occurring within the sample. This clearly affects not only the sample surface, otherwise the metallization would have prevented it. This can be due to the interaction pear of the electron beam, which goes deeply on the sample at high voltage, and which causes a charge effect affecting the capacitive gauge of the nanoindenter. This phenomenon happens, whereas there is no significant imaging evidence of charge effects. It does not occur when the tip is scanned, probably because the tip is conductive enough and grounded.

This charge effect can be totally avoided when using a low accelerating voltage. Typically, the oscillations shown in figure 3.24 disappear on fused silica for accelerating voltage of 2-3 kV. This reveals the need for an optimisation of the accelerating voltage when using a poorly conductive sample, which is even more crucial than the optimisation usually made for standard SEM imaging.

As a result, *in situ* SEM nanoindenter has been successfully implemented. Reducing drift sources allows the positioning of indents on small objects, with a spatial precision better than 100 nm. The validity of mechanical testing in SEM environment have also been checked.

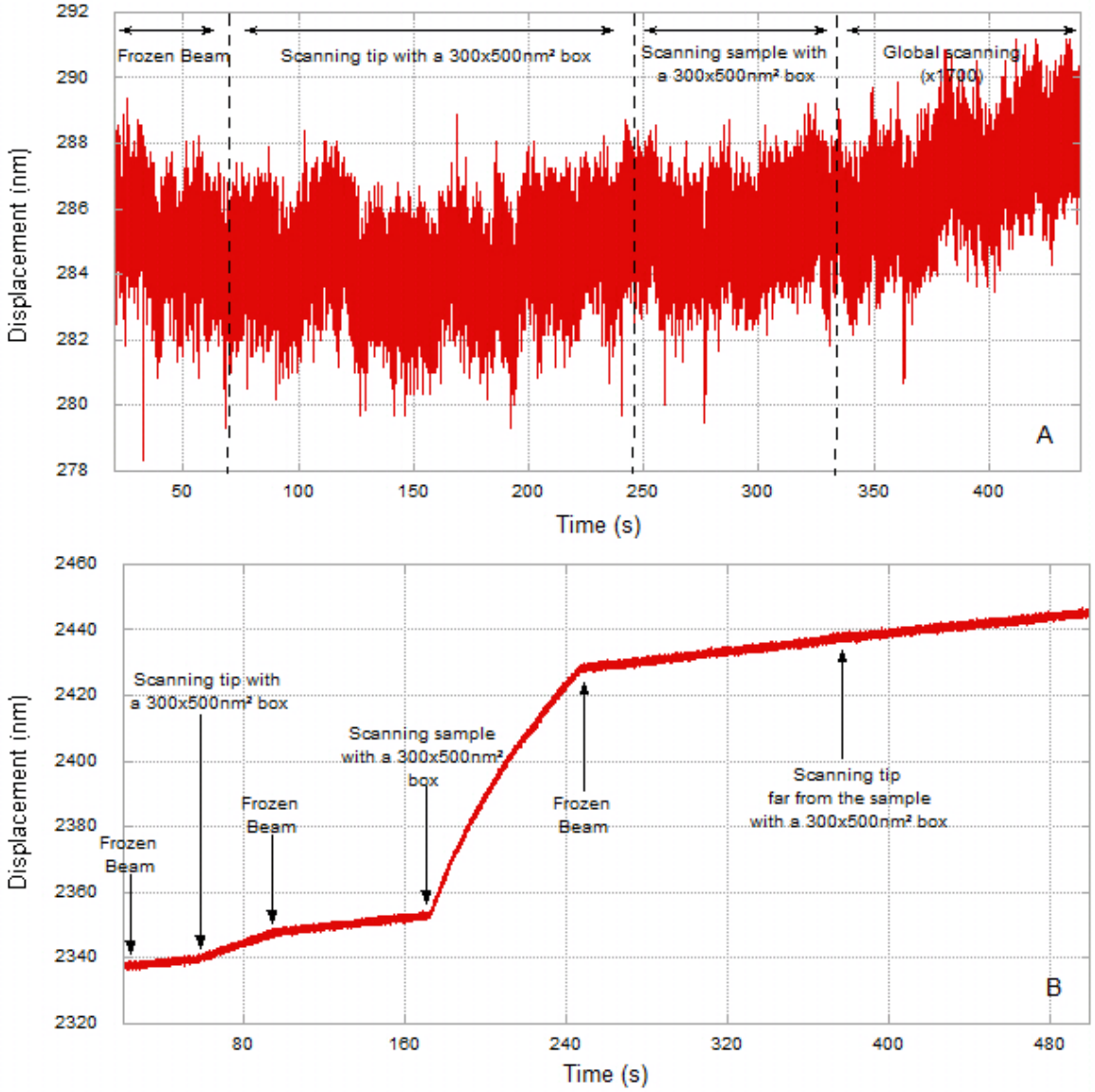

Figure 3.25: Effect of the beam on the nanoindenter column displacement at 2 µm from the contact (A) and at 150 nm of indentation depth (B) (metallized fused silica, 60 µm diameter diaphragm, EHT = 10 kV).

3.3 Coupling with electrical measurements

The "3-axes" experimental set-up described above has been adapted for nanoindentation coupled with electrical measurements. In parallel, electrical measurements have been implemented on a commercial XP nanoindenter from MTS, but it is much more anecdotal within frame of this project.

This paragraph describes the experimental set-ups, and focuses on mechanical and electrical validations. The integration *in situ* SEM of the electrically coupled set-up is also detailed.

3.3.1 Electrically coupled set-ups and resistive measurements

Set-ups for resistive measurements

Two set-ups have been developed for resistive measurements. One was integrated on the home made Inforce 3-axes set-up described above, which can be integrated *in situ* SEM. It is the most extensively used set-up during this Ph.D. Another one was integrated directly on a commercial XP nanoindenter from MTS.

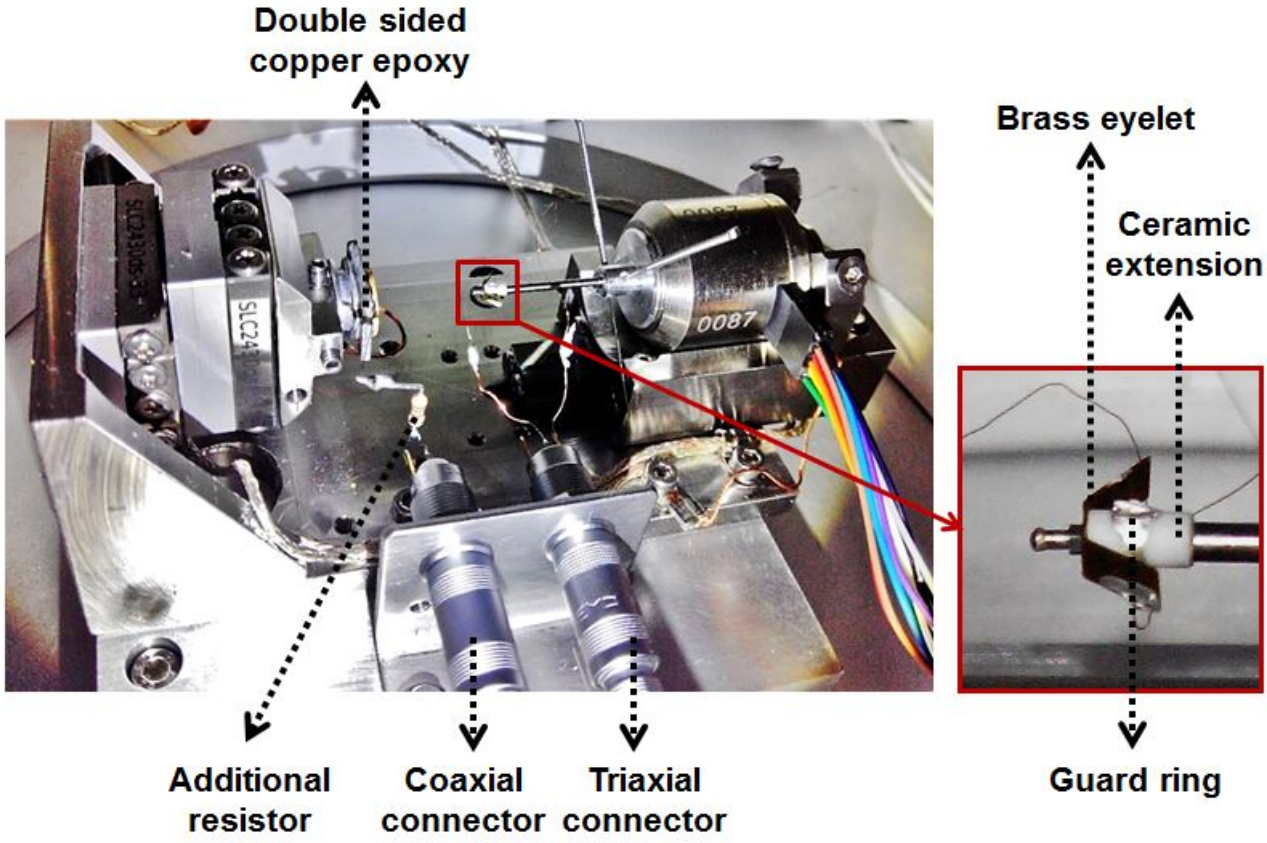

Figure 3.26: Electrically functionalized *in situ* set-up.

Inforce head

Coupled electrical measurements are based on the following principle: the sample is polarised at either DC or AC signal. When tip and sample are in contact, the current passing through the contact is measured directly from the tip of the indenter. Figure 3.26 shows the 3-axes set-up functionalized for electrical measurements. Three points are crucial, as schematized in figure 3.27:

- The sample is fixed on a double-sided copper epoxy board. One side of the epoxy is

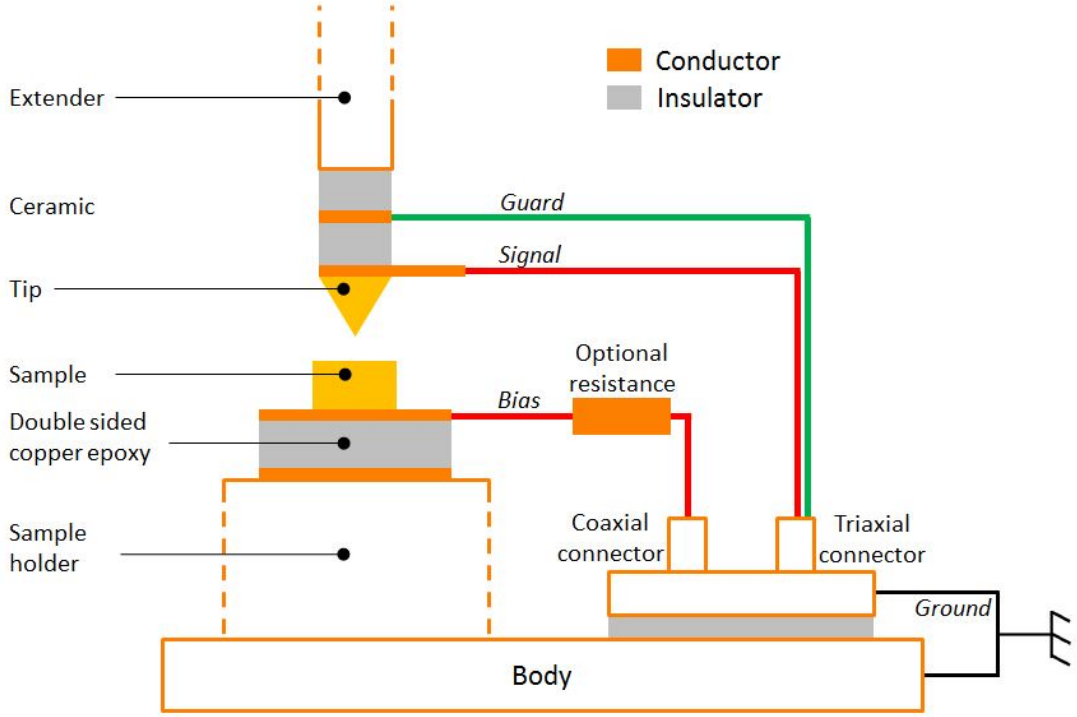

Figure 3.27: Schematic of electrically coupled Inforce 3-axes set-up.

connected to the sample holder, which is grounded as previously described. The other side is connected to a coaxial cable, which forces the sample polarisation.

- The tip is insulated from the nanoindenter head by a ceramic extension. The current signal is taken on a brass eyelet, directly connected to the tip, and mechanically pressed between the tip and the ceramic extension. To reduce the leakage currents through the ceramic, a guard ring is drawn on it with silver paste. Both the signal and the guard are connected to a triaxial cable.

- To avoid ground loops, the coaxial and triaxial connectors fixed on the nanoindenter are insulated from the body of the nanoindenter.

Additional resistors can also be connected in series with the sample to prevent burn-out issues when tip-sample resistance fells below critical impedance.
Moreover, the Inforce 3-axes set-up can be integrated to an home-made vacuum chamber allowing electrical measurements under intermediate vacuum ($\sim 10^{-2}$ mbar).

XP head

A similar configuration is used for electrical coupling with XP nanoindenter, as shown in figure 3.28. The sample is put on a double sided copper epoxy. Tip signal and guards are taken on

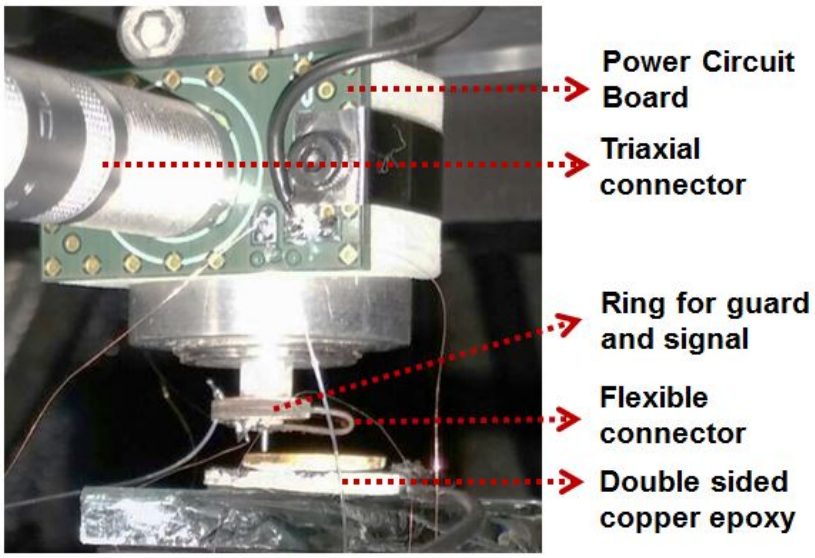

Figure 3.28: Electrical functionalization on XP nanoindenter.

a ring, connected to the tip by a flexible connector. A Power Circuit Board (PCB) transmits both guard and signal to a triaxial connector.

Electrical apparatus for resistance measurements

As mentioned previously, electrical apparatus used for electrical measurements must be able to measure sharp resistance or current changes over several decades, without being blinded by a range change. In order to catch fast mechanical events, it also has to register data at high acquisition rate.
Within the frame of this project, two electrical apparatus are used:

- A ResiScope [150] apparatus from Scientec/CSI company (figure 3.29), which is the most widely used apparatus during this project.
- A conventional Keihtley 6430 (Source Measurements Unit System, SMU).

The ResiScope was originally developed at the LGEP (Supelec, France) for conductive AFM [151]. It optimizes in real time the current passing through the contact to limit current density and thus avoid electrical burn-out. It can measure resistance change over ten decades (from 100 Ω to 1 TΩ), with acquisition rate up to 1 kHz. When the measured resistance is below 100 Ω, an additional resistance is required in series with the sample.
The ResiScope is composed of three constituents: a digital module, an analog module and a graphical interface (figure 3.30). From the graphical interface (figure 3.31), data to be displayed

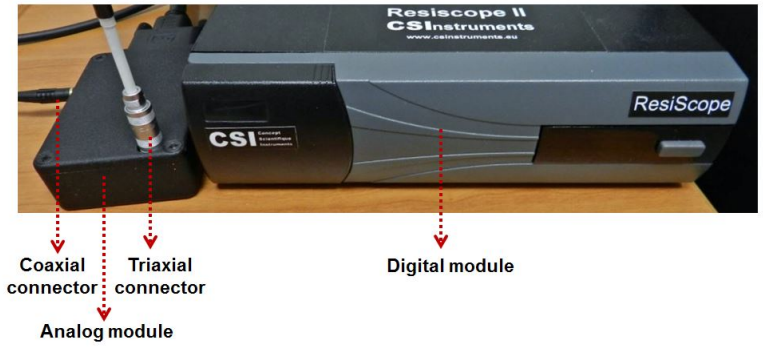

Figure 3.29: Digital module and analgo module of the ResiScope.

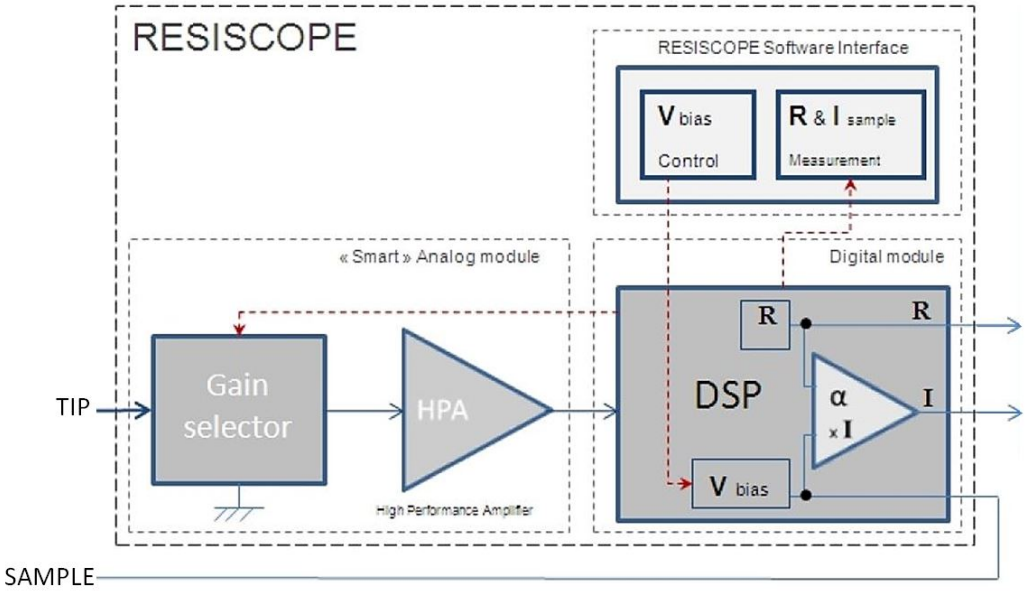

Figure 3.30: Schematic of the ResiScope from CSI website [150].

can be chosen among resistance, current and bias. User can also chose whether measurements are done under "Normal" configuration ([-10,+10] V), or under "Low Voltage" configuration ([-1,+1] V). Two modes can be chosen for the bias control: in "Automatic" mode a DC bias is directly controlled by the graphic interface. In "External control" mode, the bias is controlled by an input signal. It can either be DC or AC, which is of great interest for spectroscopy measurements.

Before each measurement campaign, a calibration must be done when tip and sample are not in contact. The measured resistance is then considered as the infinity.

The ResiScope is optimized to limit the current density through the contact. For small contact resistance the applied bias is much lower than the set-point bias. During indentation the contact area increases, leading to a contact resistance decrease. Thus, during indentation, the sample

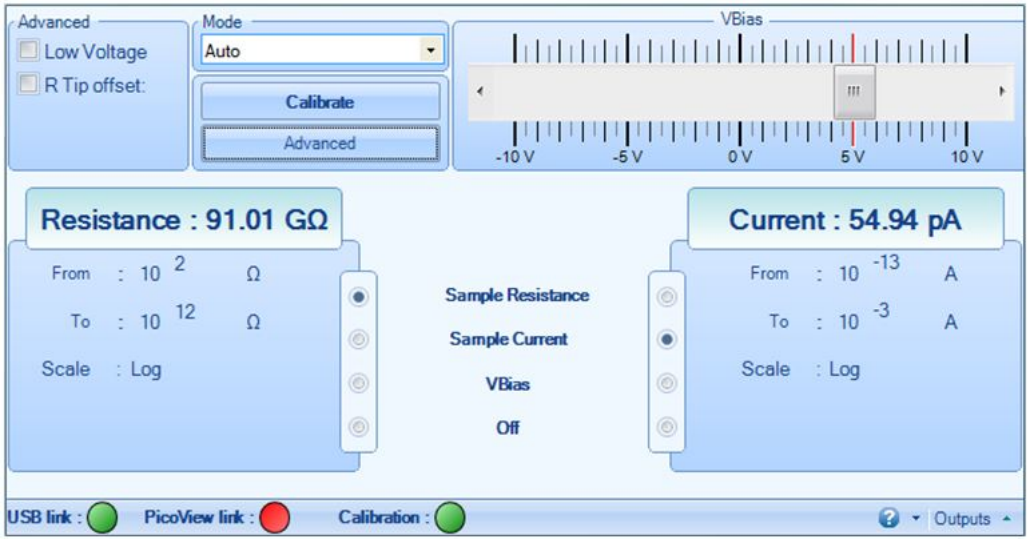

Figure 3.31: Graphical interface of the ResiScope.

bias is expected to decrease. For confidentiality reasons the relation between the set-point bias and the applied bias is not given in this communication.

By testing a series of reference resistors, it appears that the resistance measurements of the ResiScope slightly deviates from the nominal values of the resistors, as shown in figure 3.32. Therefore, resistance measured by the ResiScope must be corrected. The correction can be determined by fitting the data of figure 3.32. The correction used within the frame of this project is given by equation (3.2), with $R_{corrected}$ and $R_{measured}$ the corrected and the measured resistance.

$$R_{corrected} = 0.825 * R_{measured}^{1.046} \tag{3.2}$$

However, the ResiScope fails to measure low resistance under AC bias, even with relatively low frequency (1 Hz). For instance, resistance measurements performed on a 630 Ω resistor for 1 Hz AC bias and DC bias are shown in figure 3.33. The error in AC bias is up to 35 %, against 2 % for a DC bias. The maximal error occurs at low voltage but is still high for high voltage. As shown in table 3.2, this error is less important for higher measured resistance, but is amplified for higher signal frequency.

Thus, for spectroscopy measurements the Keihtley 6430 is preferentially used instead of the ResiScope. The Keihtley 6430 is also used to compare data obtained with the ResiScope. Nevertheless, contrary to the ResiScope this apparatus cannot operate in the entire resistance range [100, 1T] Ω without being blinded by range changes.

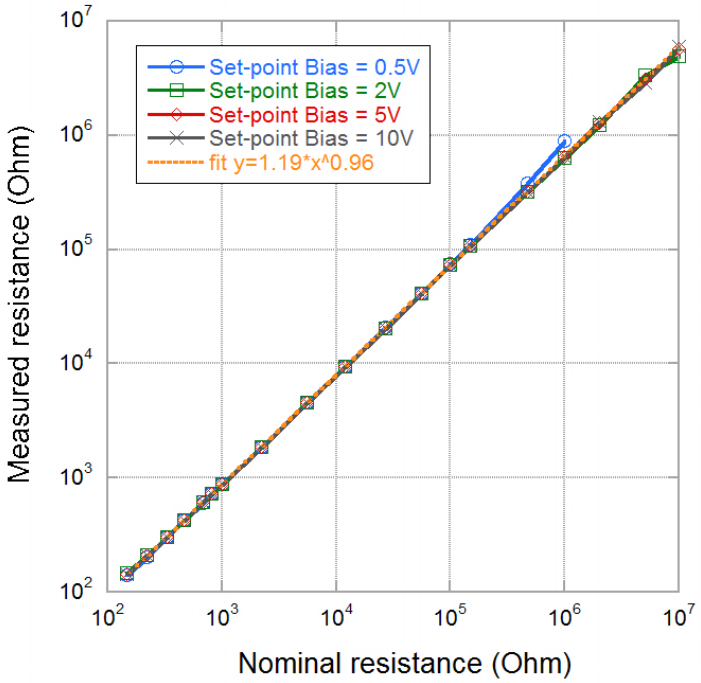

Figure 3.32: Resistance measured by the ResiScope versus nominal resistance.

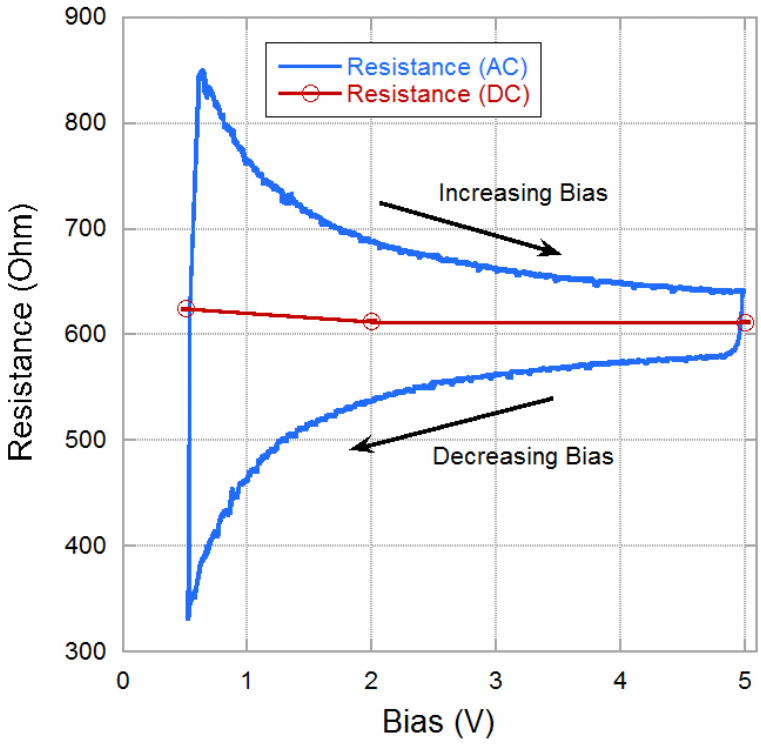

Figure 3.33: Resistance measurement performed on a 630 Ω resistor for 1 Hz AC bias and DC bias.

Nominal Resistance	Maximal error for DC bias	Maximal error for AC bias	Triangular signal frequency
630 Ω	2 %	35 %	1 Hz
2 kΩ	2 %	-	1 Hz
100 kΩ	1 %	3 %	1 Hz
1 MΩ	-	3 %	1 Hz
1 MΩ	-	20 %	10 Hz

Table 3.2: Maximal error when measuring resistors at DC and AC bias.

Measure chain for electrical measurements

As shown in figure 3.34 electrical data are collected via a data acquisition card from National Instruments (NI 6259). Home-made Labview programs fetch data from the NI DAQ and can either directly write them on a .txt file, or send them to the InView software. Using the Inview software, electrical data are directly synchronized with mechanical data, but the acquisition rate is limited to 500 Hz. When data are directly written on a .txt file the acquisition rate reaches 2 kHz. Specific Inview methods were developped for indentation coupled with electrical measurements.

The NI DAQ can also be monitored by Labview programs to generate AC signals (sinusoidal or triangular). This signal is then send to the ResiScope as an input (mode "External Control" of the ResiScope). This allows spectroscopic measurements.

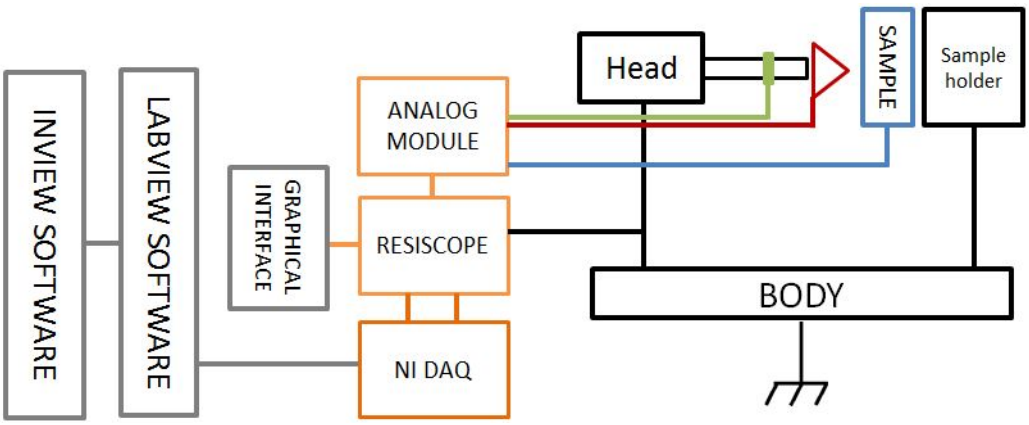

Figure 3.34: Schematic of the acquisition chain for electrical measurements.

A same acquisition chain is used for measurements with the Keightley. The only difference is that the digital module and the analog module are replaced by the Keihtley.

The measurement procedure is also slighty different when operating with the ResiScope and

with the Keihtley. The ResiScope optimizes the current passing through the sample, and so electrical measurements can be performed at the earliest stages of contact, without any risk of electrical breakdown. However, with the Keihtley, a maximal current compliance is set, and electrical measurements are only performed when the contact depth is large enough to avoid electrical breakdown (typically larger than 30 nm for a bias around 1-2 mV).

3.3.2 Mechanical validation

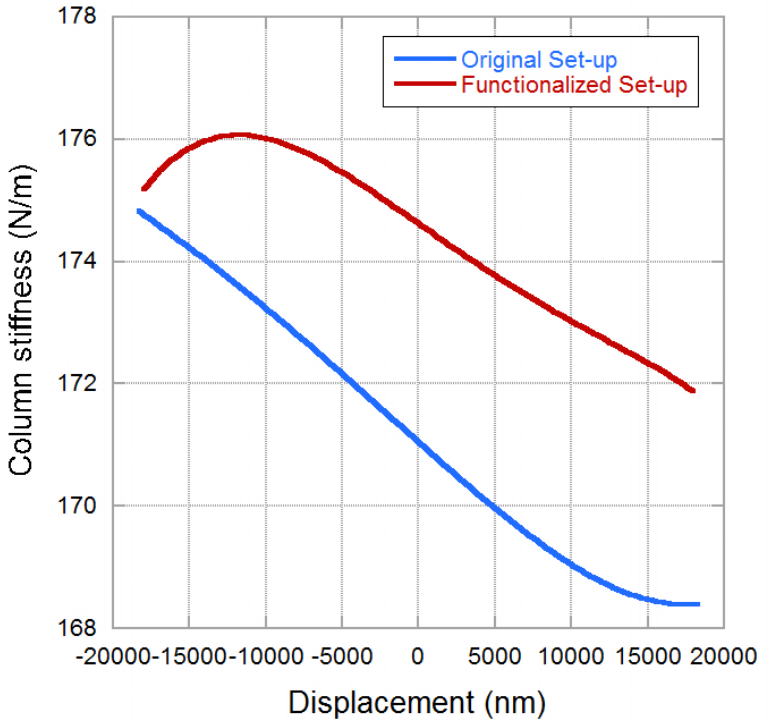

Figure 3.35: Column stiffness versus depth for the original set-up and the set-up functionalized for electrical measurements.

Following the same procedure as in section 3.1.2 (page 89), vibrations level and column stiffness were determined for the set-up functionalized for electrical measurements, and compared to the values obtained for the initial set-up.

Both vibration levels are quite similar, with standard deviations of 1.4 nm for the electrically functionalized set-up, against 1.7 nm for the original set-up. Maximal vibrations for the functionalized set-up is below 5 nm.

The column stiffness of the functionalized set-up is also comparable to that of the original set-up, as shown in figure 3.35. The gap between both stiffness is due to the additional stiffness brought wires connected to the tip. This deviation does not exceed 4 $N.m^{-1}$ ($\sim$ 5 %).

To go further, this value of column stiffness can be verified by measuring the resonant frequency curves of the actuator in CSM mode. The harmonic displacement is measured for various CSM frequency by using a home-made Labview program. Measurements are performed with a column displacement of $\sim$ 2 µm, which corresponds to the value at which indentation are usually performed. The harmonic force is set at 1 µN.

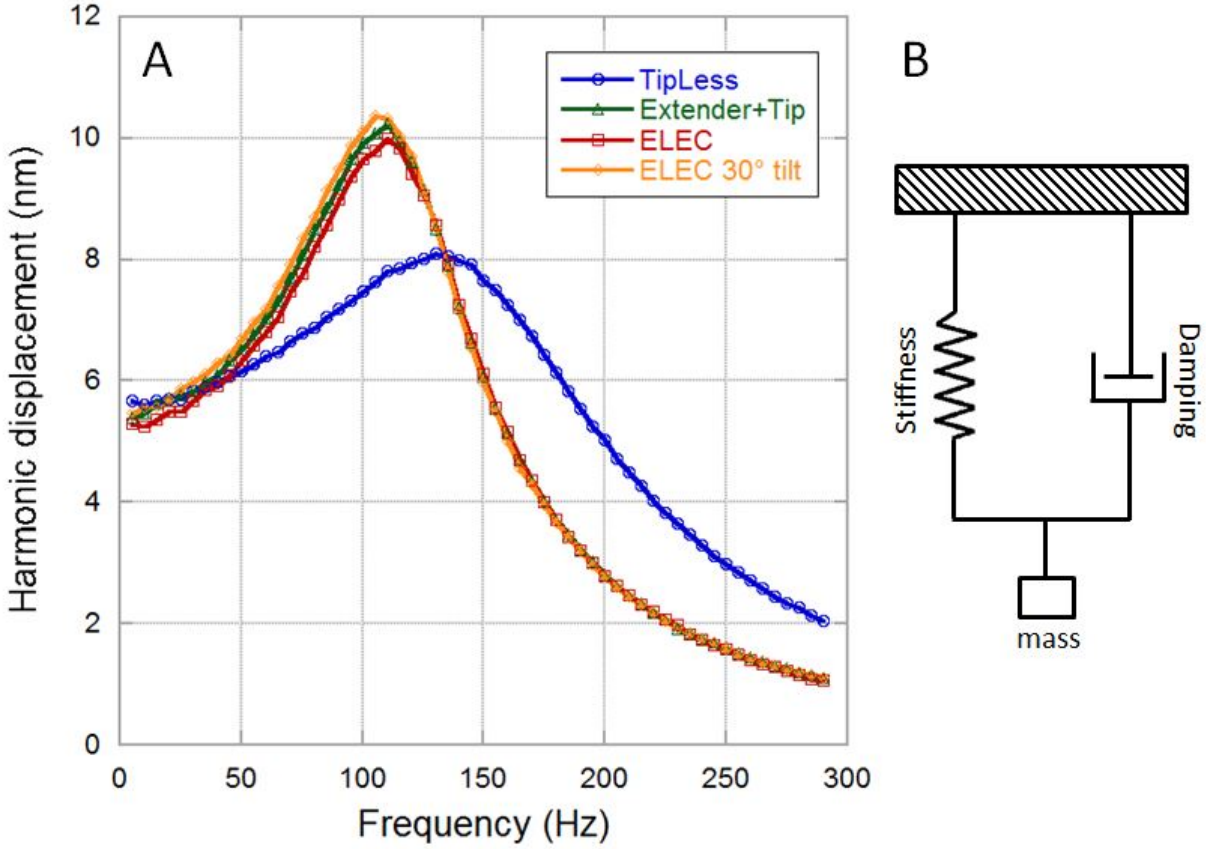

Figure 3.36: A: Harmonic frequency-versus-harmonic displacement curves for various set-up configurations: without tip and extender (blue), with tip and extender but no electrical connections (green), with electrical connections on the tip and the extender (red), with electrical connections and the set-up tilted at 30° (orange) and B: corresponding mechanical diagram.

This leads to the resonant curves of figure 3.36. The measurements have been performed both without electrical connection (green curve) and with electrical connections to the tip and to the ceramic work-piece on the extender (red curve). For comparison, measurements have also been performed without the tip and the extender (blue curve), and with the set-up tilted at 30° as for the *in situ* SEM configuration.

The obtained curves can be fitted to obtain the mass of the column, the damping coefficient and the column stiffness. Results are given in table 3.3. The use of an extender and a tip

increases the mass column of 130 mg. The damping coefficient is roughly constant whatever the configuration of the set-up. The column stiffness only increases of $\sim$ 5 N.m^{-1} due to the electrical connections, which is coherent with the 4 N.m^{-1} found in figure 3.35. With the same electrical connections, a 30° tilt tends to decrease the column stiffness.

	Resonant Frequency	**Column Mass**	**Damping Coefficient**	**Column Stiffness**	**R^2**
No Tip	130 Hz	180 mg	0.135 Ns.m^{-1}	175 N.m^{-1}	0.999
Extender + Tip	108 Hz	310 mg	0.137 Ns.m^{-1}	179 N.m^{-1}	0.998
Electrical connections	110 Hz	310 mg	0.137 Ns.m^{-1}	184 N.m^{-1}	0.999
Electrical connections, 30° tilt	105 Hz	320 mg	0.136 Ns.m^{-1}	177 N.m^{-1}	0.998

Table 3.3: Resonant frequency, column mass, damping coefficient and column stiffness obtained by fit of the harmonic frequency-versus-harmonic displacement curves for various set-up configurations and corresponding fit correlation coefficient R^2.

3.3.3 Electrical sensitivity

Electrical measurements have been conducted while indenting a gold single crystal with a Berkovich BDD tip. Indentations were performed with CSM mode at 100 Hz and 150 Hz, with dynamic amplitudes of 1 nm or 2 nm. The data acquisition rate was 500 Hz. The signature of CSM oscillations during nanoindentation can be seen on resistance-versus-time curves, as shown in figure 3.37. Fast Fourier transformations (FFT) where performed on the resistance data, leading to figure 3.38. Peaks at 100 Hz and 150 Hz respectively are clearly visible on the FFT amplitude. Thus resistance measurements are sensitive enough to account for mechanical oscillations as low as 2 nm. One can notice that the power supply frequency (50 Hz) is also visible (black arrow).

Mechanical oscillations are visible up to 400 nm depth for 2 nm amplitude and up to 200 nm depth for 1 nm amplitude. This corresponds to relative variations of the contact area of 1 % with a Berkovich tip.

Thus, for BDD tips, the resistance sensitivity is high enough to sense variation of the contact area as low as 1 %. Nevertheless, for more conductive tips, such as carbides tip, the sensitivity is much less, and resistance variations due to mechanical oscillations are not visible. This underlines the usefulness of BDD tips to account for mechanical changes of the contact area,

and thus the interest of BDD tips for electrical monitoring of the contact area. This point will be adressed in chapter 6 (page 179).

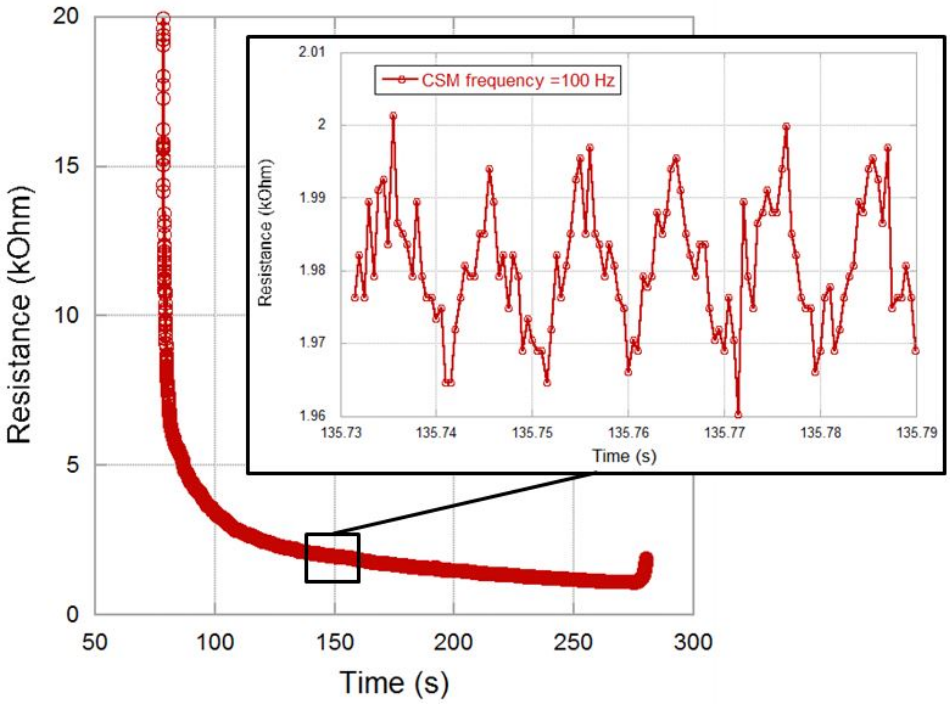

Figure 3.37: Resistance variation due to CSM mode during nanoindentation.

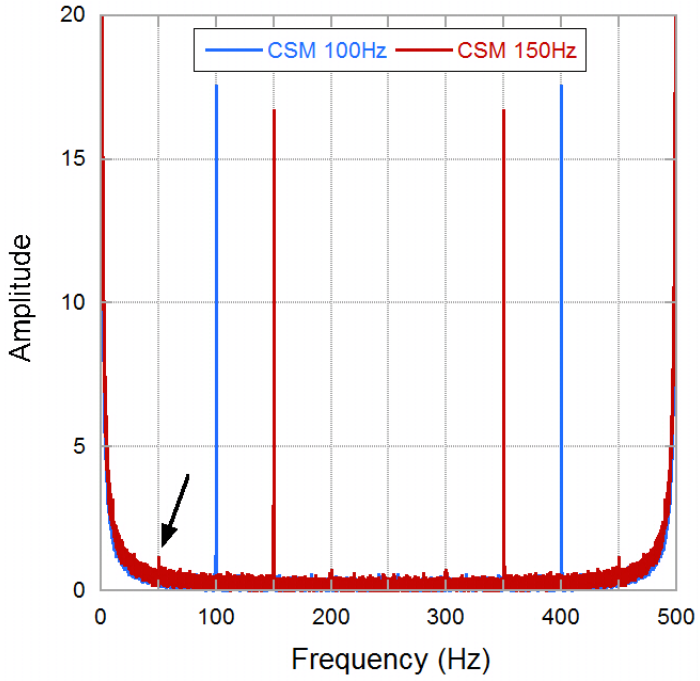

Figure 3.38: FFT amplitude on resistance measurements depending on the CSM frequency (1 nm dynamic amplitude). Black arrow corresponds to the power supply frequency (50 Hz).

3.4 *In situ* SEM nanoindenter coupled with electrical measurements

The two previous sections dealt with the integration *in situ* SEM of a nanoindenter and the electrical functionalization of this nanoindenter. This section associates both *in situ* SEM integration and electrical coupling.

Electrical measurements *in situ* SEM is of great interest, since it allows electrical characterisation of small objects. For instance, capacitive measurements *in situ* SEM could enable the computation of the dielectric constant of micrometric or submicrometric objects. Resistive measurements *in situ* SEM could give access to the resistivity of different phases of a multiphase alloy.

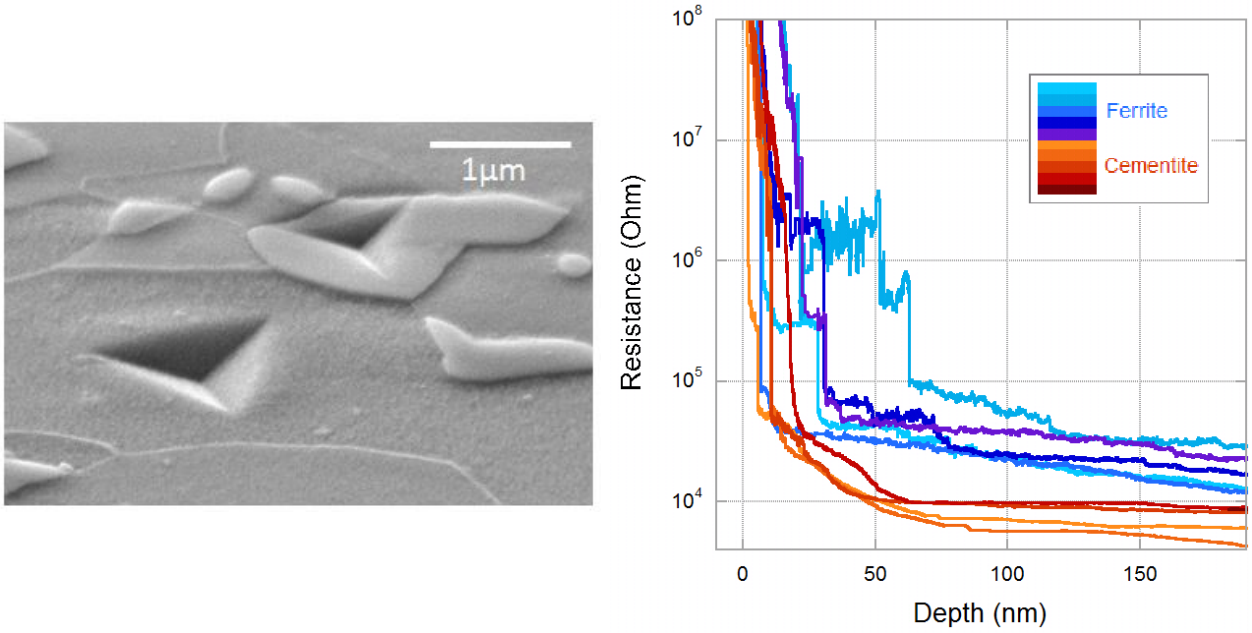

Figure 3.39: Electrical measurements during indentation of ferrite and cementite. Left: SEM picture with residual indents. Right: Resistance-versus-depth curve (set-point bias 5 V).

The electrical measurements *in situ* SEM operates exactly as at room atmosphere. The only attention point is that both sample and tip have to be grounded while imaging, whereas they are not grounded during electrical measurements. Obviously electrical measurements cannot be performed simultaneously with SEM imaging. Sample and tip are either grounded or connected to the ResiScope. Thus, the procedure for electrically coupled nanoindentation *in situ* SEM is:

1. Sample and tip are grounded. Using SEM imaging the object to indent is targeted, as described in 3.2.2 (page 94).

2. The beam is frozen. Sample and tip are connected to respectively the coaxial cable and the triaxial cable of the ResiScope. Indentation and electrical measurements can then be performed.

3. After indentation, sample and tips are grounded again to image the residual imprint.

Exploratory testing has been performed on a steel sample composed of a ferritic matrix with large cementite carbides. The sample was provided by the LEM3 laboratory in Metz. Figure 3.39 shows different resistance behaviors when indenting ferrite or cementite. Although the ferrite is known to have a lower resistivity than the cementite, the resistance of the ferritic phase appears to be higher than that of the cementite. This is most likely due to an oxide layer which forms on the ferrite. Even if a complete analysis is needed to fully understand the electrical behavior of both phases, these results show the feasibility electrical measurements during *in situ* SEM nanoindentation.

3.5 Conclusion and development prospects

To conclude, a nanoindenter *in situ* SEM coupled with electrical measurements has been successfully developed. Thanks to the SEM integration, this device allows indent positioning with a precision better than 100 nm. This enables the mechanical study of submicrometric systems. Moreover the electrical measurements during indentation can be performed either at air, under intermediate vacuum or *in situ* SEM. The ResiScope used for resistance measurements can measure resistance change over 10 decades, with acquisition rate up to 1 kHz. The sensitivity in resistance is promising for electrical investigation of mechanical events.
The main axis for further development is the implementation of the 5 axes set-up. This set-up will allow the use of *in situ* SEM analytical facilities such as EDX or EBSD.

Chapter 4

Various applications to material science

In order to benefit from the performances of the *in situ* set-up described in chapter 3 (page 81), several studies have been performed on various materials and are described in this chapter. Three points are developed:

i/ The nanoindenter ability to locate precisely indents into small objects or individual phases (section 4.1, page 116). A study performed with an XP MTS apparatus is first described, but this nanoindenter is no longer appropriate for complex geometries and smaller phases, where the Inforce nanoindenter is preferentially used. Steels with different scale sizes are investigated with the Inforce set-up, from an architectured duplex stainless steel with micrometric phases to a ferritic steel with submicrometric cementite phases.

ii/ The nanoindenter ability to perform large statistics and mechanical properties maps and profiles, thanks to high speed nanoindentation (section 4.2, page 128). Model materials (Au and Al single crystal, fused silica) as well as more complex samples (ferrite cementite steel with submicrometric carbides, dissimilar metal weld) are studied.

iii/ The ability to perform nano-compression on small-scale systems (section 4.3, page 137). *In situ* SEM micro-compression tests have been conducted on AlN coated polymer scaffolds by using a flat punch with the Inforce setup.

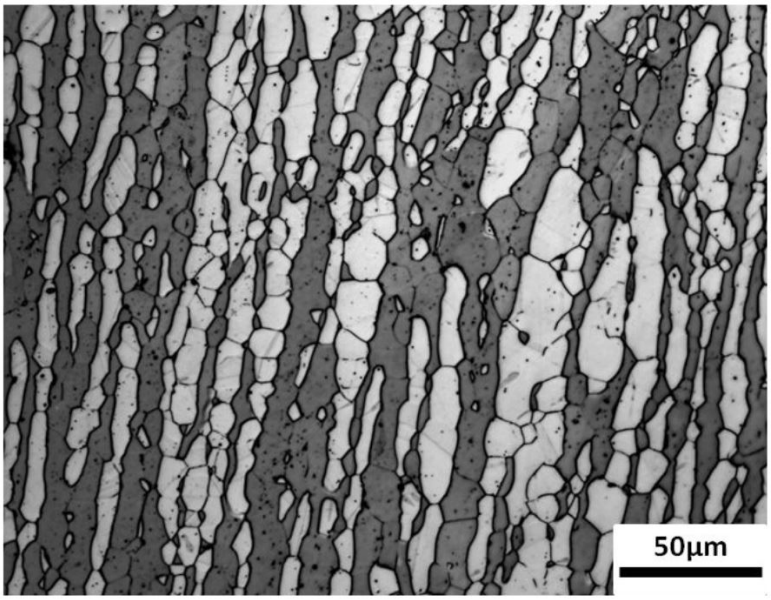

Figure 4.1: Optical micrograph along rolling direction illustrating the initial duplex microstructure, with ferritic phase (dark grey) and austenitic phase (light grey), from [153].

4.1 Mechanical properties of individual phases

4.1.1 Mechanical properties of individual phases in a duplex stainless steel

Evaluation of the hardness in a duplex stainless steel exhibiting a TRIP effect with an XP apparatus

Duplex stainless steels consist of a two phase microstructure, involving a ferritic phase and an austenitic phase in roughly equal proportion. These alloys are characterised by a good strength/ductility compromise, an excellent corrosion resistance, a high capacity of weight saving due to their high strength and a reasonable price due to their low Ni content in comparison with conventional austenitic stainless steels. That's why they are a good alternative in various industrial applications.

New grades of duplex stainless steel using the transformation-induced plasticity (TRIP) effect has recently been developed [152]. In those alloys, austenite remains stable under low stress but transforms into martensite under high stress.

Within the frame of the Ph.D of Lechartier at SIMaP [153, 154], new duplex stainless steel compositions, experiencing a well-controlled TRIP effect, has been developed in order to improve the strength/elongation compromise during tensile tests. In particular a grade of duplex stainless

TRIP steel with the following chemical composition Fe-22.15Cr-4.58Ni0.34Si-0.3Mn-0.20Mo-0.20Cu-0.007N-0.021C has been studied . The microstructure of this alloy is characterized by bands of austenite in a ferritic matrix, as shown in figure 4.1. These bands result from the rolling process. The size of each phase is about 10-20 µm.

Since the phase transformation that occurs during straining has an impact on the macroscopic mechanical behavior, it is necessary to characterize its effect on the partitioning of deformation in the composite.

The strain of each phase (ferrite and austenite+martensite respectively) was determined by microscale digital image correlation and compared to the macroscopic strain, as shown in figure 4.2 A. Up to 0.05 % deformation, the average plastic strains within the ferrite and within the austenite + martensite mixture exhibit similar values and they are equal to the macroscopic plastic strain. Above 0.05 % deformation the strain partitioning increases, namely ferrite takes an increasing fraction of macroscopic strain. This evolution is correlated to austenite transformation into martensite, which was quantified by *in situ* high energy X-ray diffraction (figures 4.2 B and 4.2 C).

The difference between average plastic strains of ferrite and austenite + martensite comes from martensite transformation, which causes an hardening of the austenite + martensite mixture. This leads to higher deformation within ferrite phase.

We aim at getting the individual strength of each phase and its evolution during deformation. In order to clarify the strength of each phases, complementary nanoindentation tests have been carried out with an MTS XP apparatus. Indents were performed up to 200 nm depth with a diamond Berkovich tip at a 0.05 s^{-1} strain rate. Measurements were carried out before deformation (without martensite) and after 38 % of macroscopic strain (transformation completed: all the austenite is transformed into martensite). To avoid edge effects, only indents far from a phase boundary (typically three times their diameter) were included in the analysis. Young's modulus and hardness are computed using Oliver and Pharr method [28]. Mean hardness and modulus values obtained at 200 nm depth are shown in figure 4.3. Initially, ferrite and austenite exhibit similar hardness of respectively 3.7 ± 0.3 GPa and 3.8 ± 0.3 GPa. This is consistent with the absence of strain partitioning at the initial state, also found by Asgari *et al.* [155] who reported hardness of ∼ 4.5 GPa for both ferrite and austenite in duplex stainless steel.

During straining austenite transforms into martensite leading to a change of plastic flow. The hardness value for martensite in the deformed sample was found to be 6.0 ± 0.3 GPa whereas the ferrite had an hardness value of 3.9 ± 0.3 GPa. Similar hardness values were found for

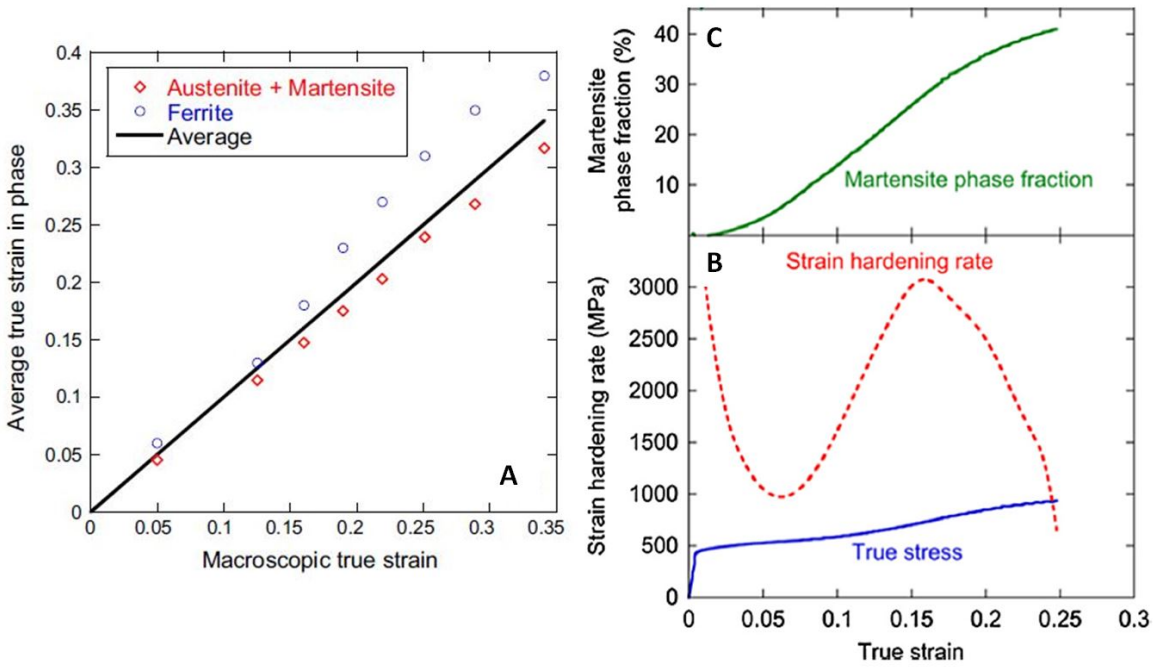

Figure 4.2: A: Evolution of the strain partitioning: average deformation within the ferrite and within the austenite + martensite as a function of the macroscopic strain. B: Stress-strain curve and associated strain-hardening rate during tensile test. C: Corresponding martensite fraction measured by *in situ* high energy X ray diffraction. From [154].

martensite and ferrite in a dual phase steel by Delince *et al.* [156].

This work shows the advantage of nanoindentation to asses local mechanical properties of a multiphase alloy. However, the optical imaging system of the MTS XP apparatus does not allow the precise positioning of indents on small phases. Thus, the use of this apparatus is no longer appropriate for alloys with more complex geometries and smaller phases. In that case, it is necessary to switch to a nanoindenter coupled with imaging techniques showing better resolution, such as the *in situ* SEM Inforce nanoindenter described in chapter 3 (page 81). In what follows, we will use the *in situ* SEM Inforce nanoindenter to investigate mechanical properties of individual phases.

This work was published at *Metallurgical and Materials Transactions A*, **48**, 20-25 (2017) [154].

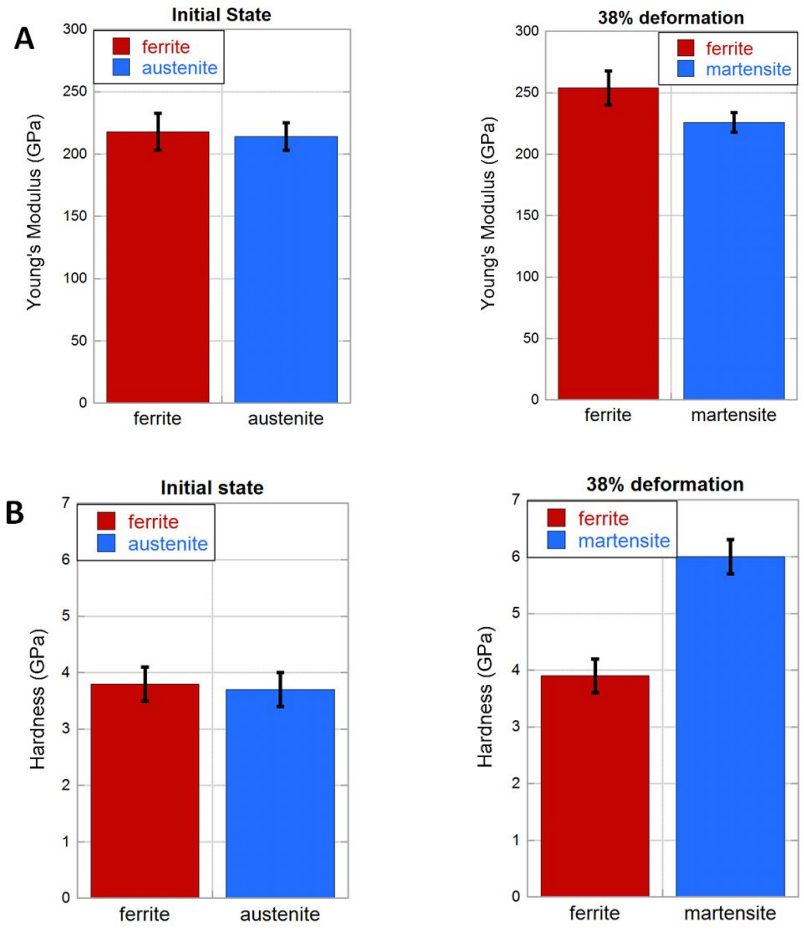

Figure 4.3: Young's modulus (A) and hardness (B) values for individual phases of duplex stainless steel alloy before and after 38 % deformation.

Micro-composite duplex stainless steel

Within the framework of the Ph.D of Naser at SIMaP [157], micro-composite duplex stainless steel has been manufacturing using accumulative drawing and re-bundling process (ADB). Materials used were ferritic stainless steel 430LNb rich in Niobium and austenitic stainless steel 316L. As detailed in [157] and schematized in figure 4.4 A, the manufacturing process can be described as follows:

0/ Wires of austenite 316L or ferrite 430LNb are arranged in an austenite 316L tube, which constitutes the first elementary pattern, also shown in figure 4.4 B.

1/ The previous pattern is drawn, leading to the (re)-bundling composite. During wire drawing the composite diameter is reduced from 6 mm to 1.5 mm through 14 steps.

2/ The new composite is annealed in a vacuum furnace, in order to recover mechanical properties and the capacity of further plastic deformation.

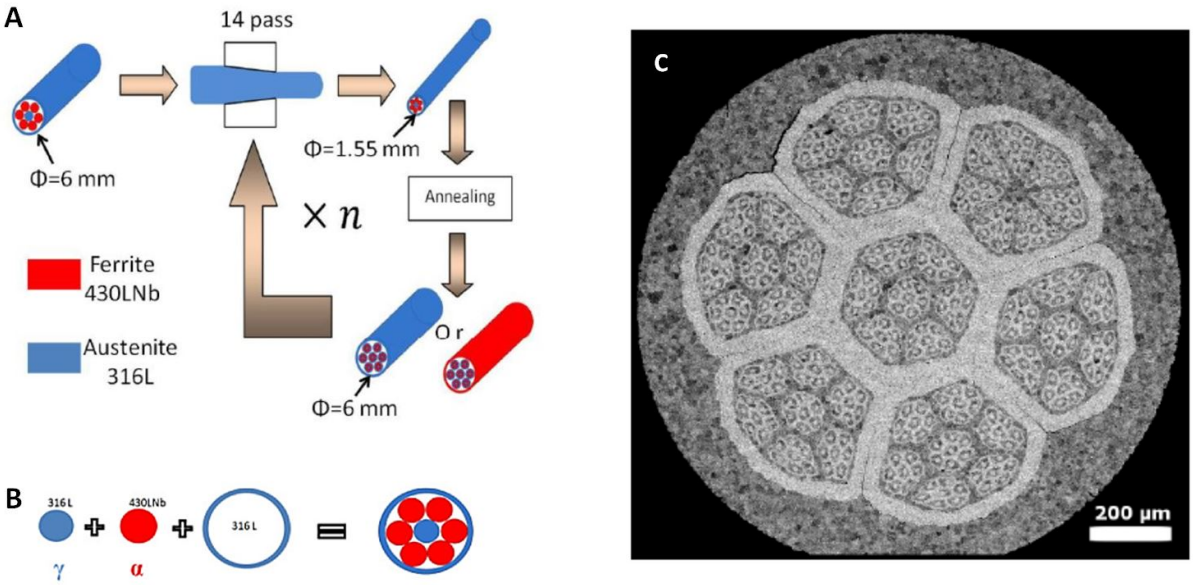

Figure 4.4: A: Schematic illustration of the ADB process, B: Configuration of the first composite, C: SEM image for a $n = 4$ composite, with ferrite in light grey and austenite in dark grey. From Naser [157].

3/ Wires of this composite are arranged in a ferritic or an austenitic tube, which constitute the new pattern.

Steps 1 to 3 are repeated n times, with n the scale reduction factor.

As first assessment to evaluate the performances of the Inforce nanoindenter described in chapter 3 (page 3), nanoindentation testing has been performed on the transverse surface of $n = 4$ duplex stainless steel composites from Naser PhD. Since these samples exhibit a 1D geometry, they are homogeneous in depth, and thus ideal for nanoindentation testing. Two $n = 4$ composites were investigated, corresponding respectively to the state after final annealing (5 mn at 850°C) and to the as-drawn state.

Both $n = 4$ composites have undergone four successive scale reductions, leading to ferrite and austenite from different generations, as shown in figure 4.5. Thus, ferrite $F1$ coming from the ferrite wires of the initial pattern, has been reduced four times. Ferrite $F2$ from the ferrite tube of the second scale reduction has been reduced three times. Ferrite $F3$ from the tube of the fourth scale reduction has only been reduced once. Both austenite $A1$ and $A1'$ comes from the initial pattern and corresponds to the first austenite wires ($A1$) and to the first austenite tube ($A1'$). $A1$ and $A1'$ have been reduced fourth times. Lastly, $A2$ corresponds to the austenite tube from the third scale reduction and has been reduced twice. Each phase is annealed after every drawing steps, except for the last reduction scale of the as-drawn sample. The final

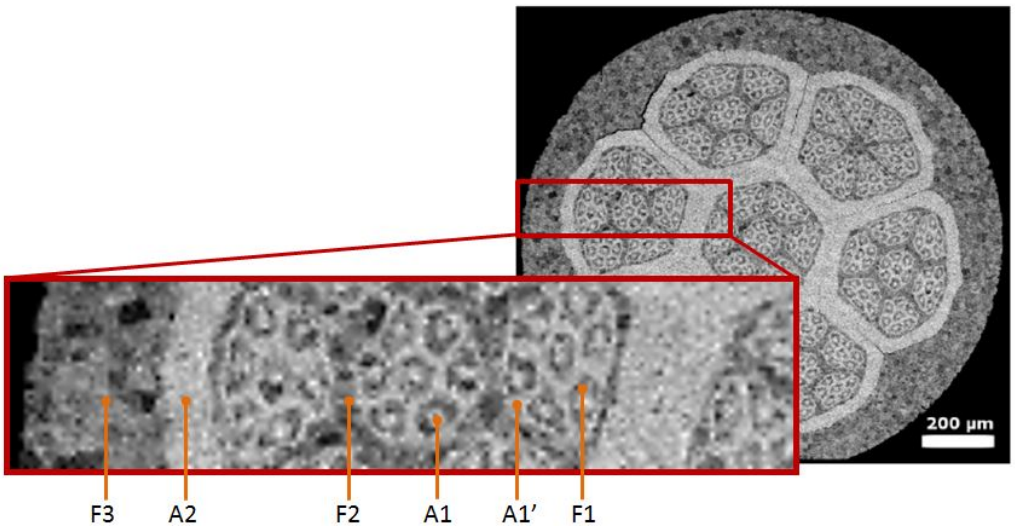

Figure 4.5: Different generations of ferrite and austenite on $n = 4$ composites.

average size for each austenitic and ferritic phases are shown in table 4.1.

One of the issues raised by such samples is the mechanical properties recovery after each annealing: Do the phases from different scale reduction equally recover mechanical properties after annealing?

Thanks to SEM imaging, individual nanoindentation testing has been performed with a Berkovich diamond tip on ferrite and austenite from different generations. Constant strain rate of 0.05 s^{-1} was used. The nanoindenter was operated in CSM mode (1 nm of dynamic amplitude). Maximal depth of 300 nm was applied.

Corresponding results are shown in figure 4.6. Results were computed with at least 5 indents for each generations of ferrite and austenite. Both Young's modulus and Hardness were calculated using Oliver and Pharr method [28]. As expected, hardness of as-drawn sample is higher than hardness of annealed sample, although their modulus are quite similar. Austenitic phase is harder than ferritic phase, especially for the as-drawn sample where the mean hardness value at 300 nm depth is 5.8 $\pm$ 0.2 GPa for the austenite and 4.2 $\pm$ 0.2 GPa for the ferrite. This trend is less pronounced for the annealed state, with hardness values of 4.0 $\pm$ 0.4 GPa for the austenite and 3.5 $\pm$ 0.2 GPa for the ferrite. For the annealed state, this slight difference is essentially due to the $A2'$ austenite which is much harder than $A1$ and $A2$ austenite.

The high hardness value for $A2'$ austenite of annealed sample can be explained by the work of Naser [157]. Indeed, Naser showed that a Ni-depleted area was formed during annealing within austenite phase near ferrite/austenite interface. This area promotes austenite transformation into martensite upon cooling. Thus, martensite layers from 1 to 2 μm were found at the

	F1	**F2**	**F3**	**A1**	**A1'**	**A2**
Size (μm)	8	10	132	10	5	40

Table 4.1: Size of austenitic and ferritic phases of $n = 4$ composite, according to [157].

boundary of austenite phase. However, the size of $A2'$ austenite is around 5 μm. As a result the remaining pure austenite should be really small and indentation are necessary affected by the presence of harder martensite. This issue does not seem to appear for $A1$ and $A2$ austenitic phases which are larger.

Ferritic phases and austenitic phases $A1$ and $A2$ of annealed sample exhibit similar hardness values of respectively 3.5 ± 0.2 GPa and 3.8 ± 0.2 GPa. Similar values were obtained within the work of Lechartier [153, 154] with the XP nanoindenter.

The youngest generations of ferrite and austenite of as-drawn sample (respectively $F3$ and $A2$) seems to have lower hardness value than older generations. This might show that the annealing steps are not sufficient so that the phases recover their entire capacity of plastic deformations. This trend appears to a lesser extent for ferrite generations of annealed sample. This can be compared to the results obtained by Naser [157] with micro-hardness. Naser have found that the oldest generation of ferrite and austenite had higher hardness. He attributed these results to the grain size, which were significantly finer for the old generations of austenite and ferrite ($\sim$ 1.7 μm for $A1$ and $A1'$, $\sim$ 3.7 μm for $A2$, $\sim$ 10.5 μm for $F1$ and $F2$ and $\sim$ 18 μm for $F3$). However, since the size of each phase is below 10 μm, micro-hardness measurements might have been compromised due to the extension of the plastic zone around indents outside the investigated phase.

The morphology of residual imprints also differs between as-drawn and annealed sample, as shown in figure 4.7. Residual imprints on annealed sample (C,D) are characterized by large and asymmetric pile-ups along a preferential direction, whereas residual imprints in as-drawn sample (A,B) are more homogeneous. Well defined Slip bands traces from dislocations characterize the upheaval around the annealed austenite (D). Loading curves of annealed sample also presents several pop-ins (figure 4.8). The difference of mechanical response between both samples could be due to dislocation nucleation which is easier in as-drawn sample where a large density of dislocations is initially present.

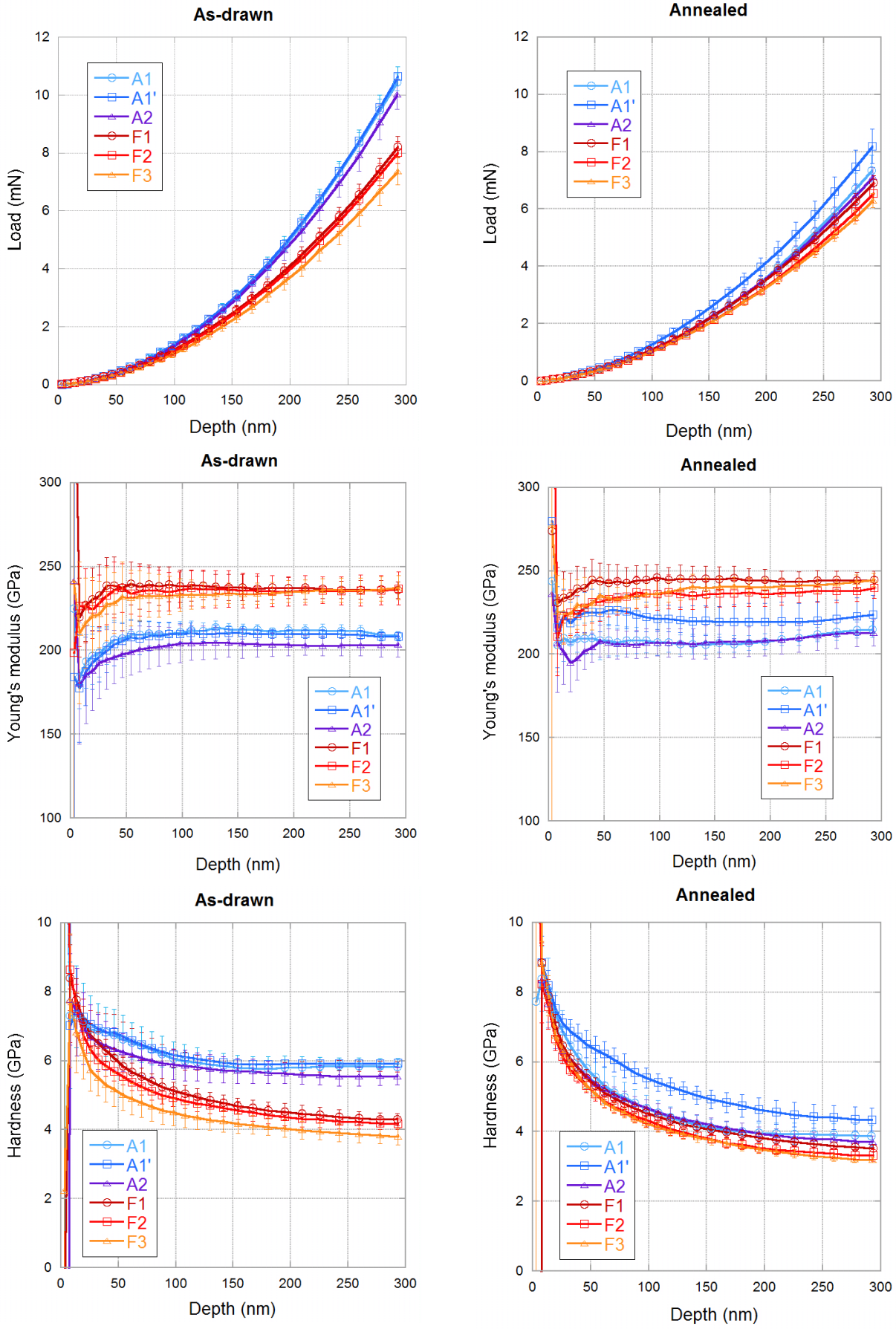

Figure 4.6: Indentation, modulus and hardness curves on as-drawn (left) and annealed sample (right) for ferritic and austenitic phases from different generation.

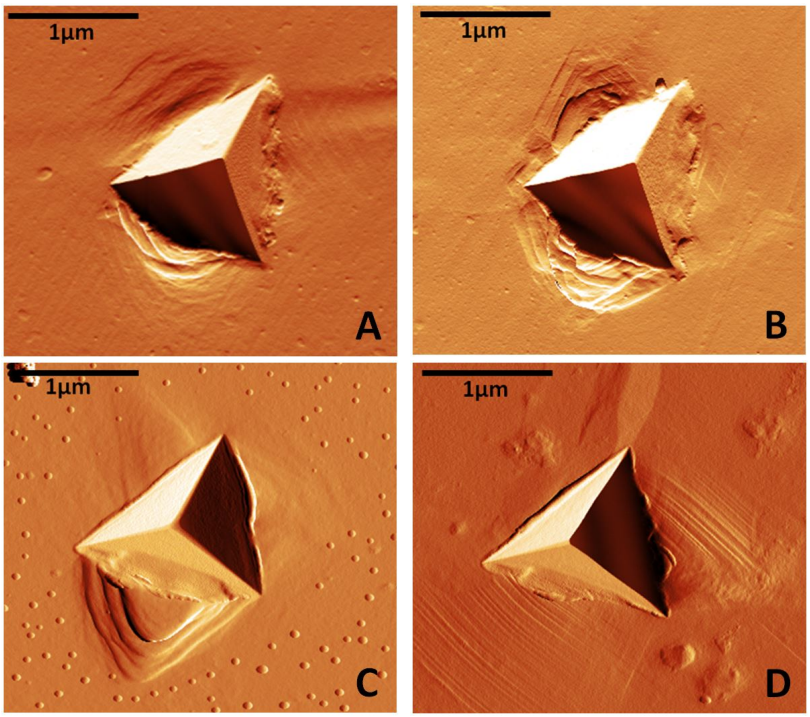

Figure 4.7: AFM amplitude image of indents on ferrite (A,C) and austenite (B,D) phase for as drawn (A,B) and annealed (C,D) samples.

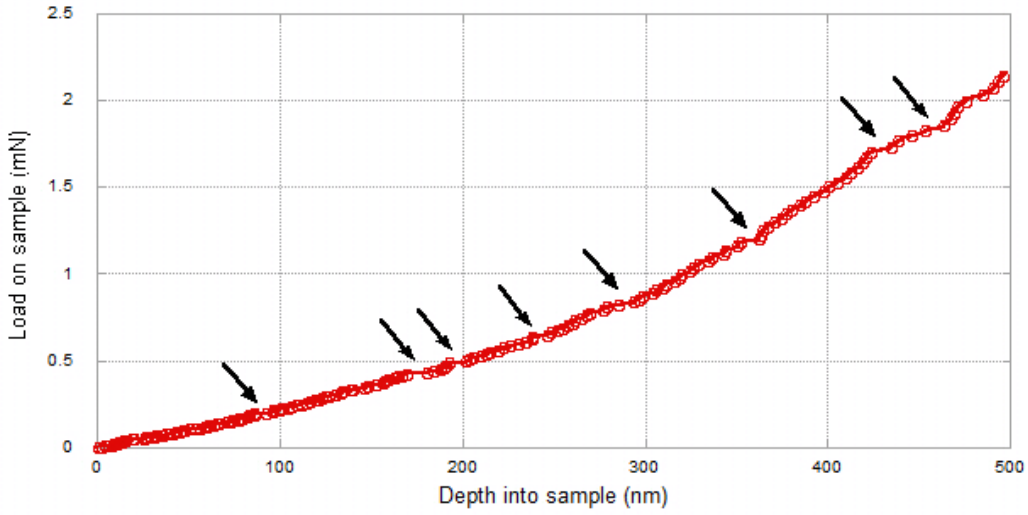

Figure 4.8: Loading curve during indentation of the ferrite phase of annealed sample, showing the evidence of several pop-ins.

As a result to this study, nanoindentation data have revealed a difference of hardness between the youngest generations of ferrite and austenite and the oldest generations. This shows that the annealing steps are probably not sufficient so that the phases recover their entire mechanical properties. Nanoindentation tests also tends to confirm the formation of a martensite layer at the ferrite/austenite interface. Note that the effect of residual stresses within the composites

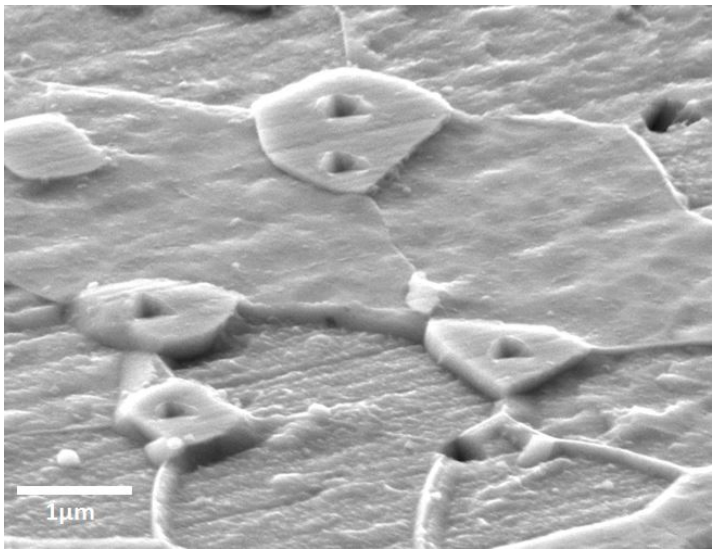

Figure 4.9: *In situ* SEM nanoindentation on micrometric cementite.

has not been studied in this case study.

4.1.2 Local mechanical properties of a ferritic steel with micrometric carbides

Last paragraph dealt with the capacity of measuring mechanical properties of individual phases with sizes above 5 µm, where the use of *in situ* SEM nanoindenter is required. In this case study a two-phase 2C40 steel (Fe-0.4C-0.7Mn-[0.1,0.4]Si) provided by the LEM3 laboratory in Metz is studied. It is constituted of a ferritic matrix and micrometric cementite particles. Cementite particles size is around 1 µm diameter (much smaller than the phases of paragraph 4.1.1, page 119). Moreover, the sample has a 3D configuration, since all the cementite particles are surrounded by the ferritic matrix.

In situ SEM nanoindentation testing with the Inforce nanoindenter has been performed on each particles (figure 4.9). The motivation is the determination of the mechanical properties of cementite with respect to the ferrite. Indentations were performed with a diamond cube corner using CSM mode (1 nm dynamic amplitude) and with a strain rate of $0.05\ s^{-1}$. Maximal depth of 150 nm was applied. Mean hardness and modulus values for each indentation on cementite at [50-70]nm depth are shown in figure 4.10, with respect to the distance between the center of residual imprints and phase boundary. Corresponding values for ferrite are calculated from 25 measurements and are shown in figure 4.10 at zero distance from the interphase. Hardness and modulus are computed using Oliver and Pharr method [28]. The decrease in hardness and

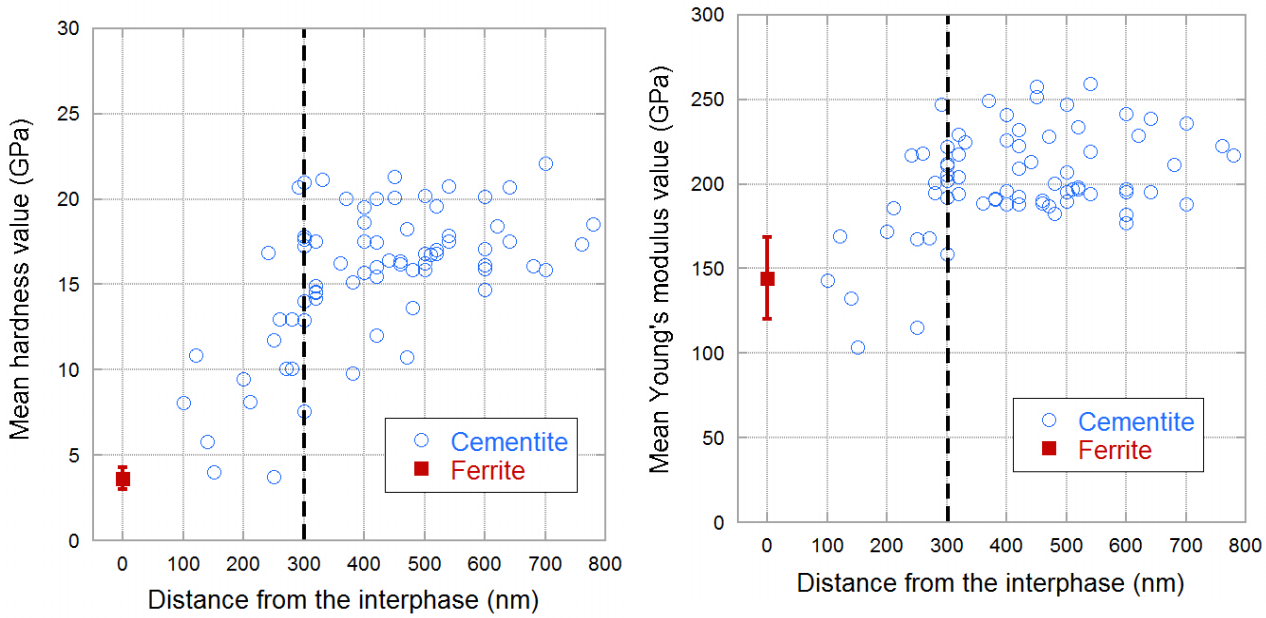

Figure 4.10: Modulus and Hardness values obtained by nanoindentation on cementite and ferrite with respect to the distance from the center of the residual imprint to the interphase boundary (zero for the ferrite).

modulus for the indents close to the interphase boundary is due to the influence of the ferritic phase on measurements. From figure 4.10 it appears that hardness and modulus are roughly constant for a distance from the interface higher than 300 nm.

However, even by selecting only the indents which are more than 300 nm away from phase boundaries, mechanical data obtained for cementite have to be taken with extreme caution. Indeed, the sample have a 3D geometry contrary to the stainless duplex steel composites presented in 4.1.1. Ferritic matrix below the investigated carbides can affect the measurements (figure 4.11). The configuration is close to the "hard films on soft substrate" configuration. In that case, numerical approach are necessary to extract mechanical properties of thin films. According to a study of Saha and Nix [158], mechanical results on thin films could be reliable if the indenter displacement did not exceed 10 % of the film thickness. In the frame of this study, there is no way of knowing the cementite size below the indenter. However, it seems reasonable to attribute constant hardness-versus-depth curves below 100 nm depth as mainly due to the cementite contribution.

Hardness and modulus values on cementite are computed in the depth range [50-70] nm using indents that meet these two criteria: i/ distance between the residual imprint and the interphase boundary is larger than 300 nm; ii/ hardness and modulus-versus-depth curves are roughly constant below 100 nm depth, which guaranties a limited effect of the ferritic phase below the

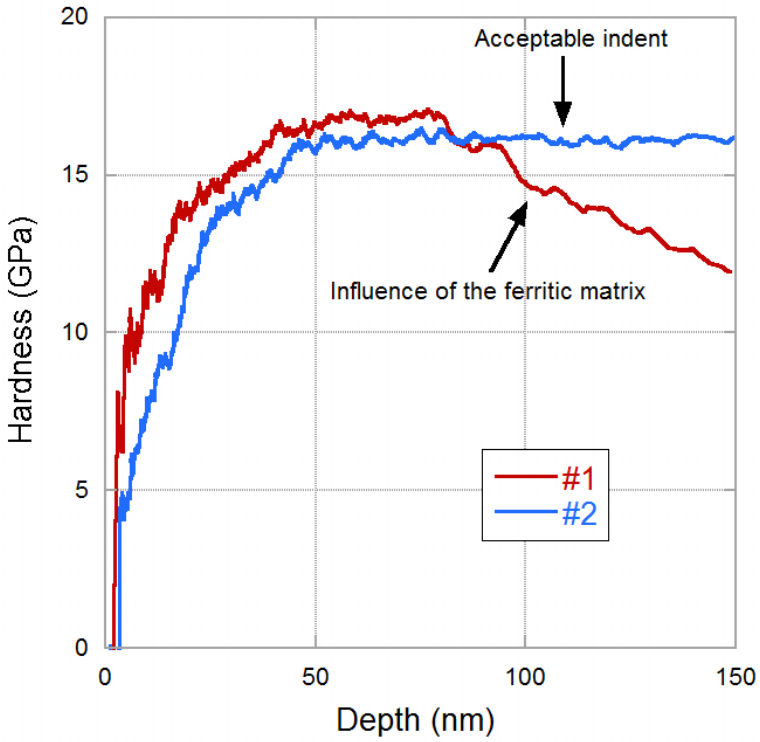

Figure 4.11: Hardness-versus-depth curves on two cementite carbides.

cementite. 28 indents were found to meet both criteria.

The modulus for the cementite is found to be 198 ± 16 GPa and its hardness 16.9 ± 1.7 GPa, whereas ferrite modulus and hardness were found to be 144 ± 24 GPa and 3.6 ± 0.6 GPa respectively. Similar hardness values were found by Ouahab [159] on bainitic steel with cementite size up to several microns. Thus, Ouhabab found hardness value of 3.9 ± 0.4 GPa for the ferritic phase. However, they used a MTS nanoindenter which were not able to locate precisely the indents on cementite, and only two carbides were indented, given values of respectively 20.0 GPa and 13.8 GPa. This is also close to the hardness values of 12-13 GPa found by Fernandez-Vicente [160] on 250 µm cementite.

In conclusion, thanks to the *in situ* SEM nanoindentation, several indents have been precisely positioned on micrometric cementite particles, given more confident data concerning the case of inclusion in a matrix.

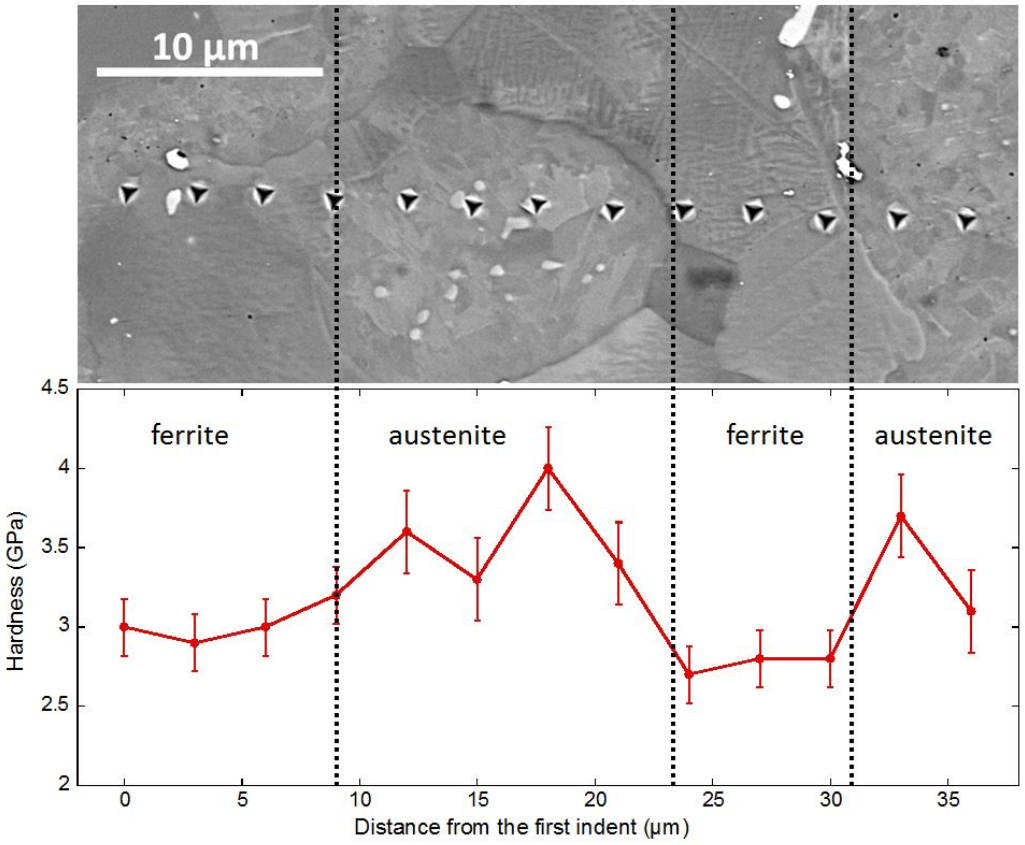

Figure 4.12: Hardness profile on duplex stainless steel micro-composite. The error corresponds to the hardness standard deviation calculated for each phase.

4.2 Mechanical properties mapping and statistics

Last section have shown the Inforce nanoindenter ability to assess mechanical properties of micrometric phases. Another interest of the nanoindenter is to perform hardness and modulus profile along different phases. This can be done using conventional nanoindentation in CSM mode, as shown in figure 4.12 for the duplex stainless steel composite of paragraph 4.1.1 (page 119). However, with $\sim$ 100 s by indent, this method is time consuming, especially for fine profile. The Blitz 3D method developed by Nanomechanics Inc. [147] allows to perform one indent by second, resulting in large indentation maps for a reasonable time. In this method, a maximum force is set as a target and mechanical properties are extracted only from the unloading part of the nanoindentation curve. This method allows both a statistic study of complex microstructure [161] and the mapping of hardness and modulus.

4.2.1 Statistical analysis

Blitz 3D nanoindentation testing has been performed with the Inforce nanoindenter on various material, respectively glass (Fused SiO_2), single crystals (Au and Al) and polycrystalline material (ferrite cementite steel with micrometric carbides). The purpose was to statistically determine both hardness and Young's modulus of each material. The preparation conditions of each sample and their RMS roughness are given in table 4.2. Figure 4.13 provides example of AFM image corresponding to Au and ferrite + cementite sample.

Sample	**Preparation conditions**	**Roughness (RMS)**
Fused SiO_2	Standard calibration sample for nanoindentation	$\sim$ 1 nm
Au single crystal	Diamond polishing (1 µm)	8-12 nm
Al single crystal	Electrochemical polishing 80 % $HClO_4$ 20 % CH_3OH (10V)	10-15 nm
Ferrite + Cementite	Diamond polishing (1 µm)	50-60 nm

Table 4.2: Samples summary.

Large indentation map of 200 to 2000 indents have been performed on four samples, with $\sim$ 200 nm maximal depth and 2.5 µm spacing. Results for Young's modulus and hardness are shown in figures 4.14 and 4.15. Data are characterized by a normal distribution with a tail toward low modulus values. This tail is more significant for rough sample such as Au and Al single crystal. This is less visible on the polycrystalline ferrite, probably because it is hidden by the large standard deviation.

Mean values and standard deviations come from the normal distribution obtained by iteratively excluding data points which do not obey to the Chauvenet criterion[1] until a constant average value is reached. The standard deviation is lower for fused Silica where the roughness is low. Single crystals (Au and Al) have intermediate standard deviations, which are probably due to their relatively high roughness. Polycrystalline ferrite shows very large standard deviation. This cannot be due to the influence of the cementite carbides which would have move the average towards higher modulus value. This can be a roughness effect combined with the modulus variation due to the polycrystalline material. Measured hardness appear to be low compared to usual values for those materials. This is most likely due to a wear tip.

[1] The Chauvenet criterion defines as outlier a data point y such as $\frac{|\mu - y|}{\sigma} > \sqrt{2} \cdot \mathrm{erfc}^{-1}(\frac{2}{4n})$, where n is the number of data points, and μ and σ the corresponding average and standard deviation.

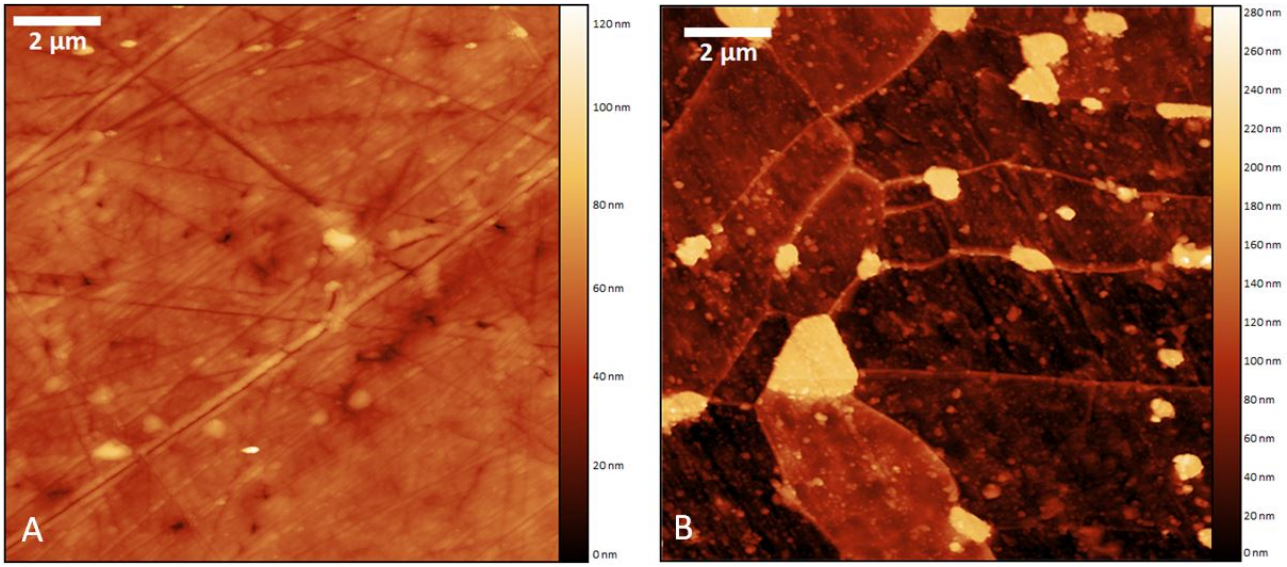

Figure 4.13: AFM image of Au sample (A) and ferrite + cementite sample (B).

No bimodal distribution appears on hardness and modulus curves for ferrite sample with micrometric cementite particles. This can be explained by the maximal indentation depth chosen for the matrix (200 nm), which corresponds to contact radius of $\sim$ 500 nm, to be compared to the carbides size ($\sim$ 1 µm). Within these conditions, a single test cannot give access to material properties of carbides only, but either to mechanical properties of a mixture between ferrite and cementite, or to ferrite only. The resulting hardness and modulus values corresponds to a weighted average between both constituents. As proposed by Constantinides *et al.* [161], an indentation depth h much smaller than the carbide size must be chosen to get mechanical properties of each constituent, with a step size l larger than the imprint to avoid interference between indents, and with a number of test N so that $l\sqrt{N}$ is much bigger than the carbides size, to avoid statistical bias with respect to the spatial distribution of both phases.

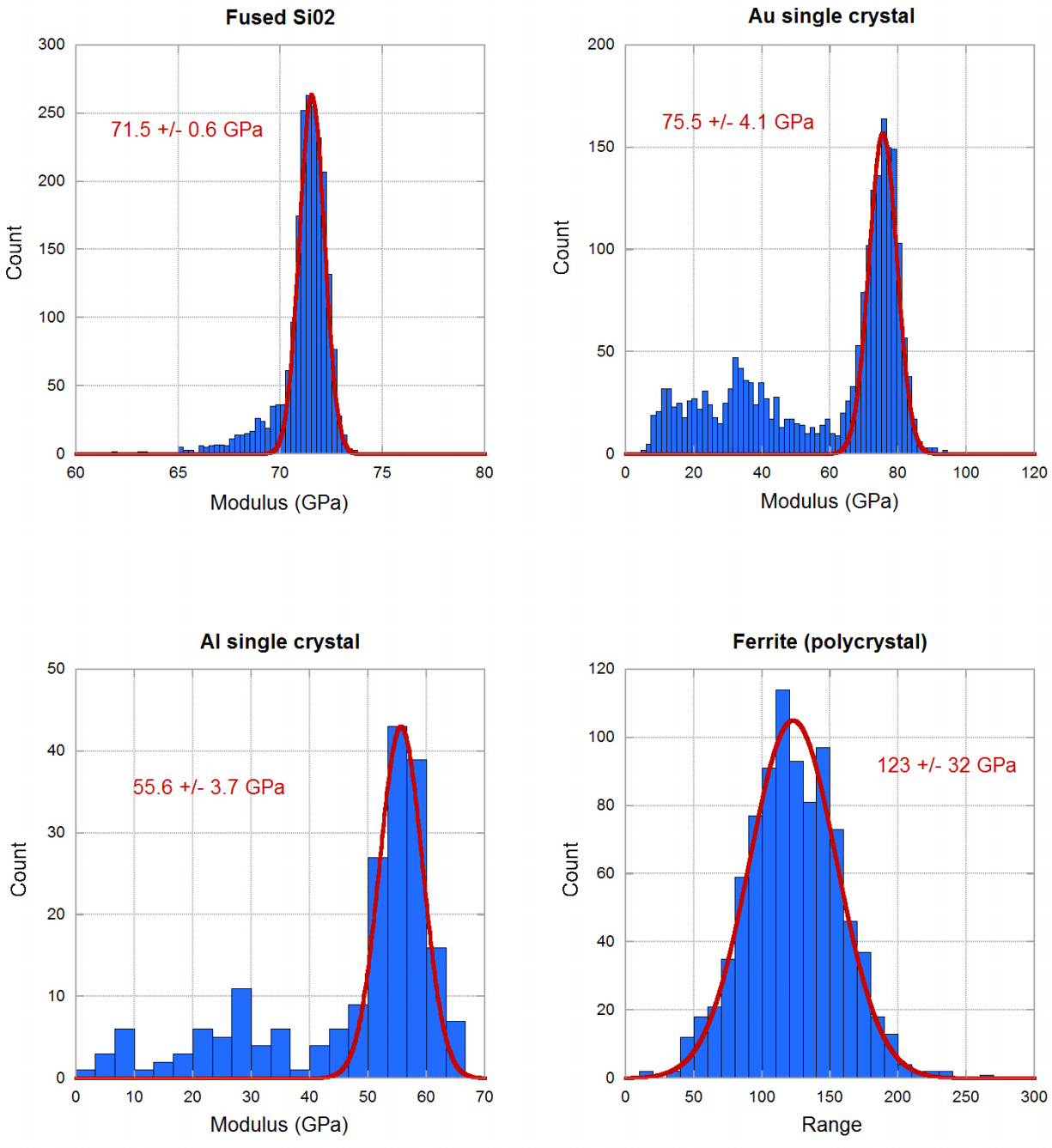

Figure 4.14: Young's modulus extracted from Blitz 3D nanoindentation.

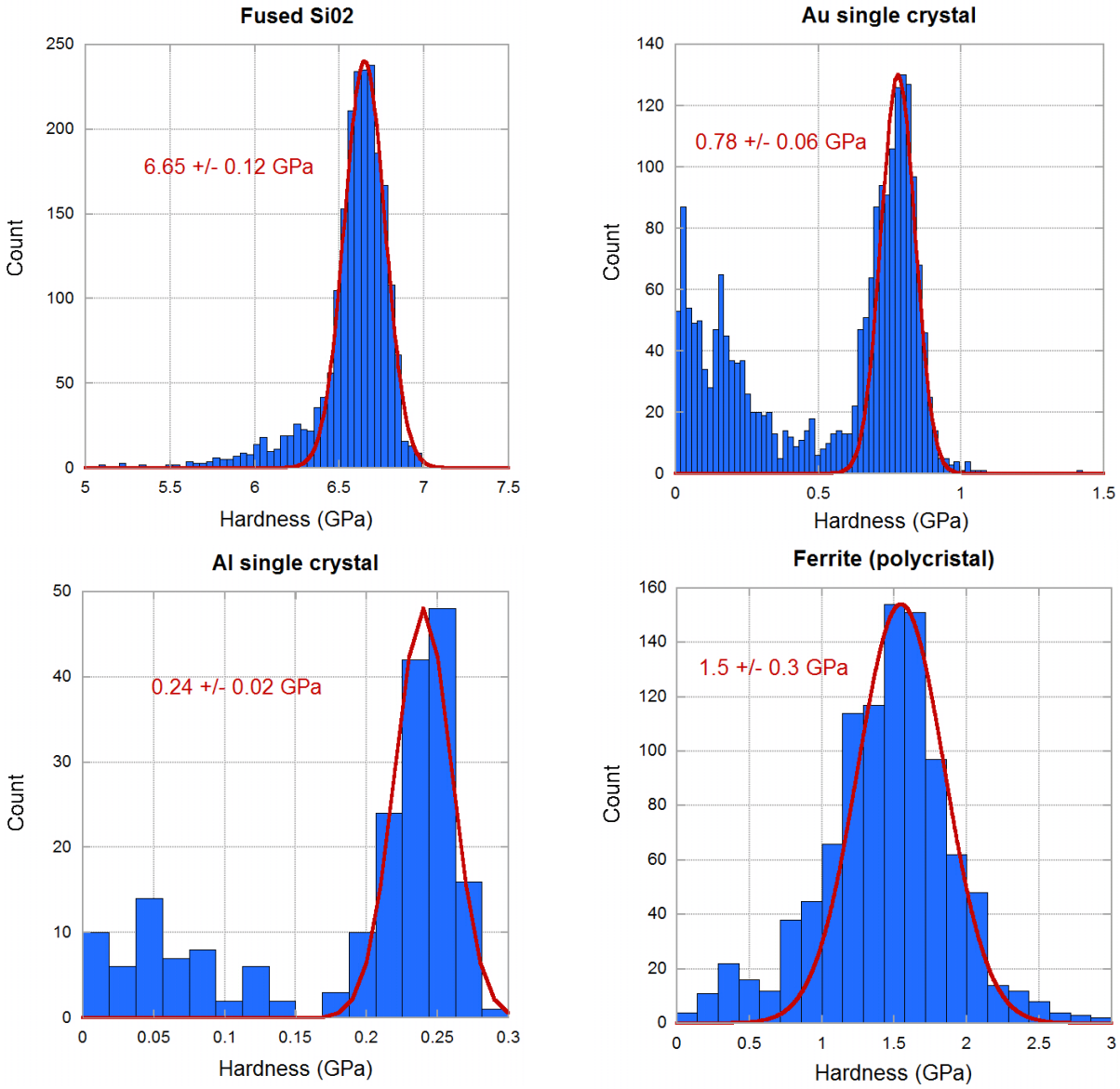

Figure 4.15: Hardness extracted from Blitz 3D nanoindentation.

4.2.2 Map

Blitz 3D nanoindentation is also a powerful technique to obtain maps and profiles of mechanical properties. Within the framework of the master internship of Das (under the guidance of Tassin, SIMaP and following the Ph.D of Mas [162]), a dissimilar metal weld has been investigated in terms of chemical composition and mechanical properties by coupling electron probe micro analysis (EPMA) and Blitz 3D nanoindentation.

The investigated dissimilar metal weld is composed of a low alloy steel (ferritic steel 18MND5) and a nickel base alloy (Inconel 52). In this study the Inconel is used as a filler to join a ferritic part and an austenitic part together in a pressured water generator. However, only the ferritic steel / Inconel weld is investigated. This weld differs from the most widely used dissimilar metal welds, which usually involve two ferritic steels with different chromium amount or a ferritic low alloy steel and an austenitic stainless steel [162].

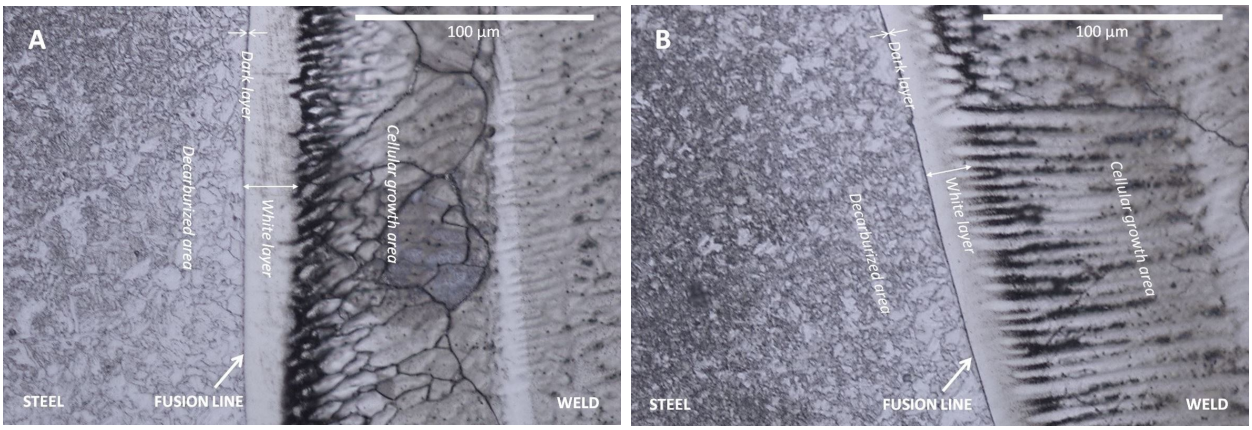

Figure 4.16: Optical micrographs of the fusion line on as-weld+PWHT (A) and as-weld+PWHT+ageing (B) samples, after chemical etching.

During the welding, melting occurs, resulting in the mixing of low alloy steel and Inconel. After welding, solid phase transformations that occur during cooling and the differences of thermal expansion coefficient are responsible for high residual stresses on both sides of the fusion line. A post welding heat treatment (PWHT) is then performed to reduce these residual stresses. The PWHT is composed of an heating ramp from room temperature to 610°C with an heating rate of 30°C/h, a plateau of 16 hours at 610°C, a decreasing ramp with a rate of 25°C/hour down to 300°C and finally air cooling. PWHT is characterized by large carbon diffusion from the carbon-rich region (18MND5) towards the carbon-poor region (Inconel 52). As shown by Mas [162] and Das, this leads to a decarburized area in the ferritic low alloy steel near the fusion

line. On the contrary, an increase in carbon content and carbides precipitations are expected in the Inconel part.

In order to evaluate the mechanical strength of these dissimilar metal welds in the long term, an additional artificial ageing of 50 000 hours at 350°C has been performed after PWHT.

Within the frame of the master of Das, the state after PWHT and after ageing have been investigated on two different samples, respectively called as-weld+PWHT and as-weld+PWHT+ageing samples. Micrographs of both samples are shown in figure 4.16. Micrographs are characterized by a steel region and a weld region delimited by the fusion line. The steel region corresponds to cementite (dark grey) and ferrite (light grey) grains. Decarburization near the fusion line is responsible for ferritic grain growth, leading to a lighter area. The weld region corresponds to a mixture of 15.5 % of ferritic steel and 84.5 % of Inconel. It is characterized by a white layer where no microstructure is revealed and a cellular growth area following the fusion line. The size of the white layer deeply varies along a same fusion line, depending on the overlapping region of successive passes during the welding process.

Composition gradients across the fusion line has been determined by electron probe microanalysis (EPMA). Measurements have been performed by F. Robaut at the characterization platform of Grenoble INP (CMTC). Carbon content was analysed with a Cameca SX50 and a JEOL JXA 8900 microprobe with a tungsten/silicon multilayer monochromator. A liquid nitrogen cold trap and a low pressure jet of gaz were used to limit carbon contamination due to residual organic molecules cracking. An accelerating tension of 15kV and a beam current of 900 nA were used. Measurements have been carried out on both samples, choosing areas with similar white layer sizes. In addition, Blitz 3D nanoindentation have been used to determine hardness profiles on these areas. Matrices of 10x100 indents with 2.5 µm step size and maximal load of 3mN ($\sim$ 160 nm depth) have been performed.

Hardness and modulus maps are shown in figure 4.17. Corresponding hardness and carbon content profiles are drawn in figure 4.18. Both samples exhibits similar profiles, with an increase in carbon content after the fusion line in the weld side.

This increase in carbon is perfectly correlated with an increase in hardness. Two hardness peaks can be dissociated, the first one being located inside the white layer and the second at the beginning of the cellular structure. The second peak might be due to carbides precipitations at the beginning of the cellular structure, as revealed by SEM and high angular annular dark-field STEM (figure 4.19). The as-weld+PWHT+ageing sample shows slightly higher hardness than the as-weld+PWHT sample. This could be due to additional carbon diffusion during the

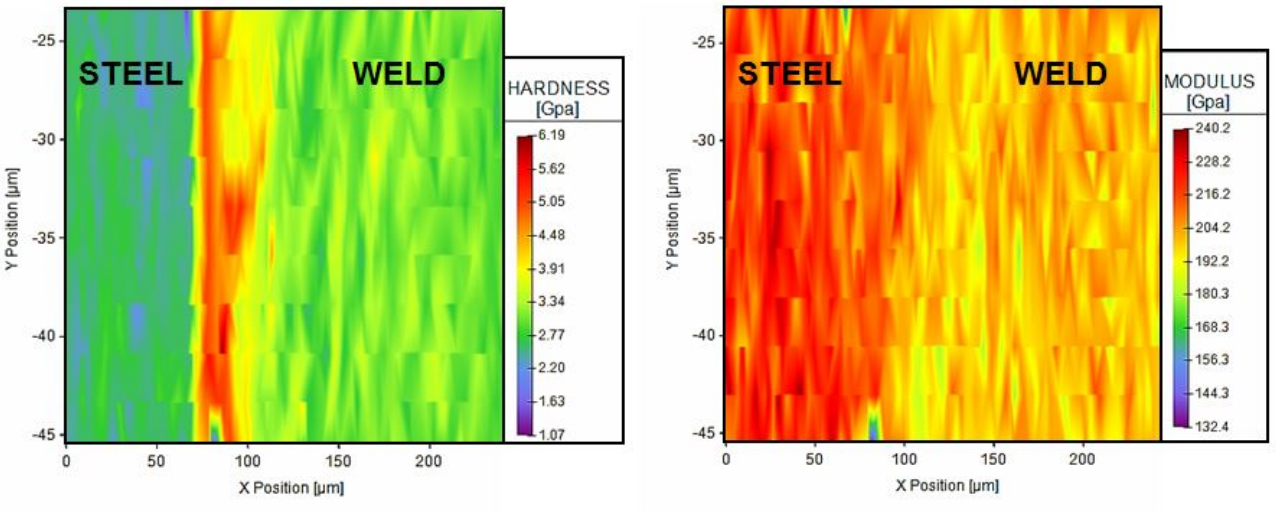

Figure 4.17: Hardness and modulus maps across the fusion line for As-weld + PWHT sample.

ageing. However, the great disparities in white layer sizes inside a same sample makes difficult a comparison between both samples and the interpretation should be taken with extreme caution. In conclusion to this case study, an excellent quantitative correlation is obtained between local carbon content and hardness. Thanks to Blitz 3D nanoindentation, large statistics can be obtaines, with spatial resolution around 1 µm.

Blitz 3D nanoindentation is then interesting for statistical purposes, but also for the mapping of mechanical properties over large areas. The main interest of this method is the time saving compared to traditional static or dynamic indentation. However, this combines with a loss of information compared to dynamic indentation where hardness and modulus are continuously measured during the loading step. One can also notice that Blitz 3D nanoindentation seems to be very sensitive to roughness effect.

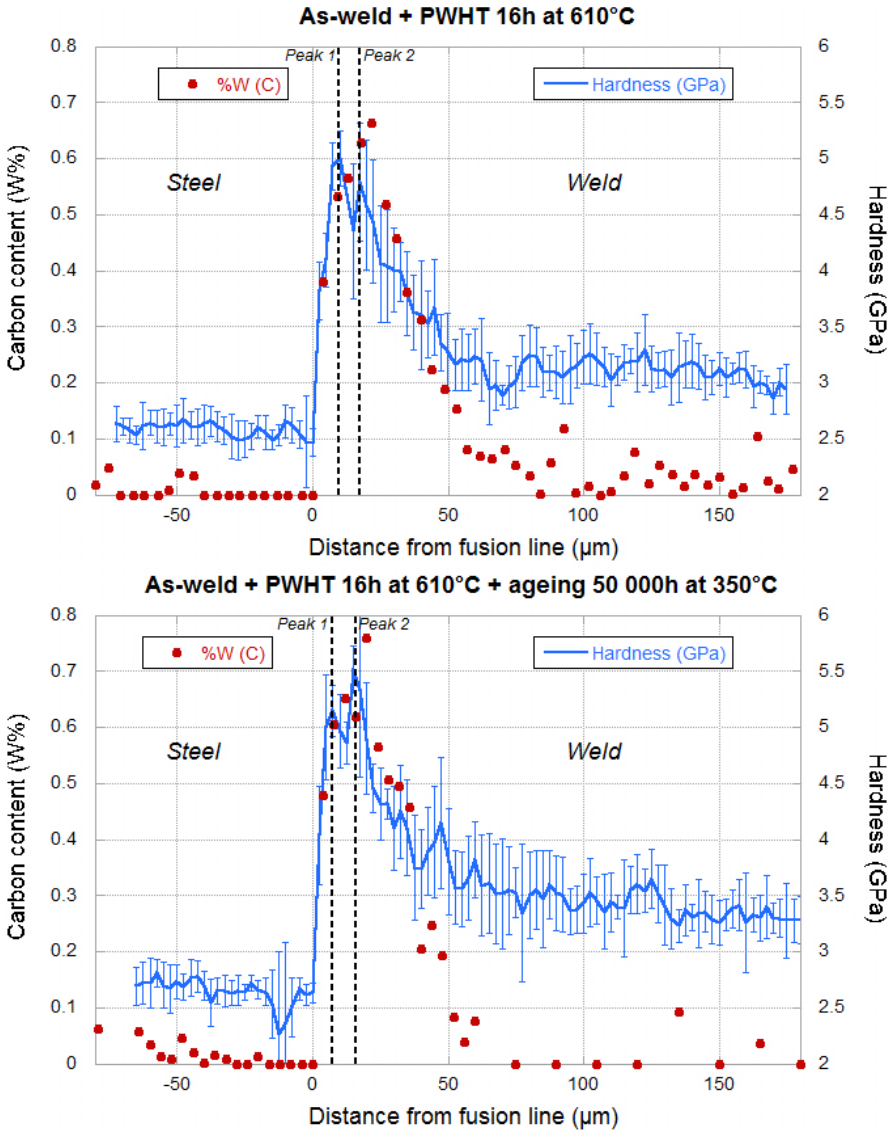

Figure 4.18: Carbon profiles measured by EPMA and hardness profiles across the fusion line on dissimilar metal welds. Scales are different along x and y axes.

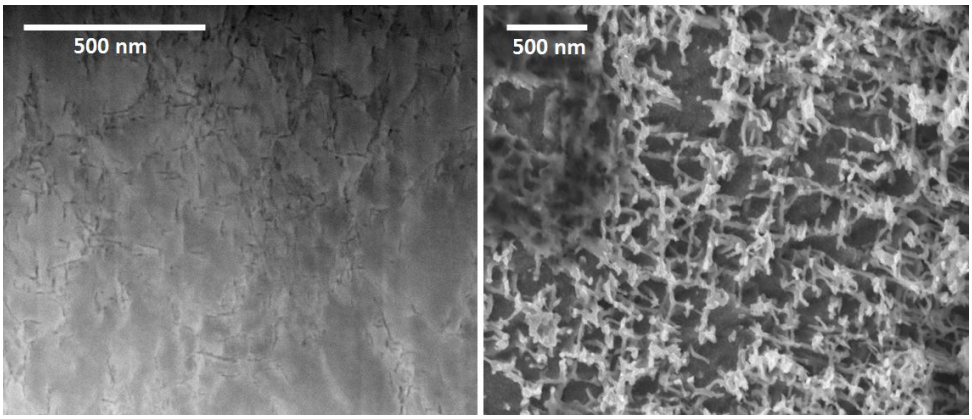

Figure 4.19: HAADF-STEM pictures (left) and SEM pictures (right) of cellular structure in weld side showing evidence of carbides.

4.3 Micro-compression of AlN coated architectured polymer scaffold

Natural materials such as cancellous bones, shells or sea sponge skeleton are characterized by high strength-to-weight and stiffness-to-weight ratios combined with high toughness [163, 164, 165]. Their excellent mechanical properties are attributed to their specific architecture. Some authors have tried to copy such structures, by elaborating ceramic micro-lattices. Thus, Bauer *et al.* [166] have investigated polymer micro-truss and shell structures coated with alumina. They obtained compressive strength up to 280 MPa with densities below 1000 kg.m^{-3}. Fracture mechanisms were found to depend on both architecture and alumina thickness. For cubic micro-lattice architectures, brittle fracture was found to dominate for alumina coating thicker than 50-100 nm. On the contrary, buckling was found to dominate for thinner alumina thickness. For bending-dominant structures, global buckling preferentially occurs, whereas local buckling preferentially occurs on stretching-dominant structures. Meza *et al.* [167] have investigated similar alumina scaffolds, but after removing the polymer structure. They reported excellent recovery of the scaffold after compression up to 50 % strain in case of low thickness-to-radius ratio (t/a<0.02) of ceramic tubes. For high thickness-to-radius ratio, severe brittle fractures were also observed.

A recent work of Bauer *et al.* [168] also reports glassy carbon nano-lattice and honeycomb structures obtained by pyrolysis of polymer scaffolds. Their nano-lattices exhibit strong size effect, with increasing strength and modulus while decreasing lattice cells length. Strength and modulus are significantly higher when the structures are coated with 10 nm alumina. Strength up to 1.2 GPa and modulus up to 9.8 GPa are obtained for honeycomb structures. These lattices achieve the highest strength-to-density and modulus-to-density ratios obtained so far for macro- and micro-architectured lattice materials as well as for natural cellular solids.

Within the framework of the Master internship of H. Jain (under the guidance of F. Mercier, SIMaP), polymer scaffold coated with AlN has been investigated. AlN was chosen for its biocompatibility, good mechanical properties, resistance to failure due to thermal stress and piezo-electric properties.

A commercially available OrmoComp polymer was used for the initial scaffold. The structure was carved out from individual polymer droplets on a glass substrate using a special machine developed by LIPHY laboratory [169], based on two-photon initiated polymerisation technique with a microlaser. Unexposed parts are then dissolved with acetone and dry with supercritical

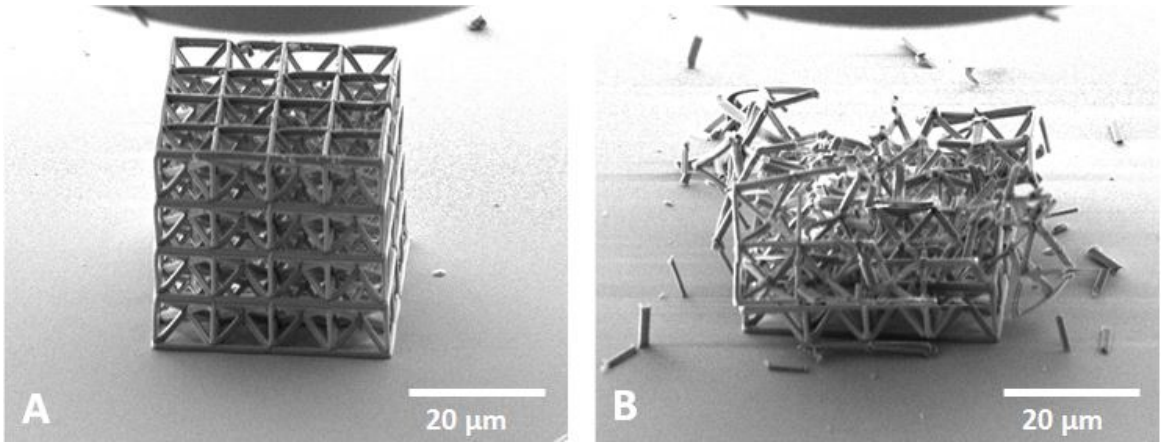

Figure 4.20: AlN coated polymer scaffold before nanocompression (A) and final collapse after several loadings (B).

CO_2 to keep the structure intact. A pre-bake at 80°C is carried out to ensure evaporation of any solvents. Subsequently, a laser with wavelength of 560 nm was used to cure the polymer and a post-exposure bake was conducted to ensure that the curing reaction completes totally. Scaffolds are finally hard-baked at 150°C for 3 hours to ensure proper adherence on the glass substrate. AlN thickness of respectively 60 nm and 120 nm are then deposited by atomic layer deposition (ALD).

A typical final structure is shown in figure 4.20 A. The cube is composed of 64 cubic cells with their four cube diagonals. Mechanically these scaffolds are supposed to be stretching-dominant due to the cube diagonals added to the cubic design.

Mechanical properties of scaffolds has been investigated by using the *in situ* SEM Inforce nanoindenter with a 120 µm diameter flat punch. A constant loading rate of 0.1 $mN.s^{-1}$ with 10 nm dynamic displacement have been used for compressive tests. Several cyclic loading has been performed up to final failure. Violent brittle fracture occurs for both samples.

During compressive tests, stiffness measured by CSM is found to increase with depth up to a maximum, and then decreases before brittle fracture (figure 4.21).

Stiffness values during cyclic loadings are highly reproducible after several tests (after test #4 in figure 4.21). The very first non reproducible tests probably account for imperfections that deforms plastically at the scaffold surface.

Stiffness curves are characterized by periodic oscillations (with length constant around 50-60 nm). This might be the elastic buckling-like signature of each constituent parts of the scaffold.

Engineering strain stress curves can be extracted from load-displacement curves by defining the contact area as the mean cross-sectional area and the initial scaffold length as the scaffold height.

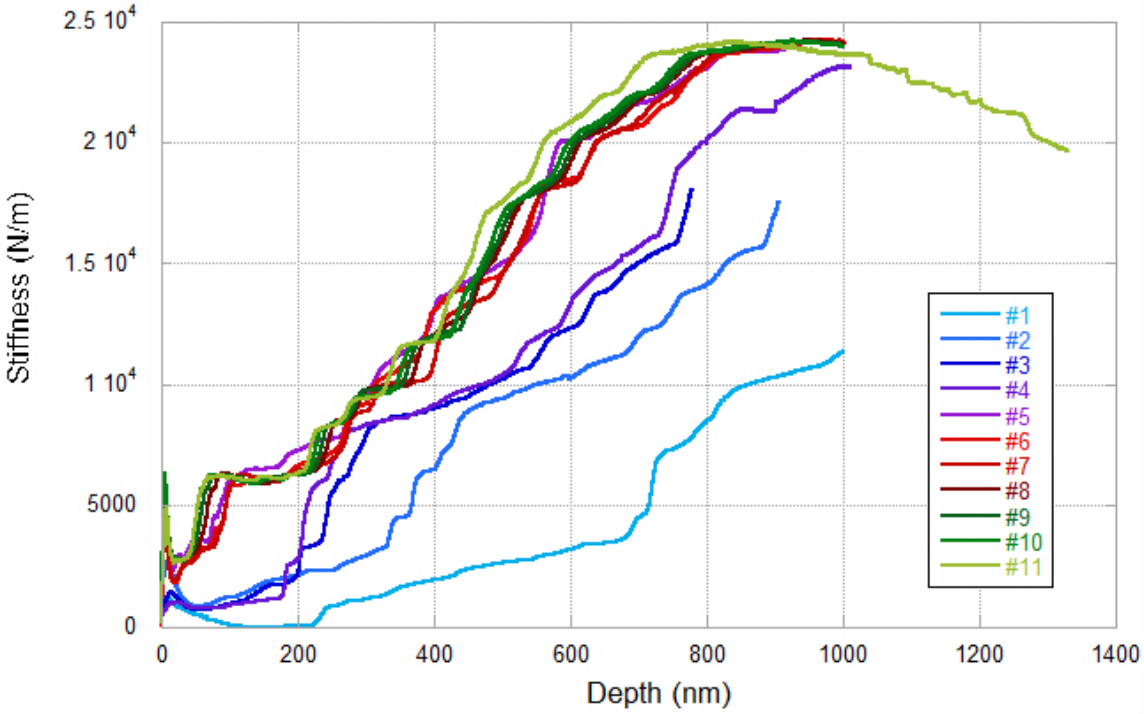

Figure 4.21: Stiffness measured by CSM during successive compressive tests (120nm AlN coated sample).

To be comparable with the studies found in literature, the mean cross-sectional is computed by calculating the volume of each constituent parts of the scaffold - including polymer and ceramic parts - and by divided the total volume by the scaffold height (see appendix B, page 279). However, this is an approximation since the scaffold is constituted of parts loaded in compression as well as in shear.

Figure 4.22 (left) shows engineering stress strain curves obtained during compression of a 60 nm AlN coated sample and a 120 nm AlN coated sample. Both curves exhibit non linear behavior at small strain, which are related to misalignment issues or roughness at the surface of the scaffolds. This was also observed by Bauer *et al.* [166]. The Young's modulus can be extracted from the linear part of the curve, and the compressive strength corresponds to the maximal stress before failure and the maximal strain is the maximal strain before collapse. They have been extracted for six 120 nm-coated scaffolds and for three 60 nm-coated scaffolds. Young's modulus was found to be 7.2 $\pm$ 1.7 GPa for 120 nm AlN coated scaffolds and 0.7 $\pm$ 0.3 GPa for 60 nm AlN coated scaffolds. Compressive strength and maximal strain were found to be 155 $\pm$ 21 MPa and 3.8 $\pm$ 0.6 % respectively for 120 nm AlN coated scaffolds and 19 $\pm$ 7 MPa and 4.0 $\pm$ 0.5 % respectively for 60 nm AlN coated scaffolds.

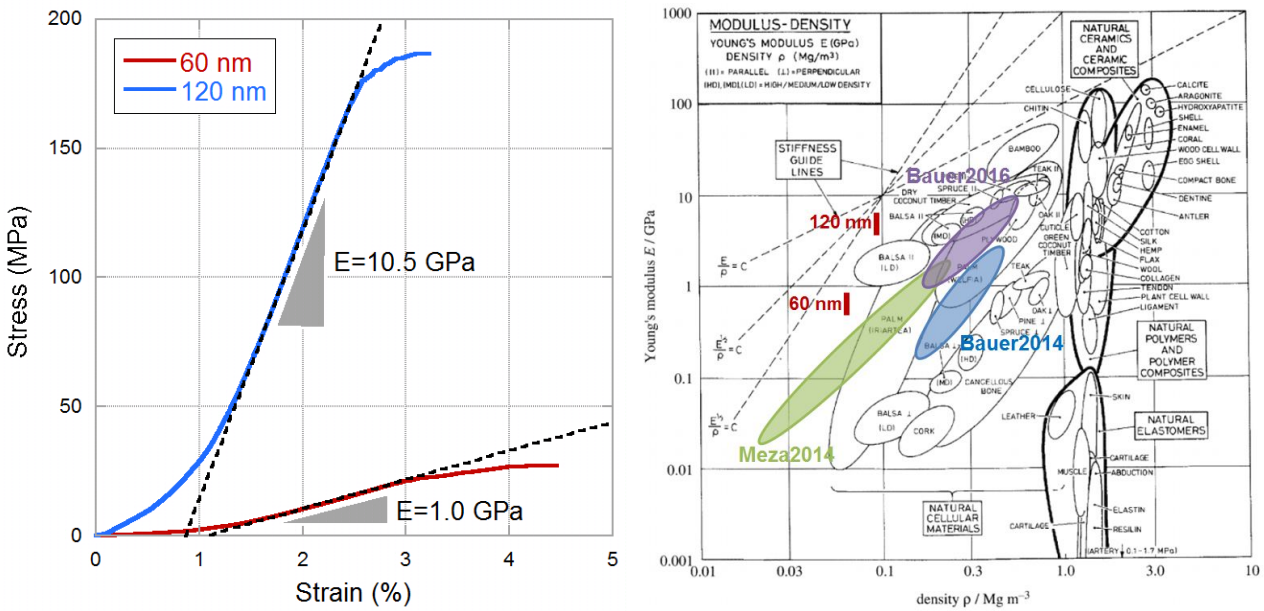

Figure 4.22: Stress Strain curves during compression of 60 nm and 120 nm AlN coated samples (left) and modulus-density Ashby map (from [170]) (right), with AlN coated scaffolds from this study (red), 10 to 200 Al_2O_3 coated scaffolds from Bauer *et al.* [166], brittle free standing alumina scaffolds from Meza *et al.* [167] and glassy carbon nano-lattices from Bauer *et al.* [168]

Thus, AlN thickness plays a major role in determining the mechanical properties of scaffolds. An increase in thickness considerably increases the Young's modulus and the compressive strength of the structure.

The maximal strain obtained is also remarkably high compared to the maximal strain of bulk AlN (10 to 100 times higher).

Young's modulus and compressive strength obtained for 60 nm AlN coated scaffolds are really close to that obtained by Bauer *et al.* [166] for their 50 nm alumina coated polymer scaffold, but they also found an higher maximal strain (8 %). However, Young's modulus and compressive strength obtained for 120 nm AlN coated scaffolds are much higher than that obtained by Bauer *et al.* for 100-200 nm thickness of alumina (< 2 GPa and < 35 MPa respectively). That is likely due to the difference between both architectures. Indeed, the cubic scaffolds used for their study only have face diagonals although the scaffolds used in within the framework of this project have cube diagonals.

For equivalent material density, Young's modulus obtained in the frame of our study is also much higher than that obtained by Meza *et al.* [167] for brittle free standing alumina scaffold. Similar value of Young's modulus have only be reached in the recent work of Bauer *et al.* for

carbon honeycomb with submicrometric triangular unit cells obtained by pyrolysis [168]. Data coming from our study and from literature are summarized in figure 4.22 (right).
In conclusion AlN coated polymer scaffolds from our study show really promising mechanical results compared to other scaffold in literature with equivalent material density. This case study also demonstrates the ability to perform micro compression *in situ* SEM with our experimental set-up.

4.4 Conclusion

A large variety of samples has been investigated using the *in situ* SEM Inforce nanoindenter. Complex architectured materials (duplex stainless steel composite and AlN coated polymer scaffolds) as well as multiphase alloys with submicrometric phase (ferritic steel with cementite carbides) and samples with composition gradients (dissimilar metal weld) has been tested. These studies have shown the convenience of *in situ* SEM Inforce nanoindenter to measure mechanical properties of small individual phases. Thanks to Blitz 3D nanoindentation method large maps and profiles can also be performed across samples, which save a lot of time compared to conventional indentation methods.

Chapter 5

Mechanical response of gold micro-crystallites on sapphire

5.1 Introduction

In the last two decades, small scale objects have captured the attention of the scientific community due to their significantly different properties compared to their bulk counterparts.
The motivation for studying small scale objects (thin films, micro-crystallites...) is driven by the work of Brenner [171] in 1950's on the deformation of copper and silver whiskers with micrometric diameter size. Brenner used a dedicated set-up for tensile test, which was able to interrupt the plastic flow just after yielding. Then the whiskers were slowly reloaded to investigate plastic flow. He obtained typical strain-stress curves of figure 5.1. Brenner divided these curves into four regions:

1. An extremely sharp yielding point, which is close to the maximal shear stress ($\sim G/30$, with G the shear modulus), followed by a sudden mechanical discontinuity. Brenner also showed that the yield strength decreased for increasing whiskers diameter size (a).

2. A small amount of flow during reloading after the yield point (b).

3. The "easy glide" region characterized by no work-hardening and the propagation of Lüders bands (c).

4. Final work-hardening when the Lüders bands reach the extremity of the whiskers (d).

Such high yield strength have been confirmed in literature [172, 173] with nano-wires reaching yield strength up to 100-1000 times higher than yield strength of corresponding bulk materials.

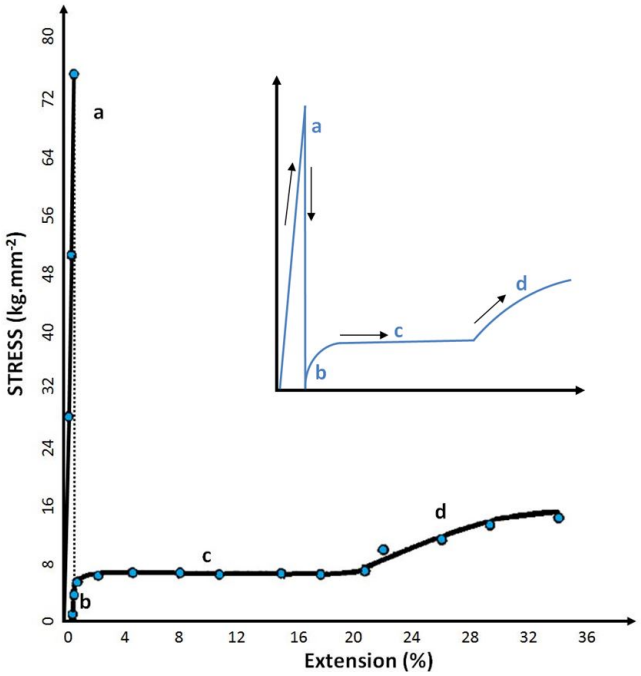

Figure 5.1: Stress-extension curve of a [111] copper whisker, adapted from [171].

Östlund *et al.* [174] have also shown a significant change in mechanical properties of small systems. This team showed that although bulk silicon is known to be brittle at room temperature and to become ductile at high temperature, silicon pillars with diameter below 300 nm are ductile even at room temperature.

On the contrary, face centered cubic (FCC) materials, that are known for their ductile behavior, were found in literature to exhibit discontinuous mechanical behavior with large displacement bursts at micro and submicrometric scales [171, 175, 176, 177]. This corresponds to the sudden mechanical discontinuity after yielding shown by Brenner. The elastic-plastic transition characterized by those bursts occurs with significant statistical scattering, which reveals a stochastic behavior.

For all cases the change in mechanical behavior at small scale is attributed to a change in contribution of dislocation nucleation, motion and annihilation mechanisms. However, these mechanisms can strongly differ, depending both on the processing route and on the chosen mechanical loading.

Focused Ion Beam (FIB) machining has been extensively used in order to investigate submicrometric objects [177, 178]. However, this technique has been shown to produce crystal defects close to the surface (implanted Ga^+ ion, precipitates or small dislocation loops) which affects the mechanical behavior of the material [179, 180]. Other techniques have been developed

to avoid these defects, such as electroplating [178], molecular beam epitaxy [173], directional solidification [181] or solid-state dewetting [182, 183, 184].

The increase in strength of small scale systems can be due to strain gradient within the sample, as mentioned in the strain gradient plasticity theory developed by Nix and Gao [185]. These strain gradients can be caused by strong boundary conditions, such as that imposed by epitaxial relations with a substrate. It can also be due to nanoindentation testing, which is known to produce inhomogeneous strain and stress fields within a confined volume beneath the indenter, resulting in a severe strain gradient [178].

However, increase in strength is also seen for materials under compression, where there is no strain gradient [181, 177, 178, 182, 183, 184]. In that case the strengthening is due to other factors. As described by Mordehai *et al.* [183], dislocation nucleation within a sample can either be due to the activation of bulk dislocation sources (such as Frank-Read sources) or can occur at the surface of the sample. The first mechanism involves high initial defect density, as for sample elaborated by FIB [177, 178] or electroplating [178]. The second mechanism is preponderant for nearly defect-free samples, as obtained by molecular beam epitaxy [173], directional solidification [181] or solid-state dewetting [182, 183, 184].

In that second case, the increase in strength is often attributed to a lack of initial defect in small scale volumes [186]. Thus, the plasticity is controlled by the nucleation of a finite number of defects, which is assumed to be responsible for the stochastic deformation behavior. Greer and Nix have also proposed the concept of dislocation starvation during mechanical testing of small scale sample with free surfaces, in order to account for this strength increase [187]. In small crystal, dislocations rapidly vanish at the free surfaces, which prevent dislocations multiplication phenomenon, as commonly observed in bulk.

In the particular case of FCC crystallite, Mordehai *et al.* [183, 188] have confirmed both experimentally and with dynamic molecular simulation that during nanocompression of nearly defect-free samples, the plasticity is controlled by the nucleation of partial dislocations at the neighbouring of surface vertices during nanocompression and by their annihilation on the lateral free surfaces of the crystal. Mordehai *et al.* [182] have also shown that during nanoindentation the deformation mechanism is due to dislocations nucleation below the indenter and by either their annihilation at the free surface of particles or their accumulation around and beneath the indenter in the case of thin films. This accumulation of dislocations leads to even higher strength, due to complex sessile dislocation structures.

From all these studies it appears that the initial content of defects within FCC structures and

the first generations of crystallographic defects during mechanical loading play a major role in deformation response. During his Ph.D, Dupraz [189] has studied the relationship between the structural stability and the mechanical response of submicrometric crystals. In particular, he investigated the early deformation stages in a gold crystallite during indentation. He used Bragg Coherent Diffraction Imaging (BCDI) to analyse defects formation in a gold crystallite during ex-situ and in-situ nanoindentation performed with an Atomic Force Microscope (AFM). In particular he confirmed the nucleation of prismatic loops beneath the indenter during mechanical loading, which is in good agreement with atomic simulations previously reported [54, 182]. He also demonstrated the interaction of nucleated defects with some interfacial recovery mechanism, leading to a so-called mechanical annealing.

In this chapter and following the work of Dupraz, the mechanical behavior of gold micro-crystallites obtained by solid state dewetting technique during nanoindentation and nanocompression is studied. Nanoindentation and nanocompression are performed with the *in situ* SEM Inforce set-up described in chapter 3 (page 81). This allows both force and displacement recording during mechanical testing, in contrast with the use of an AFM, which only gives access to displacement data.

This work has two parts, which are based on two motivations:

- **The determination of a deterministic plastic behavior:** Despite the stochastic nature of mechanical events during initial mechanical loading of gold crystallites, there is a need for a predictable mechanical law. In order to assess general trends during mechanical testing, a statistical study of the mechanical behavior of gold crystallites, based on the investigation of a large number of crystals, is performed.

- **The relationship between crystal defects and mechanical properties.** A few crystals are analysed with BCDI before and after nanoindentation or nanocompression. Note that only qualitative results are given at this stage of the study.

5.2 Materials and methods

5.2.1 Preparation and description of the samples

Sample preparation

Within the frame of this study, gold islands on sapphire has been chosen due to the large surface energy between Au and Al_2O_3, which promotes solid state dewetting. The resulting residual strain is mainly due to the mismatch between thermal expansion coefficients of gold and sapphire. Previous X-Ray diffraction measurements realised in our group have estimated residual strain below 0.1 % for samples similar to ours [190]. Low residual strain within the islands is a crucial point to perform Bragg Coherent Diffraction Imaging (BCDI). Indeed, the 3D displacement field within a structure cannot be reconstructed in case where the structure is too heterogeneously strained [191].

Sapphire substrates have also been chosen due to the high hardness and modulus of sapphire compared to gold, which avoids plastic deformation of the substrate during mechanical loading.

Samples preparation is based on solid state dewetting technique. The dewetting technique has been optimized within the frame of the master 1 internship of R. Rupp [190] at the PTA platform from Minatec (Grenoble).

A polycrystalline gold thin film of thickness t_{film} is first deposited at room temperature by Electron Beam Physical Vapour Deposition (EBPVD) under high vacuum on a (0001) oriented single crystal sapphire substrate provided by NEYCO (France). The miscut angle of the sapphire is less than 0.2^o. Substrates are provided epi-ready and cleaned, however additional annealing step (7 hours from room temperature to 1110° and kept 1 hour at 1100°C) have been carried out on some of them (RR09 and RR12, table 5.1) in order to obtain atomic step terrace morphology.

During EBPVD, an electron beam vaporises a gold target inside a high vacuum chamber. Gold atoms condense on the substrate with a controlled deposition rate of 0.5 $nm.s^{-1}$. To ensure the homogeneity of the film the substrate is rotated at 0.5 $rad.s^{-1}$.

At room temperature, atomic motion during thin film formation is limited, and the resulting film is unstable. The sample is then annealed, allowing atomic surface mobility. Due to the large surface energy difference between gold thin film and sapphire substrate, the system tends to minimize the interface between film and substrate and spontaneously dewets (figure 5.2).

In order to control the volume of the gold particles, a hard mask with holes of constant diameter

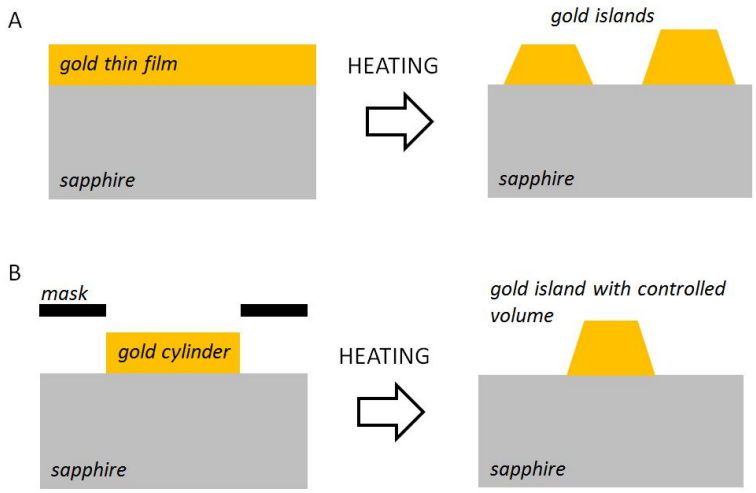

Figure 5.2: Schematic of the dewetting process without hard mask (A) and with hard mask (B).

d_{holes} is used during EBPVD (figure 5.3). Masks are provided by DuraSIN company. After thin film deposition, a pattern of similar gold cylinders of diameter d_{holes} is obtained. During heating, the entire cylinder is supposed to dewet leading to gold islands with constant material volume $V = \pi(d_{holes}/2)^2 \cdot t_{film}$. The use of masks also avoids the nucleation of dry spot and allows large spacing between crystals, which is needed for BCDI measurements. Indeed, the microfocused X-ray beam is characterized by large tails which can illuminate nearby crystals if they are too close to the investigated crystal.

Sample name	**Substrate annealing**	**Film thickness**	**Mask**	**Annealing**
RR09	1 h at 1100°C	20 nm	-	1 h at 900°C
RR12	1 h at 1100°C	20 nm	d_{holes} = 6.5 µm, spacing 12 µm	1 h at 900°C
45nm	-	45 nm	d_{holes} = 2 µm, spacing 12 µm	18+65 h at 950°C
60nm	-	60 nm	d_{holes} = 2 µm, spacing 12 µm	18 h at 950°C
120nm	-	120 nm	d_{holes} = 2 µm, spacing 12 µm	18+65 h at 950°C

Table 5.1: Gold island samples summary table .

An overview table of the samples used during the project with the corresponding film thickness, holes diameter and spacing, and annealing conditions is given in table 5.1. For RR12 sample, the dewetting process fails to produce a unique island for each deposited cylinder (figure 5.4 A). As a result the volume of each island is not constant. For RR09 sample, no mask has been used, leading also to gold islands with different volumes of material (figure 5.4 B). Both

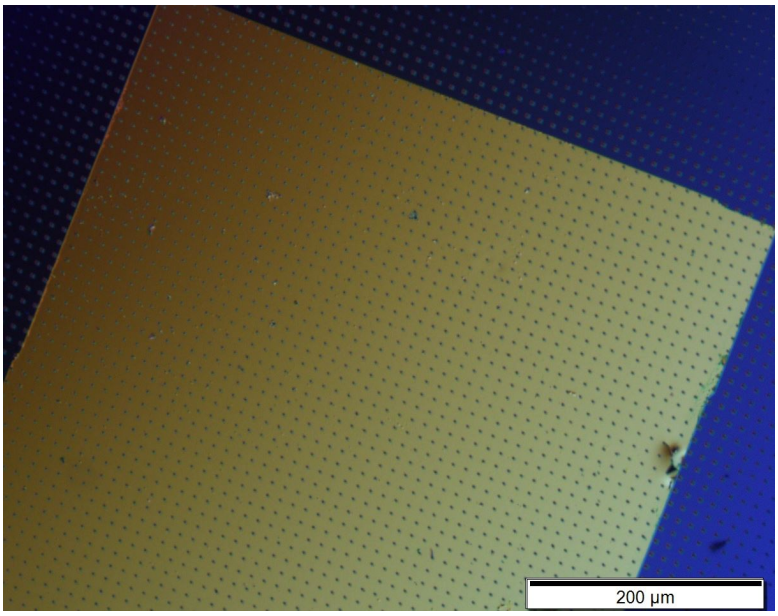

Figure 5.3: Optical micrograph of a 2 µm diameter mask from DuraSIN.

these samples have been used at the beginning of this project. Then, samples 45nm, 60nm and 120nm have been used (figures 5.4 C and D).

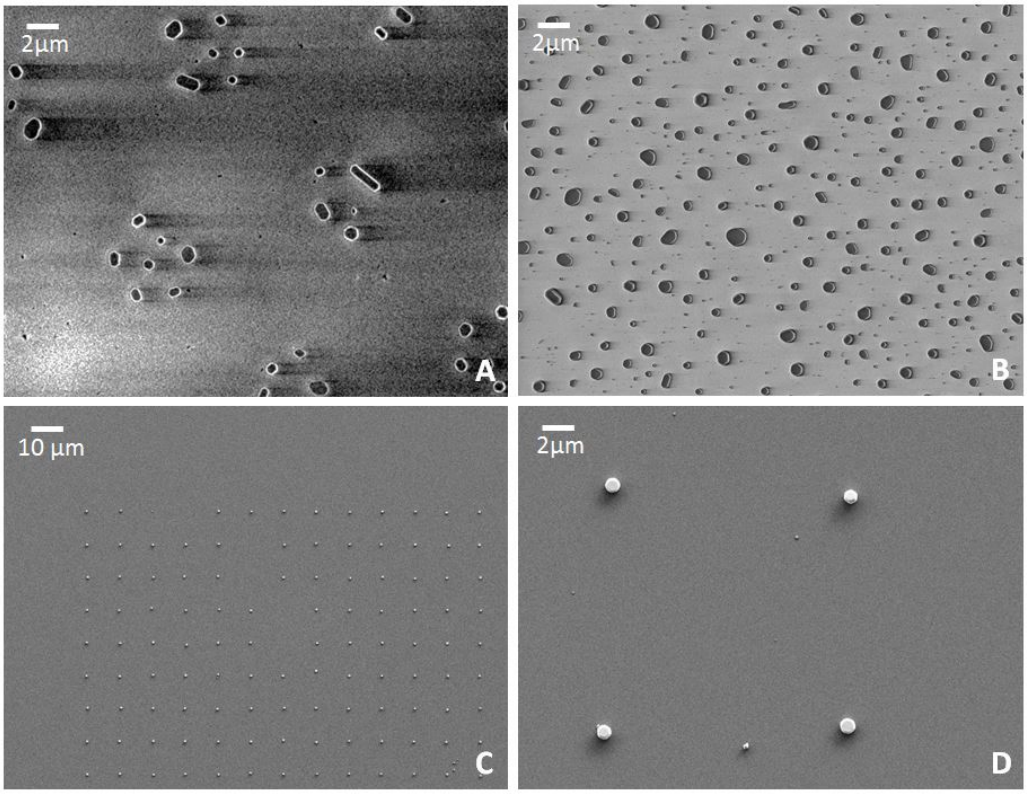

Figure 5.4: SEM image of A: RR12 sample, B: RR09 sample, C and D: 45nm sample.

Equilibrium shape of islands

At the end of the dewetting process and after sufficient annealing, one can assume that the particles have reached their equilibrium state: the shape of the particles is governed by the anisotropy of the surface energy and the influence of the substrate.
Considering the case of a liquid droplet on a substrate, the shape of the droplet is perfectly defined by Young's equation (5.1), where θ is the contact angle between the droplet and the substrate and where γ_{LV}, γ_{SL} and γ_{SV} are the liquid/vapour, substrate/liquid and substrate/vapour interfacial energies respectively.

$$\gamma_{SV} - \gamma_{SL} = \gamma_{LV} \cos(\theta) \tag{5.1}$$

Young's equation must be adjusted in case of a solid arranged particle, where the shape of the particle depends on the crystallographic planes. Wulff [192] first proposed to determine the equilibrium shape of a solid particle through a free energy plot, or γ plot. The equilibrium shape of the particle is given by equation (5.2), which means that the distance h_{hkl}, which is the perpendicular to the (hkl) surface passing through the particle center, is proportional to the surface tension γ_{hkl}. As a result the crystallographic planes with the lowest surface energies are the closest to the particle center and give the largest facets (typically the (111) planes for FCC structures).

$$\gamma_{hkl} = \lambda h_{hkl} \tag{5.2}$$

By adapting the model of a liquid droplet on a substrate, Winterbottom [193] has modified the Wulff solution to take into account the effect of the particle/substrate interface. He defined the general surface tension γ^* as $\gamma^* = \gamma_{PV}$ for all orientations corresponding to free surfaces and $\gamma^* = \gamma_{SP} - \gamma_{SV}$ for the particle/substrate interface, with γ_{PV}, γ_{SP} and γ_{SV} the particle/vapour, substrate/particle and substrate/vapour interfacial energies. The shape of the particle is determined from γ^* plot construction.
Four cases can be discriminated, depending on the contact angle between the particle and the substrate:

- $\theta = \pi$: non wetting with $\gamma_{SP} - \gamma_{SV} = \gamma_{PV}$. The shape of the particle corresponds to that of a free particle, as described by Wulff solution (figure 5.6 a).

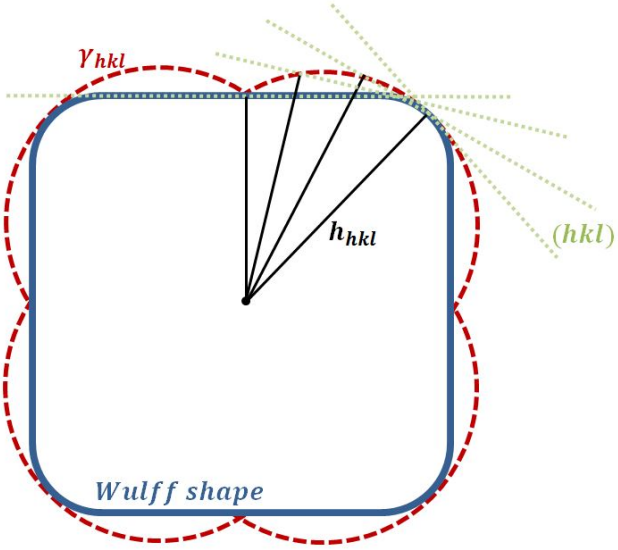

Figure 5.5: Construction of a Wulff plot at the equilibrium of a 2D system: The normal to the crystallographic planes passing through the origin are first drawn (black). On each normal, the point at the distance h_{hkl} (corresponding to the value of the free energy γ_{hkl}) is plotted. The resultant plot (red) corresponds to the γ plot. The Wulff shape (blue) corresponds to the internal envelop of all the (hkl) planes tangent to the γ plot (red).

- $\theta = 0$: total wetting with $\gamma_{SV} - \gamma_{SP} = \gamma_{PV}$. The film is thermodynamically stable and there is no dewetting (figure 5.6 b).

- $0 < \theta < \pi/2$: partial wetting with $0 < \gamma_{SV} - \gamma_{SP} < \gamma_{PV}$. At the particle/substrate interface, γ^* is negative. The $-\gamma^*$ construction plane corresponds to the base of the particle in equilibrium with the substrate (figure 5.6 c).

- $\pi/2 < \theta < \pi$: partial wetting with $0 < \gamma_{SP} - \gamma_{SV} < \gamma_{PV}$. At the particle/substrate interface, γ^* is positive. The γ^* construction plane corresponds to the base of the particle in equilibrium with the substrate (figure 5.6 d).

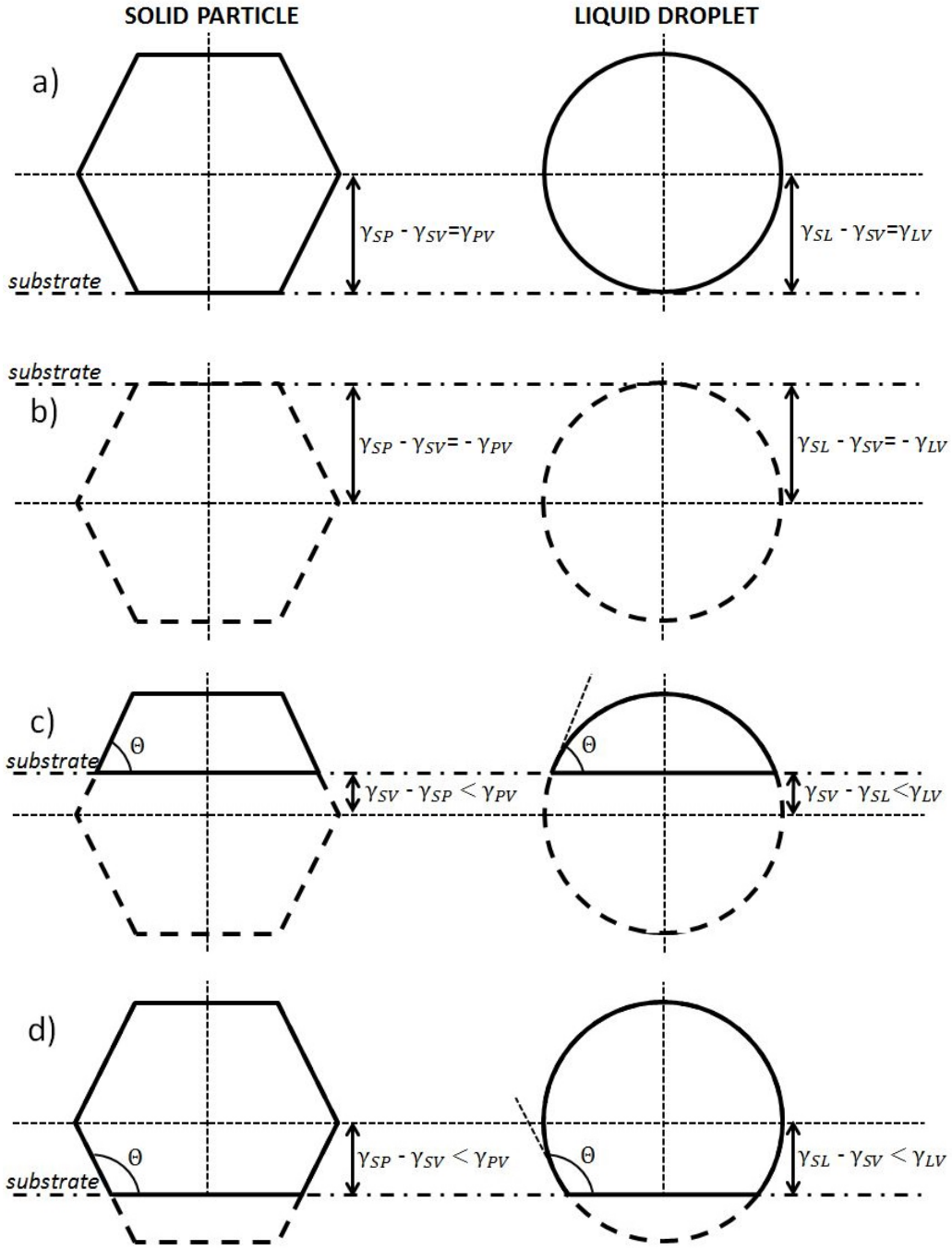

Figure 5.6: Equilibrium shape for a 2D solid and a liquid for different dewetting conditions: a) non-wetting, b) total wetting, c) partial wetting with $0 < \gamma_{SV} - \gamma_{SP(L)} < \gamma_{P(L)V}$, d) partial wetting with $0 < \gamma_{SP(L)} - \gamma_{SV} < \gamma_{P(L)V}$, adapted from [193].

Sample description

Solid phase dewetting process is carried out close to the melting temperature (950-1000 °C). Resulting samples consist of an assembly of islands with various size and shape (figure 5.7). All sample have <111> normal direction. Typical height and diameter of gold islands for each samples are given in table 5.2. The shape of gold islands can be categorized as follows:

- Particles which have reached their equilibrium shape: The Winterbottom-shaped particles, characterized by more or less pronounced faceted free surfaces (figure 5.7 a). The superior facet and lateral hexagonal facets are oriented <111>, although lateral square facets are oriented <001>. This was confirmed by X-ray diffraction measurements in a previous work from our group [190].

- Particles which have not reached their equilibrium shape: The Pancake-like particles (figure 5.7 b) or the Cigar-like particles (figure 5.7 c). Pancake-like particles are characterized by no or only slightly faceted surfaces. Cigar-like particles are oriented along preferential directions. It has been shown in literature [182, 194] that Cigar-like particles remain stable even by increasing the annealing time, and that they do not transform into Winterbottom-shaped particles. This means that these particles are kinetically stable - but thermodynamically metastable. Typically the particles are elongated along the <110> directions.

Sample	Island height	Island diameter	Island volume
RR09	400-1100 nm	200-400 nm	-
RR12	400-1100 nm	200-600 nm	-
45nm	200-400 nm	200-800 nm	0.14 μm^3
60nm	200-400 nm	500-900 nm	0.19 μm^3
120nm	300-450 nm	600-1000 nm	0.38 μm^3

Table 5.2: Gold islands size.

The islands population in 45nm, 60nm and 120nm samples is mainly characterized by pancake-like and Winterbottom-shaped particles, with $\sim$ 20 % of Winterbottom-shaped islands. However, RR09 sample is mostly constituted of cigar-like and pancake-like particles, and only few Winterbottom-shaped particle have been investigated in this sample. RR12 sample corresponds to a transition sample, with about $\sim$ 10 % of Winterbottom-shaped island.

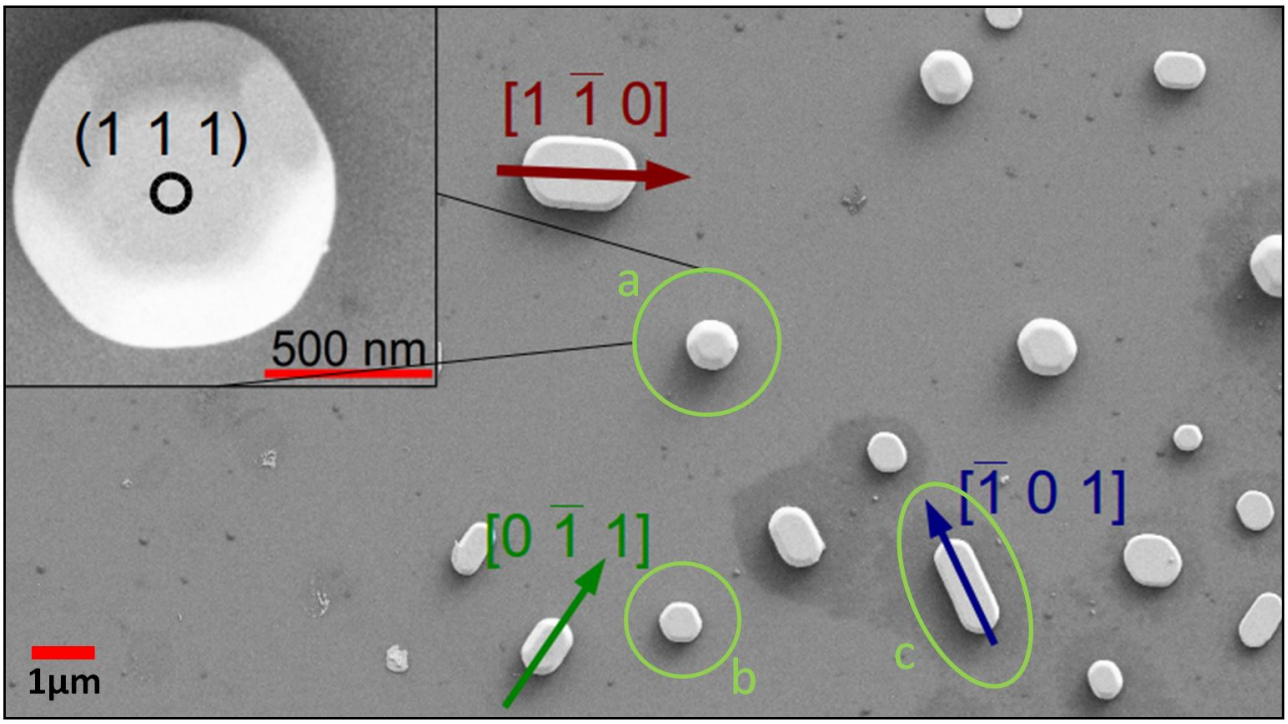

Figure 5.7: SEM image of an assembly of islands.

Effect of pre-deformation on dewetting process

Kovalenko and Rabkin [195] have shown that the proportion of Winterbottom-shaped particles could be increased by introducing defects with an AFM (scratching and indentation) within particles, before additional annealing time.

In the frame of this project, this has been verified by several compression and indentation testing on gold islands of 45nm and 120nm samples, just after dewetting. Then an additional annealing step (65 hours at 950°C) has been performed. Figure 5.8 provides various examples of islands before and after several conditions of mechanical loading. Islands which have undergone severe compression (up to 40-50 % of reduction) exhibit a strong shape change after additional annealing, getting closer to perfect Winterbottom-shaped particles (figures 5.8 a and b). The results is much less pronounced after nanoindentation testing with a cube corner (figure 5.8 c). Particles which have undergone reversible compression and particles which have not been mechanically tested exhibit only slight shape changes due to the annealing, but without reaching a perfect Winterbottom shape. This confirms the work of Kovalenko and Rabkin: although some crystallites are in blocked configurations after initial annealing, introducing defects allows them to evolve toward Winterbottom-shaped particles during a second annealing.

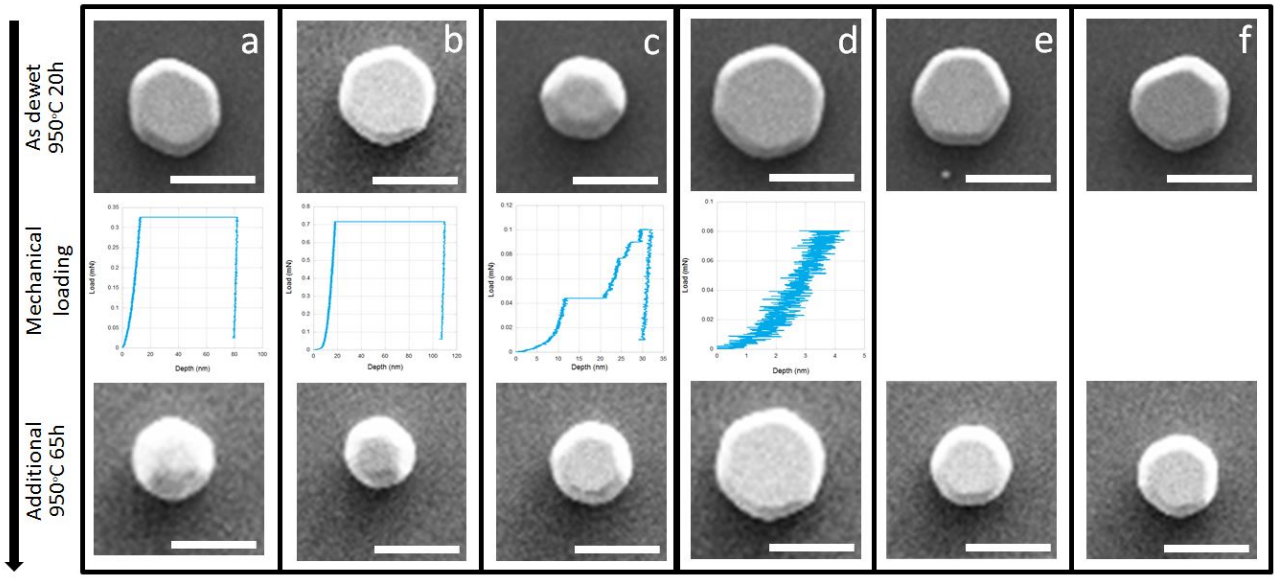

Figure 5.8: SEM images of gold island as-dewetted (top images) and after mechanical loading and additional annealing (bottom images), and corresponding load-displacement curves (middle curves) for several mechanical tests: a-b) severe compression (40-50 % of reduction), c) nanoindentation with a cube corner (30 nm depth), d) reversible flat punch, e-f) no mechanical loading. Scale bar = 1 µm.

5.2.2 Methodology

For the statistical study of the mechanical properties of gold islands, several mechanical tests have been performed *in situ* SEM on gold islands:

- **Nanocompression** testing with a 5 µm flat punch has been performed intensively on 45nm sample. For comparison a few additional tests have been performed on 60nm and 120nm samples. Nanocompression testing has been performed without the CSM mode, with constant loading rate of 0.05 $mN.s^{-1}$

- **Nanoindentation testing with a cube corner tip** has been performed on RR09, 45nm and 120nm samples. These tests have been performed without CSM mode, at constant strain rate of 0.05 s^{-1}.

- **Nanoindentation testing with a Berkovich tip** has been performed on RR12 sample. Tests have been performed both without and with CSM mode (1 nm amplitude at 100 Hz). A constant strain rate of 0.05 s^{-1} has been used.

All tests are force driven.

The advantage of the cube corner tip with our experimental set-up, is that it is possible to perform simultaneous indentation and SEM imaging, contrary to indentation with a Berkovich tip or nanocompression. However, the tip defect height is usually bigger for a cube corner tip than for a Berkovich tip. In our case the tip defect heights of both tips are estimated at 22 nm for the cube corner and at 11 nm for the Berkovich.

Winterbottom-shaped particles have been preferentially tested on RR12, 45nm, 60nm and 120nm samples, whereas pancake-like particles have mainly been tested on RR09 sample due to the few occurrence of Winterbottom-shaped particles on this sample.

For the investigation of the relationship between crystal defects and mechanical properties, the gold islands closest to the ideal Winterbottom shape have been selected by SEM imaging on the 45nm and 60nm samples. Their initial state has then been investigated with BCDI measurements (see section 5.2.3, page 157) at ESRF facility (European Synchrotron Radiation Facility, Grenoble). A few of them have then been mechanically tested in nanocompression with the 5 µm flat punch or in nanoindentation with the cube corner tip (same conditions as previously). The final state of a few islands was investigated using again BCDI.

For each island, the size of the top facet has been carefully measured with SEM imaging before and after mechanical loading (figure 5.9). The height of each island before and after loading has been measured either with AFM or using SEM imaging with a 30° tilt angle. The correspondence between results obtained with AFM and with SEM has been verified on several islands.

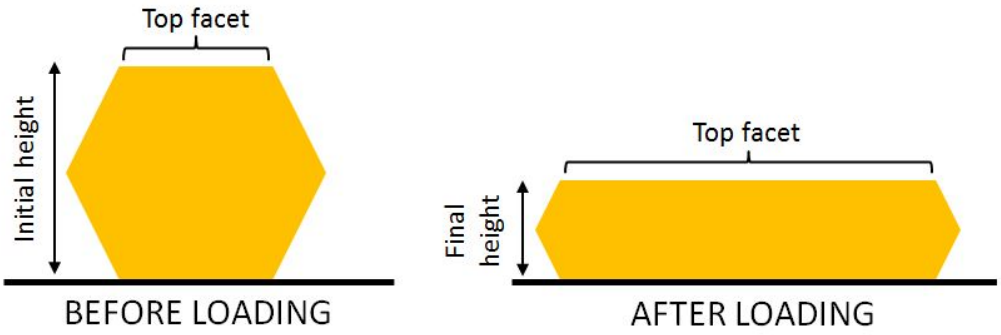

Figure 5.9: Schematic of the island top facets and the island heights before and after mechanical loading.

For the analysis of nanoindentation data, only islands which exhibit a well-centered residual print have been selected (*i. e.* with a distance from the residual print to the island edges corresponding at least to 35 % of the island diameter).

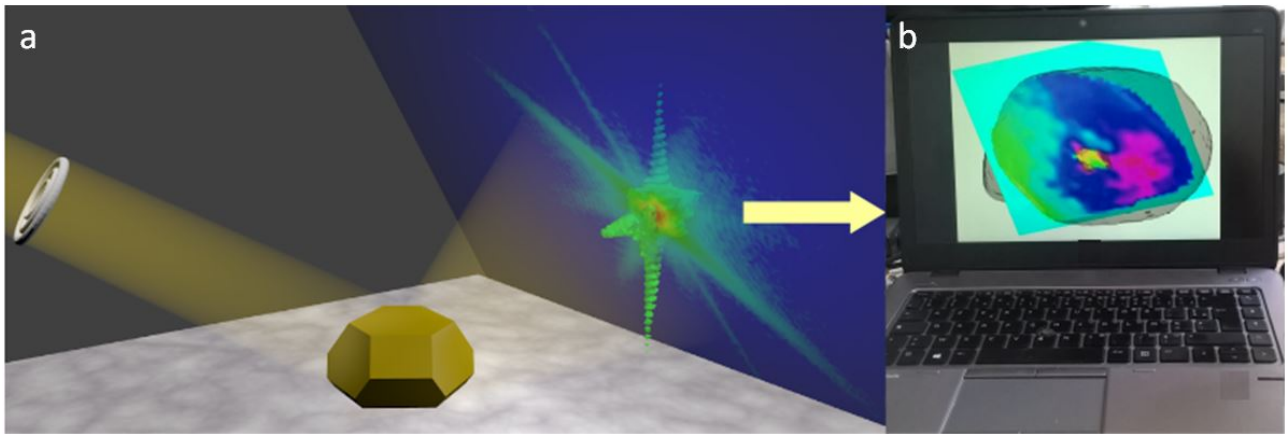

Figure 5.10: BCDI is performed by recording with high resolution the intensity distribution in the vicinity of a Bragg reflection, using an incident coherent X-ray beam (a). The direct-space image is obtained by phase-retrieval algorithms (b). The colour of the reconstructed nanocrystal corresponds to the phase, which encodes a projection of the 3D displacement field. From Dupraz [197].

5.2.3 Bragg Coherent Diffraction Imaging

Principle

Bragg Coherent Diffraction Imaging (BCDI) is a lens-less microscopy technique which allows 3D imaging of both the electronic density and the atomic displacement field in nanocrystals [196].

By illuminating a sample with a coherent beam and sampling its reciprocal space with high resolution, it is possible to obtain a direct space image of the sample [198] (figure 5.10). The method relies on iterative phase retrieval algorithms, which are used to recover the phase data missing from the measurement of the scattered intensity. Using hard X-rays in Bragg geometry, the direct space image is a function of the electronic density and of the crystal lattice displacement field projected onto the diffraction vector [196]. Three non-coplanar Bragg reflections must be measured if one wants to fully determine the displacement field [199]. However, a single projection is often sufficient to evidence the displacement field caused by epitaxial strain and by structural defects such as dislocations [189, 197]. This is the approach we employed here to characterised the structure of the gold nanocrystals before and after mechanical loading.

More information about BCDI and phase-retrieval algorithm is given in appendix C (page 281).

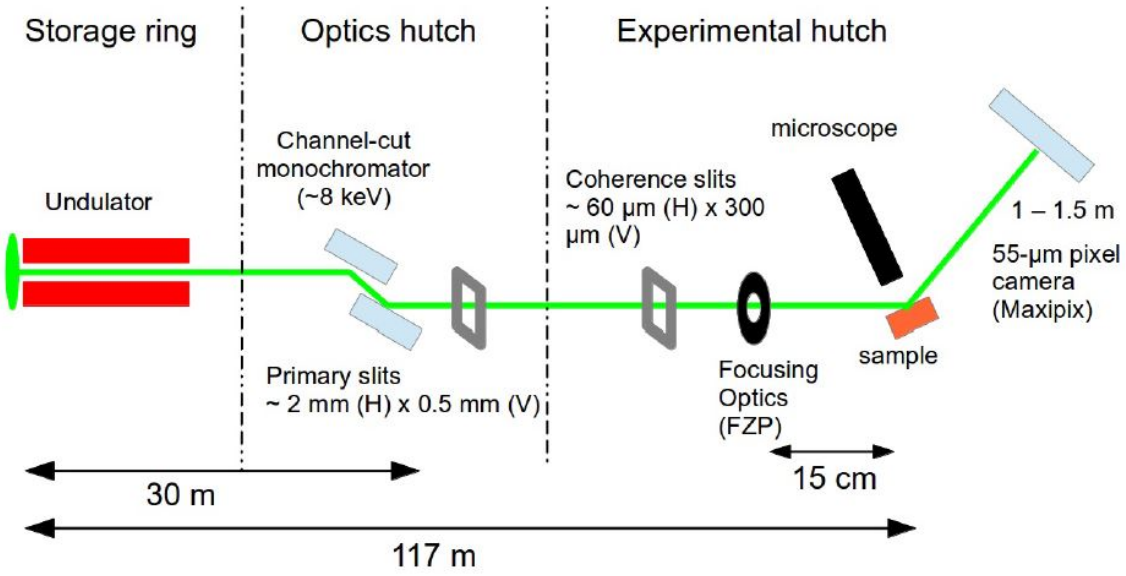

Figure 5.11: Experimental set-up on the ID01 beamline at the ESRF, from Dupraz [189].

Experimental set-up

BCDI experiments performed during this project are based on the work of Dupraz [189]. Measurements are conducted on the ID01 beamline at the ESRF (Grenoble, France) with a 8 keV beam. The same set-up as that described by Dupraz is used (figure 5.11). The main features are the following:

- **The X-ray source** is an undulator, delivering a beam of brilliance[1] (the figure of merit for coherent beams) of the order of 10^{20} ph.s^{-1}.mm^{-2}.mrad^{-2}/0.1%BW, as of 2016, when the measurements were performed. An increase of two orders of magnitude is foreseen with the upgrade of the ESRF in 2019-2020.

- **The monochromator** is a channel cut double crystal Si (111) monochromator, providing a monochromaticity of $\Delta\lambda/\lambda \sim 10^{-4}$ at 8 keV.

- **The coherence slits** allow extracting a coherent beam from the full monochromatic beam, which is poorly coherent. The slits gaps are adjusted to the transverse coherence lengths (60 (H) x 300 (V) µm^2), in order to optimize the flux while enforcing nearly full coherence of the filtered beam.

- **The focusing optics,** a Fresnel Zone Plate (FZP) diffractive lens, which is made of

[1] The brillance is the number of photon per second within the bandwidth of 0.1 % of the central wavelength divided by the angular divergence and by the cross sectional area of the beam.

alternatively opaque and transparent concentric rings spaced so that X-ray interfere at the desired focal point. A beam stop prevents the zero order diffraction and a pinhole prevents diffraction with order higher than one, so that only the first diffraction order is used. Typically, focused beam size of 150 (H) x 50 (V) nm^2 can be reached, but in order to fully illuminate the island to investigate, the FZP is moved so that the sample is 1 mm out of focus. Final beam size of about 800 (H) x 500 (V) nm^2 and typical flux of 10^9 $ph.s^{-1}$ are obtained within these conditions.

- **A diffractometer** is used to perform the diffraction experiment. It consists of 3 sample axes and 2 detector axes, allowing various diffraction geometries. We used a simple geometry since we measuered the symmetric 111 Bragg reflection from <111> orientated crystals. The sample stage of the diffractometer is equipped with a 3-axes piezo-stage topped by an optical microscope, allowing easy positioning of submicrometric crystals.

- **The detector** is an X-ray camera with 256x256 pixels of 55 µm. It has a high dynamical range (up to 10^4 $ph.s^{-1}.pixels^{-1}$), low noise and fast readout, allowing acquisition of a full BCDI dataset in a few minutes. The detector was mounted 1 m away from the sample, such that the pixel size provides enough resolution to oversample the smallest diffraction features.

In order to perform coherent X-ray diffraction measurements, the beam and the crystal must first be perfectly aligned at the center of rotation of the diffractometer.

The direct X-ray beam must also be measured, so that the wavefront of the beam can be reconstructed, which is essential to run phase-retrieval algorithm.

Then diffractometer axes are moved in order to select the chosen Bragg reflection (111 in our case). Diffraction maps allow the identification of each particle and the selection of one particle of interest. In the frame of this study, the 3D image of the intensity is then acquired by performing a rocking curve, which means a small angular scan around the selected Bragg reflection 111 [200]. Rocking curve step size was chosen to be 0.005°. For each step, the 2D diffraction pattern is recorded. This angle variation corresponds to a translation of the plane of the detector in the reciprocal space. The angle step must be small enough to oversample the smallest relevant features in reciprocal space.

5.3 Characterization of the mechanical response of gold islands

5.3.1 Stochastic behavior of gold crystallites during mechanical testing

Nanocompression

Various *in situ* SEM nanocompression tests have been performed on the 45nm sample. Nanocompression tests are force driven and a maximum depth target is set. Once this target is reached the force is unloaded. Figure 5.12 A provides examples of load-displacement curves corresponding to the nanocompression of several gold islands from the 45nm sample - and thus for crystallite with equivalent volume of material. Their mechanical behaviour is similar to that observed by Mook *et al.* [184]: the islands load elastically and then undergo catastrophic collapse up to 70 % of their initial height, as shown in figure 5.13. This collapse is associated with a large mechanical discontinuity, or displacement burst in load-displacement curves.

Most often, there is only one displacement burst in the load-displacement curves. This mechanical discontinuity is generally attributed to a sudden dislocations avalanche within the structure. This is actually due to the continuous operation of dislocation sources at a critical stress, thus inducing a sudden mechanical softening. Whatever the feedback control mode (either force or deformation control mode) these events operate in less than 80 ms [184]. Taking into account our force controlled feedback and the stored energy in the nanoindenter the occurrence of a single deformation burst is expected. Analogously with the work of Brenner [171] we put a software displacement limit to stop the burst (maximum depth target).

As predicted by elastic solutions, the load-displacement curves are linear during loading before the displacement burst and after a short transition regime which account for misalignment between the tip and the sample.

As a first approach, load-displacement curves can be transformed into stress-strain curves by dividing the load by the area of the crystallite top facet before the compression and by dividing the depth by the initial island height. Results are shown in figure 5.12 B.

As reported in literature, the results are characterized by a stochastic behavior: samples with equivalent volume of material produce dissimilar strain-stress curves characterized by a critical stress before failure ranging from 400 MPa to 5.7 GPa and maximal strain ranging from 3 %

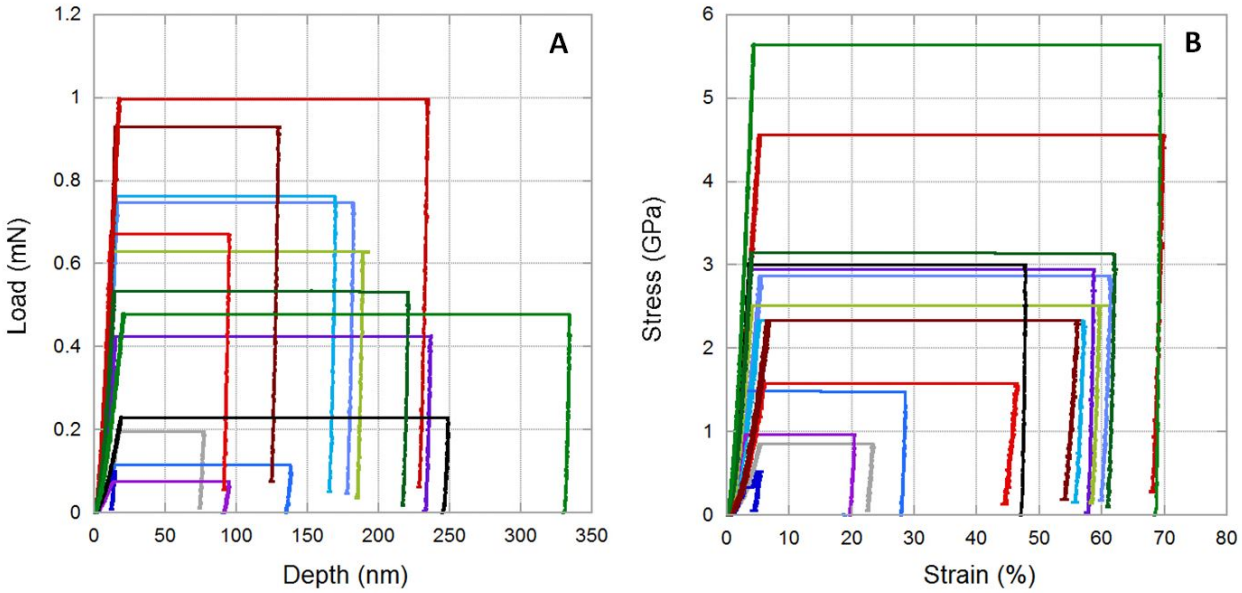

Figure 5.12: A: Load-displacement curves from nanocompression of various crystallites of 45nm sample and B: corresponding stress-strain curves.

to 70 %. These values are consistent with what is found in literature for gold nano-pillars [178] or gold crystallites [183].

Nanoindentation

Mechanical response of gold islands during nanoindentation (figure 5.14) is similar to that occurring during nanocompression. As for compression tests, nanoindentation tests are force driven, and a maximal depth target is set. Figure 5.15 A shows the load-displacement curves corresponding to the indentation with the cube corner tip on the RR08 sample. As for nanocompression, the mechanical response is characterized by elastic loading followed by large displacement bursts. The amplitude of the bursts and the load at which it occurs strongly differ from one crystal to the other, with burst amplitude ranging from 10 nm to 80 nm and maximal load ranging from 0.01 mN to 0.12 mN.

Some crystal responses are characterized by several bursts of small amplitude under relatively small loading (figure 5.15 C and corresponding curve), although others are characterized by a large displacement burst under high loading (figure 5.15 B and corresponding curve). Crystals from figures 5.15 B and C have been indented under the same experimental conditions, and in particular with the same target of 50 nm maximal displacement. However, the large displacement burst which occurs during indentation of the crystallite of figure 5.15 B leads to much larger residual imprint than for crystallite of figure 5.15C.

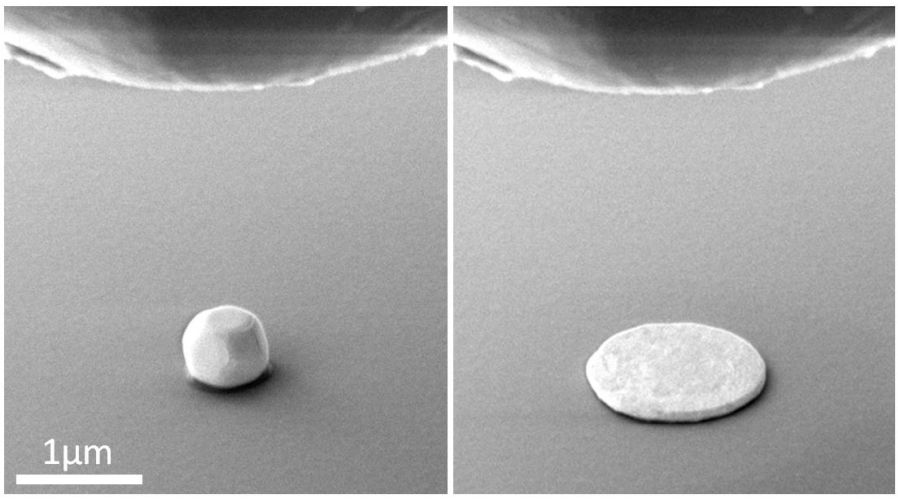

Figure 5.13: SEM images of a gold island before and after nanocompression. The displacement burst during nanocompression corresponds to 70 % of the initial height.

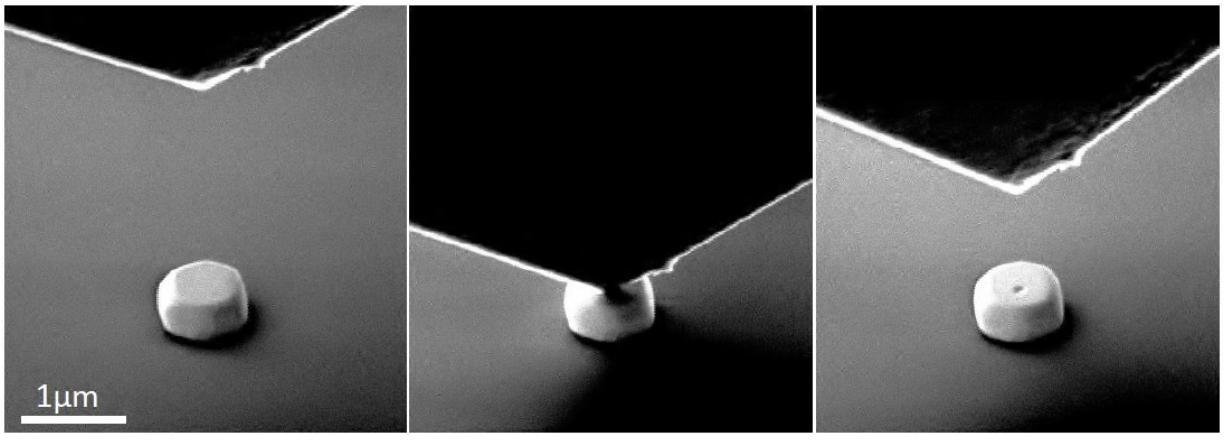

Figure 5.14: SEM images of a gold island before, during and after nanoindentation with a cube corner.

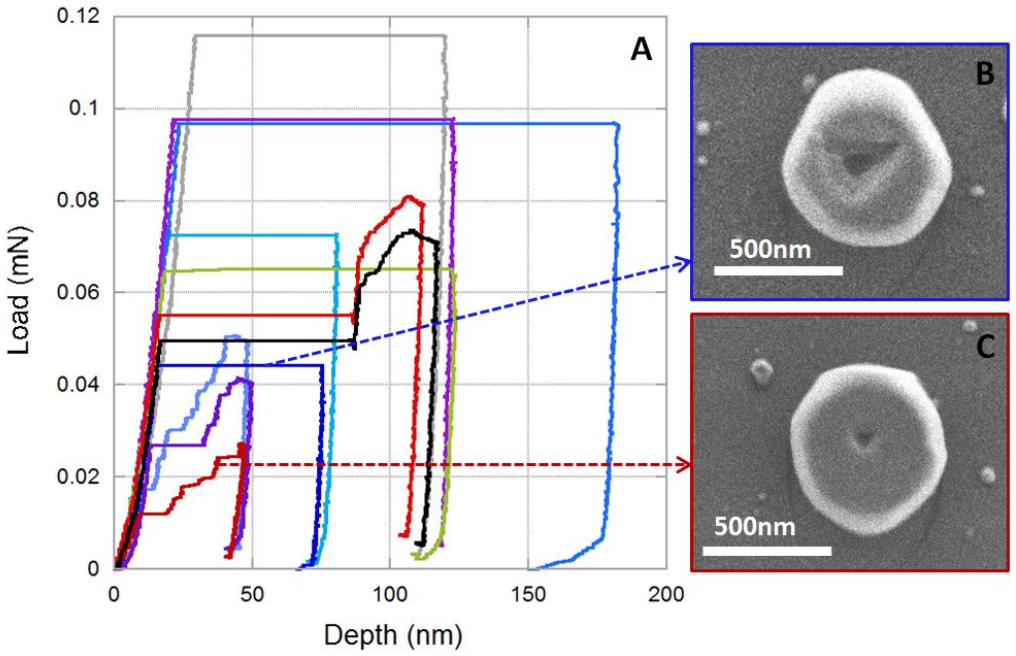

Figure 5.15: A: Load-displacement curves from nanoindentation with a cube corner of various crystallites of RR08 sample and B-C: corresponding SEM pictures after loading for two different mechanical response.

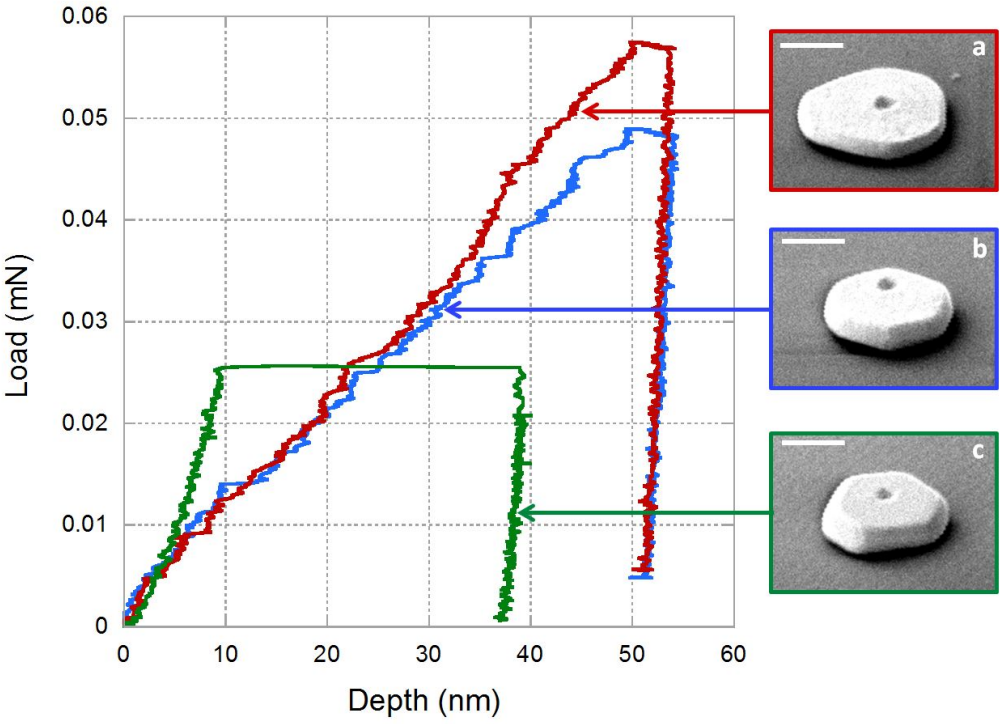

Figure 5.16: Load-displacement curves corresponding to nanoindentation with a cube corner of crystallites of 45nm sample after previous compression test (a-b) and at the as-dewetted state (c). Scale bar = 500 nm.

Influence of initial defects

The difference in behavior between crystals exhibiting a large displacement burst and crystals characterized by several small displacement bursts can be attributed to a different initial defect content within the islands. This can be verified by performing indentation on gold island after a pre-compression test. Figure 5.16 shows indentation curves corresponding to the nanoindentation with a cube corner of three pancake-like crystallites of 45nm sample, with similar size and shapes. However, the (a) and (b) islands have undergone a nanocompression test up to 20-30 % of reduction prior to nanoindentation testing, while the (c) island is as-dewetted. Consequently, the state before indentation of (a) and (b) islands is characterized by a large amount of defects, while the (c) island is a nearly defect-free crystal. Load-displacement curves of (a) and (b) islands are roughly continuous, with only few evidence of small dislocation bursts, to be compared to the load-displacement curve of (c) sample, which exhibits a single large displacement burst. This reveals the effect of the initial content of defects on the mechanical properties of a structure.

In literature [186], this effect is generally explained by the difficulty to nucleate a first dislocation in the nearly defect-free particle. In that case the mechanical behavior is characterized by an elastic loading up to a critical load or a critical stress - much higher than the yield strength of the corresponding bulk sample - at which a first dislocation is created. Once created, this first dislocation is supposed to act as a source for dislocation avalanches within the structure. However, if there is a large initial content of defects within the particle, dislocations can be continuously created as the load increases, leading to continuous mechanical curves.

Post-mortem imaging

One can notice in figures 5.12 A and 5.15 A that the amplitudes of the displacement bursts as well as the load at which they occur during nanoindentation are smaller than those during nanocompression (up to one order of magnitude smaller for the load). This comes from the nucleation mechanisms which strongly differ for both cases.

As shown by Mordehai *et al.* [183], during compression dislocations are generated near the edges between the flat punch and the crystallite. In order to accommodate the entire deformation of the crystallite under loading, dislocations must be generated in three (111) slip plane systems. An evidence of the activation of these slip planes can be seen in post mortem AFM image (figure 5.17 A), where slip bands normal to these planes can be seen, leading to a triangular

pattern.

Post-mortem AFM images on strongly deformed crystallite (above 70 % of deformation) also reveals specific patterns (light-colour regions in figure 5.17 B), which look like the creation of new surfaces, as already reported by Mook *et al.* [184] during *in situ* SEM nanocompression of gold islands.

The deformation mechanism during nanoindentation is intrinsically different from the nucleation mechanism during nanocompression. According to the literature, prismatic loops were found to primary occur below the indenter tip [54, 182, 189], and the deformation is then supposed to be accommodated by geometrically necessary dislocations [185]. In our case, post-mortem AFM image (figure 5.17 C) reveals moderate pile-ups localized near the edges of the imprint left by the indenter. These pile-ups are much less pronounced than those observed by Mordehai *et al.* [182] on thin films. This can be due to a material transfer towards the free surfaces of the crystallite, whereas the deformation stays confined below and around the indenter tip in the case of thin films.

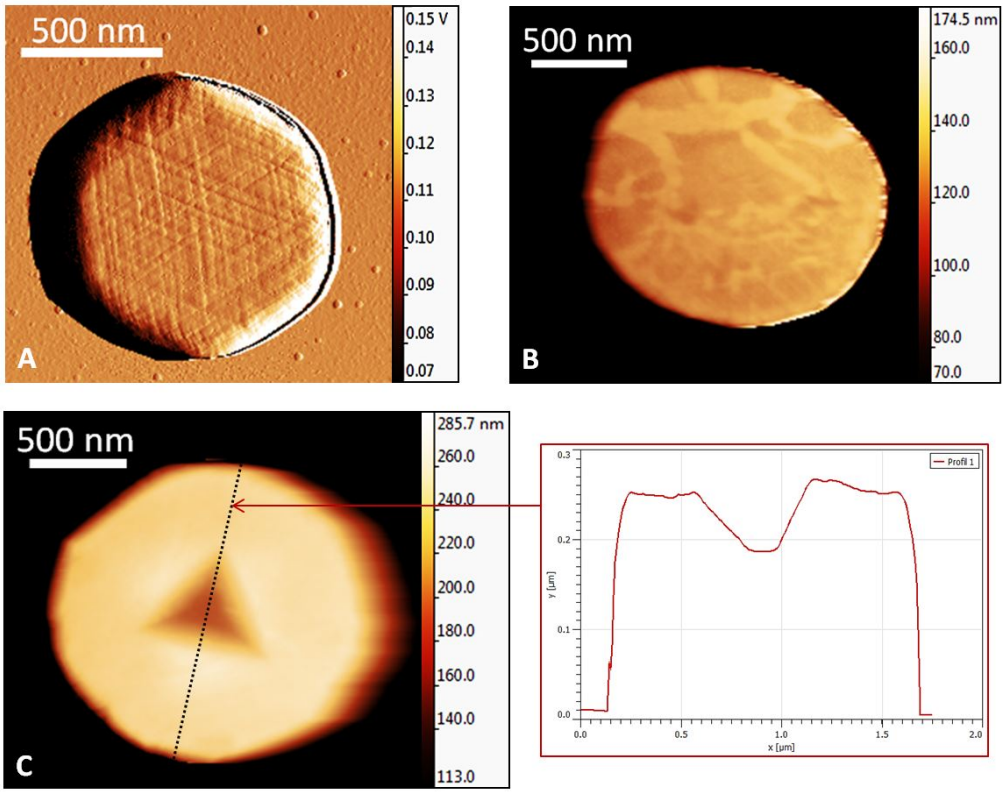

Figure 5.17: A: Differential AFM image (amplitude) of a gold island after nanocompression showing evidence of slip bands (balanced activity of (111) planes). B: AFM image of a gold island after nanocompression. C: AFM image of a gold island after nanoindentation with a cube corner tip and corresponding height profile showing pile-up around the residual print.

5.3.2 Towards a statistical determination of a mechanical deformation law

Deterministic stress-strain law from nanocompression data

Despite the fact that the mechanical response of gold islands is characterized by a stochastic behavior (bursts of deformation), one can wonder if a deterministic deformation law could be extracted from nanocompression and nanoindentation data. We are interested in finding a universal law independent of the deformation bursts by collecting a large number of experiments. This law would define a 'lower-bound' estimate of the plasticity of the small scale crystallites. From nanocompression data, the critical stress can be computed as the load at which the displacement burst occurs - *i. e.* the load before yielding - divided by the contact area between the tip and the flat punch. The corresponding plastic strain is calculated as the burst length divided by the initial height of the gold island.

In first approximation, the contact area at the yielding point can be chosen as the top facet area of the crystallite. This gives the open markers of figure 5.18 obtained after nanocompression tests performed on 45nm, 60nm and 120nm samples. The obtained curve can be seen as an equivalent "stress-strain" curve for gold crystallites, and is characterized by a surprisingly high work hardening. This correlates well with previous experimental observations where a deterministic law for the critical force has been obtained (figure 5.19) [184].

However, using this definition of the contact area is equivalent to considering the representative flow stress as the point of the stress strain curves exactly before the first displacement burst. This is not absolutely true, since at this point the mechanical equilibrium is not reached: due to the instantaneous nature of the displacement burst, the displacement values measured by the indenter just before and during the burst are subjected to the machine inertia.

By contrast, the end of the displacement burst corresponds to the point where an additional displacement of the indenter cannot be performed without any additional loading. This means that the mechanical equilibrium is reached. We propose to use this point as the representative flow stress. The load is obviously unchanged but the contact area corresponds to the area of the top facet of the gold island after the displacement burst. This leads to the solid markers of figure 5.18. The behavior of gold crystallite is much closer to that of a conventional plastic material displaying some hardening before a saturation stress is reached. Not that by interpolating, the solid marker curve intercepts the zero plastic deformation axis around 60-100 MPa, which is consistent with the elastic limit of gold.

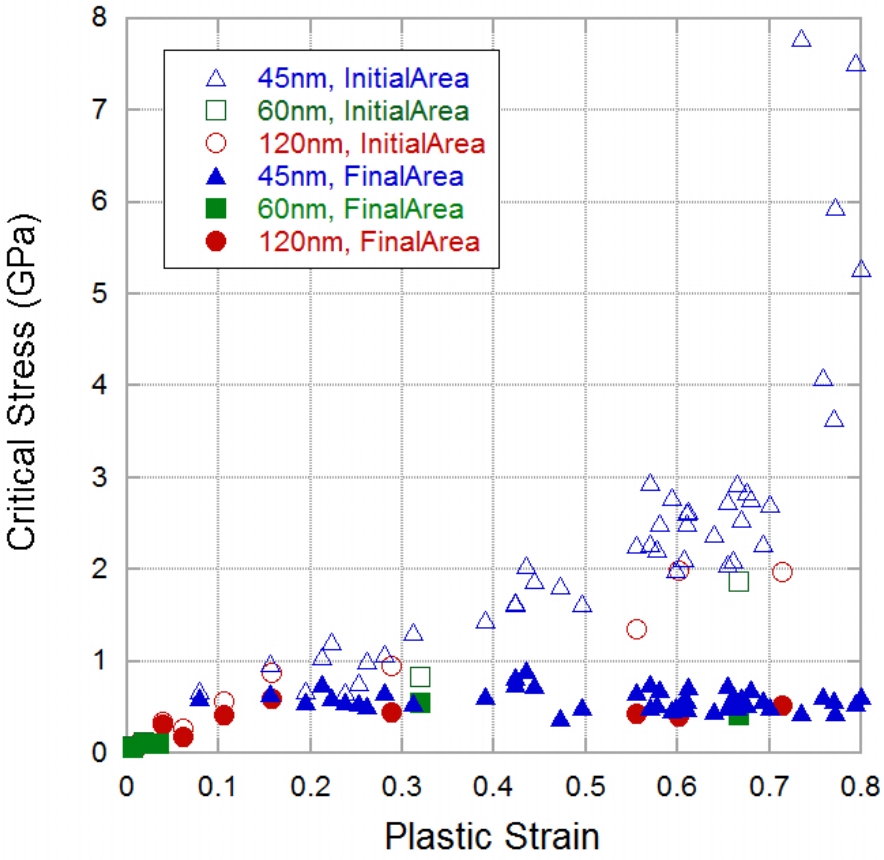

Figure 5.18: Critical stress-versus-plastic strain curve obtained after nanocompression of gold crystallite. The representative flow stress is taken as the load at the displacement burst divided by the size of the crystallite top facet before the displacement burst (open markers) or after the displacement burst (solid markers).

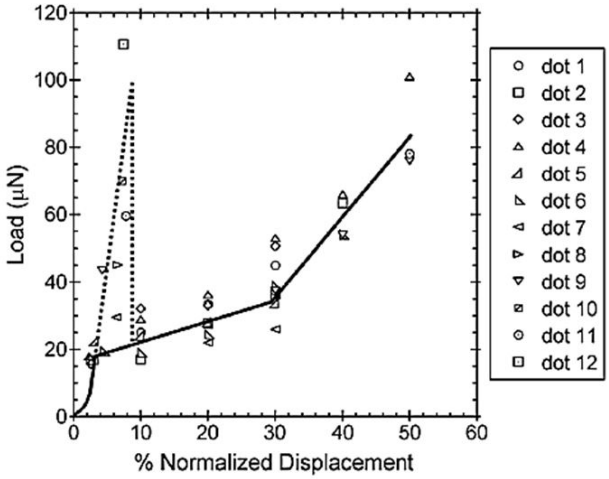

Figure 5.19: Gold islands behaviour from Mook *et al.* [184]. The dashed line represents the stochastic yielding, while the solid line represents what would be the burst-free behaviour.

The shape of this curve is really close to that obtained by Brenner [171] on copper and silver whiskers after a first sharp yield point.

The key point here is that, even if gold islands exhibit a stochastic behavior under loading, the deformation in compression without this discontinuity obeys to a deterministic law. This law is totally independent of the shape of the gold particles.

This defines the lower (safe) bound for the deformation behavior of metallic submicrometric systems: in appendix D (page 289), we conducted 3D finite element method (FEM) calculations on the compression of a faceted crystallite. We show that the apparent stress (force divided by the current area) and strain (height relative reduction) representations is indeed very close to the representative deformation law of the solid.

Gold micro-crystallites in compression exhibit a yield stress around 80 MPa, a linear work hardening of 570 MPa in 20 % strain reduction, reaching a saturation stress around 500 MPa. Figure 5.20 shows both experimental results and results from FEM calculations for a linear hardening. This large linear hardening $\Theta = 285$ MPa is a fraction of the theoretical maximum work hardening observed in uniaxial testing of FCC single crystal, corresponding to stage II: $\mu/200$, or $E/50$ (1.6 GPa) [201]. What is more surprising is its extent in the deformation range (around 20 % reduction). This could be related to the finite size (free surfaces) of the crystallite.

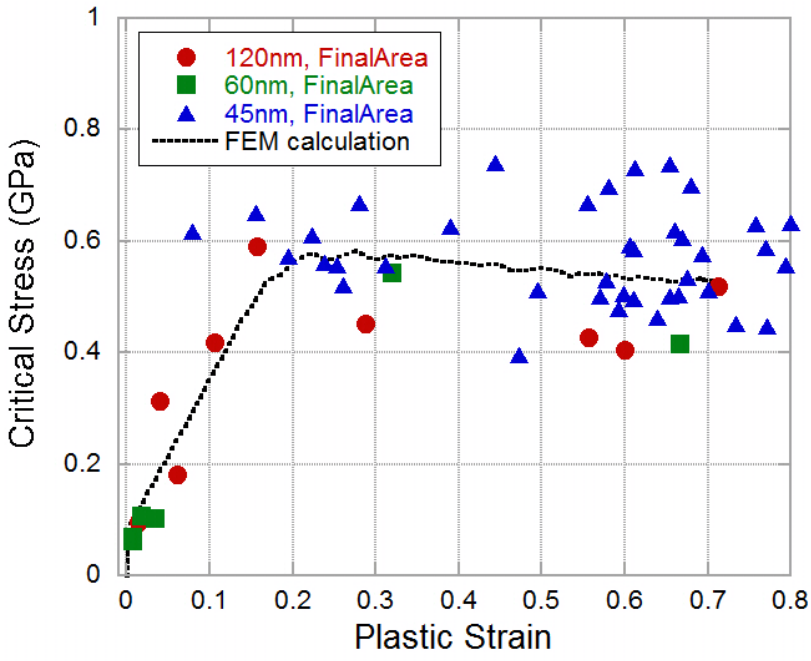

Figure 5.20: Critical stress-versus-plastic strain curve obtained after nanocompression of gold crystallites, and corresponding FEM calculation for a linear hardening ($E = 79$ GPa, $\nu = 0.4$, $\sigma_y = 80$ MPa, $\Theta = 285$ MPa).

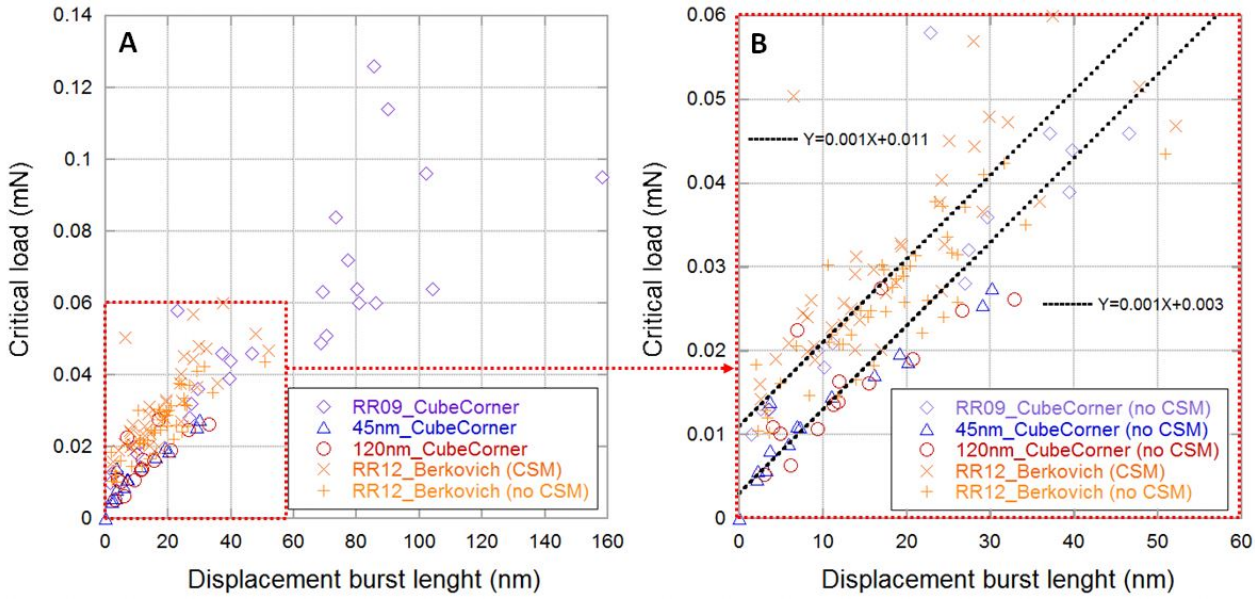

Figure 5.21: Critical load-versus-displacement burst length determined after various nanoindentation tests with cube corner and Berkovich tips. (B) image is a zoom of (A).

Continuous law from nanoindentation data

An attempt can be made to obtain such continuous law from nanoindentation data. For that purpose, several nanoindentation tests have been performed both with a cube corner tip (on RR09, 45nm and 120nm samples) and with a Berkovich tip (on RR12 sample).

The main issue is then to determine an equivalent critical stress and the corresponding strain. First the load at which the displacement burst occurs versus the length of the displacement burst can simply be drawn 5.21. Roughly continuous linear curves are obtained, which is rather intuitive: more elastic energy is stored during loading, higher is the displacement burst.

Although the slope of the curve is similar for both Berkovich and cube corner tips, the curve for indentation with Berkovich is slightly translated towards higher critical load. This was expected since the cube corner tip is sharper, which enhances the defect nucleation.

Data with and without CSM mode for the RR12 sample do not exhibit significant difference, which establishes that the use of the CSM mode do not disturb the determination of the mechanical law (by introducing more defects for instance).

An other point is that for similar indentation with cube corner tip, critical load values obtained for RR09 sample are much smaller than that obtained on 45nm and 120nm sample. This can be due to the fact that the gold particles of RR09 sample are more pancake-like particles than Winterbottom-shaped particles, compared to the other samples. We can assume that

in this case the particles behave more like thin film, with dislocations accumulating beneath and around the indenter tip, instead of being annihilated on the free lateral surfaces, as for Winterbottom-shaped particles. In literature, this was shown to deeply increase the critical load of thin film [182].

As a result, for nanoindentation testing, mechanical discontinuity also obeys to a deterministic law, which does not seem to be affected by the islands shape and size.

As proposed by Corcoran *et al.* [175], the hardness, *i. e.* the load divided by the projected contact area, can also be drawn versus depth for nanoindentation data. As previously, the computation of the contact area is done with depth values after the displacement burst. The contact area is calculated by taking into account the exact shape of the tip, and in particular its tip defect height (see paragraph 1.2.6, page 37). The obtained curves are given in figure 5.22 for both cube corner and Berkovich tips.

The hardness values obtained with the Berkovich tip ranges from 500 MPa to 2 GPa. Surprisingly, the values are quite similar to that obtained by Corcoran *et al.* [175] but for thin films. Hardness values obtained with the cube corner tip are much higher than that with the Berkovich tip. This is totally expected since the cube corner tip provides much smaller contact area. However, the curves obtained for both tips exhibits similar shape.

An interesting fact here is that a roughly linear relationship is found between the square of the hardness versus the reciprocal of the indentation depth (figure 5.23), especially in the case of the RR09 sample. This verifies the strain gradient plasticity theory developed by Nix and Gao [185]. The strain gradient plasticity theory is known to apply to nanoindentation, where inhomogeneous strain and stress fields are produced within a confined volume beneath the indenter [178]. Here again the reason why RR09 sample follows quite well this theory could be due to its pancake-like particles, which behave like thin film, with dislocations accumulating within a confined volume. We can suppose that this increases the strain gradient around and below the indenter.

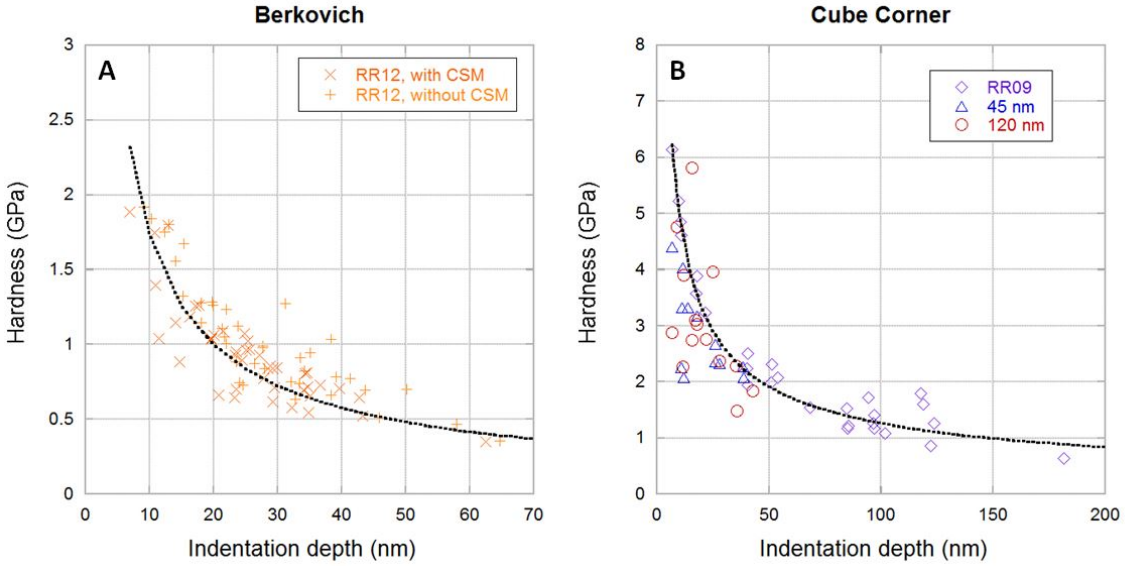

Figure 5.22: Hardness-versus-depth curves obtained after nanoindentation of gold crystallite with a Berkovich tip (A) and a cube corner (B).

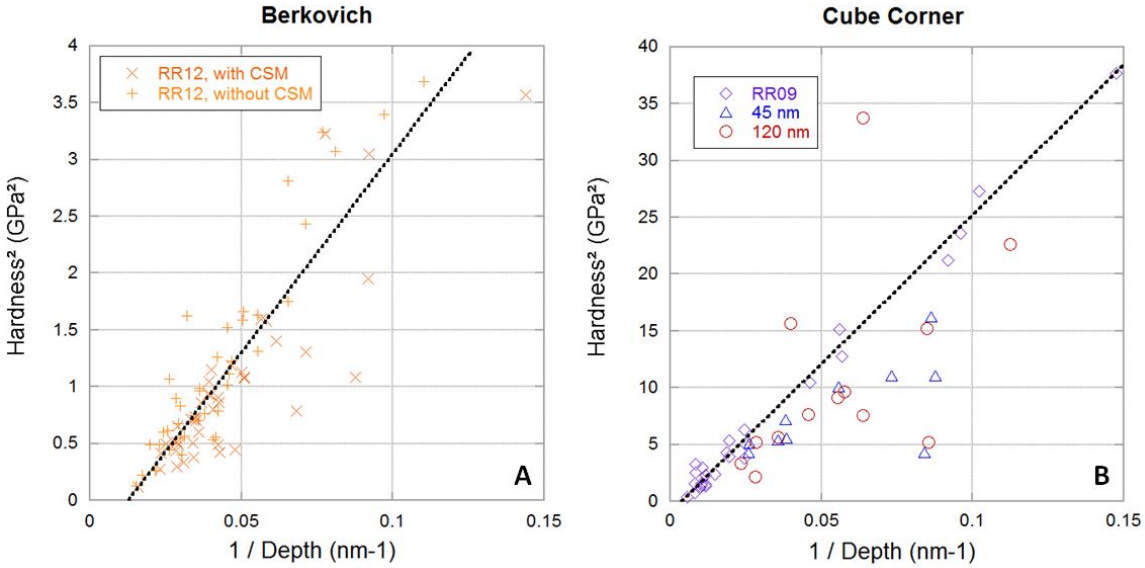

Figure 5.23: Linear relationship between the square of the hardness and the reciprocal of the indentation depth (nanoindentation of gold crystallite with a Berkovich tip (A) and a cube corner (B)).

5.3.3 Island size and shape effect on mechanical behavior

The deterministic laws from the previous paragraph allow to know how a crystallite collapse when it collapses, but they cannot predict why this crystallite collapses at a given critical stress, load or hardness.

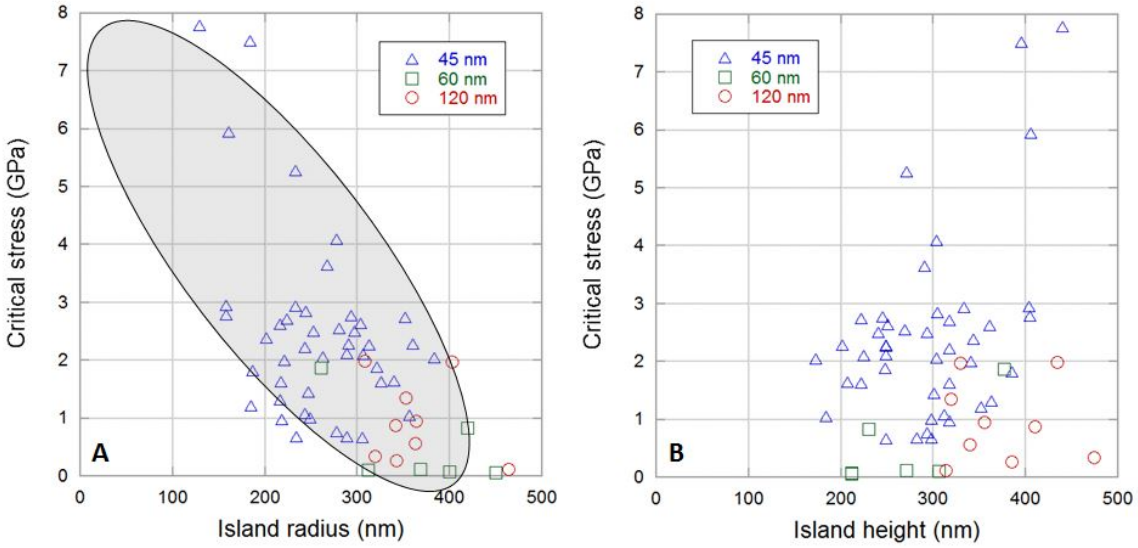

Figure 5.24: Critical stress versus A: island radius and B: island height, from nanocompression tests on various crystallites.

Some authors have investigated the effect of crystal size on the critical load (nanoindentation) and stress (nanocompression). During nanocompression, Greer *et al.* [178] have established an inverse relationship between the critical stress and the top diameter of particles (ranging from 300 nm to 7.5 µm). It has been confirmed by Mordehai *et al.* [183, 188] for particles with diameter from 200 nm to 1 µm. Mordehai *et al.* have also shown an inverse relationship between the critical stress and the crystal height. These results have to be balanced by the study of Bei *et al.* on the nanocompression of single crystal molybdenum micro-pillars, where no size effect was seen for pillar size from 360 nm to 1 µm.

Figure 5.24 shows the critical stress versus the island radius and the island height, from our nanocompression experiments. A slight decrease of the critical stress with increasing island radius can be seen, but the dependency do not follow a power law as described by Mordehai [183]. No obvious dependence is seen on the critical stress-versus-island height curve. However, these results must be put in perspective, since the panel of radius and height used during this study is relatively small.

Since the volume of material is constant for each of the 45nm, 60nm and 120 nm samples, the critical stress can also be drawn versus the island volume, with the error bar corresponding to the dispersion of the critical stress values for each sample. This leads to figure 5.25. The critical stress appear to decrease with increasing island volume from 0.56 to 0.75 μm^3, but from 0.75 to 1.51 μm^3 the effect is hidden by the measurements dispersion.

Regarding nanoindentation data, the critical load can be drawn versus the island radius or height, as shown in figure 5.26. Here again, there is no visible effect of the particle size on the critical load.

Thus, clear relationship between the island size and the critical stress / load cannot be established in the frame of this study.

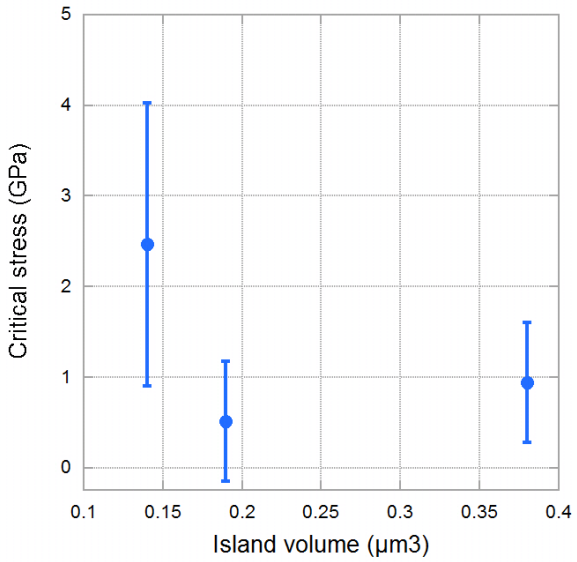

Figure 5.25: Critical stress versus island volume, from nanocompression tests on various crystallites.

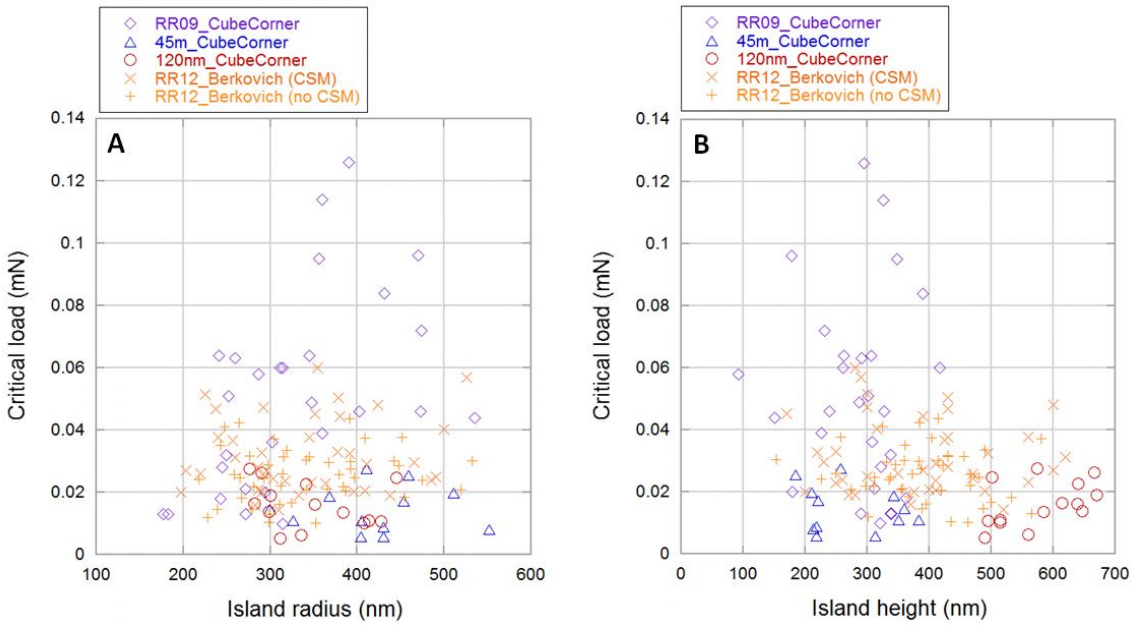

Figure 5.26: Critical load versus A: island radius and B: island height, from nanoindentation tests on various crystallites.

5.4 Results from Bragg Coherent Diffraction Imaging

From the last section it appears that the large dispersion of the mechanical behavior of gold islands under loading cannot be explained by a size effect. This dispersion is likely to be due to initial defects content within the crystallites. Thus, microstructural defects play a major role in deformation mechanisms.

In this part, the relationship between crystallographic defect and mechanical properties is investigated. In that purpose, a large number of crystals from 45nm and 60nm samples have been imaged by Bragg Coherent Diffraction Imaging (BCDI) in their initial state, then tested in nanoindentation with a cube corner tip or a flat punch, and finally measured again by BCDI. Data corresponding to these experiments are not fully analysed and in this part, only qualitative results are given.

By measuring the 111 reflection of our crystals, which are orientated with the <111> axis perpendicular to the substrate plane, BCDI provides a phase image encoding the $u_z(r)$ displacement field. Sharp phase jumps of $2\pi/3$ are of particular interest in this case, as they correspond to the signatures of stacking faults [202].

Figure 5.27 provides an example of crystal before and after nanocompression. The load-displacement curve (figure 5.27 A) is nearly reversible and do not exhibit displacement bursts events. The SEM images of the crystal before and after nanocompression are similar (figure 5.27 B), showing no evidence of residual plastic deformation. However, the diffraction data suggest plastic change within the crystal during nanocompression: the projection of the reciprocal space (figure 5.27 C) evolves from a nearly perfect Winterbottom-shaped diffraction pattern to a more strained pattern. One may suspect a partial splitting of the central peak in figure 5.27 C2, which is a typical signature of a stacking fault [202].

Figures 5.27 D and E show the corresponding real space reconstruction. The colour of the figure corresponds to the phase of the reconstructed wave (and thus is the signature of the 3D displacement field within the lattice). The colour intensity corresponds to the electronic density. In particular the reconstruction in the plane normal to the substrate after nanocompression (figure 5.27 E1) shows evidence of a $2\pi/3$ shift in the phase between two parts of a crystal (white arrow). This is the signature of a stacking fault in (111) plane, which was created under loading. This defect nucleation occurs without the occurrence of large displacement bursts (pop-in). This shows that defects are nucleated prior to these displacements bursts. This confirms that the origin of displacement bursts are due to plastic softening (together with a

machine feedback control), and are not due to dislocations nucleation.

As an additional example, figure 5.28 shows a real space reconstruction of a gold island performed before and after nanoindentation with a cube corner. The mechanical behavior of the island is characterized by a displacement burst of about $\sim$ 10 nm (figure 5.28 A). The SEM images show a permanent residual imprint after mechanical loading (figure 5.28 B). This plastic deformation affects the diffraction pattern (figures 5.28 C2 to be compared to figure 5.28 C1).

5.5 Conclusion

In this chapter, the *in situ* SEM setup described in chapter 3 (page 81) has been used for nanoindentation and nanocompression of a large number of submicrometric gold islands on sapphire, obtained by solid state dewetting.

The stochastic nature of the mechanical behavior of gold islands under mechanical testing has been underlined. However, the crucial point is that despite this stochastic behavior, deterministic mechanical laws can be extracted from nanocompression and nanoindentation data.

The deterministic stress-strain law extracted from nanocompression tests is characterized by a strong linear hardening, a fraction of the maximum hardening observed in stage II of FCC single crystal.

The deterministic hardness-depth law obtained from nanoindentation data fit well the Nix and Gao relation for strain gradient plasticity.

First qualitative results from a BCDI experiments to investigate crystals microstructure before and after mechanical loading have been given. Even if the analysis is still in progress, we demonstrate that deformation defects are nucleated prior to the large deformation bursts. It confirms that the origin of those bursts are linked with the occurrence of plastic softening together with a machine feedback control, and not with dislocations nucleation.

Finally, we propose a reliable methodology based on statistical measurements to investigate the mechanical response of small-scale systems.

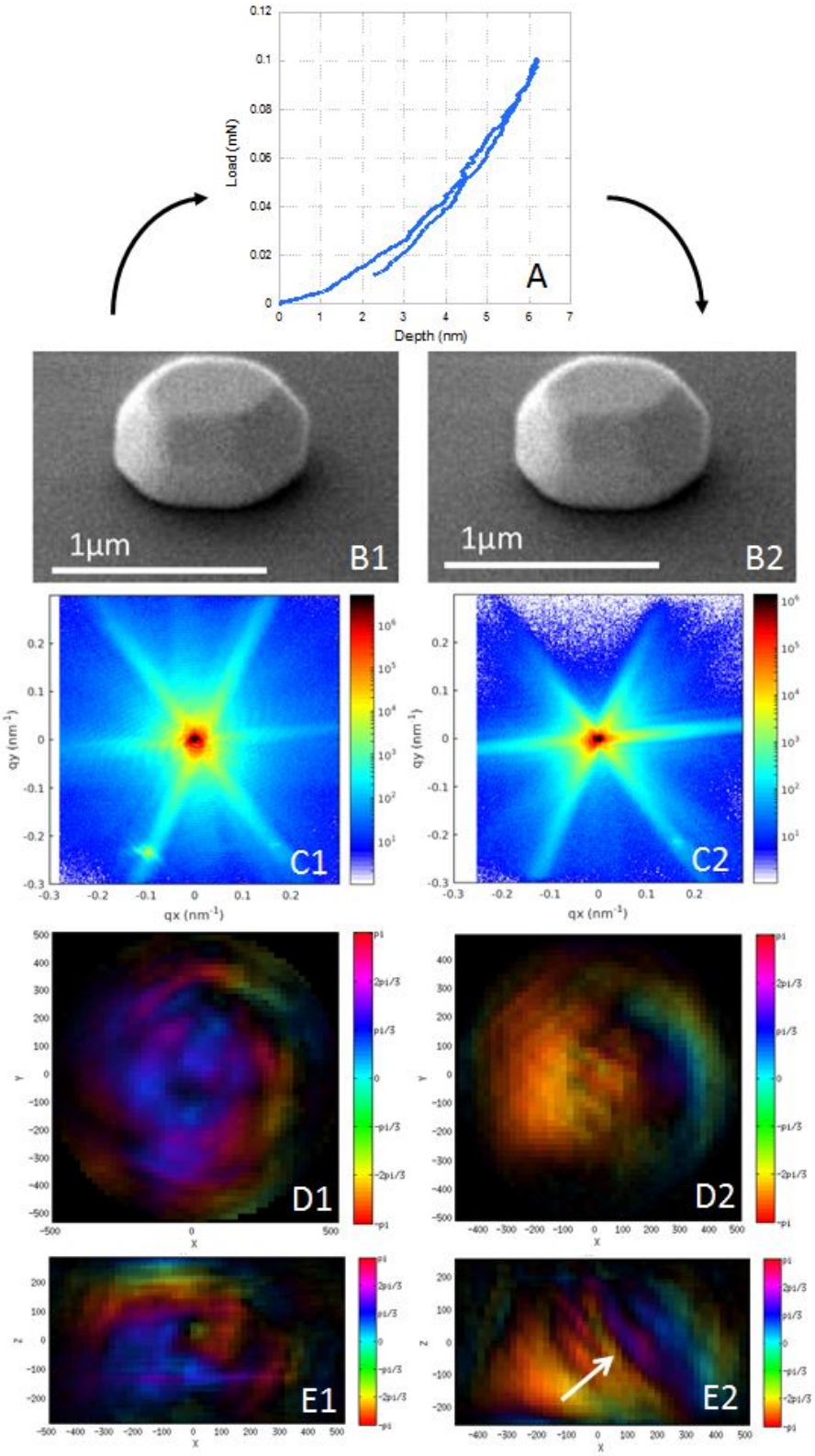

Figure 5.27: Force-versus-displacement curve during nanocompression of a gold single crystal (A), SEM image of the crystal (B), reciprocal space projection (C) and real space reconstruction parallel to the substrate (D) and normal to the substrate (E), before (left) and after (right) mechanical loading.

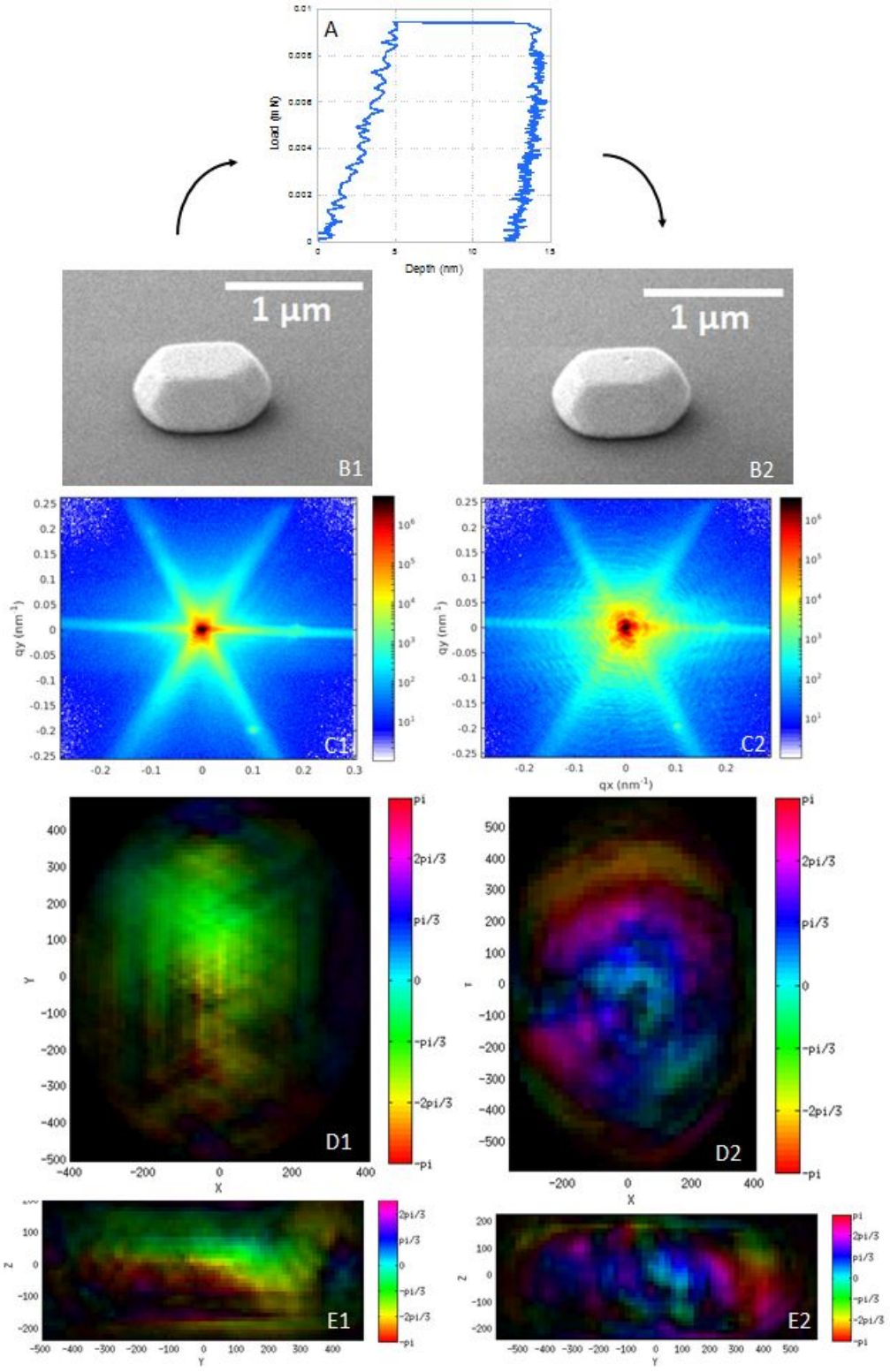

Figure 5.28: Force-versus-displacement curve during nanoindentation of a gold single crystal (A), SEM image of the crystal (B), reciprocal space projection (C) and real space reconstruction parallel to the substrate (D) and normal to the substrate (E), before (left) and after (right) mechanical loading.

Chapter 6

Resistive nanoindentation

6.1 Introduction

A multi-characterisation tool based on mechanical / electrical coupling has been developed in SIMaP lab (see chapter 3, page 81). The heart of this device is an *in situ*-SEM nanoindenter coupled with an electrical measurement apparatus. This device has several purposes:

1. **Direct mechanical contact area monitoring**, thanks to the electrical resistance monitoring during indentation. Mechanical contact area monitoring is a complex issue in nanoindentation, even for the simplest case of an homogeneous semi-infinite solid. If the sample Young's modulus is unknown, models based on material rheology assumptions [20, 21] are required for contact area calculation. The electrical monitoring of the contact area brings new inputs to the quantitative analysis of mechanical behavior and could be an alternative to models. In the past two decades, efforts have been made in literature to estimate contact area from electrical measurements. In microindentation Fang *et al.* [143], have proposed a way to relate non linear I-V curves performed during indentation to instantaneous contact area, but this approach is not enough sensitive for nanoindentation testing. More promising results were obtained by Sprouster *et al.* [144], where the resistance-versus-depth curve during indentation of a gold sample by a vanadium carbide tip was successively fitted using the Maxwell expression for the spreading resistance. This allows sample resistivity computation and theoretically allows electrical contact area monitoring. Nevertheless this last part was not discussed by Sprouster *et al.* In this chapter the contact area monitoring during electrically coupled nanoindentation is discussed.

2. **Electrical monitoring of fast irreversible mechanical events.** Fast irreversible

mechanical events (dislocation bursts, oxide cracking, thin film delamination...) can produce similar mechanical discontinuities on indentation curves (pop-in). However, they have different electrical signatures. Thus, electrical monitoring can help to decorrelate the contribution of each event. Some authors have successively used electrically coupled nanoindentation to study oxide fracture [139, 140], thin film delamination [141] and mechanically induced phase transformation [133, 134, 135, 136, 137, 138]. From these studies, electrical monitoring during nanoindentation appears to be a promising tool to obtain additional information to mechanical behavior. Within the frame of this project electrical and mechanical signatures of aluminum oxide crack are studied.

3. **Electronic transport within a structure.** In this chapter electronic transport through a metal + oxide structure is studied. In the presence of an oxide layer, electrochemical mechanisms at the tip-to-sample contact are discussed. This topic will be extended to capacitive measurements on thin dielectric films in chapter 7 (page 239).

Other applications can be foreseen, as the study of piezoelectric materials. Nevertheless, this point was not investigated within the frame of this project.
In this chapter, electrical measurements during indentation of model specimens are discussed. Noble metal (gold) or natively oxidised metals (copper and aluminum), either as bulk single crystals or as polycrystalline thin films have been tested. The effect of the material chosen for the conductive tip is also studied: both standard boron-doped diamond (BDD) and tungsten carbide (WC) tips have been tested. Different local environments have also been assessed: room atmosphere, intermediate vacuum and high vacuum.

6.2 Materials and methods

6.2.1 Electronic acquisition system

Electrically coupled nanoindentation is conducted with the "3-axes" Inforce set-up described in chapter 3 (page 81).
Electrical measurements are performed with a ResiScope from CSI/Scientec and originally developed at the LGEP (Supelec, France) [151]. A bias is applied between the indentation tip (signal measurement) and a back contact on the sample (polarisation bias).
The ResiScope can measure resistance changes over ten decades (from 100 Ω to 1 TΩ). This allows resistance monitoring from the earliest contacts to large indentation depths. High acqui-

sition rate up to 1 kHz can be reached. This allows the monitoring of fast mechanical events. When the measured resistance is below 100 Ω, an additional resistance is required in series with the sample.

The ResiScope was originally developed for conductive AFM [151]. It optimizes in real time the current passing through the contact to limit current density and thus avoid electrical burn-out. For small contact resistance the applied bias is much lower than the set-point bias. During indentation the contact area increases, leading to a contact resistance decrease. Thus, during indentation, the sample bias is expected to decrease. For confidentiality reasons the relation between the set-point bias and the applied bias is not given in this communication.

The resistance measured by the ResiScope slightly deviates from nominal values of calibration resistors and must be adjusted using equation (6.1), with $R_{corrected}$ and $R_{measured}$ the corrected and the measured resistance.

$$R_{corrected} = 0.825 * R_{measured}^{1.046} \tag{6.1}$$

Alternatively, a Keihtley 6430 (Source Measurements Unit System, SMU) can be used instead of the ResiScope for electrical measurements.

6.2.2 Environment

Electrical measurements can be influenced by the local environment. In particular, the presence of a water meniscus can affect the measurements. Measurements can also be disturbed at room atmosphere by electrochemical mechanisms occurring under oxygen. Such effects have been assessed in literature for spreading scanning resistance microscopy [131, 120, 129, 130]. Within the frame of this study, comparative tests are performed at room atmosphere, under intermediate vacuum (10^{-2} mbar) and under high vacuum (10^{-6} mbar).

6.2.3 Indentation tip

A crucial point for resistive nanoindentation is the choice of the indentation tip. Boron-doped diamond (BDD) tips are most commonly used in literature [137, 138, 143]. Such tips provide excellent mechanical properties with reasonably low resistivity ($\sim$ Ω.cm). Nevertheless some authors have proposed that dopant segregation and dopant activation heterogeneities at the tip surface may be responsible for non linear contact between BDD tips and metals [145]. Thus, transition metal carbides tips are increasingly used, due to their good mechanical properties

and high metallic-like conductivity. Transition metal carbides used in literature are essentially vanadium carbide (VC) [134, 135, 144].

Within the frame of this project, both Berkovich BDD tip and Berkovich tungsten carbide (WC) tip have been assessed. Both tips are provided by SYNTON.

The WC tip is not monocrystalline and SEM image shows evidence of two phases, which are most likely WC and W_2C (figure 6.1). XPS measurements have shown the presence of an oxide layer on the WC tip, with an oxide thickness of several nanometers. The resistivity of WC tip is around $2 \cdot 10^{-5}$ Ω.cm.

The resistivity of various boron-doped diamond provided by SYNTON has been measured, which places the resistivity of the BDD tip in the range 0.2-2 Ω.cm.

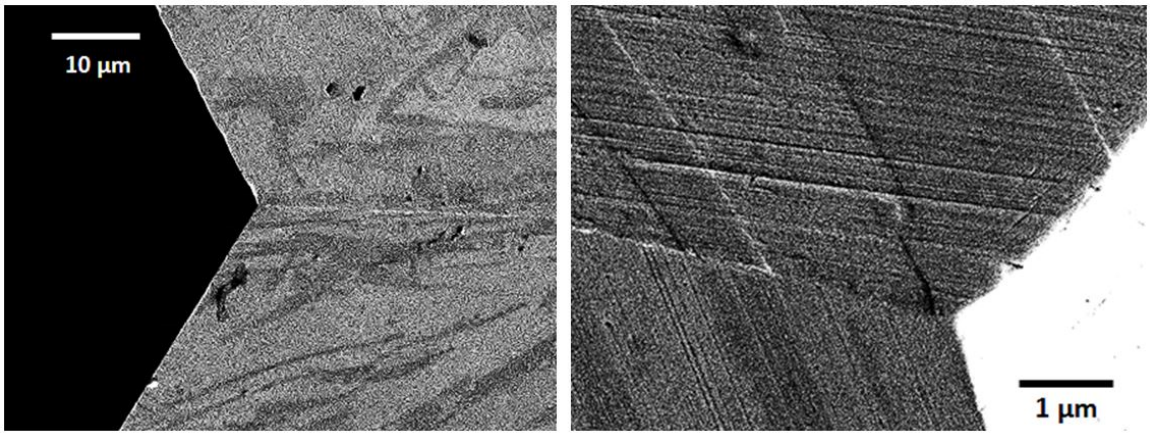

Figure 6.1: SEM image of the WC tip showing two phases.

6.2.4 Samples

Electrical measurements have been conducted on different model specimens, as shown in tables 6.1 and 6.2. Experiments were performed on bulk single crystals and on thin polycrystalline films. Noble metals (Au) as well as natively oxidised samples with either ionic conduction (Al) or mixed conduction (Cu) have been studied.

The effect of oxide thickness has been investigated by using Al_2O_3 / Al / Si / SiO_2 stacks, with different alumina thicknesses deposed by Atomic Layer Deposition (ALD). These stacks were elaborated within the frame of the Ph.D of Mercier [93, 203].

For bulk Al single crystal and alumina thin films, oxide thicknesses have been measured by X-ray reflectivity. For bulk Cu single crystal, no obvious oxide layer has been detected by XPS, which suggests that the oxide layer for this sample is less than 1 nm.

Sample description	Oxide nature and size
Au single crystal (100)	Noble metal
Cu single crystal (100)	< 1 nm native oxide (mixed conduction)
Al single crystal (111)	6-9 nm native oxide (ionic conduction)

Table 6.1: Summary of investigated bulk single crystals.

Sample description	Oxide nature and size
200nm Au + sapphire	Noble metal
10nm Al_2O_3 + 540 nm Al + SiO_2(500nm) + Si(725µm)	6-7 nm oxide (ionic conduction)
20nm Al_2O_3 + 540 nm Al + SiO_2(500nm) + Si(725µm)	18-20 nm oxide (ionic conduction)
30nm Al_2O_3 + 540 nm Al + SiO_2(500nm) + Si(725µm)	29-33 nm oxide (ionic conduction)
40nm Al_2O_3 + 540 nm Al + SiO_2(500nm) + Si(725µm)	38-42 nm oxide (ionic conduction)

Table 6.2: Summary of investigated thin films.

6.3 Preliminary results for resistive indentation with BDD tip

6.3.1 Resistance-versus-depth curves

Electrical measurements with the ResiScope have been conducted, while indenting bulk Au, Al and Cu single crystals with a BDD tip. Constant bias set-points (from 0.5 V to 10 V) have been applied to the contact. Resistance-versus-depth curve at room atmosphere and corresponding curves in logarithmic scale are shown in figures 6.2 to 6.5.

As expected, all samples exhibit a global resistance decrease with increasing indentation depth. This was expected since the electrical conductance increases with increasing contact area. However, the electrical behaviors of Au, Al and Cu strongly differ.

Bulk Au single crystal

The resistance of bulk Au single crystal continuously decreases with increasing depth (figure 6.2). Results are found to be highly reproducible. According to the logarithmic curves, the

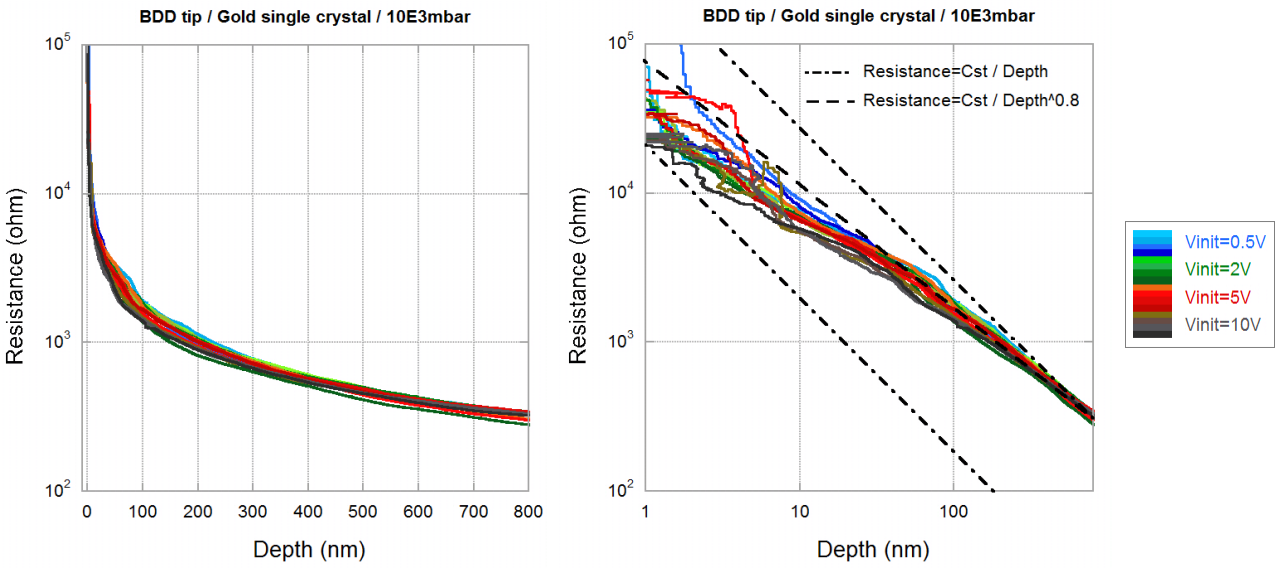

Figure 6.2: Resistance-versus-depth curve for BDD tip and bulk Au single crystal, with decimal scale (left) and logarithm scale (right).

resistance decreases as $1/\text{Depth}^{0.8}$ for indentation depth larger than 100 nm. This is close to the prediction of Maxwell theory [74] (equation 6.2, with r_c the contact radius, which can be first considered as proportional to the indentation depth). This relation can give information about local resistivity or electrical contact area. This point will be further discussed in section 6.5 (page 205).

$$R = \frac{\rho}{4r_c} \tag{6.2}$$

The deviation to Maxwell theory ($1/\text{Depth}^{0.8}$ instead of $1/\text{Depth}$) can be due to series resistance coming from the experimental set-up. For indentation depth smaller than 100 nm, the electrical behavior also deviates from Maxwell model. These two points will be adressed in paragraph 6.4 (page 189).

Bulk Al single crystal

Bulk Al single crystal exhibits a global decrease of the resistance while indenting (figure 6.3). However, this decrease is much more discontinuous, and even exhibits unexpected local resistance increases - especially for bias set-point below 2 V. Resistance signal is also much more noisy.

- Resistance curves for 0.5 V bias set-point first exhibit a high resistance plateau at small depths, which is characterized by high electrical noise. At this stage, the resistance at the

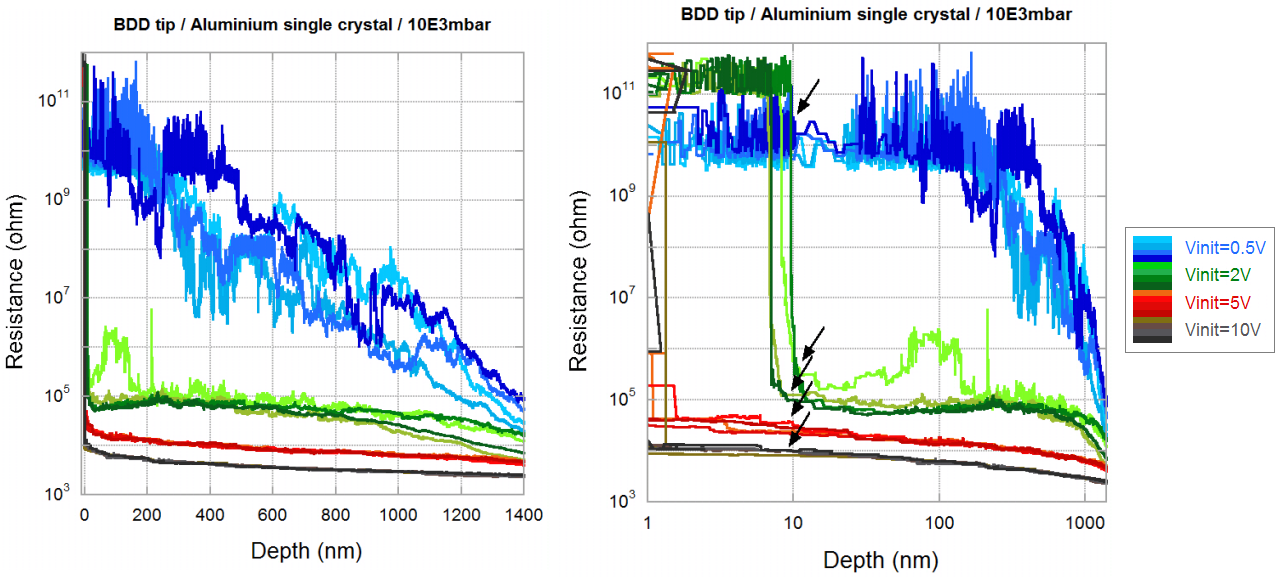

Figure 6.3: Resistance-versus-depth curve for BDD tip and bulk Al single crystal, with decimal scale (left) and logarithm scale (right). Mechanical pop-in events are represented by black arrows.

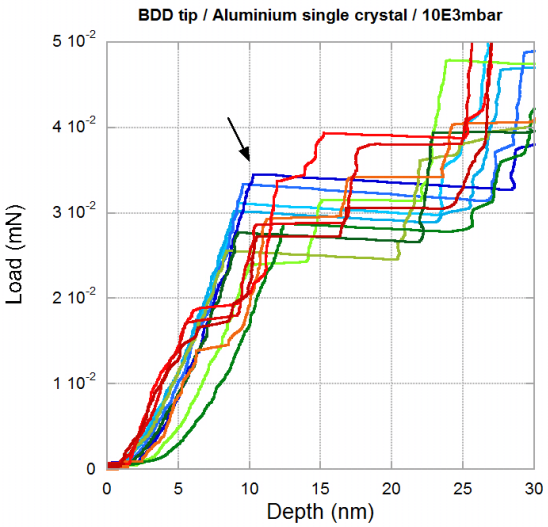

Figure 6.4: Load-displacement curves for nanoindentation of bulk Al single crystal, showing evidence of pop-in (black arrow) around 10 nm depth.

contact is too high and the ResiScope fails to accurately measure it. Then the electrical contact is gradually set for indentation depth larger than 100 nm, leading to a resistance decrease.

- Resistance curves for 2 V bias set-point also exhibit a high resistance plateau at small depths. However, at $\sim$ 10 nm depth the resistance suddenly drops, which means that the electrical contact is set. This resistance drop is followed by roughly constant resistance values up to $\sim$ 1000 nm depth, with sometimes unexpected resistance increases. After $\sim$ 1000 nm depth the resistance decreases with increasing indentation depth.
- The resistance curves for 5 V and 10 V bias set-points are quite similar to that of 2 V bias set-point curves. However in these cases the sudden resistance drop occurs for indentation depths below 1 nm.

These gradual (0.5 V set-point) or sudden (2-10 V set-point) resistance drops, seem to be independent from mechanical pop-in events which occur around 10 nm in mechanical indentation curves and which are likely to be due to oxide layer fracture (black arrows in figures 6.3 and 6.4). Indeed, this mechanical pop-in occur well before the resistance drop for 0.5 V curves, and after the sudden resistance drop for 2-10 V resistance curves. This point will be discussed in paragraph 6.6 (page 209).

Electrical measurements for Al are also much less reproducible than for Au, even if the same trend is observed for each bias set-point condition.

The unexpected resistance increase events will be discussed in paragraph 6.8 (page 218).

Bulk Cu single crystal

Bulk Cu single crystal appears to have an intermediate behavior (figure 6.5). Resistance-versus-depth curves are highly reproducible. As for Au bulk sample, the resistance continuously decreases following a law in $1/\text{Depth}^{0.8}$ for indentation depth larger than 500 nm, which is close the Maxwell theory. However, unexpected oscillations on the resistance-versus-depth curves are found, especially for high bias set-points. These oscillations will be discussed in paragraph 6.8 (page 218).

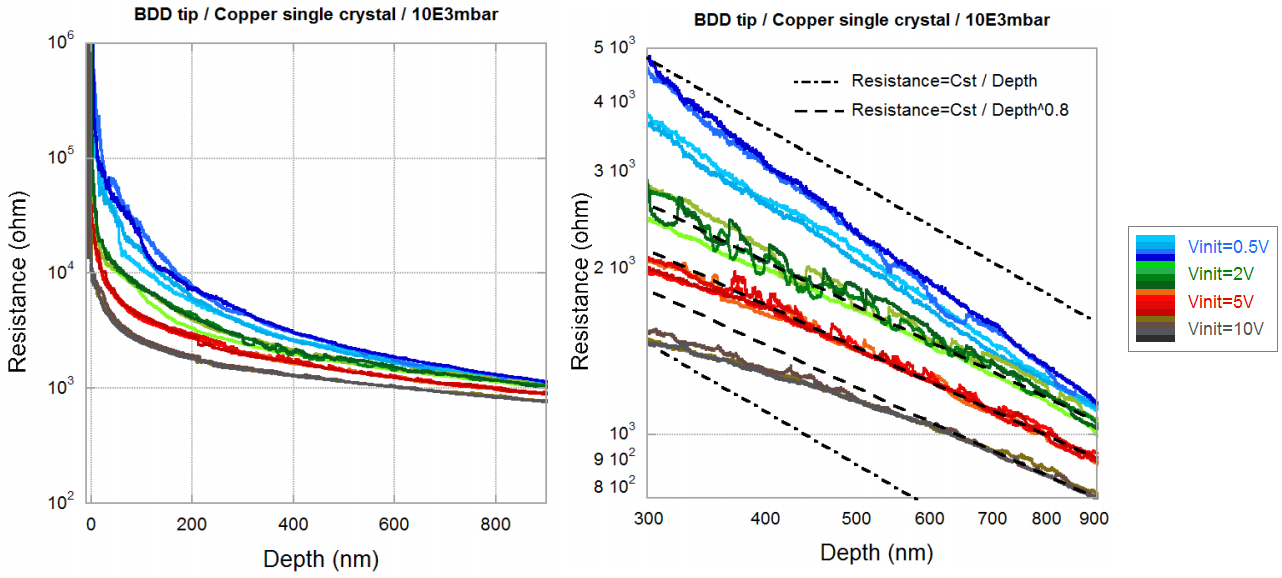

Figure 6.5: Resistance-versus-depth curve for BDD tip and bulk Cu single crystal, with decimal scale (left) and logarithm scale (right).

6.3.2 I-V measurements

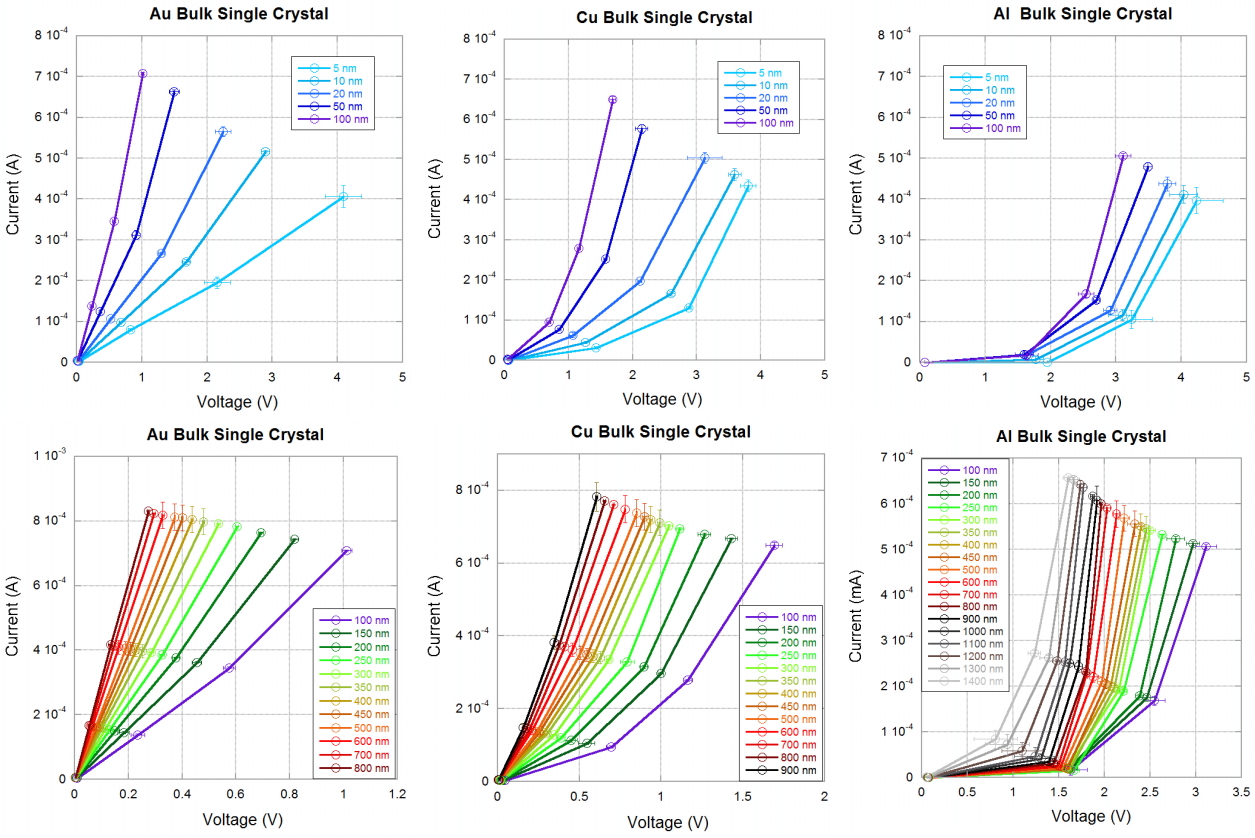

Figure 6.6: I-V curves extracted from resistance measurements at several indentation depths for Au (left), Cu (middle) and Al (right) bulk samples with BDD tip.

From above resistance-versus-depth curves on Au, it also appears that electrical measurements exhibit only little change for increasing bias set-point. Thus, the electrical contact Au/BDD is expected to be close to be perfectly ohmic. On the contrary, Al and Cu samples exhibit non linear behaviors, with decreasing resistance for increasing bias set-point. Al/BDD and Cu/BDD contacts are clearly not ohmic.

These behaviors are highlighted in figure 6.6, where the current passing through the contact is represented versus the real bias applied to the contact (I-V curves), for several indentation depths. These figures are extracted from the resistance-versus-depth curves above.

I-V curves for Au/BDD contact are almost linear, and become more linear with increasing indentation depth. They are almost perfectly linear for indentation depths larger than 200 nm. This ohmic-like behavior was also found in literature for highly-doped BDD tips [145]. Nevertheless, the contact is not perfectly ohmic, especially for small indentation depths. Using a less doped BDD tip considerably increases this non linearity, as shown in figure 6.7. This non-linearity probably comes from the BDD tip which is a semiconductor and which has not a purely metal-like behavior, despite its high dopant content.

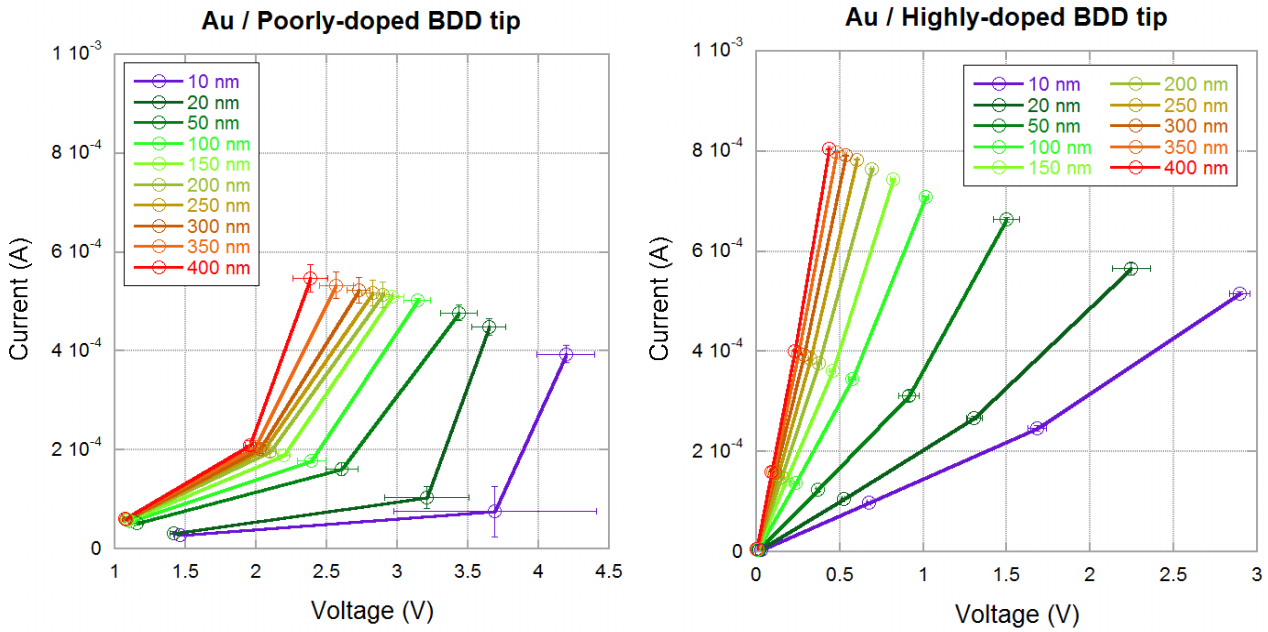

Figure 6.7: I-V curves at several depth while indented Au with poorly-doped BDD tip (dopant content estimated below $< 10^{19}$ cm^{-3}) (left) and higly-doped BDD tip (boron content estimated around $< 10^{20}$ cm^{-3}) (right).

I-V characteristics for Cu/BDD contact are much less linear than for Au/BDD contact. The contact behavior becomes more linear with increasing indentation depth but remains non-ohmic. Al/BDD contact was found to be non-ohmic even for large indentation depths.

Non linearity in case of Cu and Al samples can be attributed to the presence of their native oxides. The effect of these native oxides with thicknesses below 10 nm is quite unexpected for large indentation depths ($\gg$ 100 nm).

6.4 Modelling of electrical resistance during indentation

The aim of this section is the understanding of resistance-versus-depth curves during indentation. First, an analytical model is developed. This model is then applied to the indentation of a bulk Au sample with a BDD tip and compared to experimental data. A numerical model is then proposed.

6.4.1 Analytical model

Contributions to the measured resistances

Let us consider a mechanical contact between a pyramidal tip and a bulk sample, as illustrated by figure 6.8. In the diffusive regime, the measured resistance $R_{measured}$ is the sum of four contributions (equation 6.5):

- R_{series}, which is the sum of the series resistance added to the contact, such as the sample resistance or additional resistances coming from the experimental set-up. This contribution is constant during indentation.

- $R_{spreading-sample}$, which is the spreading resistance within the sample. This resistance comes from the constriction of the current lines through the contact. $R_{spreading-sample}$ can be estimated by Maxwell equation (6.3), with ρ the sample resistivity and r_c the contact radius. This contribution decreases during indentation.

$$R = \frac{\rho}{4r_c} \tag{6.3}$$

- $R_{spreading-tip}$, which is the spreading resistance within the tip. This resistance comes from the constrictions of the current lines along the indentation tip. The analytical expression of $R_{spreading-tip}$ will be discussed later on. This contribution decreases during indentation.

- $R_{contact}$ is the contact resistance due to the presence of a contaminant or an oxide layer. Its expression is given by equation (6.4), with ρ_c the specific contact resistivity and A_c the contact area. This contribution decreases during indentation.

$$R_{contact} = \rho_c / A_c \tag{6.4}$$

$$R_{measured} = R_{series} + R_{spreading-sample} + R_{spreading-tip} + R_{contact} \tag{6.5}$$

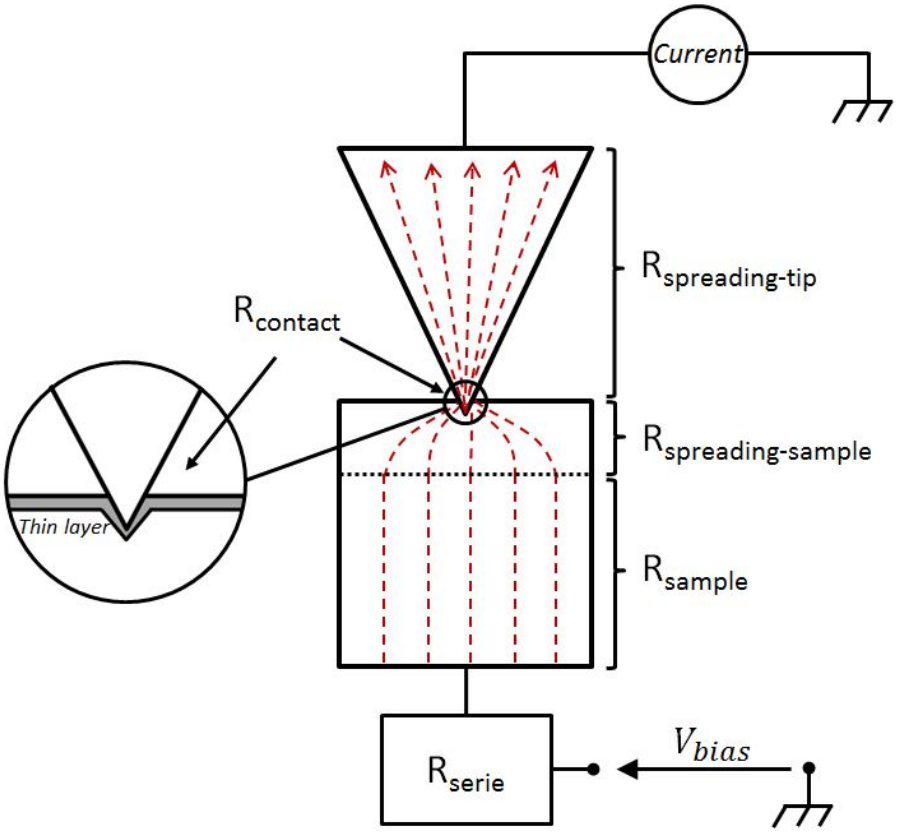

Figure 6.8: Different contributions to the resistance.

Expression of the tip spreading resistance

The spreading resistance within a pyramidal tip can be calculated using the expression proposed by Schneegans *et al.* [204] for a pyramidal AFM tip broken at its apex. This expression is given in equation (6.6) with ρ_{tip} the tip resistivity and c, d_0 and c_0 geometrical parameters as

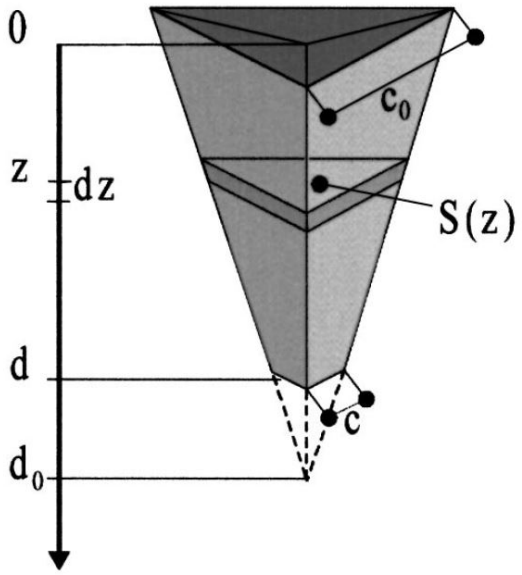

Figure 6.9: Geometry used for the computation of the spreading resistance in the case of a Berkovich tip, according to Schneegans *et al.* [204]

illustrated in figure 6.9. In our case, the missing part of the apex corresponds to the part of the tip that has already penetrated the sample, *i. e.* to the contact depth h_c. The limitation of this expression is that the part of the tip which is inside the sample is not taken into account in the spreading resistance calculation, although it can affect the distribution of the current lines.

$$R_{spreading-tip} = \frac{4\rho_{tip}d_0}{\sqrt{3}c_0^2} \cdot \frac{1 - c/c_0}{c/c_0} \tag{6.6}$$

For a Berkovich tip the ratio c/c_0 is negligible. For an ideal Berkovich tip with no tip defect, the contact depth $h_c = cd_0/c_0$. This leads to equation (6.7).

$$R_{spreading-tip} = \frac{4\rho_{tip}d_0^2}{\sqrt{3}c_0^2} \cdot \frac{1}{h_c} \tag{6.7}$$

By taking into account the Berkovich tip defect height h_0, equation (6.7) turns into equation (6.8).

$$R_{spreading-tip} = \frac{4\rho_{tip}d_0^2}{\sqrt{3}c_0^2} \cdot \frac{1}{h_c + h_0} \tag{6.8}$$

The ratio d_0/c_0 is constant for a Berkovich tip and equal to 0.133. The spreading resistance is then simply a function of the reciprocal of the contact depth h_c and of the tip resistivity ρ_{tip}.

6.4.2 Application to the indentation of Au bulk sample with a BDD tip

Simplified expression of the measured resistance

In the case of the indentation of a Au bulk sample with a BDD tip, the resistance contributions to the measured resistance can be simplified:

- The series resistance coming from the sample is estimated to few μΩ ($\rho_{gold} = 2.2 \cdot 10^{-6}$ Ω.cm) and is negligible. However, other series resistance coming from the experimental set-up are not negligible.
- For indentation depth above 10 nm, $R_{spreading-sample}$ is below 1 Ω and it can be neglected compared to the tip spreading resistance.
- The contact resistance can be neglected in the case of Au/BDD contact where there is no oxide layer.

Since the resistivity of the BDD tip is high ([0.2-2] Ω.cm), the tip spreading resistance is the main contribution to the measured resistance $R_{measured}$. This resistance is expected to decrease with increasing indentation depth. Using equation (6.5) and (6.9), the measured resistance can simply be written by equation (6.9), with $A = R_{series}$ and $B = \frac{4\rho_{tip}d_0^2}{\sqrt{3}c_0^2}$.

$$R_{measured} = A + \frac{B}{h_c + h_0} \tag{6.9}$$

With this analytical model, the measured resistance $R_{measured}$ is then simply a function of the contact depth h_c, with three constant values A, B and h_0 which depend only on the experimental set-up (including the BDD tip).

Computation of the contact depth and tip defect height

- Mechanical calibration of the tip:

In order to verify the analytical model for an Au/BDD contact, the tip defect height h_0 and the contact depth h_c must first be determined.

In that purpose, the BDD tip has been mechanically calibrated on a fused silica sample, using the procedure described in section 1.2.6 (page 37). The contact radius r_c for this BDD tip was

found to be related to the contact depth by equation (6.10). This relation can be approximated by equation (6.11). The error between both expressions is less than 1 % for contact depth larger than 100 nm. The tip defect height h_0 is estimated to be 11.6 nm. A_{tip} corresponds to the tangent of the tip equivalent angle α, estimated at 69.5° in that case (against 70.3° for an ideal Berkovich tip).

$$r_c = \sqrt{\left(\frac{22.22h_c^2 + 877.88h_c - 7753.45h_c^{0.5} + 20878.43h_c^{0.25} - 14484.72h_c^{0.125}}{\pi}\right)} \tag{6.10}$$

$$r_c = A_{tip}(h_c + h_0); \quad A_{tip} = 2.67; \quad h_0 = 11.6nm \tag{6.11}$$

This relation can be verified by scanning the BDD tip with AFM. The tip defect height was estimated to be 11.8 nm with the AFM. The equivalent angle was estimated to be 70.4°. The error between the contact radius computed from calibration on fused silica and from AFM calibration is around 5-7 %.

- Contact depth computation from mechanical data

The contact depth can then be extracted from nanoindentation data of the bulk Au single crystal.

The residual imprints on Au exhibit sink-in (figure 6.10 A). This is quite uncommon for gold single crystal, but it could be explained by a surface hardening. Evidence of such surface hardening can be seen on hardness-versus-depth curves from nanoindentation data, with hardness computed using Oliver and Pharr model (figure 6.10 B).

Due to this sink-in behavior, the Oliver and Pharr model is chosen to estimate the contact area. The Oliver and Pharr model [20] relates the contact depth to the penetration depth with equation (6.12), where $\epsilon = 0.75$ for a Berkovich tip, L is the applied load and S_c is the dynamic contact stiffness.

$$h_c = h - \epsilon\frac{L}{S_c} \tag{6.12}$$

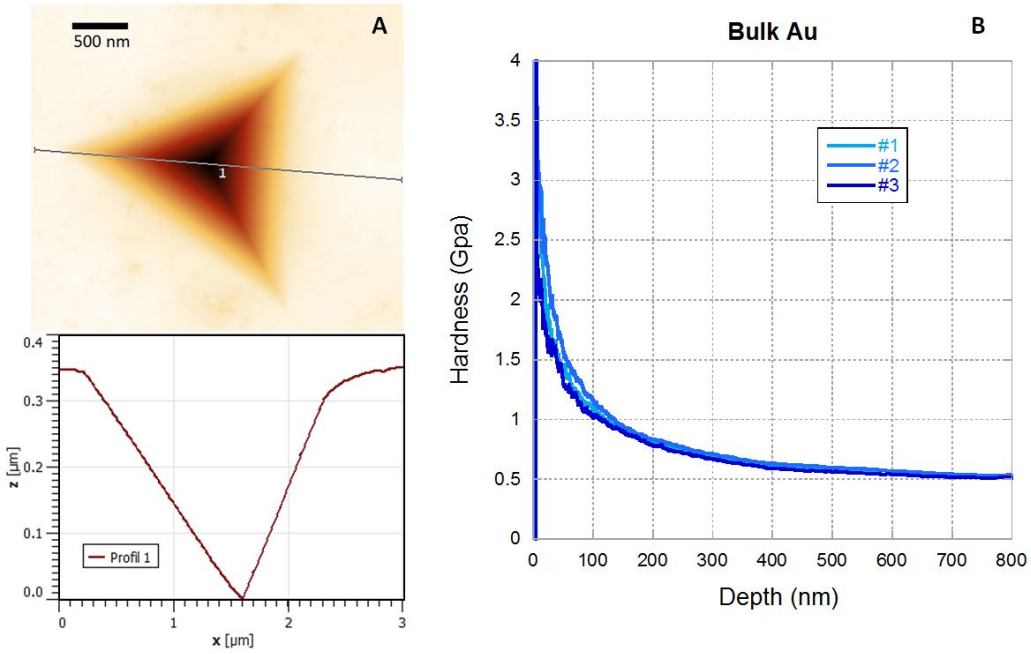

Figure 6.10: A: AFM image of residual imprint on bulk Au single crystal showing evidence of sink-in and B: hardness-versus-depth curve from indentation of bulk Au single crystal, showing surface hardening.

The values obtained for the contact depth using Oliver and Pharr model can be verified by calculating the contact radius r_c as given by equation (6.11). The contact area A_c is then computed using $A_c = \pi r_c^2$. The contact area values can be compared to residual imprint area measured by AFM. Figure 6.11 shows the contact area calculated with Oliver and Pharr model versus the indentation depth for bulk Au sample. Corresponding residual imprint areas measured by AFM for several indentation depths are also given. The Oliver and Pharr model gives a good estimation of the contact area.
The contact area can also be estimated directly from Sneddon's equation (equation 6.13) for a constant reduced Young's modulus E^*. A reduced modulus of 82 GPa - which corresponds to a sample modulus of 73 GPa - leads to a contact area computation close to the post-mortem AFM measurement and to the contact area estimated from Oliver and Pharr model.

$$S_c = \frac{2}{\pi} E^* \sqrt{(A_c)} \tag{6.13}$$

From this result, it appears that both contact depth calculation (using Oliver and Pharr model for bulk Au single crystal) and the shape function (which relates the contact radius and the contact depth) are reliable.

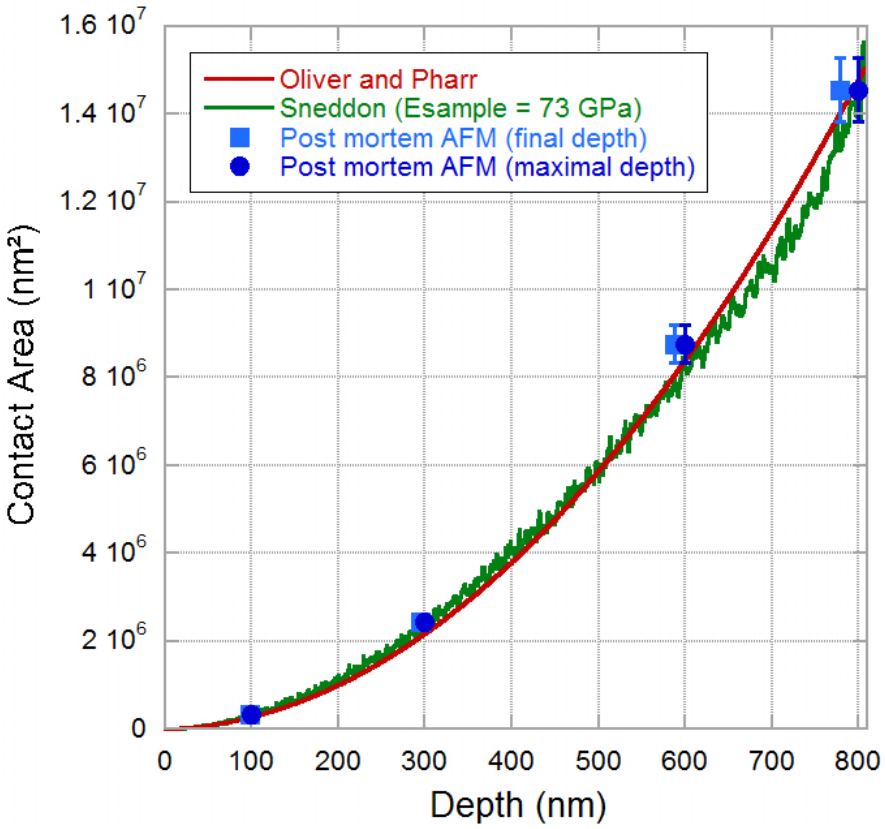

Figure 6.11: Contact area on bulk Au sample estimated from Oliver and Pharr model and Sneddon's equation and compared to post mortem AFM measurements. Post mortem AFM are given versus the maximal indentation depth (circle) and versus the final depth after unloading (square), in order to account for the elastic spring back.

Comparison to electrical measurement

In order to verify that the analytical electrical model applies to resistive indentation of a bulk Au sample with a BDD tip (equation 6.9), the resistance measured during indentation of the bulk Au single crystal has be drawn versus $\frac{1}{h_c+h_0}$ (figure 6.12). For indentation depth larger than 50-100 nm, the curve is linear which verifies the analytical model for large indentation depths.

A linear fit of this curve allows to determine A and B coefficients. From this fit, A was found to be equal to 250 Ω and B equal to $2.6 \cdot 10^5$ Ohm.nm. This corresponds to a series resistance $R_{series} = 250$ Ω and a tip resistivity ρ_{tip} of 0.6 Ω.cm, which fits within the range [0.2-2] Ω.cm previously measured on various BDD sample provided by SYNTON.

Using these values, both experimental and analytical resistance-versus-depth curves can be drawn in logarithmic scale (figure 6.13). Good agreements are found between experimental

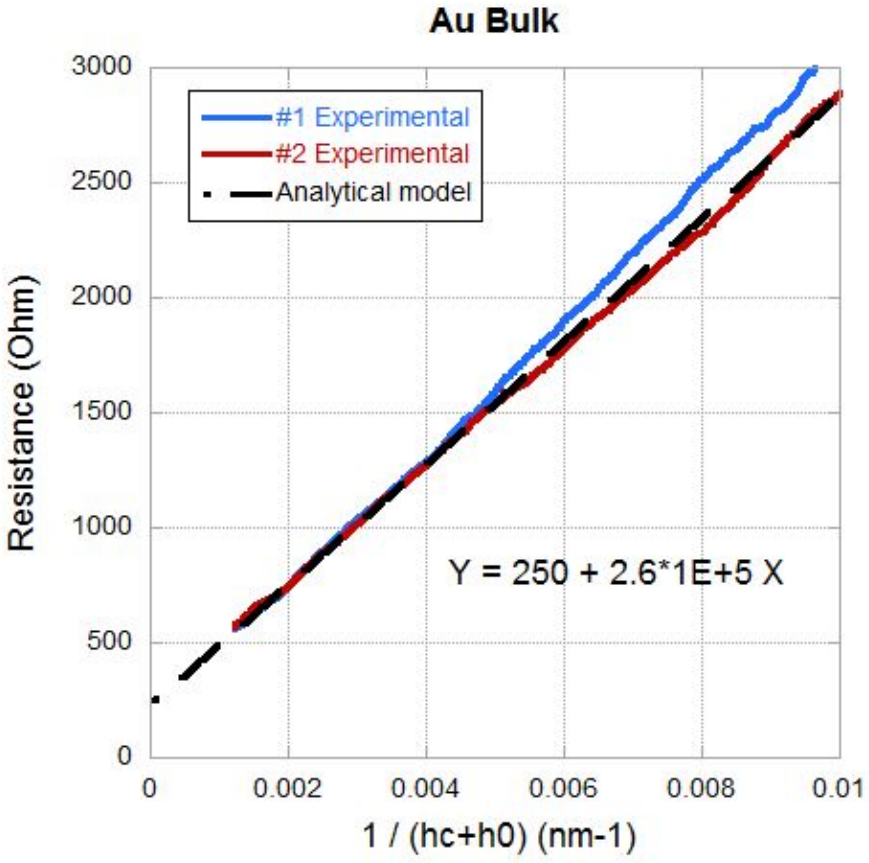

Figure 6.12: Resistance R_m versus the reciprocal of the contact depth h_c plus the tip defect height h_0 during indentation of bulk Au single crystal with a BDD tip.

results and analytical model for contact depths higher than 30 nm. As mentioned in paragraph 6.3.1 (page 183), the resistance-versus-depth curve deviates from the $1/h$ curve at large depth, which comes from the non-negligible series resistance $R_{series} = 250\ \Omega$.

For comparison, the same experimental curves can be drawn and compared to the analytical model derived without taking into account the tip defect height h_0. This leads to figure 6.14. In that case, experimental curves deviate from the analytical model for contact depth below 100 nm. This emphasizes the need to take into account the real shape of the tip in the analytical model, and especially its tip defect height.

At low indentation depth (<20 nm), the measured resistance $R_{measured}$ is much higher than predicted by the model. This deviation can be due to two factors:

- The electrical contact can be not well established due to the sample roughness or a contamination layer, leading to an electrical contact area much smaller than the mechanical contact area.

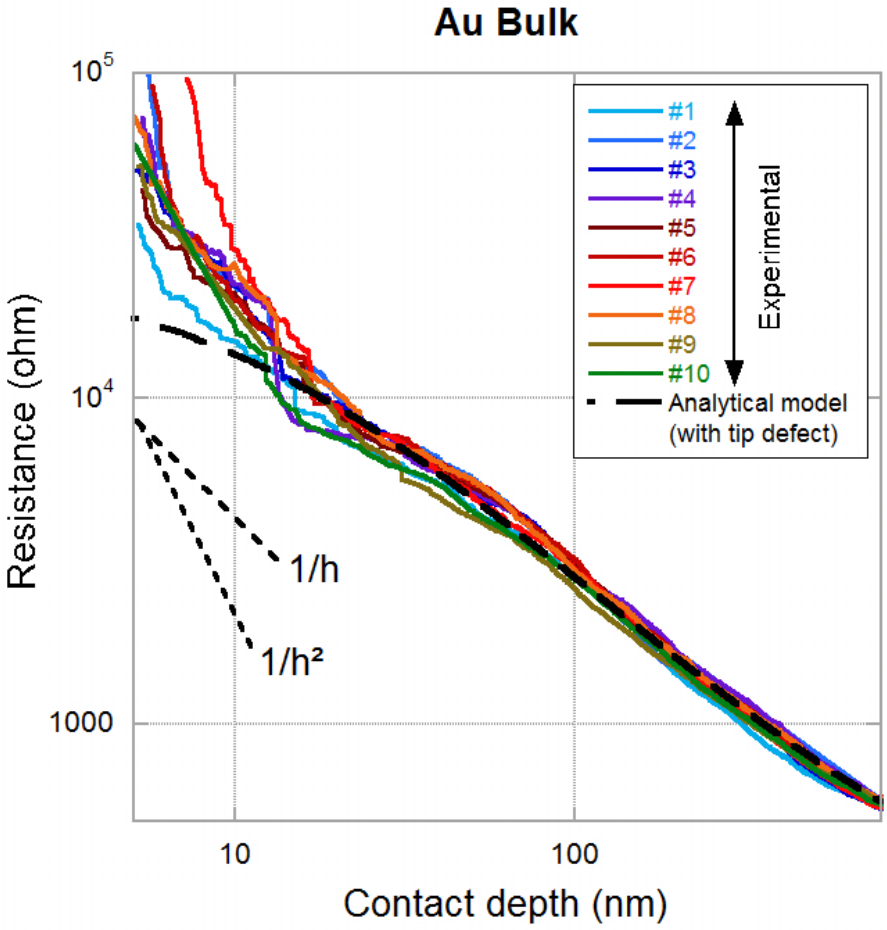

Figure 6.13: Comparison between experimental resistance-versus depth-curve (logarithmic scale) during indentation of bulk Au single crystal with BDD tip and the analytical model.

- This model only applies to the diffusive regime, were electronic transport is represented as continuous. For small contact depth, the electron mean free path λ can be of the same order than the contact radius r_c. As a result the Sharvin's component of the resistance, which accounts for a ballistic electronic transport, is not negligible anymore (equation 6.14, with λ the mean free path [81]). The Maxwell expression for the tip spreading resistance $R_{spreading-tip}$ does not apply anymore, and must be replaced by a resistance expression which takes into account the Sharvin's resistance (see paragraph 2.1.2, page 55). This adds a new resistance dependence in $1/h^2$. This is in good agreement with the trend of the resistance curve at small depth, which roughly follows a $1/h^2$ law.

$$R_{Sharvin} = \frac{4\rho\lambda}{3\pi r_c^2} \tag{6.14}$$

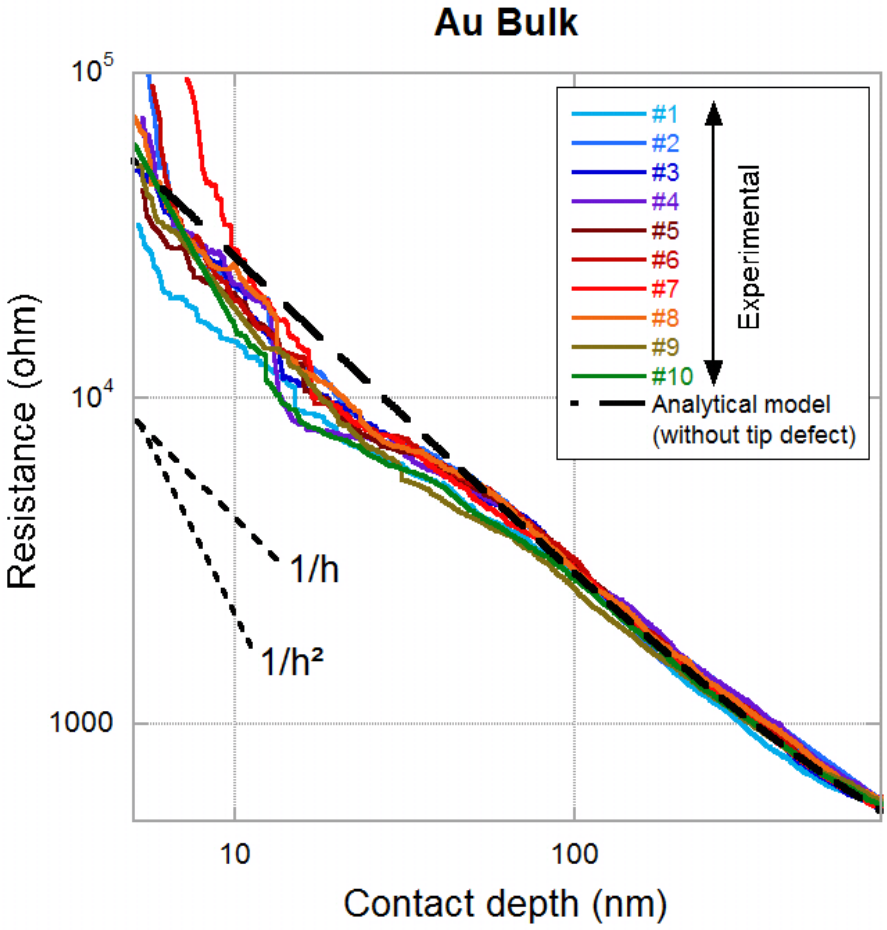

Figure 6.14: Comparison between experimental resistance-versus-depth curve (logarithmic scale) during indentation of bulk Au single crystal with BDD tip and the analytical model without taking into account the tip defect height h_0.

An other limitation of this analytical model comes from the expression of the tip spreading resistance $R_{spreading-tip}$ (equation 6.8). As already discussed, the part of the tip inside the sample is not taken into account. Thus, inside the sample the poorly conductive tip material (BDD) is neglected and assimilated to the highly conductive sample material (Au). In fact, this poorly conductive part is expected to affect the current lines coming from the tip to the sample. Thus, during indentation, current lines are expected to be localised at the periphery of the contact instead of being homogeneously distributed over the projected contact area, as schematized in figure 6.15.

The expression for the spreading tip resistance $R_{spreading-tip}$ must then be adjusted to take into account the particular shape of the current line at the contact. To compute the spreading resistance of square and circular ring contacts, Nakamura [78] has proposed to divide the spreading resistance of the corresponding square or circular contact by a shape factor SF. This

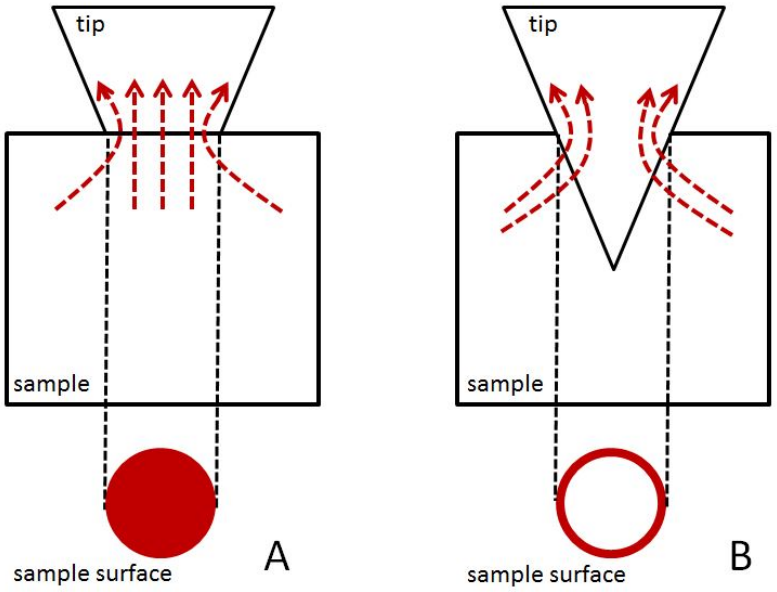

Figure 6.15: Current line distribution for a conical poorly conductive tip on a highly conductive sample: A: as simplified for the analytical model B: as expected experimentally.

shape factor is supposed to depend on the parameter t/r_c, with t the thickness of the ring and r_c the contact radius. Figure 6.16 shows the evolution of SF versus t/r_c. The shape factor for circular and square rings are too close to be separately drawn in the figure. We can assume that the shape factor for a triangular ring, as in the case of a Berkovich tip, is also close to the values computed by Nakamura.

In that case, the total measured resistance is given by equation (6.15), with $A = R_{series}$ and $B = \frac{4\rho_{tip}d_0^2}{\sqrt{3}c_0^2}$.

$$R_{measured} = A + \frac{B}{SF(h_c + h_0)} \tag{6.15}$$

However, the evolution of the parameter t/r_c during indentation is unknown and the value of the shape factor cannot be easily given by analytical expression. This brings the motivation to use a numerical model to simulate the current line distribution at the contact, as proposed in section 6.4.4 (page 201).

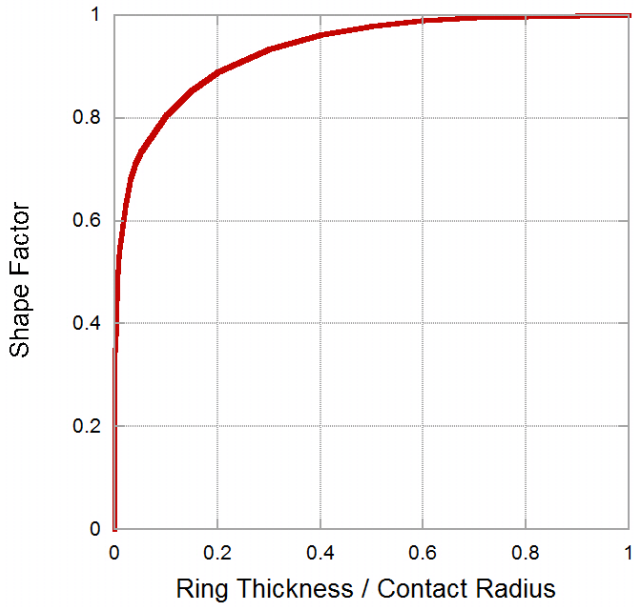

Figure 6.16: Shape factor FS versus the ring thickness over the contact radius, extracted from Nakamura [78].

6.4.3 The "RS" index

In this section, the "RS" index is introduced. The contact stiffness S_c is known to be related to the contact radius r_c by Sneddon's equation (6.13). The contact radius r_c is related to the contact depth and the tip defect height by equation (6.11).

Using equation (6.9) for the expression of the resistance, the contact stiffness multiplied by the resistance, called the "RS" index, can simply be expressed by equation (6.16), with $A' = 2E^* R_{series}$ and $B' = \frac{8E^* A_{tip} \rho_{tip} d_0^2}{SF\sqrt{3}c_0^2}$.

$$RS = A' r_c + B' \tag{6.16}$$

For a bulk material such as the bulk Au single crystal, the reduced modulus E^* is expected to be constant during indentation. Provided that the shape factor SF is constant during indentation, the A' and B' coefficients are constant.

Figure 6.17 provides example of "RS" index drawn versus the contact radius for nanoindentation data of bulk Au single crystal. RS curve displays a large linear domain, which validates the fact that A' and B' coefficients are constant. This shows that in the particular case of bulk Au single crystal indented by a BDD tip, the shape factor SF can be considered as constant during indentation. A linear fit gives access to A' and B' coefficients.

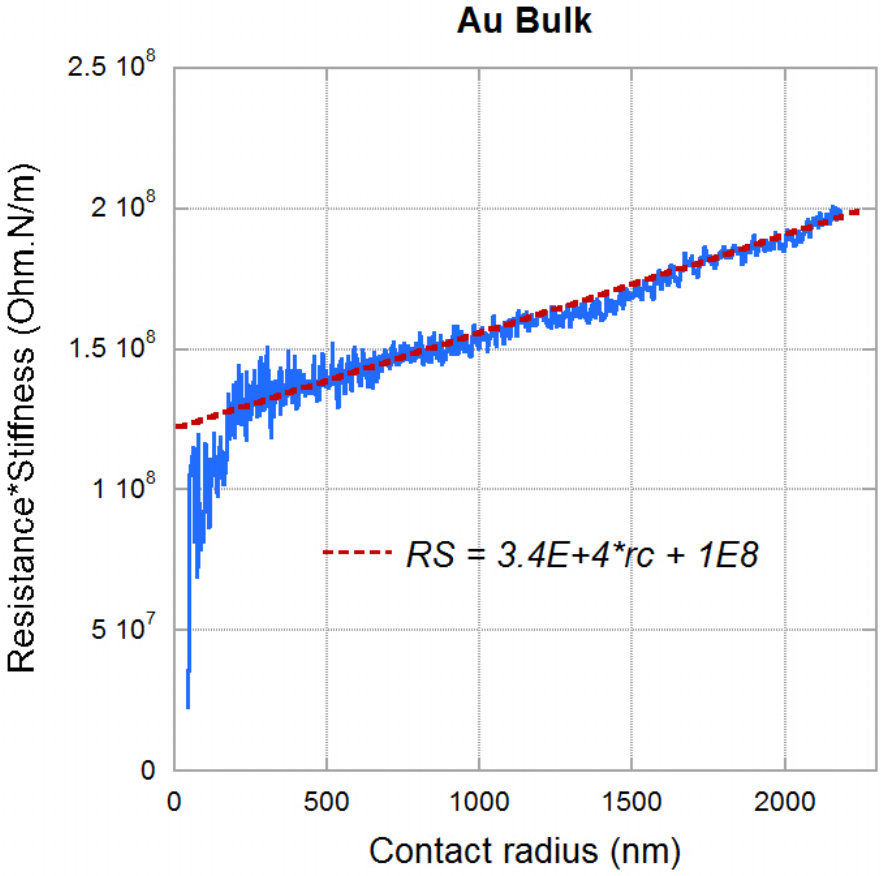

Figure 6.17: RS index from nanoindentation data of bulk Au single crystal indented by a BDD tip

In the case of bulk material with constant reduced modulus E^*, the fit on the "RS" quantity is totally equivalent to the fit previously performed on the $R_{measured}$ versus $\frac{1}{h_c+h_0}$ curve (paragraph 6.4.2, page 192). However, the RS index is more visual and can be used to immediately verified that RS is a linear function of the contact radius r_c. This validates immediately that the shape factor SF can be considered as constant, and that no contaminant layer brings additional contribution to the expression of the resistance.

This index has also the advantage to be the product of raw resistance and raw mechanical data, and thus can be computed without the use of any mechanical or electrical model.

6.4.4 Numerical model

A numerical approach has started to be developed within the frame of this work, using ABAQUS software (3D modelling with standard formulation and electrical-thermal-mechanical coupling). For simplification reasons, this model is based on the indentation of a perfectly plastic gold

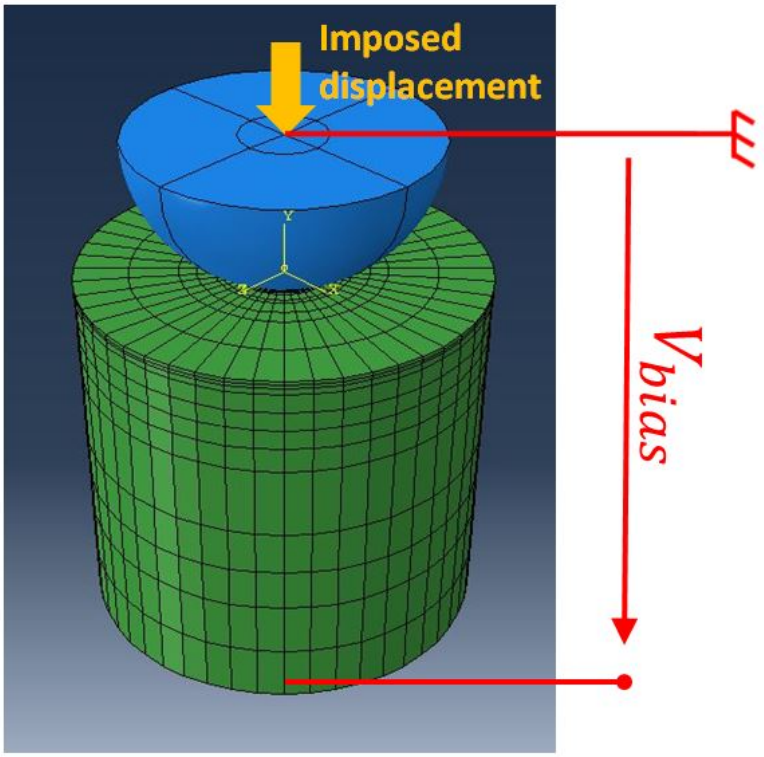

Figure 6.18: Abaqus modelling of thee electronic transport during electrically coupled nanoindentation.

sample with spherical BDD tip, instead of a Berkovich tip (figure 6.18). This model only takes into account the diffusive regime where Maxwell equation applies.

Elements used for the seeding of both tip and material parts are Q3D8, which brings two additional freedom degrees (electric potential and temperature) compared to standard 3D mechanical simulations.

The thermal modelling has not been studied in this model. For simplification, both tip and sample thermal conductivities have been set to infinity, and constant thermal boundaries conditions have been chosen.

During the simulation, a 10 V bias is first applied between the tip and the sample. A mechanical displacement is then imposed to the tip.

The interface electrical conductivity between the tip and the sample has been chosen to be infinite when the two parts are distant from less than 1 nm and to be zero otherwise. In contact the resistance is then only due to the sample and tip resistivities and to the shape of the current lines. Sample and tip resistivities were set to $2.2 \cdot 10^{-6}$ Ω.cm and 2 Ω.cm respectively.

Post treatment using a Python subroutine provides load, displacement, contact area and electrical current computation.

The equipotential lines can be represented at the contact (figure 6.19). Due to the high resistivity of the BDD tip compared to the gold sample, the potential drop mostly occurs within the tip. For a 10 V bias applied between the tip and the sample, the potential drop at the contact is estimated around 1-2 V ($\sim$ 10-20 % of the applied bias).

Figures 6.19 A and B show the amplitude of the electrical current density on the surface of the BDD tip in contact with the sample. At the beginning of the indentation (figure 6.19 A), all the current lines concentrate into a single spot, which corresponds to the mechanical contact area. While further indenting (figure 6.19 B), the current lines evolve and concentrate into a ring corresponding to the periphery of the projected contact area between the tip and the sample.

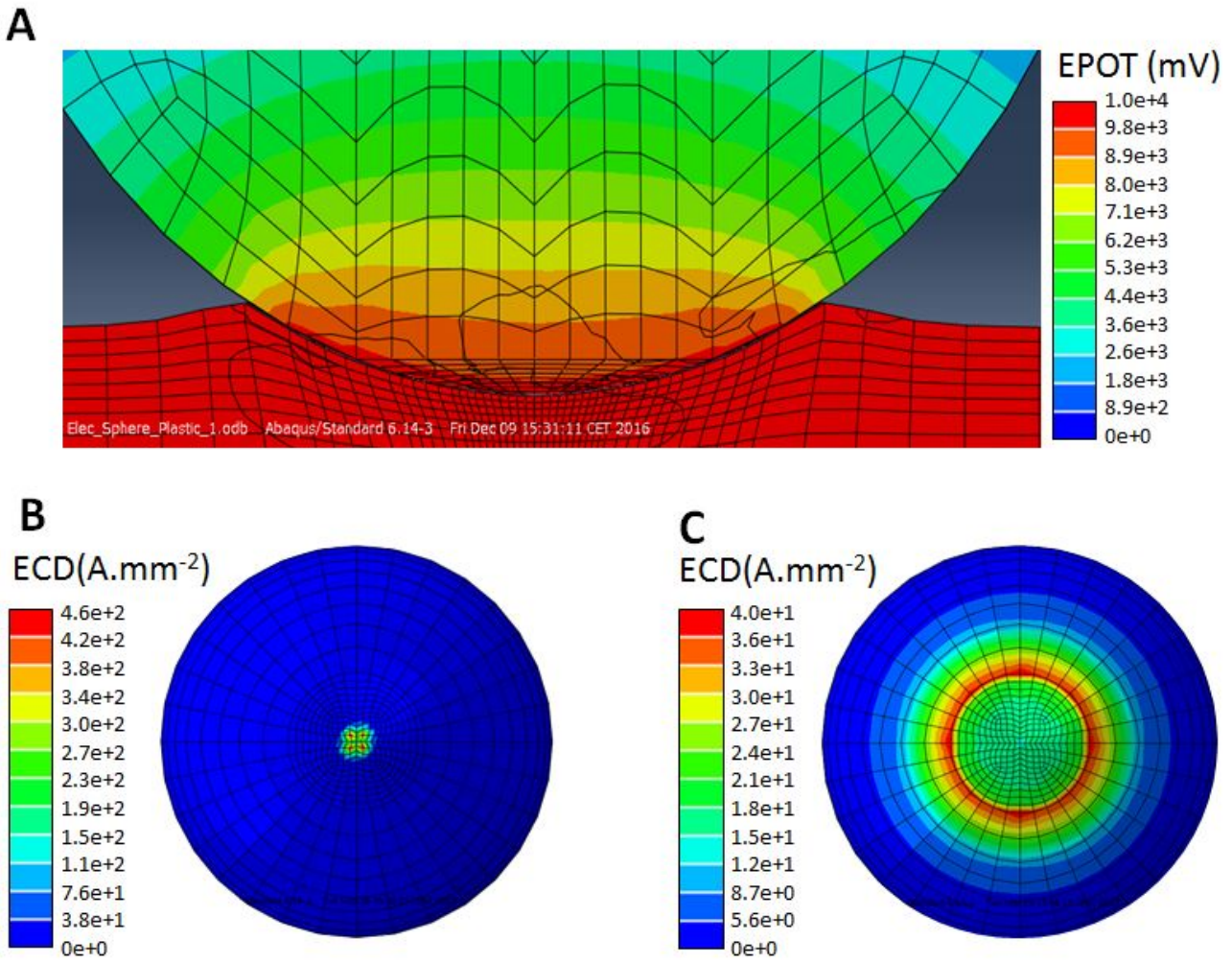

Figure 6.19: Representation of the equipotential lines during indentation of a gold single crystal by a BDD tip (A) and electrical current density representation on the spherical tip at the beginning of the indentation (B) and during the indentation (C)

.

Figure 6.20 shows the resistance-versus-depth curve from numerical modelling. By considering a spherical tip indenting a sample with contact depth h_c, the tip spreading resistance can be simplified by considering that the spherical tip is truncated, with the length of the missing part of the tip corresponding to the contact depth h_c (figure 6.21 A). This assumption is equivalent to the assumption made in section 6.4.1 (page 189) for a pyramidal tip, by using the Schneegans expression for the tip spreading resistance. In the case of a truncated sphere, the expression of the spreading resistance is given by equation (6.17), with R the tip radius.

$$R_{spreading-tip} = \frac{\rho_{tip}}{\pi R} \cdot \text{argth}(\frac{R - h_c}{R}) \tag{6.17}$$

The analytical model clearly leads to resistance values much lower than the numerical model. This was expected since the analytical model does not take into account the effect of the part of the tip which is inside the sample (figure 6.21 B).

This case shows the interest of using a numerical approach for the understanding of resistance-versus-depth curve. However, further effort are needed to adapt this model to the case of the indentation with a Berkovich tip and to compare numerical results with the experiment.

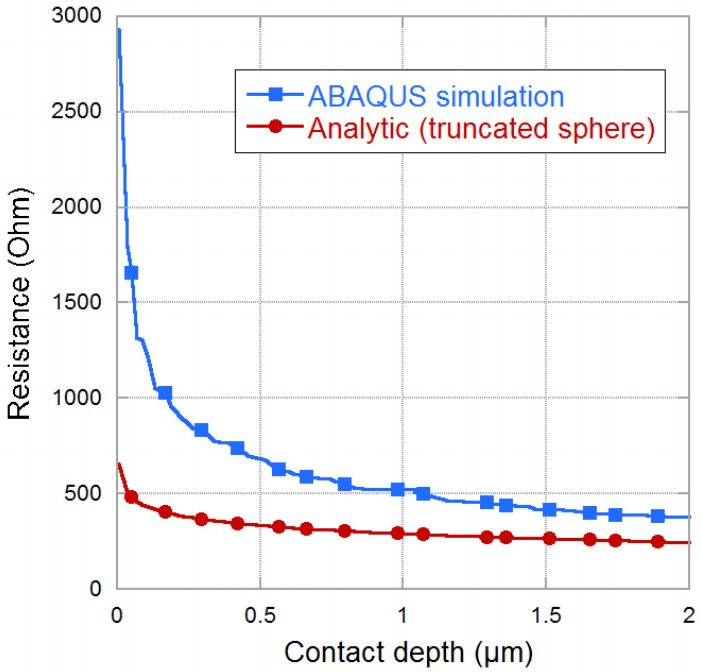

Figure 6.20: Resistance-versus-contact depth curve from ABAQUS simulations and analytical expression for a truncated sphere.

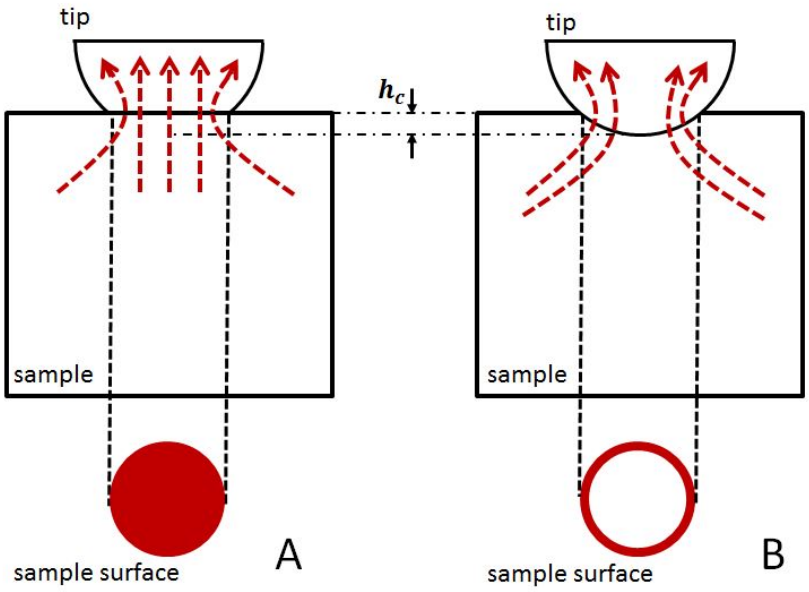

Figure 6.21: A: Schematic of a truncated spherical tip with the length of the missing part corresponding of the contact depth h_c and B: Schematic of the equivalent spherical tip, with a length h_c inside the sample.

6.5 Toward electrical contact area monitoring

6.5.1 Calibration sample

In the last section, an analytical expression of the measured resistance (equation 6.18) has been successively given, with good agreement with the experimental results. The measured resistance depends only on two coefficients A and B/SF and to the contact depth or contact radius.

In section 6.4.2 (page 192), A and B/SF have been determined on the bulk Au single crystal (with $SF = 1$). Bulk Au single crystal can be seen as a calibration sample for electrical measurements. A and B/SF values were found to be 250 Ω and $2.6 \cdot 10^5$ Ω.nm respectively. These coefficients depend on the experimental set-up so they are supposed to remain unchanged during indentation of other samples.

$$R_{measured} = A + \frac{B}{SF(h_c + h_0)} \tag{6.18}$$

Once these set-up coefficients are known, they can be used whatever the indented material. In that case, the measured resistance $R_{measured}$ only depends on the contact radius or the contact

depth ($r_c = A_{tip} \cdot (h_c + h_0)$). This means that the electrical contact area can be directly computed from resistance monitoring.

The hidden assumption here is that we consider that the shape factor SF does not change when indenting a sample different from the calibration sample. This assumption seems reasonable if the investigated sample has a resistivity of the same order of gold resistivity, and much lower than the resistivity of the BDD tip.

6.5.2 Contact area monitoring: application to a Au thin film

In this section, an attempt is made to compute contact area from resistance measurements during indentation of a gold thin film.

Electrical measurements are performed during indentation of a 200 nm polycrystalline Au thin film. Maximal indentation depths are chosen to be 50 nm, 100 nm and 150 nm. Figure 6.22 provides examples of resistance-versus-depth curves obtained during nanoindentation.

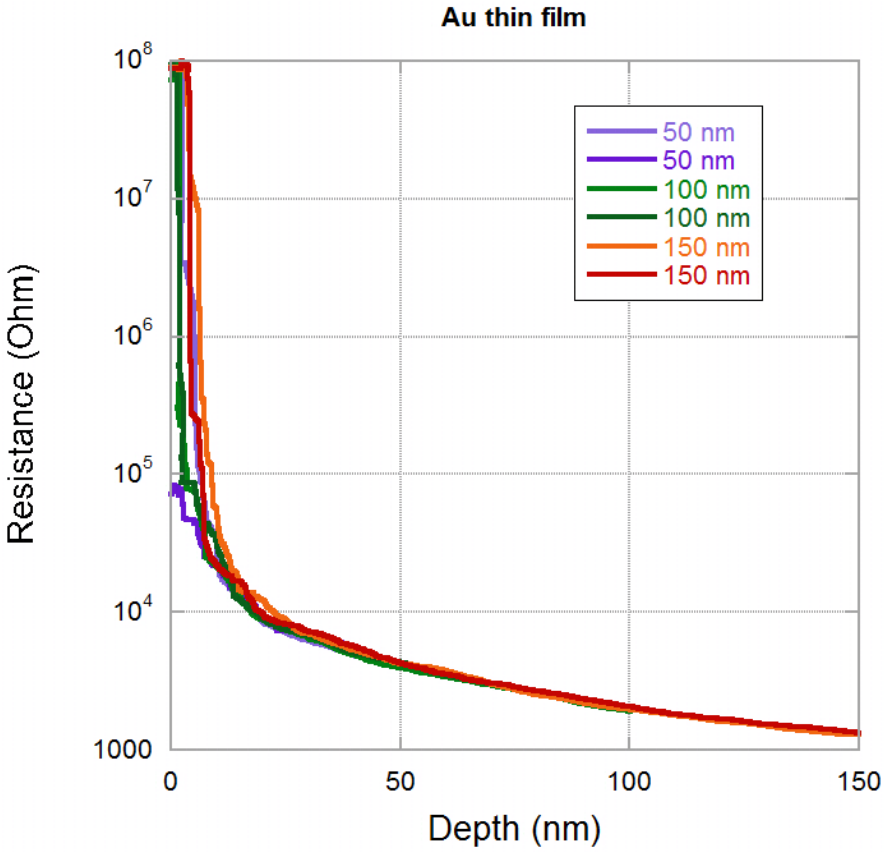

Figure 6.22: Example of resistance-versus-depth curves during indentation of a 200 nm Au thin film with a BDD tip.

The analytical expression of equation (6.18) - with A and B/SF previously calibrated on the

bulk Au sample - is then used to compute the electrical contact area from the resistance curves. For each maximal depth, the contact area-versus-depth curves are drawn in figure 6.23 for two selected indents (corresponding to the two extrema in terms of size of the contact area). For comparison, post mortem AFM measurements of the residual imprint size are performed for each indent, and added to figure 6.23.

Really good agreements are found between contact area computed from electrical data and post mortem AFM measurements.

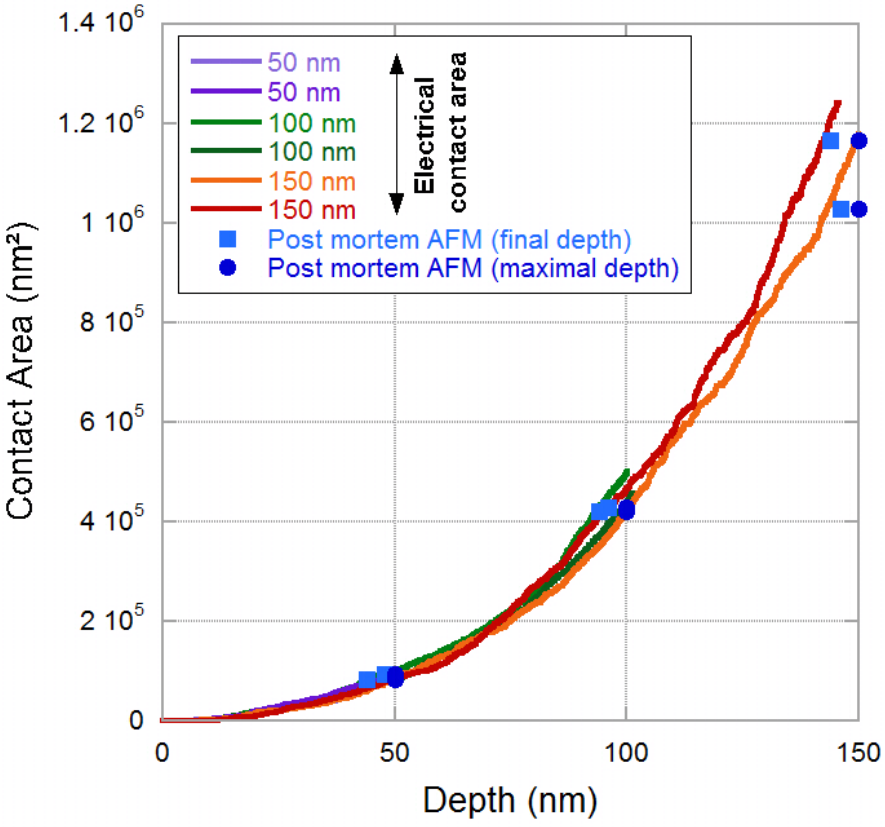

Figure 6.23: Contact area computed from electrical measurements during indentation of a 200 nm Au thin film with a BDD tip and corresponding post mortem AFM measurements. Post mortem AFM are given versus the maximal indentation depth (circle) and versus the final depth after unloading (square), in order to take into account the elastic spring back.

Note that indents on Au thin film exhibit strong pile-up (figure 6.24), contrary to indent on the calibration sample (bulk Au), which exhibit sink-in. Thus, electrical contact area during indentation is promising and seem to be a powerful tool for contact area computation, even for samples with a rheology different from the rheology of the calibration sample.

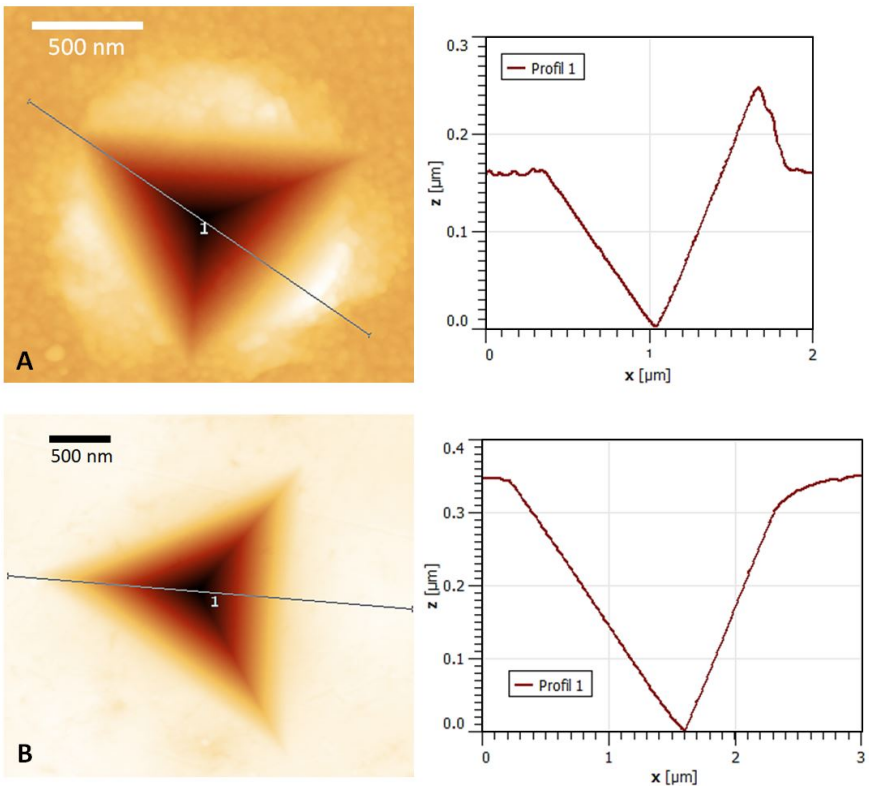

Figure 6.24: AFM image of a residual imprint on A: 200 nm Au thin film (pile-up) and B: bulk Au single crystal (sink-in).

6.5.3 Conclusion on electrical contact area monitoring

Electrical contact area monitoring is shown to be very promising. Nevertheless, the investigated material in this section (Au thin film) is the same as the material used for calibration (bulk Au single crystal). Using a material different from the one used for the calibration can bring new issues:

- The presence of an oxide layer can introduce a specific contact resistivity, which has to be taken into account in the analytical expression of the resistance.
- The shape factor SF can be different from the the shape factor of the calibration material.
- The electrical contact can be non-ohmic, as seen in section 6.3.2 (page 187) for Al and Cu samples. The analytical expression for the resistance is then erroneous.

6.6 Effect of an oxide layer

6.6.1 Resistance-versus-depth curves

The effect of an oxide layer on resistance measurements has been studied on alumina thin films. Several oxide thicknesses of alumina have been assessed: from 10 nm to 40 nm. As mentioned in paragraph 6.2.4 (page 182), samples are constituted of Al_2O_3 / Al / Si / SiO_2 stacks, with Al_2O_3 deposed by Atomic Layer Deposition (ALD) (figure 6.25). These stacks were elaborated within the frame of the PhD of Mercier [93, 203]. A summary of these samples is given in table 6.3.

Sample description	Oxide nature and size
10nm Al_2O_3 + 540 nm Al + SiO_2(500nm) + Si(725µm)	6-7 nm oxide (ionic conduction)
20nm Al_2O_3 + 540 nm Al + SiO_2(500nm) + Si(725µm)	18-20 nm oxide (ionic conduction)
30nm Al_2O_3 + 540 nm Al + SiO_2(500nm) + Si(725µm)	29-33 nm oxide (ionic conduction)
40nm Al_2O_3 + 540 nm Al + SiO_2(500nm) + Si(725µm)	38-42 nm oxide (ionic conduction)

Table 6.3: Summary of investigated thin films.

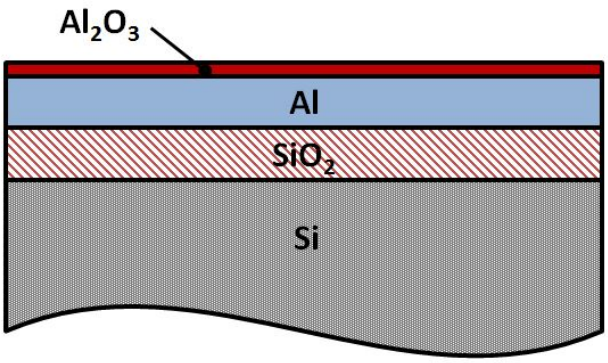

Figure 6.25: Schematics of the Al_2O_3 + Al + Si + SiO_2 stacks

Nanoindentation tests have been performed with the BDD tip. The resistance has been measured during indentation with the ResiScope for bias set-point from 0.5 V to 10 V. Resulting resistance-versus-depth curves are shown in figure 6.26.

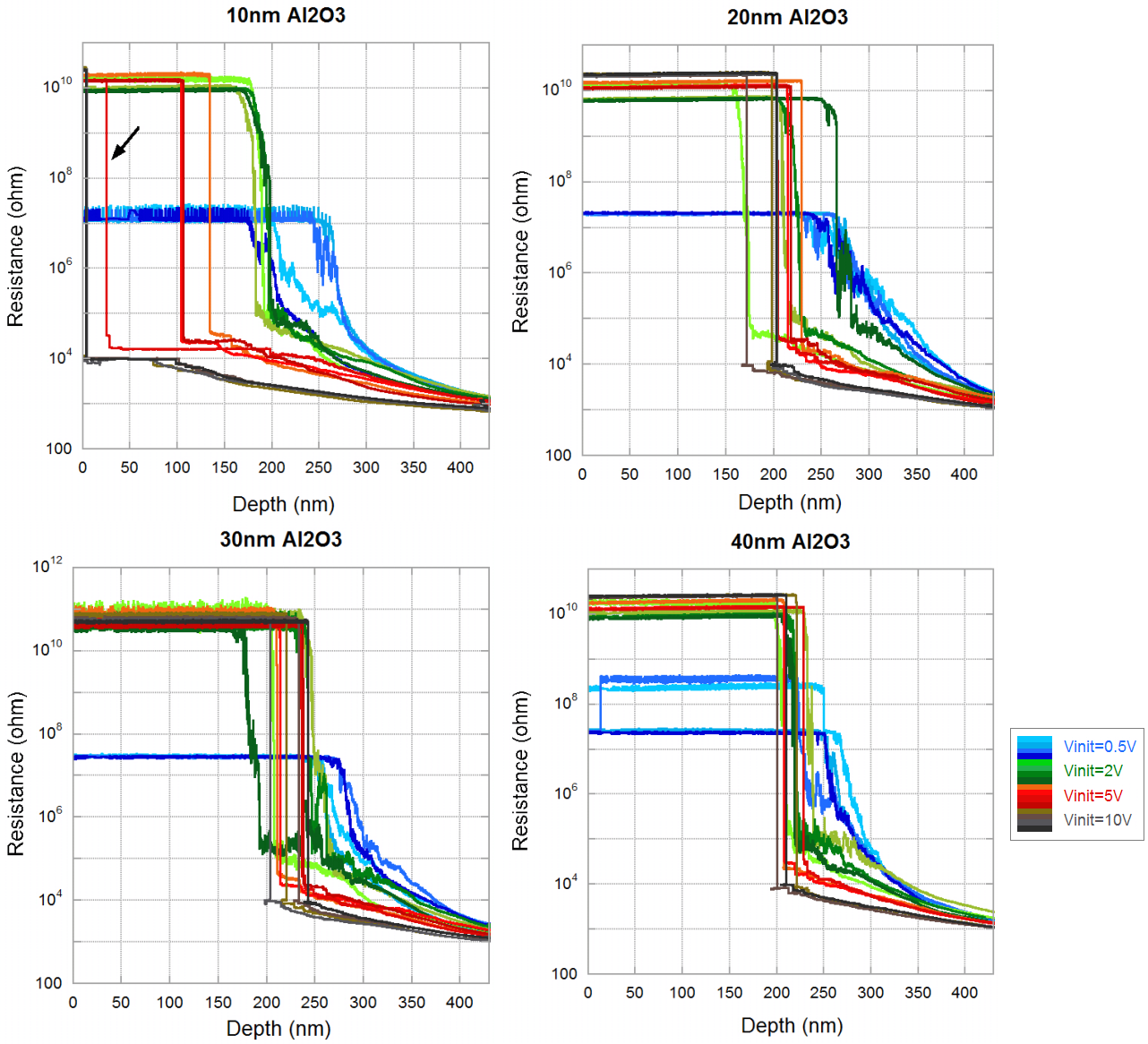

Figure 6.26: Resistance-versus-depth curve during indentation of aluminum samples with different oxide thicknesses.

Resistance values clearly depend on the polarisation bias, which shows that the contact is not ohmic. The shape of resistance curves is similar to that measured on the bulk Al single crystal (figure 6.3, page 185) and can be characterized as follows:

1. A constant resistance plateau which means that the ResiScope does not detect any signal. The electrical contact is not established: the resistance is too high to be measured.

2. Then resistance decreases, either with a sudden drop (for bias set-point $V_{bias} \geq 2V$) or gradually (for bias set-point $V_{bias} \leq 2V$). When the decrease is gradual the resistance can unexpectedly increase before decreasing again.

3. Finally the resistance decreases more slowly with almost no unexpected resistance in-

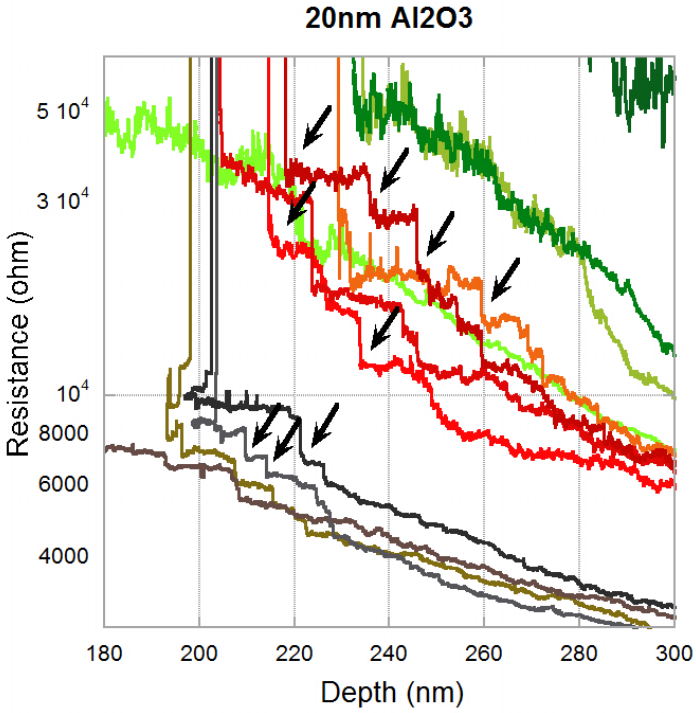

Figure 6.27: Resistance decrease "by step" during indentation of 20nm $Al2O_3$ on aluminium at 5V and 10V of polarisation bias.

crease. The resistance dependence on polarisation bias diminishes with increasing indentation depth. At the beginning of this step, resistance curves at 5V and 10V of polarisation bias are characterized by a decrease by steps (figure 6.27).

6.6.2 Correlation between mechanical events and electrical events

As already stated, the electrical contact establishment is characterized by two behaviors: a sudden resistance drop or a gradual resistance decrease. But whatever the oxide thickness or polarisation, for these two behaviors load-displacement curves show that a severe oxide layer fracture is made much before the electrical contact establishment, or after for the 10nm sample at 10 V bias (figure 6.28). An exception is found for the 10nm sample at 10 V bias, where the electrical contact is established after this oxide layer fracture.

- When the electrical contact is not established before this oxide fracture event, most of the time there is no signature of this fracture in the resistance curve, as shown in figure 6.29 A. A sudden electrical drop correlated to this first fracture event was only seen for one indentation test (figure 6.29 B), corresponding to a test at 5 V bias on the 10nm sample, indicated by a black arrow in figure 6.26.

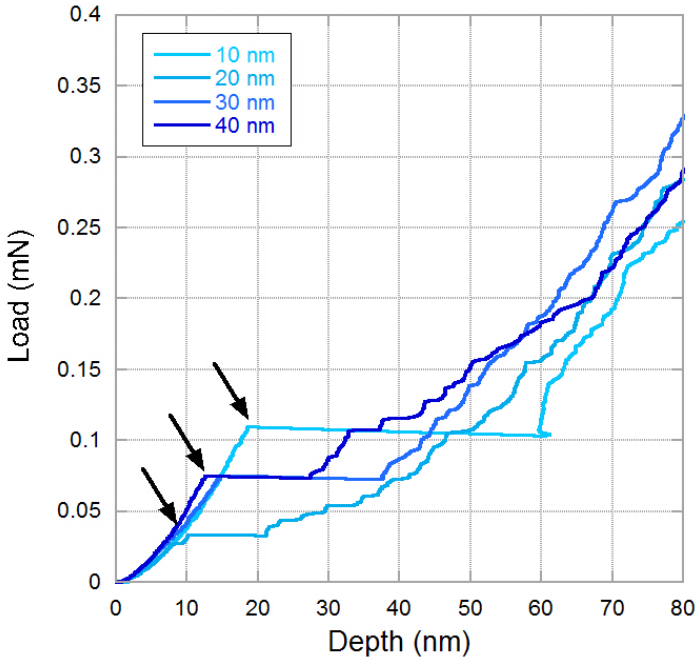

Figure 6.28: Load-displacement curves during indentation of aluminium thin film with different oxide thicknesses (0.5 V set-point bias). Evidence of oxide layer fracture occur around 10-20 nm of indentation depth (black arrow).

◦ When the electrical contact is established before the oxide fracture (10nm sample at 10 V bias), this mechanical event is combined with a sudden resistance change (black arrow in figure 6.30 A).

Other oxide fracture may occur after this first oxide fracture and they are often correlated with a resistance change, but which can be either a resistance increase or a resistance drop (figure 6.30). For largest indentation depth, mechanical events are only slightly visible on the load-displacement curves, although they are combined with a strong electrical signature (figure 6.30 C). This shows the interest of following mechanical events with electrical signature: the resistance is sensitive to mechanical events even for large indentation depth, where the signature of such events is less visible on mechanical curves.

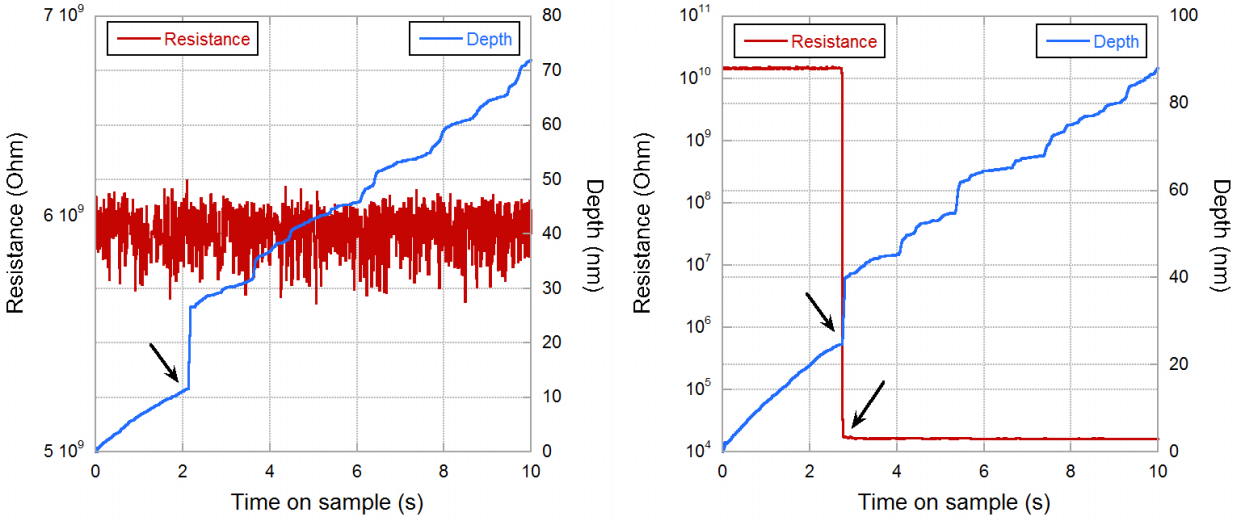

Figure 6.29: Evidence of oxide fracture mechanism on depth-versus-time curve, showing: (A) no electrical signature in resistance-versus-time curve and (B) correlation with a sudden resistance drop in resistance-versus-time curve.

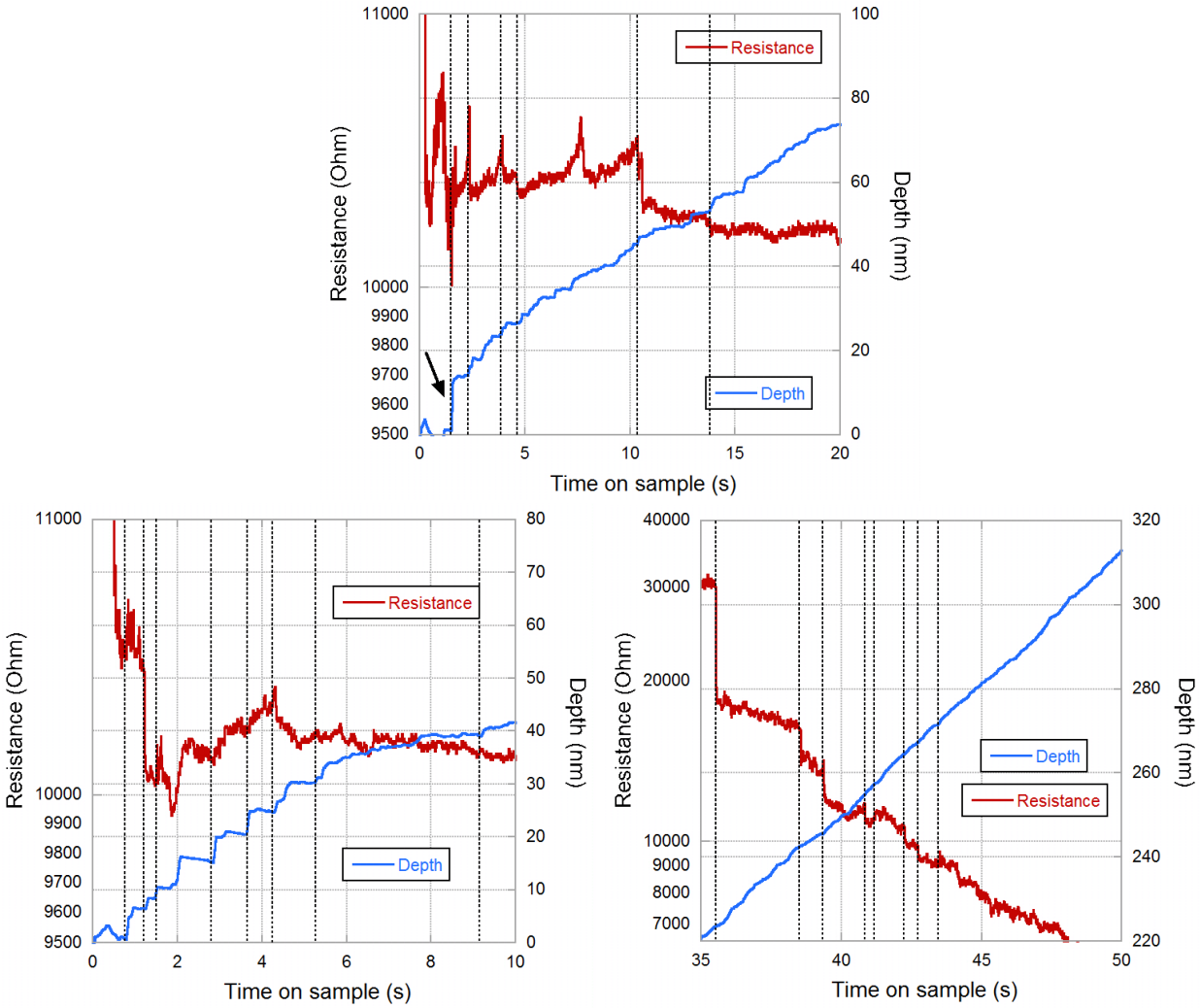

Figure 6.30: Correlation between mechanical events and electrical events (dotted lines).

6.6.3 Different behaviors for electrical contact establishment

As previously shown, two behaviors are observed for electrical contact establishment: a sudden resistance drop (for $V_{bias} \geq 2V$) and a gradual resistance decrease (for $V_{bias} \leq 2V$). This suggests that two different mechanisms are involved:

- **For low bias set-point**, the electrical contact is set progressively. This suggests that the mechanical contact between the underlying conductive aluminium and the BDD tip is set progressively. The progressive resistance decrease always happens after the first oxide layer fracture. The indentation depth (200-250 nm) at which this resistance decrease occurs seems roughly independent from the oxide thickness. This corresponds to a load onto sample of 1.5-2.5 mN.

  This behavior seems coherent with the mechanism described by Mohamed and Washburn [96] for electrical contact between two metal and their oxide under loading. If the oxide film is harder than the metal, Mohamed and Washburn explained that dislocation pile-ups at the metal-oxide interface are relieved by a crack opening in the oxide, normal to the interface. Free metallic areas overlap then one above the other, provided that the load is sufficient for metal extrusion to occur through the created gap. This mechanism was experimentally verified by Le *et al.* [94, 95].

- **For high bias set-point**, the resistance drops suddenly during electrical contact establishment. Figure 6.31 A shows the depth at which the resistance drop occurs versus the bias applied to the sample.

  For the 10nm sample, the indentation depth at which the resistance drops clearly depends on the voltage applied to the sample. Here we can suspect an electrical breakdown to occur through the oxide. Figure 6.31 B shows the maximal electric field applied to the sample for each set-point bias. This electric field is overestimated since the bias applied to the sample is not entirely applied to the contact, but a significant fraction of the voltage drop occurs within the poorly conductive BDD tip (as shown in section 6.4.4, page 201). The real electric field applied to the sample can roughly be estimated at 10-20 % of the maximal electric field. However, the applied electric field for large set-point bias corresponds to a high fraction of alumina dielectric strength (0.1-0.3 $MV.cm^{-1}$). The high electric field applied to the 10nm sample for a 10 V set-point bias explains why the resistance drops instantly at the beginning of the indentation in these conditions.

An other explanation to this sudden resistance drop involving an electrochemical reaction with the propagation of a reduction front will also be discussed in section 6.8.2 (page 227).

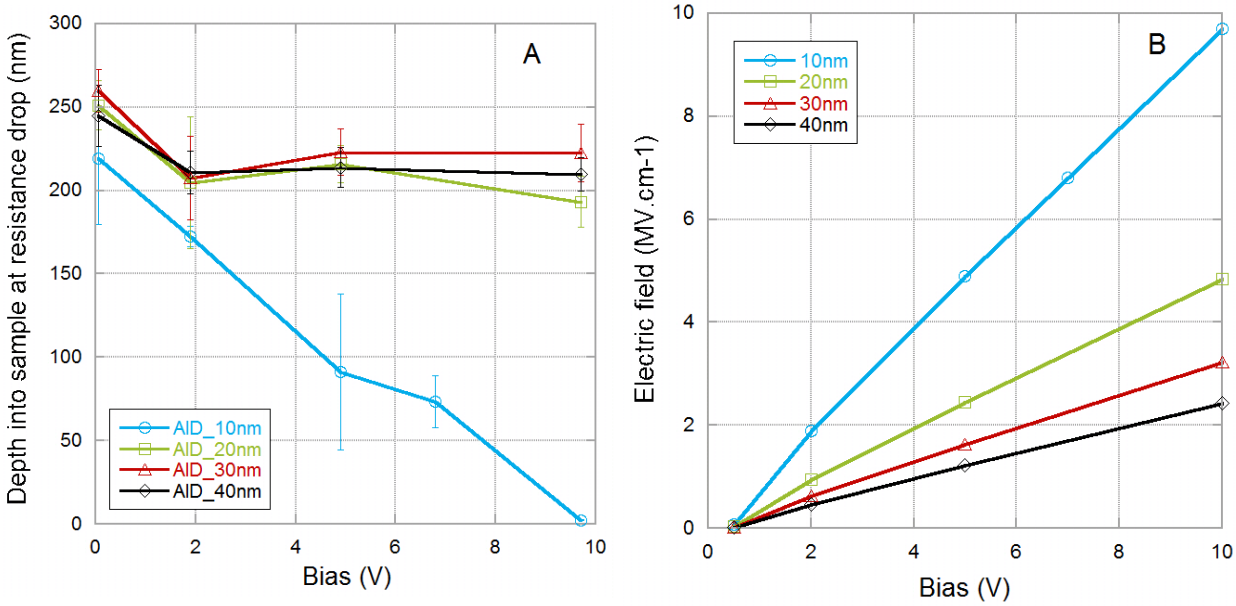

Figure 6.31: A:Depth into sample at first resistance drop versus the applied bias for sample with various oxide thicknesses. B: Electric field applied between the tip and the sample during resistance measurements versus the bias set-point.

6.7 Preliminary results for resistive indentation with WC tip

The relatively high resistivity of the BDD tip compared to the sample resistivity ($\sim 10^5$ times higher) might be an advantage: in that case both the resistance of the sample and the spreading resistance within the sample are negligible compared to the spreading resistance within the tip (section 6.4.2, page 192). This leads to the simple expression of the measured resistance $R_{measured}$ as given by equation 6.18, where the coefficients are only set-up dependant. Resistance measurements with a BDD tip are highly sensitive to a change in contact area. The computation of the contact area from electrical measurement can then be performed, as shown in section 6.5 (page 205).

However, resistance measurements with a BDD tip are not sensitive enough to follow mechanical mechanisms involved in highly conductive samples. In section 6.6 (page 209), it has been shown that electrical measurements with a BDD tip can follow mechanical mechanisms such as oxide

layer fractures. However, in that case the oxide layer is much more resistive than the BDD tip. If the aim is to monitor mechanical events within the conductive sample (plasticity, dislocations avalanche...), the use of highly conductive tips is required.

In that purpose, several resistance measurements during nanoindentation have been performed with a carbide tungsten tip (WC), using the ResiScope. Bulk Au, Al and Cu single crystals have been tested for several set-point biases. Since the WC tip is highly conductive, most of the applied bias between the tip and the sample is applied to the contact. This differs from measurements with the BDD tip, where a significant potential drop occurs within the BDD tip. Thus, only bias set-point lower than 5 V were chosen (respectively 0.5 V, 2 V and 5 V). In order to stay in the measurement range of the ResiScope, a 100 Ω resistor is added in series with the sample.

Results at room atmosphere are given in figure 6.32. Due to the low resistivity of the WC tip, resistance values are much lower than for measurements with the BDD tip. However, results strongly differ from what was already observed.

For bulk Au sample (6.32 A), resistance only slightly decreases with increasing indentation depth. Resistance curves are also characterized by strong resistance variations (successive increase and decrease).

These unexpected resistance variations are even stronger for the bulk Al sample (figure 6.32 B), with resistance increase up to four orders of magnitude.

Such resistance variations were also seen to a lesser extent with the BDD tip while indenting bulk Al single crystal (see section 6.3, page 183).

For the bulk Cu single crystal, these resistance variations are much less visible (6.32 C). However, the shape of the resistance-versus-depth curve is also unexpected, with almost constant resistance values while increasing indentation depth.

For all samples, the resistance appears to be bias dependant, with decreasing resistance for increasing bias.

Such severe resistance variations have been verified by using a Keihtley 6430 (SMU) (instead of the ResiScope), with positive and negative bias. This leads to similar features on resistance-versus-depth curves (figure 6.33).

These unexpected behaviors prevent any quantitative analysis of the resistance measurements as performed in section 6.5 (page 205).

In the next section, efforts are made to understand the phenomena leading to such electrical behaviors.

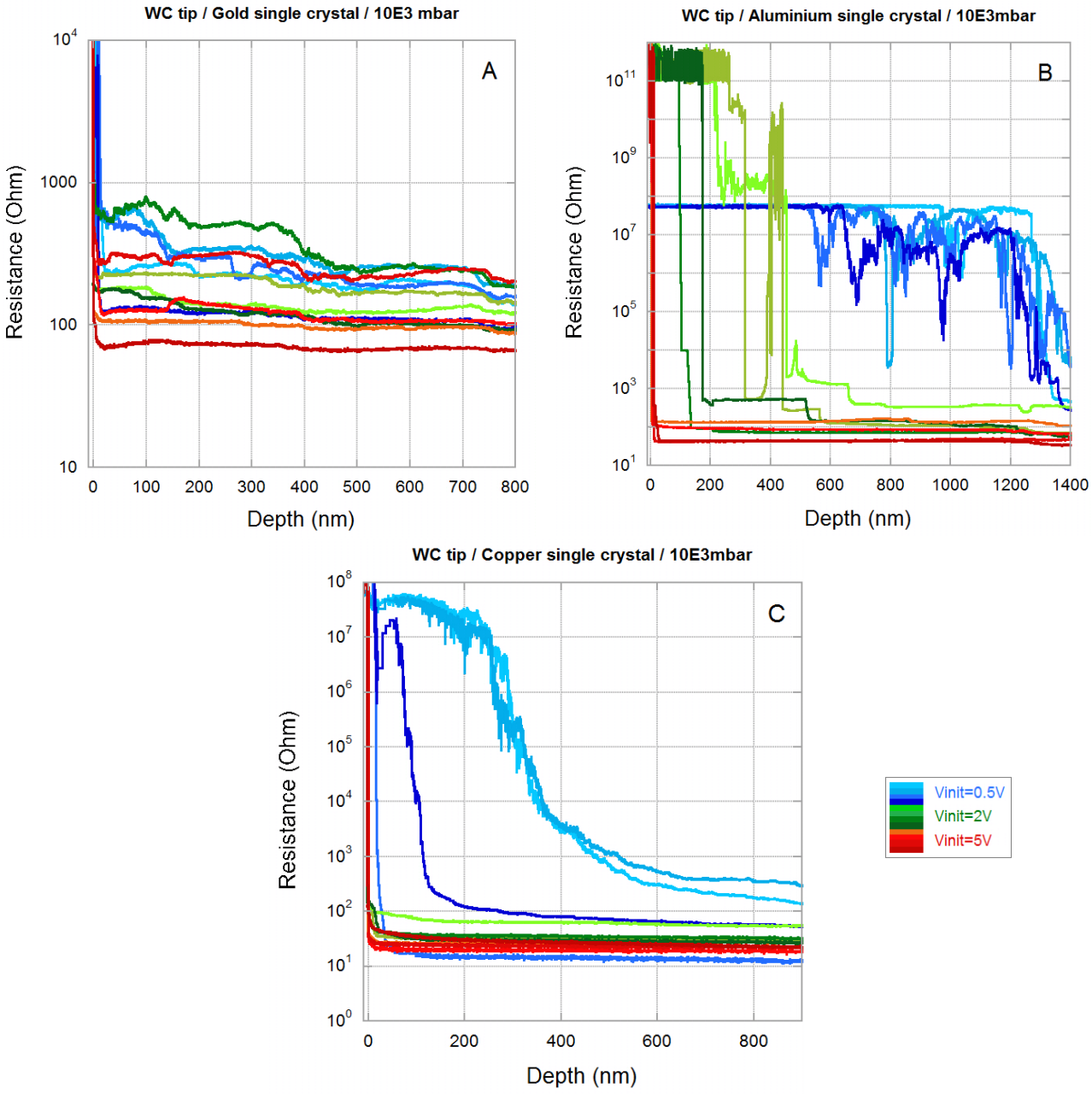

Figure 6.32: Resistance-versus-depth curves for WC tip and Au single crystal (A), Al single crystal (B) and Cu single crystal (C) at room atmosphere

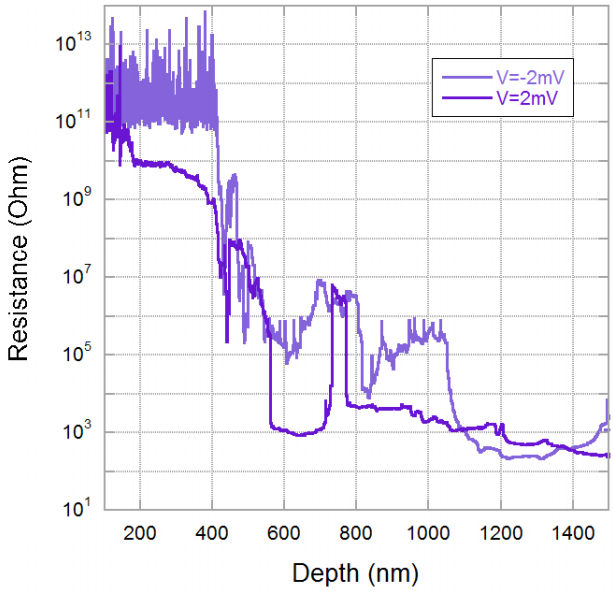

Figure 6.33: Example of resistance variations obtained while indenting bulk Al single crystal with a WC tip, measured with a Keihtley 6430 (SMU). Current density varies from $8 \cdot 10^5$ A.cm^{-2} to $3 \cdot 10^3$ A.cm^{-2} and indentation time is 80s.

6.8 Discussion on electrochemical mechanisms involved during nanoindentation

Electrical measurements allow the resistance monitoring during nanoindentation. Since the contact area between the material and the tip increases during indentation, a decrease of the resistance is expected while indenting. This general trend is obtained in most of the cases with BDD tip, and lead to the exploitations conducted in section 6.5 (page 205) for contact area computation.

However, unexpected increases and drops in resistance occur in several cases and especially with the WC tip, as shown in section 6.7 (page 215). These resistance variations look like the resistance changes observed by Bouchoucha *et al* [100] (figure 6.34) for a copper/steel contact, due to oxide growth. The difference is that in our case the resistance can increase by a factor 10^6 (against a factor 4 in the work of Bouchoucha *et al*), for a time constant two orders of magnitude lower (80 s against 60 mn). The current density involved in the work of Bouchoucha *et al* is also 3-4 orders of magnitude lower than the current densities involved within the frame of this work.

Thus, the unexpected resistance increases could be the signature of electrochemical phenomena which occur at the contact during indentation.

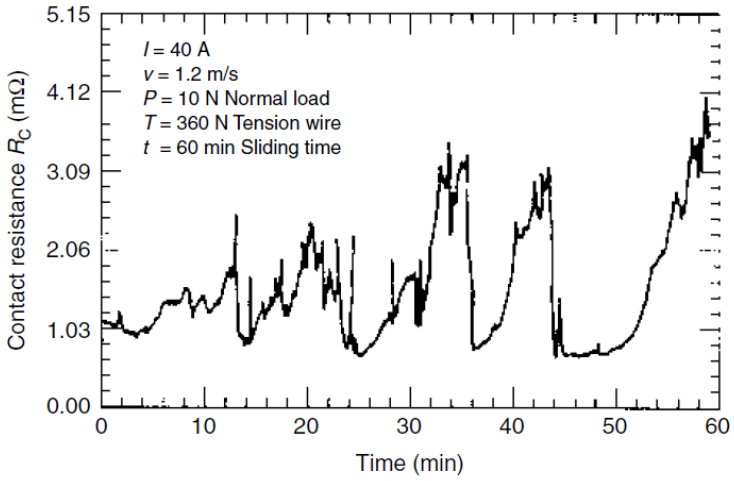

Figure 6.34: Evolution of electrical contact resistance versus time of a copper-steel contact, according to Bouchoucha *et al.* [100] (with current density around $2.6 \cdot 10^2$ A.cm^{-2}).

In order to investigate this phenomenon, the effect of the environment (respectively room atmosphere, intermediate vacuum (10^{-2} mbar) and high vacuum (10^{-6} mbar)) on resistive-nanoindentation is studied in this section. Indentations are performed with both BDD and WC tips on bulk single crystals of noble metal (Au) or natively oxidised metals (Cu (mixed conduction) and Al (ionic conduction)). Finally, several guidelines are given to understand these mechanisms from the electrochemical point of view.

6.8.1 Effect of the environment

Indentation with BDD tip

- Bulk Au single crystal

There is no visible change while indenting the bulk Au sample with a BDD tip at room atmosphere or under intermediate vacuum (figure 6.35). In both cases the resistance decreases with depth, following the reciprocal of the indentation depth, as detailed in section 6.4 (page 189). There is no unexpected increase in resistance, and thus no evidence of electrochemical processes in this case.

- Bulk Cu single crystal

For the Cu sample (figure 6.36), unexpected resistance oscillations appear under both atmospheres (room atmosphere and intermediate vacuum). These oscillations consist of a first drop in resistance, and then a succession of resistance oscillations, confined within a continuous

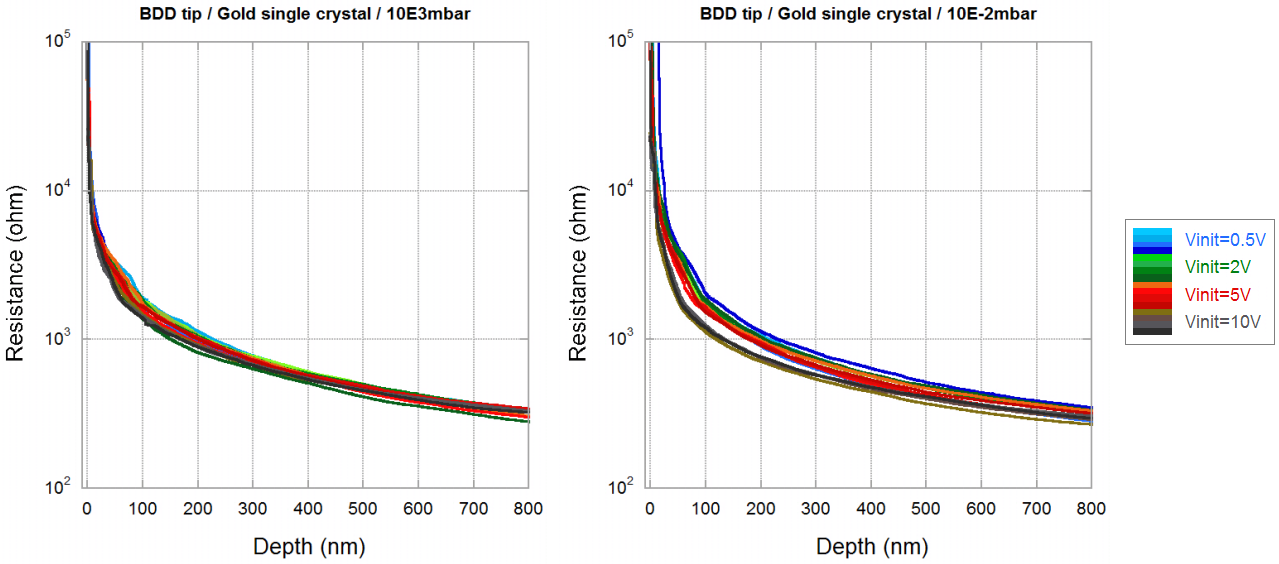

Figure 6.35: Resistance-versus-depth curves for BDD tip and bulk Au single crystal, under room atmosphere (left) and intermediate vacuum (right).

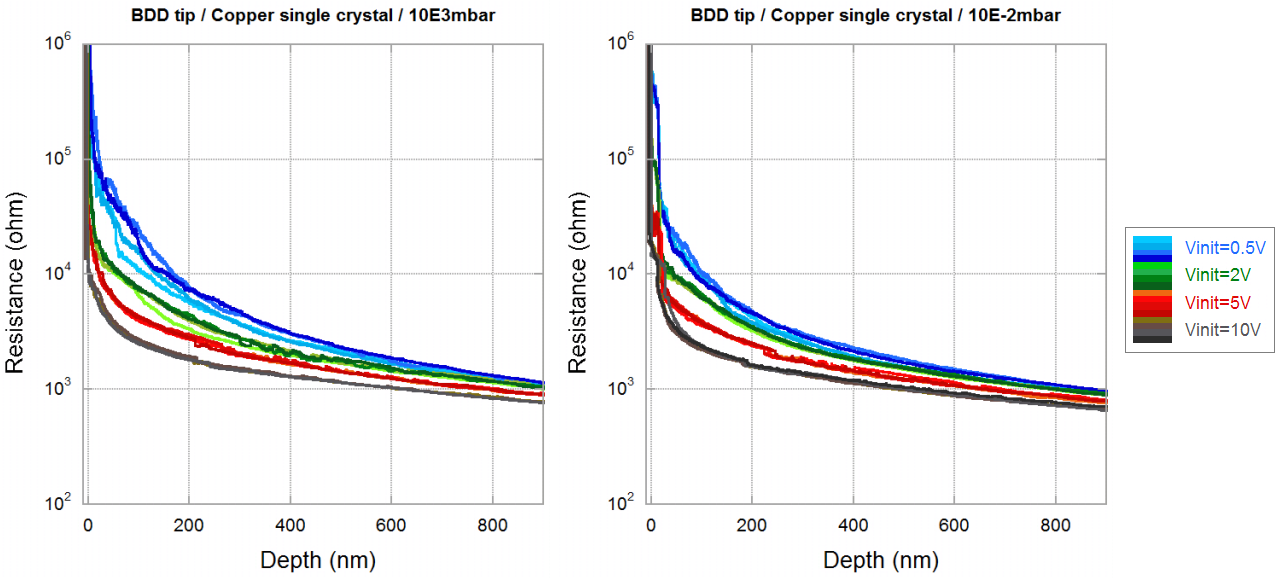

Figure 6.36: Resistance-versus-depth curves for BDD tip and bulk Cu single crystal, under room atmosphere (left) and intermediate vacuum (right).

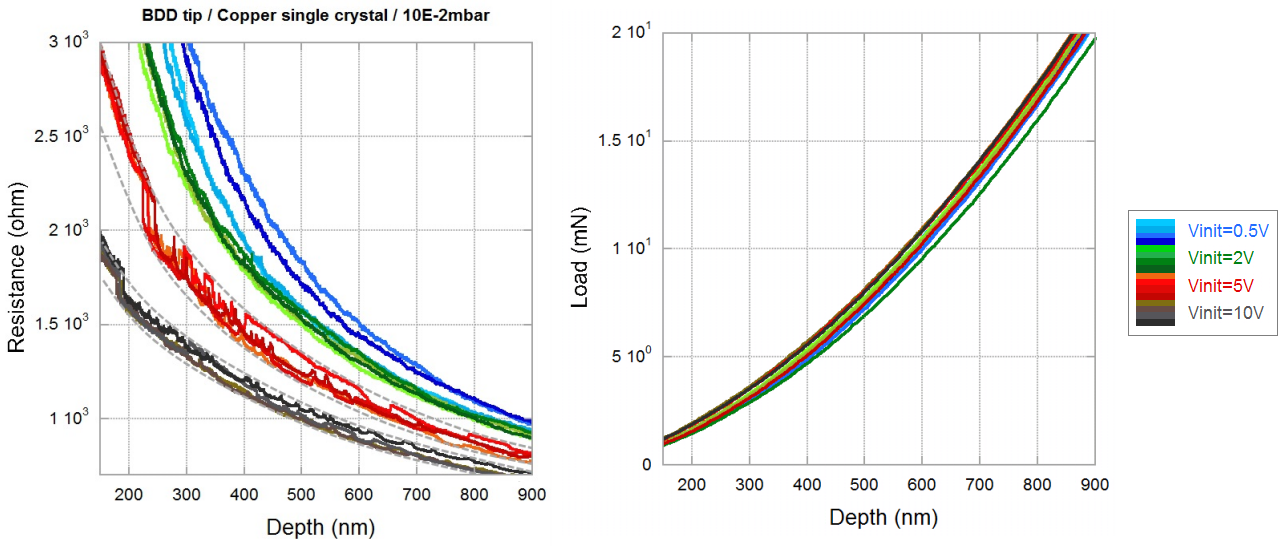

Figure 6.37: Zoom on resistance oscillation during indentation under intermediate vacuum of the copper single crystal by the BDD tip (left) and corresponding mechanical curves (right).

envelop (dotted line in figure 6.37 left). These relatively small resistance oscillations are not related to any mechanical discontinuities on the load-displacement curves (figure 6.37 right).

Figure 6.38 shows the effective bias applied to the contact when resistance oscillations first occur versus the penetration depth at which they occur. It is clear that the lower the applied voltage, the deeper in the sample resistance oscillations occur.

This phenomenon appears for any bias at room atmosphere, but it does not appear under intermediate vacuum for applied voltage lower than 0.7 V. Thus, the mechanism responsible for these resistance oscillations seems to be directly affected by the atmosphere.

- Bulk Al single crystal

For Al, resistance increases occur but in a different way (figure 6.39). Resistance variations are much larger, with amplitude of several orders of magnitude. These variations are also more noisy and are not confined within a continuous envelop, as for the Cu sample. Resistance drops and increases occur mainly at low polarization voltage, at the very beginning of indentation, and with a more random pattern. This phenomenon is amplified at room atmosphere. These resistance increases also appear for set-point bias of 2 V and 0.5 V at room atmosphere, whereas it only appears for 0.5V set-point bias under vacuum.

- Conclusion on indentation with the BDD tip

These results suggest that several mechanisms are competing, which can either lead to resistance

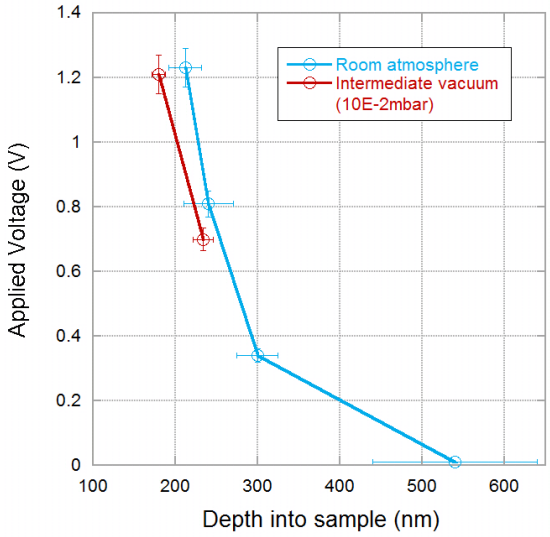

Figure 6.38: Applied voltage at the beginning of resistance oscillations versus indentation depth at which they appear for copper sample.

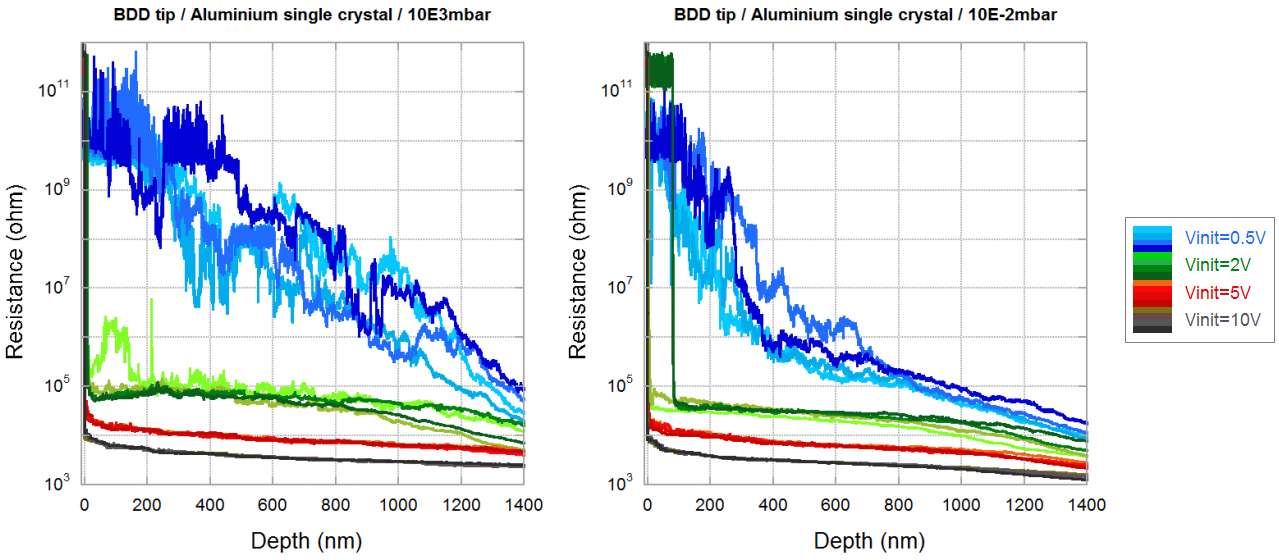

Figure 6.39: Resistance-versus-depth curves for BDD tip and bulk Al single crystal, under room atmosphere (left) and intermediate vacuum (right).

increase or resistance decrease during indentation. These mechanisms are involved only on natively oxidised metals (copper and aluminium), but never on noble metal (gold). This shows the crucial role of the oxide on the involved mechanisms. In addition these mechanisms seem to be slightly different on copper and on aluminium, which could be due to the nature of the oxide (mixed conduction for copper or ionic conduction for aluminium). These mechanisms also depend on the atmosphere under which the measurements are conducted (either room atmosphere or intermediate vacuum).

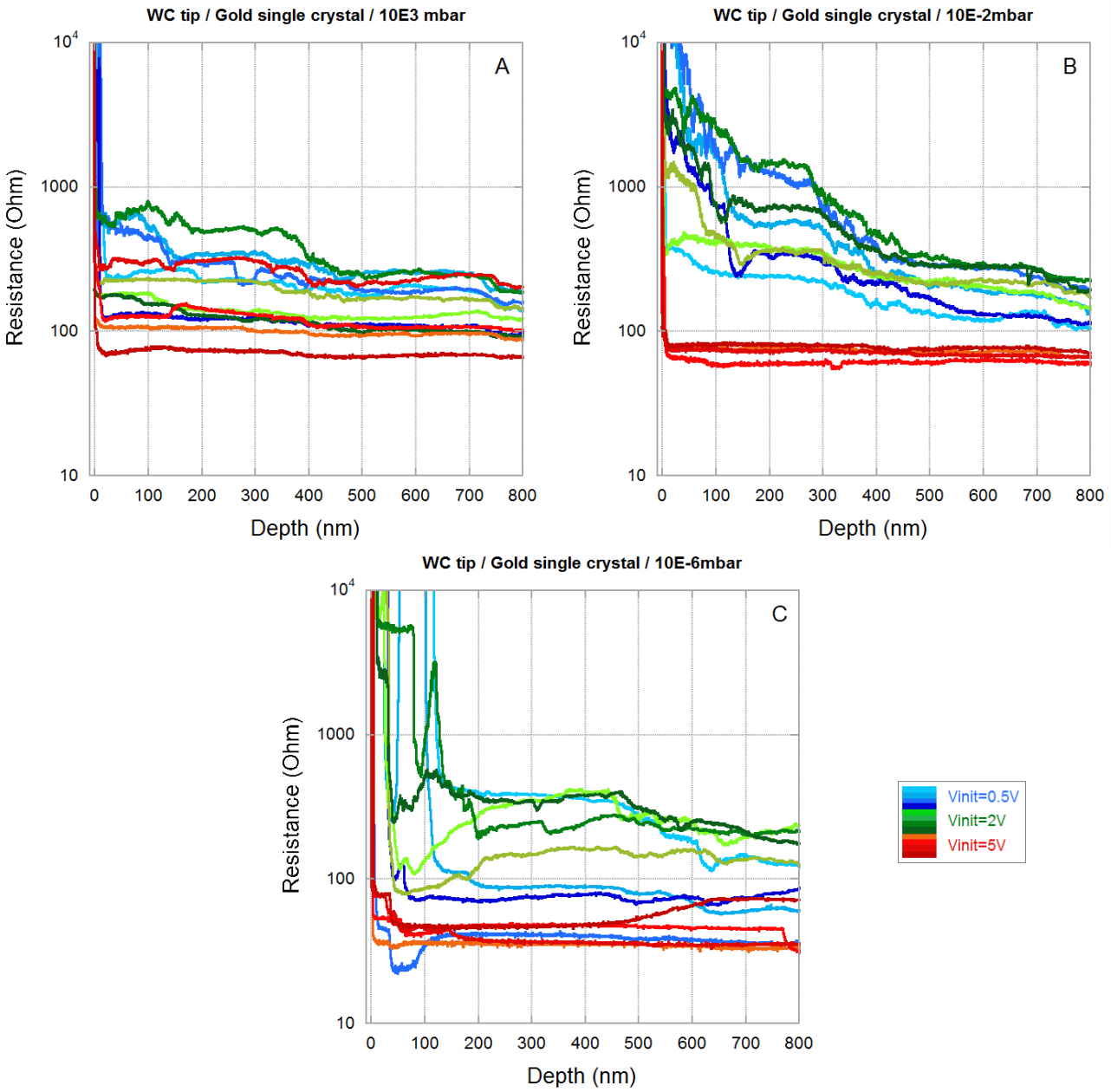

Figure 6.40: Resistance-versus-depth curves for WC tip and bulk Au single crystal, at room atmosphere (A), intermediate vacuum (B) and high vacuum (C).

Indentation with WC tip

- Bulk Au single crystal

Contrary to indentation conducted with the BDD tip, Au sample indented with the WC tip exhibits strong resistance variations (figure 6.40). There is no visible effect of the atmosphere (room atmosphere, intermediate vacuum or high vacuum) on these resistance variations.

These resistance variations also show reproducible features: figure 6.41 provides examples of resistance-versus-depth curves for successive indentation performed with the WC tip for different locations on Au. Even if the whole curves are not reproducible, some resistance increases

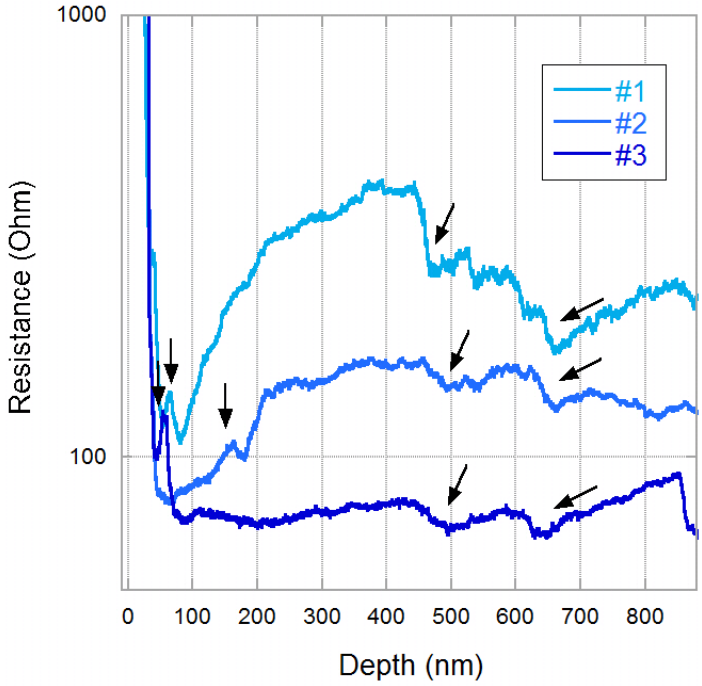

Figure 6.41: Reproducibility of resistance variations during indentation of Au sample by WC tip.

appear at roughly similar indentation depth for each resistance-versus-depth curves (black arrows).

This reproducibility seems to indicate that the mechanisms responsible for the resistance variations now take place at the tip surface rather than at the sample surface. Since measurements with BDD tips have highlighted the role of native oxide on those mechanisms, it seems clear that the native oxide of the WC tip (estimated at several nanometers by XPS) now plays a key role on the phenomena responsible for resistance variations.

- Bulk Cu single crystal

For bulk Cu single crystal, slight resistance variations also occur during indentation with a WC tip, but to a lesser extend (figure 6.42). As for Au, these resistance variations exhibit some reproducible features, which suggest that the mechanisms responsible for the resistance variations take place at the tip surface. Here again the atmosphere does not affect these resistance variations.

- Bulk Al single crystal

Electrical measurements during the indentation of Al sample with the WC tip exhibit strong

resistance variations up to several decades (figure 6.43). These resistance variations occur for all bias set-points, and not only for bias set-point below 2V as for indentation with the BDD tip. Here again their is no effect of the atmosphere on these resistance variations.

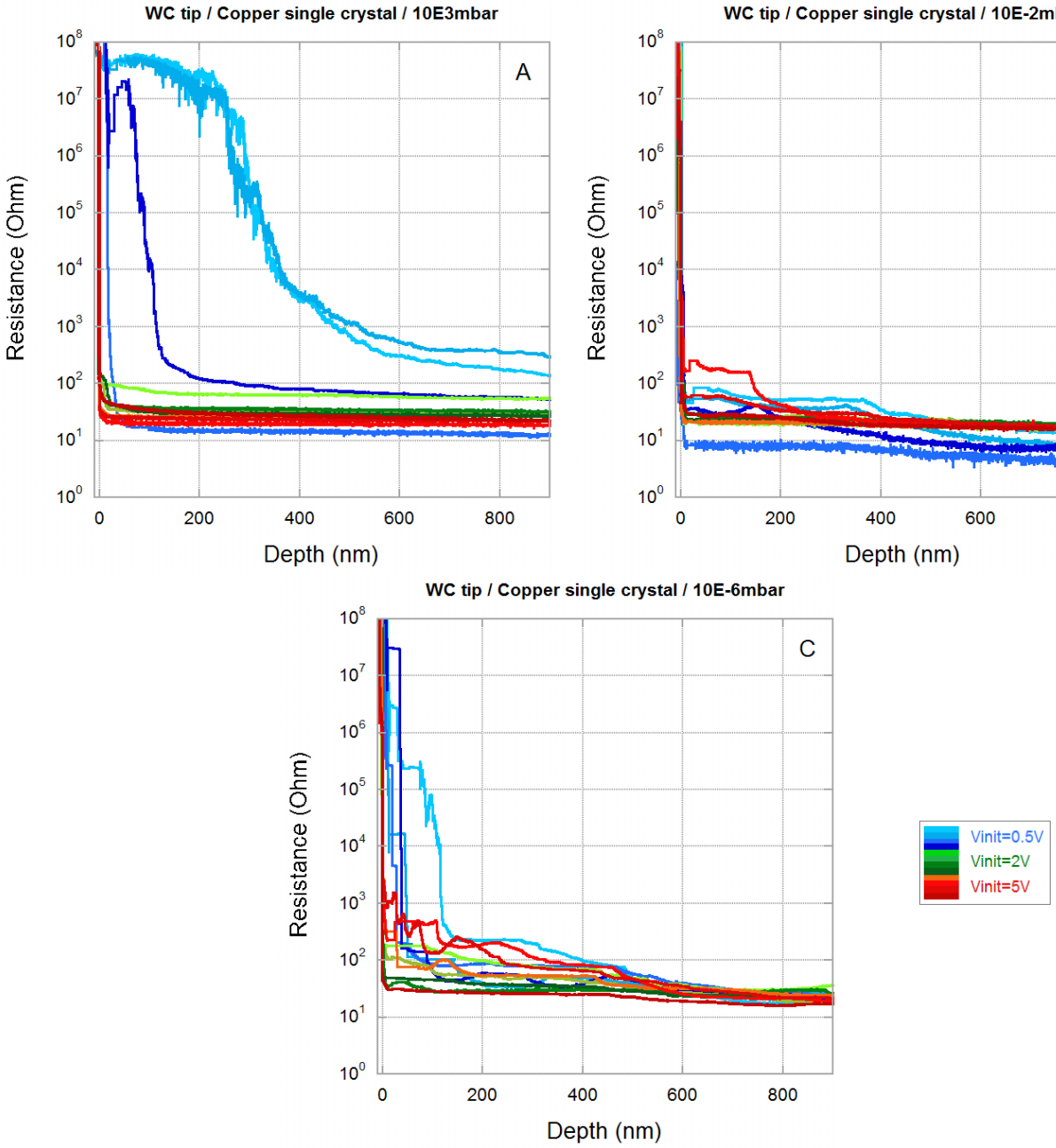

Figure 6.42: Resistance-versus-depth curves for WC tip and bulk Cu single crystal, at room atmosphere (A), intermediate vacuum (B) and high vacuum (C).

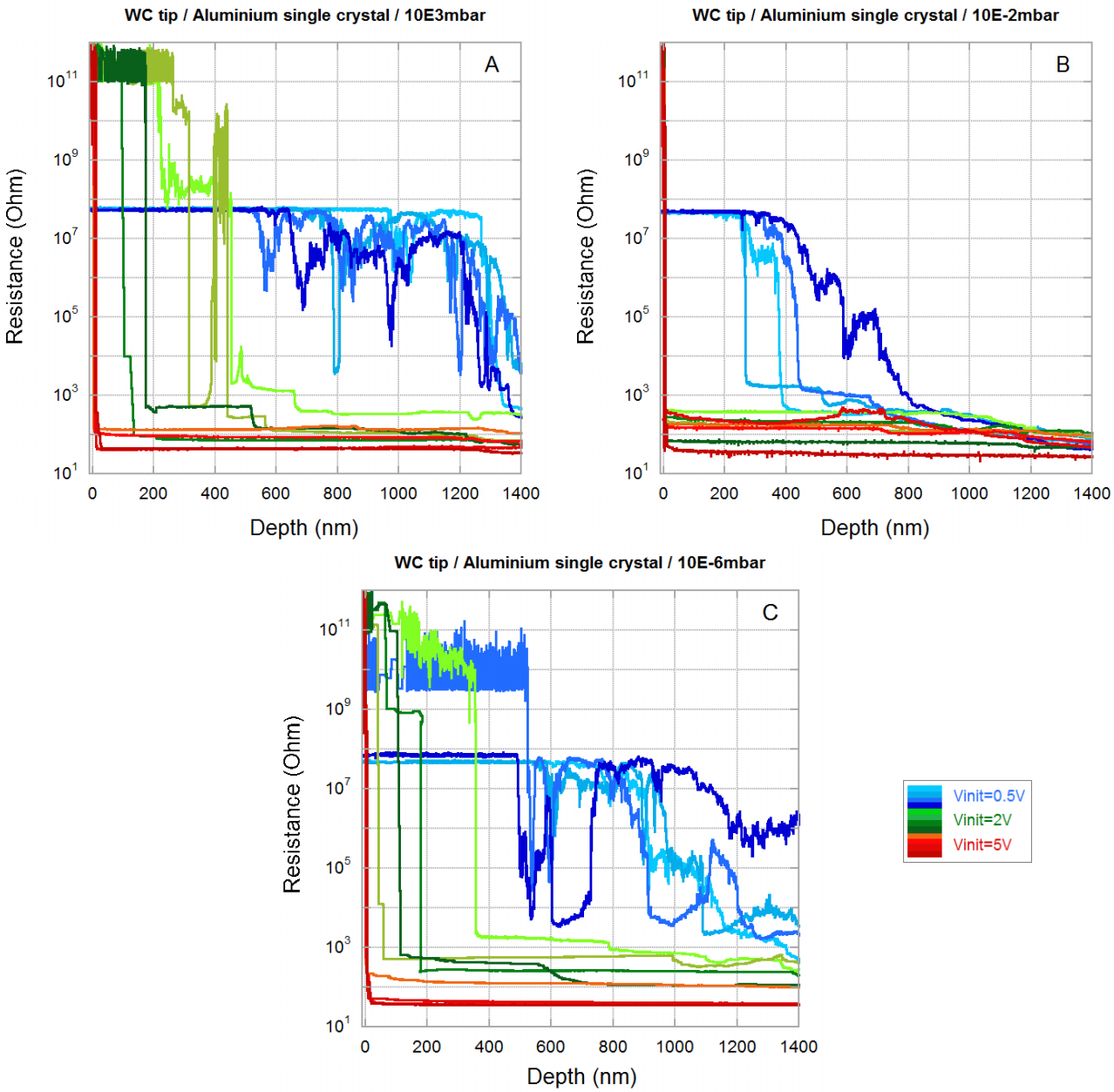

Figure 6.43: Resistance-versus-depth curves for WC tip and bulk Al single crystal, at room atmosphere (A), intermediate vacuum (B) and high vacuum (C).

- Conclusion on indentation with WC tip

Thus, experiments with WC tip also exhibit strong resistance variations, especially for aluminium and gold samples, and to a lesser extend for copper sample. The native oxide of the tip seems to play a major role in the involved mechanisms, in addition to the role played by samples oxides. The atmosphere under which experiments are conducted has not effect on these resistance variations.

6.8.2 Guidelines for further investigations on the electrochemical processes.

In previous sections, the effect of both polarization voltage and atmosphere on the "unexpected" resistance variations has been studied. Table 6.4 summarizes the effect of both contributions on these resistance variations for each tip-to-sample contact.

Sample	BDD (no oxide)	WC (few nm native oxide)
Au (no oxide)	No unexpected resistance variation. Atmosphere independent. Voltage independent.	Resistance variation with reproducible features. Atmosphere independent. Voltage dependent.
Cu (< 1 nm native oxide - mixed conduction)	Slight resistance oscillations confined within a continuous envelop. Atmosphere dependent. Voltage dependent.	Resistance variation with reproducible features. Atmosphere independent. Voltage dependent.
Al (6-9 nm native oxide - ionic conduction)	Strong "noisy" resistance variations. Atmosphere dependent. Voltage dependent.	Strong "noisy" resistance variations. Atmosphere independent. Voltage dependent.

Table 6.4: Atmosphere and polarization voltage effect on "unexpected" resistance variations for each tip/sample configuration.

The role of the native oxide on resistance variations, the effect of the polarization voltage, and the influence of the atmosphere in the case of the BDD tip are among the clues that electrochemical processes are at the heart of the mechanisms involved in these unexpected resistance variations.

Electrochemical mechanisms have not been further studied within the frame of this work. However, in view of their effects on electrical behavior during electrically coupled nanoindentation, further investigations are required to improve the understanding of electrical transport through the contact.

The aim of this paragraph is to give guidelines for further investigations of these phenomena, but they are not supported by experiments yet.

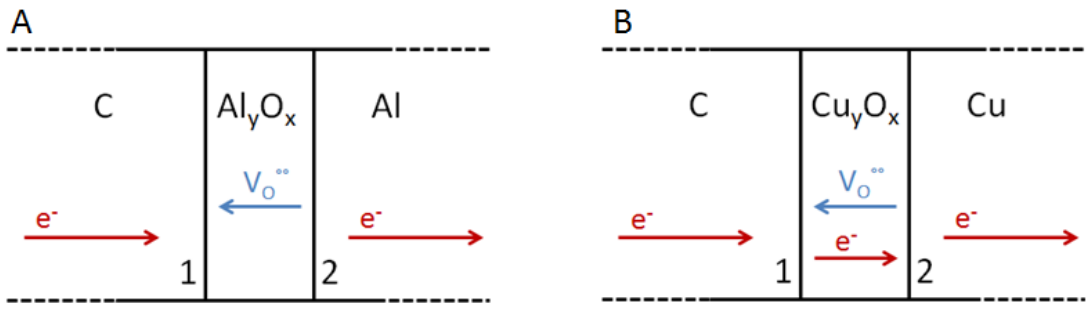

Figure 6.44: Electrochemical mechanisms involved with BDD tip and Al sample (A) or Cu sample (B).

Influence of the conduction type within the oxide

During the experiments presented in section 6.8.1 (page 219), the sample is positively polarized and the tip is grounded. Thus, electrons travel from the tip to the conductive metal, provided that there is an electronic transport within the oxide.

Electrical conduction within the oxide depends on the oxide nature: either the conduction through the oxide is purely ionic (case of Al sample); or the conduction through the oxide is mixed (case of Cu sample).

In the case of ionic conduction, the tip/oxide and oxide/metal interfaces are necessarily the place of electrochemical reactions.

During indentation with the BDD tip, the only oxide involved for electrochemical mechanism is the native oxide of the sample. The difference of conduction mechanism through the oxide (ionic or mixed) could explain the difference in resistance-versus-depth curves between Al (large noisy resistance variations) and Cu (small resistance oscillations confined within a continuous envelop). However, both samples are not truly comparable since they have different oxide thickness .

Possible electrochemical reactions involved

- Bulk Au single crystal / BDD tip

For the bulk Au single crystal indented by the BDD tip, there is no oxide on the BDD tip nor on the sample. The conduction through the interface is truly electronic. No electrochemical reactions take place at the contact. This is consistent with the resistance-versus-depth curves with BDD tip for bulk Au single crystal, where no unexpected resistance variations occur during indentation (figure 6.35).

◦ Bulk Al single crystal / BDD tip (low polarisation)

For bulk Al single crystal indented by the BDD tip, the electrical conduction within aluminum native oxide is only achieved by the mobility of ionic defects. In the case of a solid electrolyte, the ionic defects responsible for the conduction are mostly oxygen vacancies (figure 6.44 A). For low polarisation, electrochemical reactions involved at the tip/oxide (1) and oxide/metal (2) interfaces are given in equations (6.19) (an oxygen vacancy is reduced twice) and (6.20) (oxygen production) respectively.

$$\textbf{1:}\quad \frac{1}{2}O_2 + V_O^{\circ\circ} + 2e^- \rightarrow O_O^X \tag{6.19}$$

$$\textbf{2:}\quad O_O^X \rightarrow \frac{1}{2}O_2 + V_O^{\circ\circ} + 2e^- \tag{6.20}$$

These reactions can partially explain the resistance variations shown in figure 6.39, especially for low polarisation. Little conduction appears in the oxide due to the presence of oxygen in the atmosphere and the reduction of oxygen vacancies (equation 6.19). This leads to a resistance decrease. Then, if the mobility of atoms is high enough (see further in paragraph 6.8.2, page 232), there is an oxide growth at the oxide/metal interface, leading to a resistance increase (equation 6.20). Both mechanisms are into competition. They also compete with the global decrease of the resistance due to the contact area increase during nanoindentation and potential oxide fracture. This can explain the severe resistance variations while indenting. The electrochemical reactions involved are affected by the presence of oxygen in the atmosphere, which explains why the resistance variations are more pronounced at room atmosphere than under vacuum. Nevertheless, a high atom mobility is needed for these mechanisms to happen, especially for the oxide growth.

◦ Bulk Cu single crystal / BDD tip (low polarisation)

For bulk Cu single crystal indented by the BDD tip, the electrical conduction within the copper native oxide is achieved by both the mobility of ionic defects and electrons passing through the oxide (figure 6.44 B). Under low polarisation, electrochemical reactions involved at tip/oxide and oxide/metal interfaces are given by equations (6.21) and (6.21), respectively.

Since the mobility of electronic defects is four to five orders of magnitude higher than that of ionic defects, the electronic behavior is probably dominated by electronic conduction. This can explain results of figure 6.36 and 6.37 where the electrical behavior is very close to the electrical behavior of Au. The slight resistance oscillations could be due to the ionic contribution, which might explain why they are affected by the atmosphere under which experiments are conducted.

$$\textbf{1:} \quad \begin{cases} \frac{1}{2}O_2 + V_O^{\circ\circ} + 2e^- \rightarrow O_O^X \\ e_{tip}^- \rightarrow e_{oxide}^- \end{cases} \tag{6.21}$$

$$\textbf{2:} \quad \begin{cases} O_O^X \rightarrow \frac{1}{2}O_2 + V_O^{\circ\circ} + 2e^- \\ e_{oxide}^- \rightarrow e_{metal}^- \end{cases} \tag{6.22}$$

- Bulk Al and Cu single crystals / BDD tip (high polarisation)

Under high polarisation voltages, a new reduction reaction can occur for both bulk Al and Cu single crystals at the tip/oxide interface, as described by equation (6.23) (an oxygen vacancy is reduced once). In literature, this reaction is activated for polarisation bias higher than $\sim$ 2 V. It is associated with a fast reduction front moving toward the anode.

This reduction front could be an alternative explanation to the sudden resistance drops seen in section 6.6 (page 209) at the beginning of the indentation of aluminum thin film with various oxide thickness. this sudden resistance drop was previously associated to electrical breakdown.

$$\textbf{1:} \quad \begin{cases} \frac{1}{2}O_2 + V_O^{\circ\circ} + 2e^- \rightarrow O_O^X \\ (e_{tip}^- \rightarrow e_{oxide}^-) \\ V_O^{\circ\circ} + e^- \rightarrow V_O^{\circ} \end{cases} \tag{6.23}$$

This electrochemical reaction does not explain the resistance plateau seen on resistance-versus-depth curves after the sudden resistance drop. One might imagine that this reduction front creates some "conductive filaments" inside the oxide (figure 6.45), with a size which will not further increase while increasing the indentation depth. However this explanation can also apply for conducting path created by electrical breakdown.

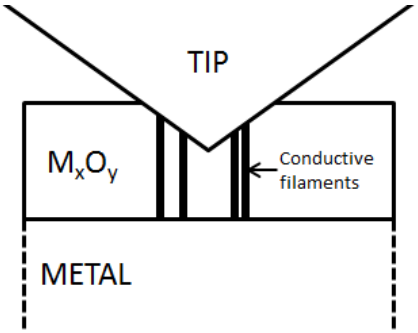

Figure 6.45: Conductive filaments created by the reduction front through the oxide.

◦ Bulk Au, Al and Cu single crystals / WC tip

Electrochemical mechanisms involved during indentation with the WC tip are probably even more complicated, because of the native oxide layer on WC. For Au, electrochemical reactions can occur at the interfaces with the tungsten carbide oxide. For high enough atom mobility, this would lead to tungsten oxide growth on the tip. This can explain the reproducibility of the resistance increase observed during successive indentations at different sample localisations (figure 6.41, page 224).

For bulk Cu and bulk Al samples, electrochemical reactions can occur both at the tungsten carbide oxide interfaces and at the sample oxide interfaces, leading to tip or sample oxide growth.

After experiments conducted with the WC tip on Al sample under high reverse polarisation (-10V), the tip has been strongly damaged (figure 6.46). In that case reduction of the WC tip (instead of oxidation) are supposed to occur. This is consistent with the SEM image showing evidence of selective reduction of one phase of the WC tip.

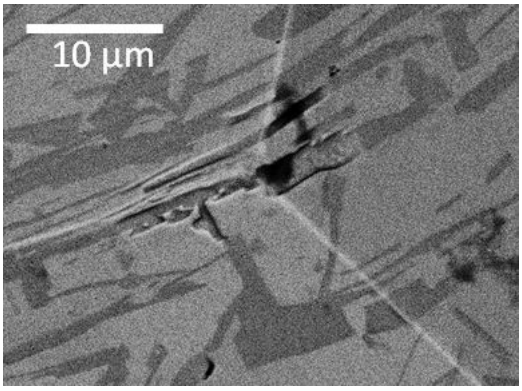

Figure 6.46: WC tip showing evidence of selective reduction after nanoindentation on Al sample at reverse polarisation bias (-10V).

Atom mobility

The resistance increases can come from oxide growth during indentation. However, this requires high atom mobility. In this section, possible explanations for this high atom mobility are given.

- High local temperature during indentation

Temperature can be estimated using Kohlraush model [102], which relates the maximal temperature at the interface T_m to the voltage drop V at the contact (equation 6.24, with $\lambda_{1/2}$ and $\rho_{1/2}$ respectively the thermal conductivity and the electrical resistivity of both solids in contact, and $T_{1/2}$ the temperature of their outer surfaces).

$$V = (2\int_{T_1}^{T_m} \lambda_1 \rho_1 dT)^{1/2} + (2\int_{T_2}^{T_m} \lambda_2 \rho_2 dT)^{1/2} \tag{6.24}$$

Figures 6.47 provides examples of temperature estimations for BDD tip (A) and WC tip (B) during indentation of bulk Cu single crystal, using Kohlraush model. The voltage drop at the contact is taken equal to the total applied bias between the tip and the sample, which is an overestimation for the BDD tip (see section 6.4.4, page 201). For WC tip, overheating appears to be more pronounced, reaching values from 70 to 40 K up to 150nm depth, and then decreasing slowly. Nevertheless, these values are far from the usual high temperature conditions required for oxide growth.

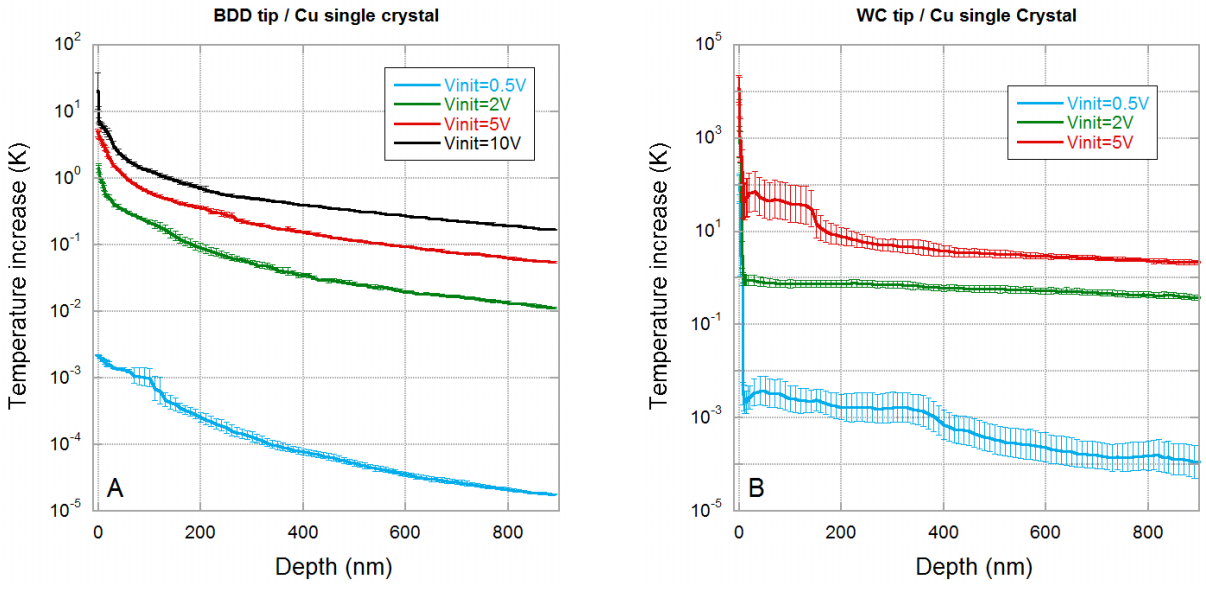

Figure 6.47: Estimation of the temperature increase using Kohlraush model during indentation of bulk Cu single crystal with BDD tip (A) and WC tip (B).

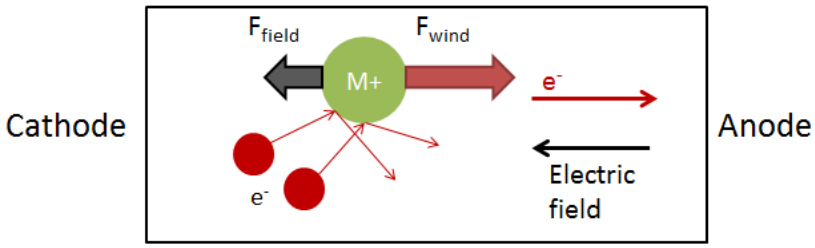

Figure 6.48: Electromigration phenomenon, adapted from Lienig [205].

◦ Electromigration

When a large current density flows through a conductor, metallic ions are exposed to two opposite forces: the electrostatic force F_{field} due to the presence of an electric field (equation 6.25, where q is the cation charge and E is the electric field); and an opposite force F_{wind} due to the momentum transfer between the conducting "electron wind" and metal atoms (figure 6.48). The resulting force is given by equation (6.26), with j the current density, ρ the material resistivity and Z^* the effective valence, which determines whether the transport is directed toward the anode or the cathode.

$$F_{field} = q \cdot E \tag{6.25}$$

$$F_{resultant} = q \cdot Z^* \cdot j \cdot \rho \tag{6.26}$$

In most cases F_{wind} [205] is much larger than F_{field} and the effective valence is found to be from 5 to 50, decreasing with temperature [206]. Typically, electromigration in copper and aluminium connectors occur for current densities from 10^6 to 10^7 A.cm^{-2}, but can appear for much lower current density in intermetallic solder joints (typically 10^4 A.cm^{-2}) [207] or when there are lots of crystallographic defects at the interface (such as grain boundaries or dislocations). According to Braunovic *et al.* [76], electromigration can occur for current density as low as 10^3 - 10^5 A.cm^{-2}. Note that copper connectors are usually more robust to electromigration than aluminium connectors, and they can sustain current density 4-5 times larger than for aluminium connectors, due to their higher melting temperature [208].

Figure 6.49 shows current densities during indentation of bulk Cu single crystal with both BDD and WC tips. For current densities calculations, the distribution of the current lines is considered as uniform within the contact, which was found to be inexact in the case of the BDD tip (see section 6.4.4, page 201). The current density values obtained are then underestimated. Very high current densities are found, with values up to 10^7 A.cm^{-2} at small indentation depth and higher than 10^3 A.cm^{-2} at large indentation depth. For such current densities, electromigration is likely to occur, giving enough atom mobility for oxide growth.

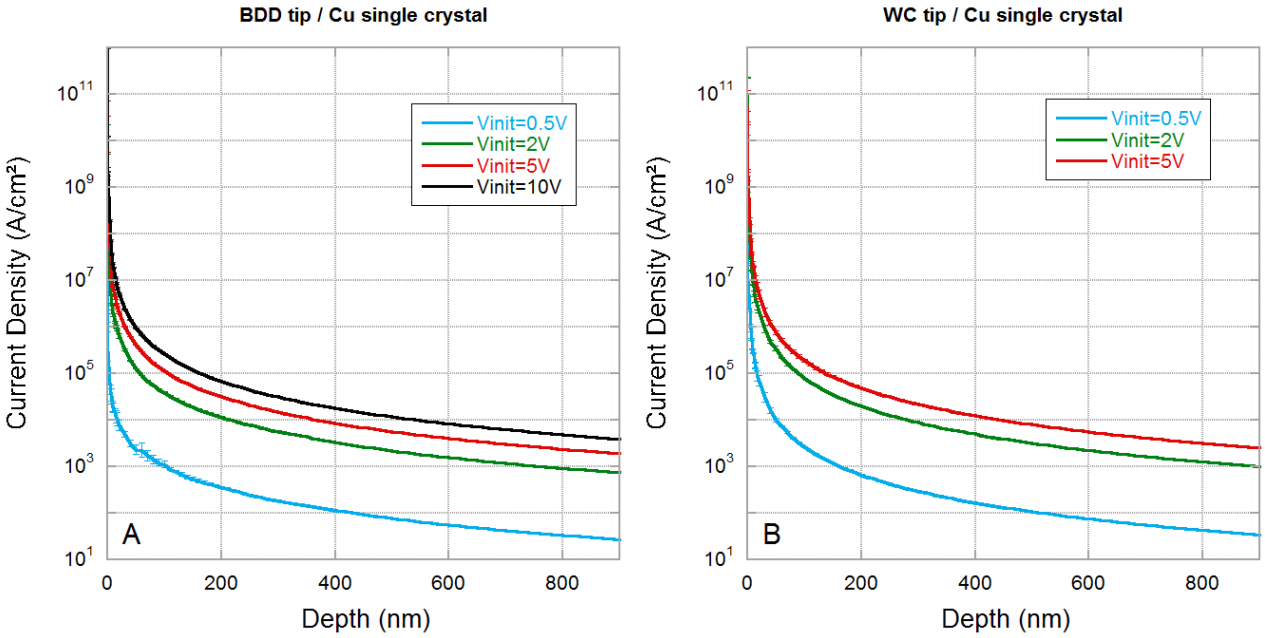

Figure 6.49: Current density estimation while indentation Cu single crystal with BDD tip (A) and WC tip (B).

- Influence of mechanical deformation

In our case, electrochemical processes occur while deep plastic mechanical deformation takes place. Plastic deformations generate large amounts of crystallographic defects, which can help atoms mobility, since these defects reduce the barrier energy for atom mobility.

In order to assess this point, an experiment has been run. The resistance was recorded versus time during an indentation composed of a first loading step until a maximal depth and then an holding step where the load onto the sample was kept constant for two minutes. This leads to the resistance-versus-time curves of figure 6.50.

These curves clearly show a change in electrical behavior when loading stops, with much less resistance increases and drops during the holding time. This shows the crucial role of mechanical deformations on electrochemical processes.

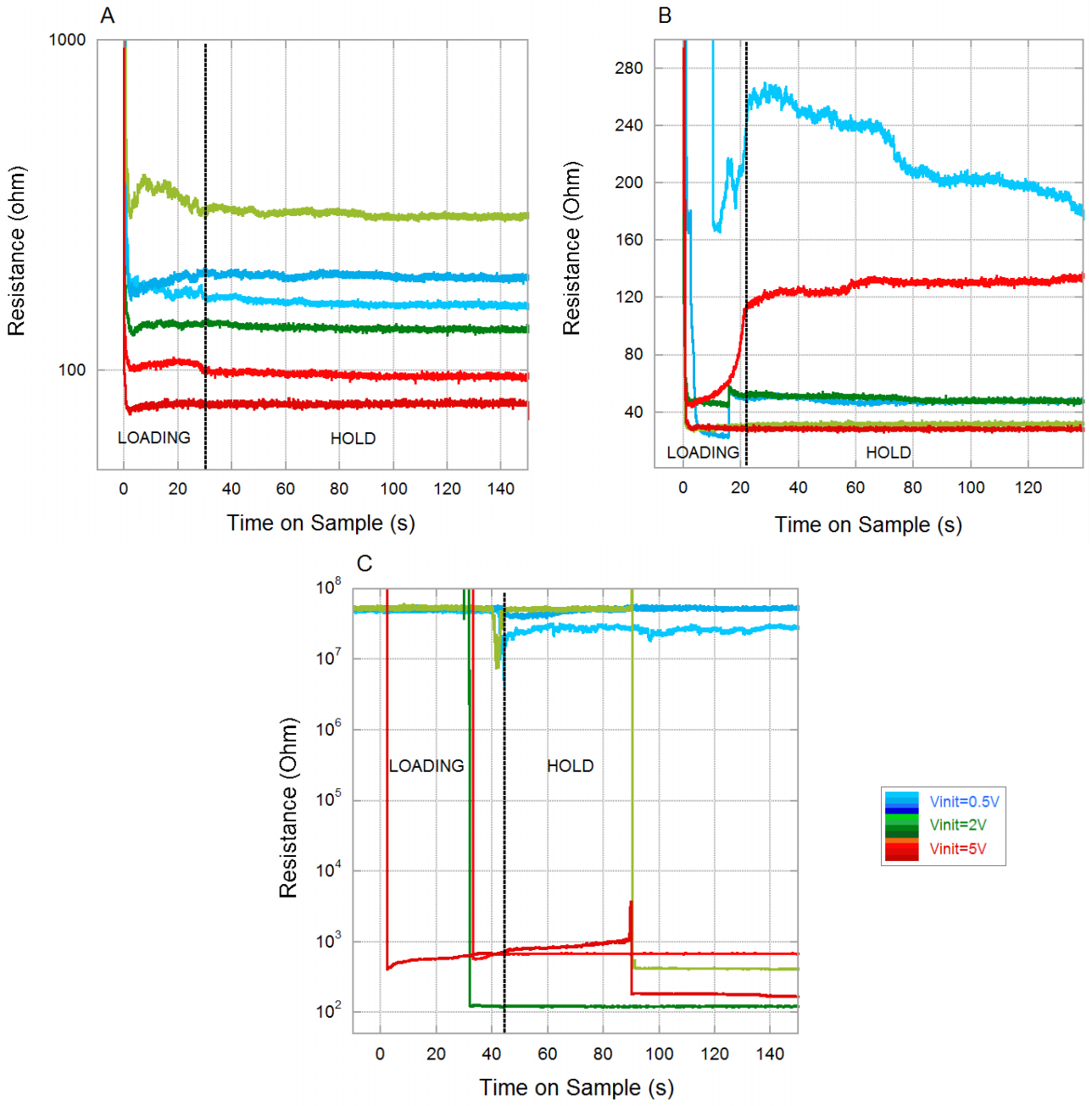

Figure 6.50: Resistance-versus-time curves during a loading step and then a two minutes hold step for WC tip on A: Au single crystal (maximal depth=150nm), B: Cu single crystal (maximal depth=100nm), C: Al single crystal (maximal depth=500nm). Experiments conducted under intermediate vacuum.

6.9 Conclusions and prospects

In this chapter resistive nanoindentations of model specimens have been performed. Noble metal (Au) and natively oxidised metals (Cu, Al), either as bulk single crystals or as polycrystalline thin films have been tested. The effect of the material chosen for the conductive tip (BDD or WC) has also been studied.

Qualitative results emphasise the importance of the oxide layer - either from the sample (Al,Cu) or from the tip (WC) - on the electrical response. In the presence of an oxide layer, strong electrochemical reactions seem to occur at the contact. However, further investigations are required in order to better understand the electrochemical mechanisms involved.

Different local environments have also been assessed (room atmosphere, intermediate vacuum and high vacuum), showing only few effect of the environment on these electrochemical mechanisms for the BDD tip, and no effect for the WC tip.

When no oxide is involved in the tip-to-sample contact (Au/BDD), resistance values during indentation are found to continuously decrease with increasing contact depth. The measured resistance can be fully described by an analytical model. A numerical model has also been derived.

In absence of oxide layer, a quantitative analysis can be performed. Analytical expressions, which relate the resistance to the contact depth, have been successively derived by performing an electrical calibration on bulk Au single crystal. This leads to equation (6.27). A, B and h_0 are constants which depend only on the experimental set-up. SF is a shape factor which takes into account the heterogeneity of the current distribution at the contact within the sample. It has been shown that SF can be considered as constant during indentation and equal for different samples with similar conductivities.

$$R_{measured} = A + \frac{B}{SF(h_c + h_0)} \tag{6.27}$$

By using the analytical expression derived on bulk Au single crystal, contact area monitoring has been computed from resistive nanoindentation of a Au thin film whith a rheology different from the Au single crystal (pile-up instead of sink-in). Results show very good agreements with post-mortem AFM measurements. Thus, the main objective of this part has been reached.

Electrical contact area monitoring during indentation is then promising. However, further investigations are required:

- A serious investigation of the electrochemical mechanisms involved in the presence of an oxide layer is required. In particular, the bias applied at the contact should be optimized in order to reduce these mechanisms.

- In order to improve the understanding of the resistance-versus-depth curve, and in particular the evolution of the shape factor SF, the numerical model must be further developed and compared to experimental measurements.

- Since the involved electrochemical mechanisms seem to be really strong with the WC tip, other metal carbides used for the tip can be considered (VC...).

- In order to perform indentation with an highly conductive tip (and to be more sensitive to electrical mechanisms within the sample), an electrical functionalization of the BDD tip by coating can also be considered. This last point has been the subject of a project of master students from PHELMA (Grenoble).

Chapter 7

Capacitive measurements on thin dielectric films

7.1 Literature review and motivation

7.1.1 Scanning Capacitance Microscopy

Impedance spectroscopy techniques characterize the dielectric properties (polarisation and charge transport) of an insulating material against frequency. However, macroscopic measurements give only access to average properties. In order to be sensitive to submicrometric properties within small-scale structures and devices, capacitive measurement techniques with increasing spatial resolution have been derived in literature. The coupling with Atomic Force Microscopy (AFM) allows determining the local material properties, with spatial resolution in the order of the probe size (*i. e.* tens of nanometers).

Historically, Scanning Capacitance Microscopy (SCM) was developed to profile dopant distribution in a semiconductor. Slinknom *et al.* [209] have first developed a SCM integrated in an AFM. Since then, SCM is generally composed of an AFM and a 1 GHz tuned inductance-capacitance-resistance (LCR) circuit [210]. During measurement, a conductive AFM tip scans the sample surface, and an AC voltage is applied between the tip and the sample. Typical AC conditions are a 1V peak-to-peak at 10 kHz signal. The tip is inductively grounded, and a contact is taken at the back side of the sample.

The LCR circuit is composed of an ultra high frequency oscillator, a LCR resonant circuit and a peak detection circuit. The tip-to-sample capacitance C_{T-S} is part of the LCR circuit. Then, a change in C_{T-S} involves a change of the resonance peak, as shown in figure 7.1. Consequently, at

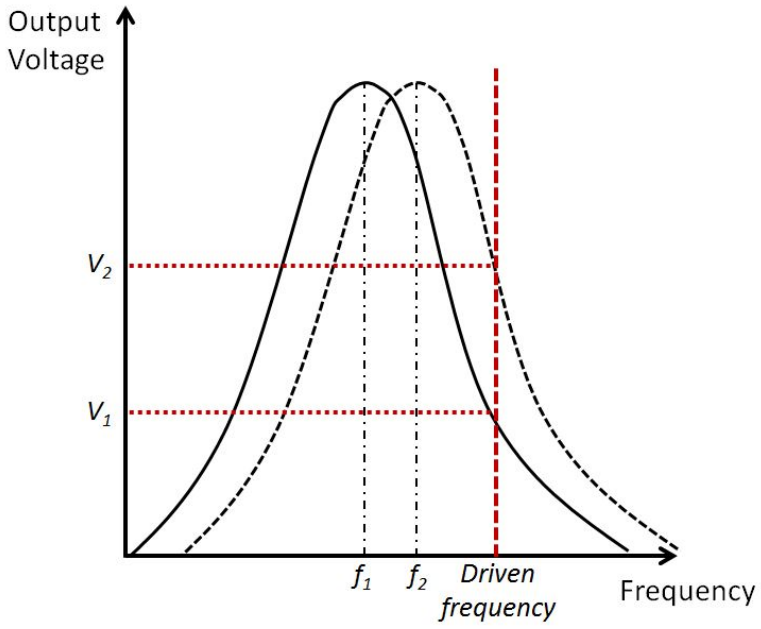

Figure 7.1: Resonance frequency change due to C_{T-S} change, leading to different output voltage.

a constant drive frequency, the output voltage varies, depending on how the circuit resonance is shifted, and thus depending on the variation ΔC_{T-S}. A high frequency lock-in detector translates the phase shift of the LCR circuit to a signal proportional to $\frac{\Delta C_{T-S}}{\Delta V}$.

Usual SCM tips are highly-doped silicon, silicon coated with metal or with boron-doped diamond. Typical sample investigated by SCM are semiconductor + oxide stacks, which constitutes a metal-oxyde-semiconductor (MOS) system with the highly conductive metal-like AFM tip.

The contrast in SCM images is due to the difference of the output voltage, depending on ΔC_{T-S}, which is also proportional to the reciprocal of the square root of dopant concentration. Thus, dopant profiling can be extracted, as shown in figure 7.2. Typically p-type dopant corresponds to darker area and n-type dopant to brighter area [210, 211].

However, during SCM measurement $\frac{\Delta C_{T-S}}{\Delta V}$ is measured rather than the absolute value of the capacitance. This technique is then limited to material with a capacitance which depends on the bias applied, and thus to semiconductors which exhibit a voltage dependant depletion layer. Consequently, this technique do not apply for dielectric films.

SCM imaging have also shown limitation on sample with non-uniform dopant concentration or low dopant concentration.

The spatial resolution during SCM is also reduced by the need for sufficiently large contact areas (and thus high contact load) to improve the signal to noise ratio during measurements. Typical spatial resolution in SCM is around 50 nm.

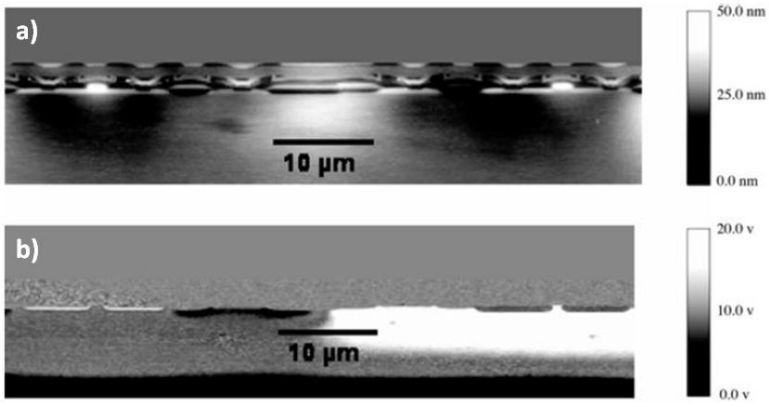

Figure 7.2: (a) AFM image of a polished cross section of a MOS pair. No contrast is seen from the doped structures; (b) corresponding SCM image showing contrast between p-type and n-type dopants. From Kopanski [210].

7.1.2 Nanoscale Impedance Microscopy

In order to overcome the limitations of SCM technique that only applies to semiconductors, efforts have been made in literature to perform absolute capacitance measurements during AFM scans. Nanoscale Impedance Microscopy (NIM) has then been developed. As for SCM imaging, an AFM scans the sample surface, while an AC voltage is applied between the tip and the sample. However, contrary to SCM, the NIM technique provides the measurement of both resistance and capacitance at the contact, thanks to the measurement of the total admittance between the tip and the sample [212].

The amplitude and phase signal are monitored by either a commercial impedance analyser [213, 214, 215] or a lock-in amplifier [212, 216]. This improves the spatial resolution up to 10 nm.

However, the main issue during NIM measurements - which also affects SCM measurements - is the influence of a stray capacitance, coming from capacitive coupling between sample and various parts of the AFM, such as the tip cone, the cantilever, the chip and the probe holder (figure 7.3). The capacitive signal of interest, which means the capacitance between the tip apex and the sample, must be extracted from this stray capacitance, which can be up to 4-5 orders of magnitude higher (typically 100-500 fF against tip apex capacitance $<$ 1fF).

The main difficulty here is that this stray capacitance is not constant, but depends on the lateral displacement of the tip on the sample and on its vertical displacements. Lee *et al.* [218] have shown that the capacitance variation during lateral displacement was about 100 aF.µm^{-1} and about 2-4 aF.nm^{-1} for vertical displacements. In lateral, this was associated to a change in

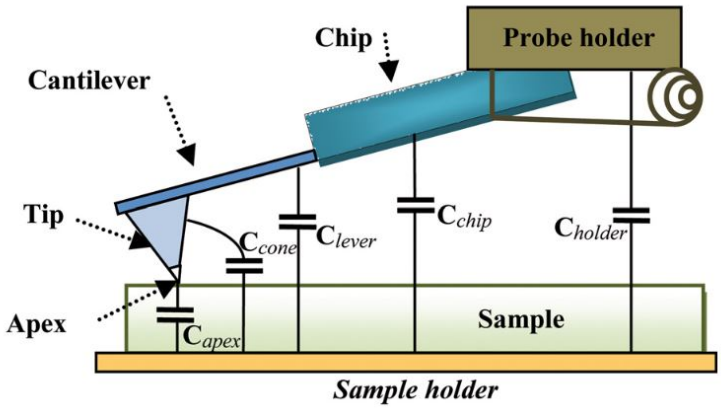

Figure 7.3: Schematic view of various capacitive contributions involved during conductive probe AFM measurement. From Estevez *et al.* [217]

the tilt of the probe assembly during scanning (figure 7.4 A). This effect is amplified for rough surface where the cantilever-to-surface distance is not constant during a scan. In vertical, this was associated to a change in the cantilever deflection (figure 7.4 B).

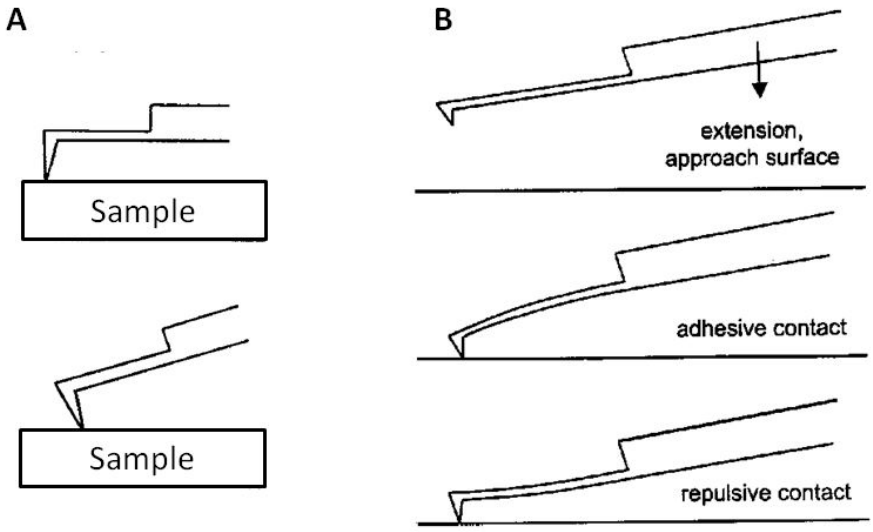

Figure 7.4: A: Change in tilt of the probe assembly during lateral displacement B: Change in cantilever deflection during vertical displacement. From Lee *et al.* [218]

Several attempts have been made to remove this stray capacitance. Lee [218] have used an additional circuit that generates a constant current which cancels the effect of the stray capacitance. By using bridge of RC dipole to remove the stray capacitance, Pingree *et al.* have successively imaged MOS test structures with various capacitances from 1 to 10 fF [212]. Fumagalli *et al.* [219] have used analytical models to determine the contribution of each AFM

probe components to the total measured capacitance. They also shielded the chip and probe holder by inserting a metal foil between the probe and the sample at the same potential as the tip. This reduced the chip and holder contribution to the stray capacitance from the hundreds of fF to the tens of fF. They successively reached the aF resolution in capacitance. Similarly, Schneegans *et al.* [216] have used guard rings around samples to supress edge effects in their so-called "Capascope".

The Capascope device developed at the LGEP (Paris, France) results from the association of the ResiScope (chapter 3, page 81, originally developed by the same team) and a lock-in amplifier, both implemented in an AFM [220]. This device allows simultaneous resistance and capacitance measurement during AFM scans, with resistance range over ten orders of magnitude. This allows the measurements at low tip-to-surface load. This team also proposed a way to determine the "true" capacitance image from two successive scans of each AFM lines [217]. The first scan was performed in contact and the second scan at a constant distance from the surface. Subtracting the "flying over image" to the "contact image" allows to remove the environmental effects. In order to take into account the contribution coming from the cantilever bending and the height of the AFM probe, capacitance-versus-distance from the surface curves have been recorded at regular intervals during the two successive scans. This team was able to reach a resolution up the 10 aF, and they concluded that the aF resolution with this method could only be reached by improving the probe design.

7.1.3 Capacitive measurements with a nanoindenter

State of the art

The highest sensitivity of capacitance to space monitoring has led to a wide integration of capacitive gauges on indentation set-ups [221, 222, 223]. In these instruments, the capacitance measurements are only used to monitor the indenter column displacement.

This approach has been further extended to capacitance measurements at the sample level. The measurement of tip-to-sample capacitance has essentially been used to monitor the sample mechanical deformation [224, 225].

However the coupling of capacitive measurements to indentation tests has been rarely used for the characterisation of dielectric properties of materials. To our knowledge, the only study reporting capacitance measurements on dielectrics through an indenter tip can be found in [226]: this study focuses on the dielectric relaxation processes induced by mechanical loading of PZT

piezoelectric thin films and the relationship with charge defect generations during loading. However, no quantitative analysis of the absolute capacitance or of the stray capacitance is reported.

Motivation

The main motivation to perform quantitative analysis of capacitance measurements with a nanoindenter probe is to control the stray capacitance compared to NIM measurements. In NIM, the contributions to the stray capacitance are local and they deeply depends on the position of the probe on the sample. These contributions come mostly from the nearby tip-to-sample environment, involving the asymmetric influence of the cantilever + chip + holder assembly.

With a nanoindenter, the nearby tip-to-sample environment is almost free from capacitance coupling: the contributions to the stray capacitance mainly come from macroscopic part of the set-up (figure 7.5). Consequently, the stray capacitance is expected to be roughly constant during measurements. It can then be more easily subtracted.

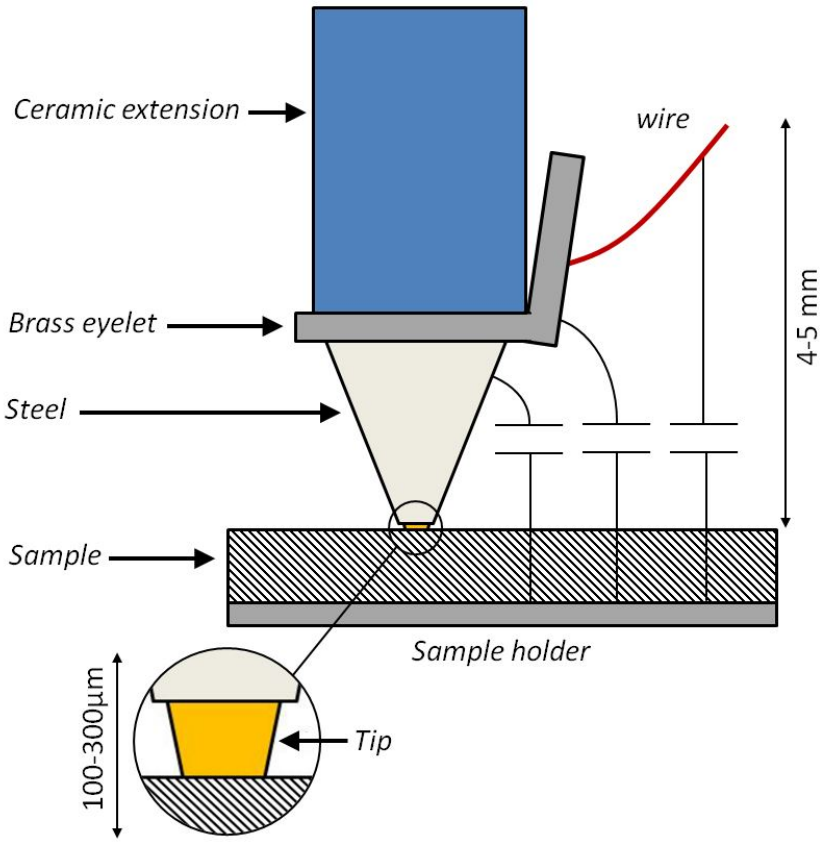

Figure 7.5: Tip-to-sample environment during capacitive measurements with a nanoindenter

However, the probe size in nanoindentation is much larger than in NIM. This leads to much higher tip-to-sample capacitance C_{T-S} values. This is an advantage since the capacitance component $2\pi f C_{T-S}$ of the admittance can then be determined for standard frequency f in the range 1-2 MHz, without dedicated electronics. However, this obviously comes with a loss in spatial resolution.

Consequently, capacitance measurements with a nanoindenter is not a competitive technique compared to AFM technique, but it is expected to fill a gap between nanometric resolution provided by capacitive AFM and macroscopic impedance measurement techniques.

The other interest for performing capacitance measurements with a nanoindenter probe is that the load applied on the sample can be precisely controlled during measurements.

In this chapter, capacitive measurements with the "3-axes" Inforce nanoindenter set-up described in chapter 3 have been performed on several model MOS stacks with various oxide thicknesses. The purpose is to assess the ability to perform quantitative analysis of capacitive measurement with this set-up.

7.2 Generalities about capacitive measurements on Metal-Oxide-Semiconductor system

The capacitance between two metallic electrodes of surface S, separated by a dielectric of thickness t and permittivity ϵ_r (figure7.6) can be expressed by equation 7.1. Capacitance measurements can then provide information about either permittivity or dielectric geometry, making it relevant for oxide characterisation. In microelectronic, the oxide layer is usually silica, which is grown on silicon. Since silicon is a semiconductor, the measured capacitance depends both on the oxide and semiconductor properties. Such Metal-Oxide-Semiconductor stacks are known as MOS systems.

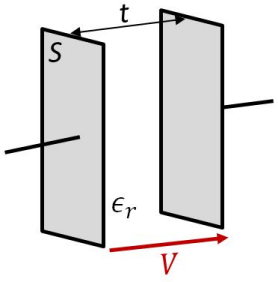

$$C_p = \frac{\epsilon_0 \epsilon_r S}{t} \qquad (7.1)$$

Figure 7.6: Parallel plate capacitor.

MOS systems are characterized by an oxide layer grown or deposited on a p-type or n-type semiconductor surface, and a metal on top of the oxide (figure 7.7 A). In this section the semiconductor will be chosen to be n-type (the majority charge carriers are electrons), which corresponds to the dopant type of our samples. In order to have the same configuration as in our set-up, the reasoning is performed with the metal part at ground potential.

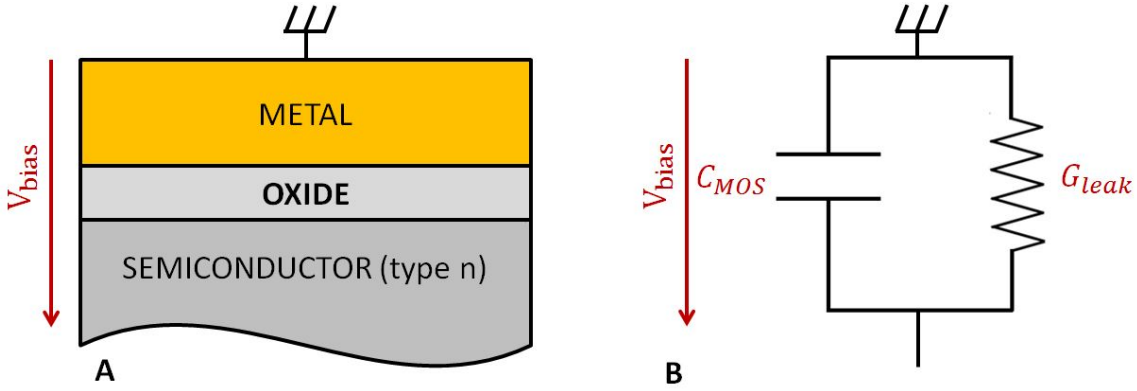

Figure 7.7: Schematic of a MOS system with metal part grounded (A) and corresponding electrical circuit (B).

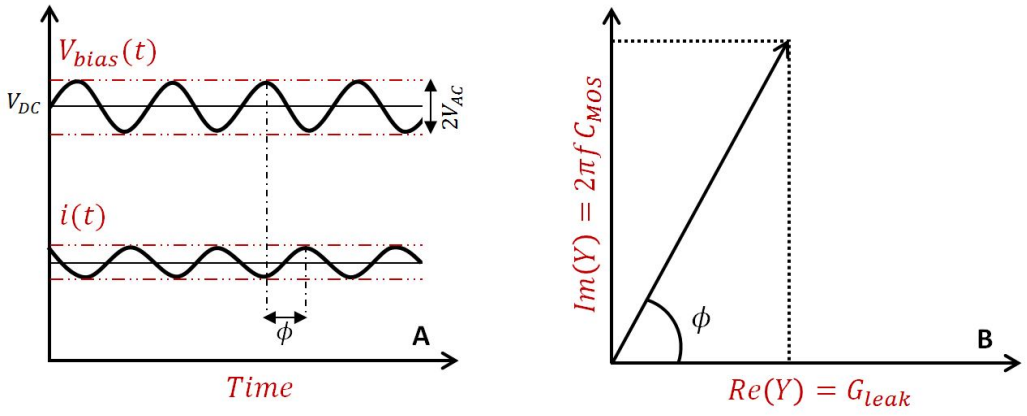

Figure 7.8: Sinusoidal bias applied during capacitive measurements and resulting current signal (A) and corresponding admittance representation (B).

During capacitive measurements, a sinusoidal bias $V_{bias} = V_{DC} + V_{AC} \cdot \sin(2\pi ft)$ is applied between the metal and the semiconductor, with V_{DC} the continuous component of the bias, V_{AC} the voltage amplitude of the sinusoid and f the signal frequency (figure 7.8 A). The resulting current signal $i(t)$ has a phase shift ϕ compared to the bias signal.
Impedance-meters measure the resulting admittance $Y = G_{leak} + j2\pi fC_{MOS}$ (figure 7.8 B), with C_{MOS} the capacitance between the metal and the semiconductor and G_{leak} which accounts for

the leakage current across the oxide (figure 7.7 B). Capacitive measurements are reliable for $G_{leak} << 2\pi f C_{MOS}$, which corresponds to a phase shift ϕ close to 90°.
The capacitance C_{MOS} can be measured for different V_{DC}, which leads to capacitance-versus-bias curves (C-V curves) as illustrated in figure 7.9. The curve is constituted by four regimes:

- **The accumulation regime:** (figure 7.9 A) For negative bias, the conduction band of the semiconductor is bent toward the oxide, coming closer to the Fermi level of the semiconductor. This causes electron accumulation close to the oxide/semiconductor interface. As a result the MOS capacitance C_{MOS} is equal to the oxide capacitance C_{ox} and can be described by equation (7.2), with ϵ_{ox} the dielectric constant of the oxide, and t_{ox} the oxide thickness.

$$C_{MOS} = C_{ox} = \frac{\epsilon_0 \epsilon_{ox} S}{t_{ox}} \tag{7.2}$$

- **The flatband point:** (figure 7.9 B) By increasing the applied bias, the band bending decreases. At a particular voltage, the bands are flat. This is the flatband voltage, which depends on the work function of both metal and semiconductor (*i. e.* the energy needed to remove one electron from the surface), and on the charge defects within the oxide. Typically the capacitance at the flat band voltage C_{FB} corresponds to the two thirds of the oxide capacitance ($C_{FB} \sim \frac{2}{3} C_{ox}$).

- **The depletion regime**: (figure 7.9 C) When the applied bias further increases, the conduction band bends toward the bulk. The electrons are repelled from the interface. A depletion layer of length W appears close to the oxide/semiconductor interface. The depletion layer is constituted of fixed positive charges, which correspond to the ionized donor dopants. The MOS capacitance C_{MOS} corresponds to the C_{ox} capacitance in series with the capacitance of the depletion layer C_{dep} (equation 7.3). C_{dep} can be described by equation (7.4), with ϵ_S the dielectric constant of the semiconductor and W the thickness of the depletion layer. As the bias increases, W increases, causing a decrease of C_{MOS}, which explains the shape of the C-V curve.

$$C_{MOS} = \left(\frac{1}{C_{ox}} + \frac{1}{C_{dep}}\right)^{-1} \tag{7.3}$$

$$C_{dep} = \frac{\epsilon_0 \epsilon_S S}{W} \tag{7.4}$$

- **The inversion regime**: (figure 7.9 D) While further increasing the applied bias, the bending of the valence band toward the Fermi level is high enough to stabilize minority carriers (holes). Locally, the semiconductor has the electrical properties of a p-type semiconductor. At high frequency, a further increase of V_{DC} increases essentially the locale hole density and consequently does not increase the depletion layer, which is fixed to its maximal value W_i. W_i can be expressed by equation (7.5), with N_d the donor density and n_i the intrinsic carrier concentration. The MOS capacitance C_{MOS} is then constant and can be described by equation (7.6).

$$W_i = \sqrt{\frac{4\epsilon_0 \epsilon_S kT \ln(N_d/n_i)}{e^2 N_d}} \tag{7.5}$$

$$C_{MOS} = (\frac{1}{C_{ox}} + \frac{1}{C_{dep}})^{-1} = (\frac{t_{ox}}{\epsilon_0 \epsilon_{ox} S} + \frac{W_i}{\epsilon_0 \epsilon_S S})^{-1} \tag{7.6}$$

  At low frequency, which means when the signal frequency of the bias is lower than the formation rate of the holes, the minority carrier generation is able to follow the sinusoidal variations of the bias, and the capacitance C_{MOS} can increase up to the oxide capacitance C_{ox}.

The difference between the Fermi levels of the semiconductor and the metal corresponds to the applied bias V_{DC} multiplied by the charge $q = -e$ of an electron.

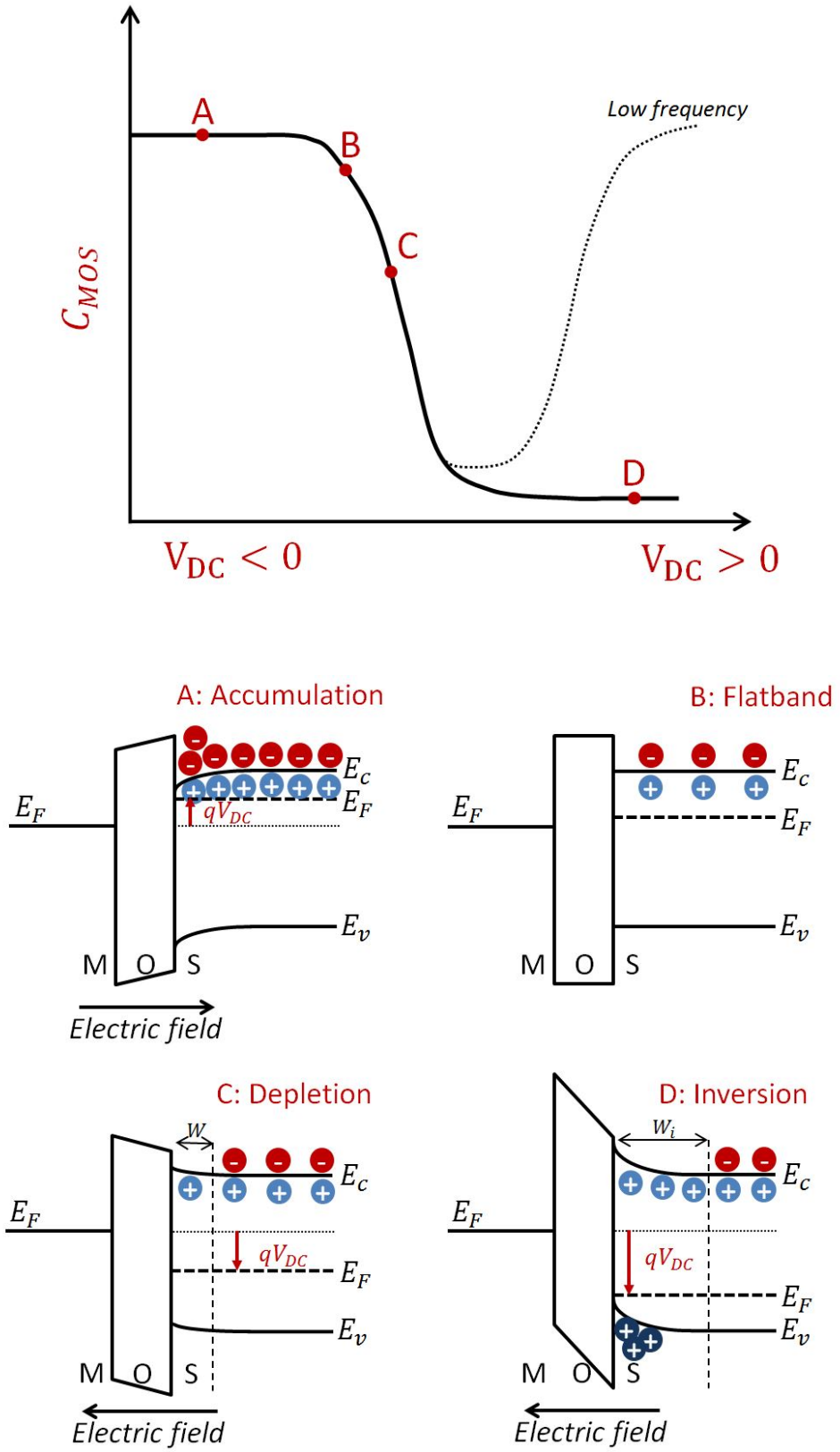

Figure 7.9: Capacitance-versus-DC bias curve of a MOS system with n-type semiconductor and grounded metal part, and corresponding accumulation regime (A), flatband point (B), depletion regime (C) and inversion regime (D).

7.3 Materials and methods

7.3.1 Experimental set-up description

Set-up for capacitive measurements

Capacitive measurements are conducted with the "3-axes" set-up described in chapter 3 (page 81) (figure 7.10 a).

The sample is insulated from the SmarAct translators with a ceramic. It is connected to the high potential terminal with a copper wire directly connected to the high potential coaxial connector.

The tip is insulated from the nanoindenter head with a ceramic extension screwed on the titanium extender (figure 7.10 c). It is connected to the low potential terminal by a 50 µm copper wire going from a brass eyelet to a printed path on a rectangular printed circuit stuck on the nanoindenter head holder (figure 7.10 b). The printed path is connected to the low potential coaxial connector by a rigid wire. This path is also surrounded by an other printed path connected to the ground. The use of an intermediate ceramic for the tip connexion reduces the work of the wires on the nanoindenter column.

The shields of the coaxial connectors are grounded on the body only.

A diode is used to illuminate the sample before capacitive measurements (see section 7.3.3, page 252).

Tip

The tip used for capacitive measurements is a boron-doped diamond (BDD) truncated cone with a 30° opening angle, leading to a 5 µm diameter flat punch. The dopant content in the tip is high enough for the tip to show a metal-like behaviour. In contact with an n-doped silicon and its oxide, the corresponding MOS stack is schematized in figure 7.11.

Impedance-meter

The Impedance-meter used for the measurements is a E4980A LCR meter from Agilent with frequency range from 20 Hz to 2 MHz and admittance range from 1 aS to 1000 ES.

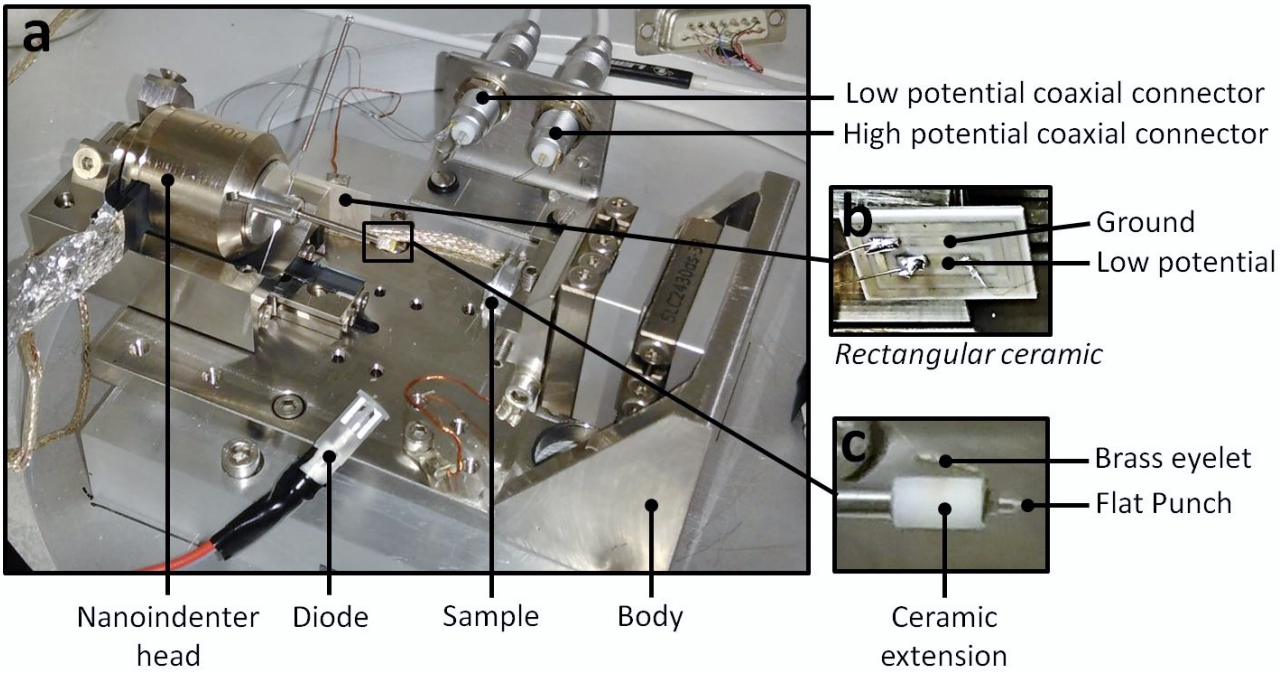

Figure 7.10: Experimental set-up for capacitive measurements.

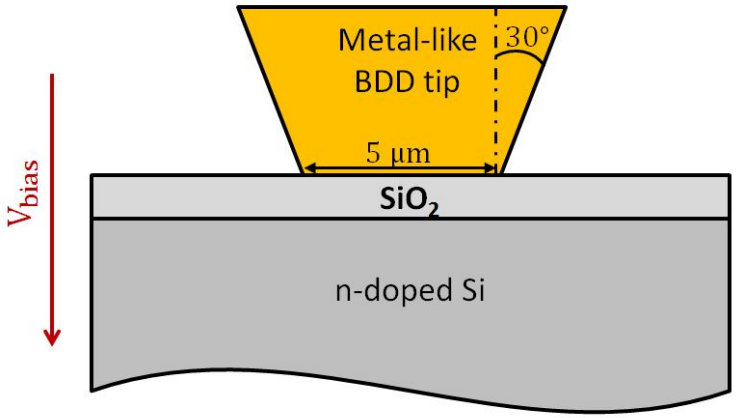

Figure 7.11: Schematic of MOS stack obtained when the tip is in contact with the sample.

7.3.2 Material description

Samples were fabricated at the CIME Nanotech platform from Grenoble INP and Joseph Fourier University (Grenoble). Silica layers with different thicknesses have been grown on n-doped silicon wafer. The donor concentration has been measured to be $\sim 6.5 \cdot 10^{14}$ cm^{-3} by resistive measurements ($\rho = 6.8$ Ω.cm). Each sample has been prepared as follows:

- A first cleaning step
- A dry thermal oxidation to produce a first 49 nm silica layer on silicon. Dry thermal oxidation is known to reduce the defects at the oxide/semiconductor interface.

- An additional silica deposition by Plasma-Enhanced Chemical Vapor Deposition (PECVD) to produce silica layer with various thicknesses.

The exact cleaning and elaboration conditions are given in appendix E (page 297).
A summary of the resulting samples is given in table 7.1. Thicknesses and refraction indexes have been measured by ellipsometry.

Sample name	**Thermal oxide thickness**	**PECVD oxide thickness**	**Total oxide thickness**
49nm	49 nm	-	49 nm
157nm	49 nm	108 nm	157 nm
184nm	49 nm	135 nm	184 nm
481nm	49 nm	432 nm	481 nm
974nm	49 nm	925 nm	974 nm

Table 7.1: Sample summary.

7.3.3 Measurement procedure

Capacitive measurements

In order to perform capacitive measurements, the 5 µm flat punch is manually put in contact with the surface, without indenting the oxide. Once the surface is reached, the nanoindenter head is controlled in force to keep a tight contact with the surface. The pressure applied to the sample has been estimated at $\sim$ 0.1 MPa.
For the capacitive measurements, a relatively high V_{AC} of 2.5 V has been chosen, in order to reduce the noise of the measured signal. The signal-to-noise ratio was also improved by working at high frequency (1-2 MHz).
The MOS structure is initially set in inversion regime. To do so, a large positive V_{DC}^{inv} bias is set for 5 s, while the sample is exposed to light (in order to enhance the inversion layer formation). Then measurements are performed for V_{DC} bias going back and forth from V_{DC}^{inv} (inversion) to V_{DC}^{acc} (accumulation), with a 1 V step. Between each measurements the inversion layer is regenerated by polarising the sample at V_{DC}^{inv}. A schematic of this "pulse" procedure is given in figure 7.12 A. The pulse duration was set at 1 s. V_{DC}^{inv} and V_{DC}^{acc} voltages are optimized for each sample (table 7.2).

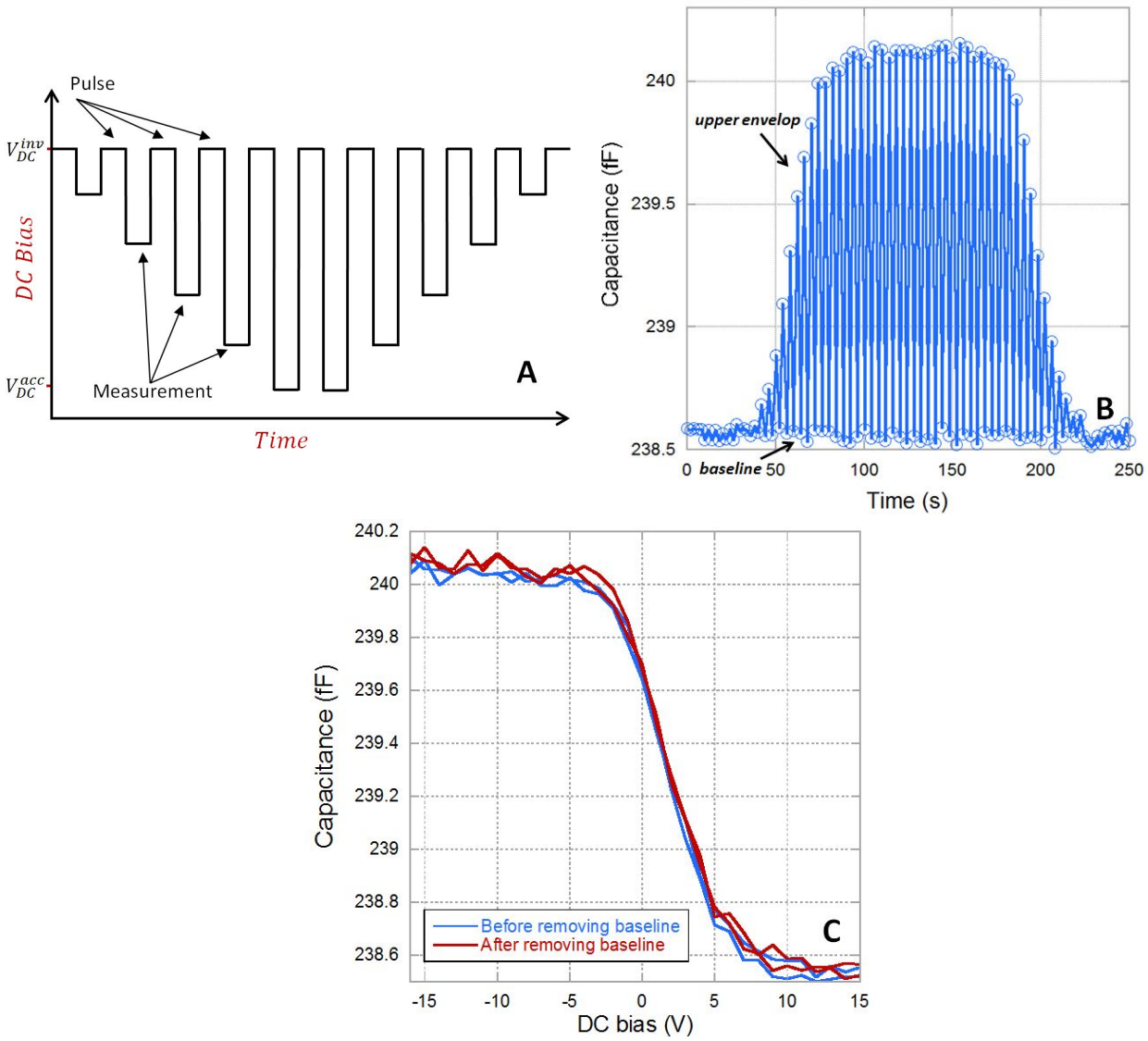

Figure 7.12: A: Schematic of V_{DC} pulse during capacitive measurements and B: measured values of capacitance (184nm sample) with C: corresponding extracted C-V curve before and after removing the baseline.

Figure 7.12 B provides an example of the capacitances measured during such a voltage scan. C-V curves are extracted from the upper envelop of the capacitance-versus-time curve (figure 7.12 C, blue curve).

The lower envelop corresponds to capacitance measurements at the inversion regime and it is expected to be constant. However, a slight drift can occur during the measurements. When measurements are intensively repeated at the same location of the sample, dielectric alteration can also cause a modification of this envelop. In order to take into account the drift effect, the baseline corresponding to this envelop is removed from the C-V curves (figure 7.12 C, red curve). However, the drift effect is negligible in most cases.

Sample	V_{DC}^{inv}	V_{DC}^{acc}
49nm	10 V	-12 V
157nm	18 V	-12 V
184nm	15 V	-16 V
481nm	28 V	-13 V
974nm	37 V	-16 V

Table 7.2: Capacitive measurements settings.

Misalignment correction

For data analysis, the knowledge of the misalignment between the flat punch and the surface is crucial (figure 7.13 A). For that purpose, surface detections have been performed with a 3x3 matrix. A representation of the obtained surface inclination is given in figure 7.13 B. The angle between the flat punch and the sample surface is computed from the vector normal to the corresponding surfaces. The misalignment angle was extracted to be ~ 0.01 rad ($\sim 0.6°$).

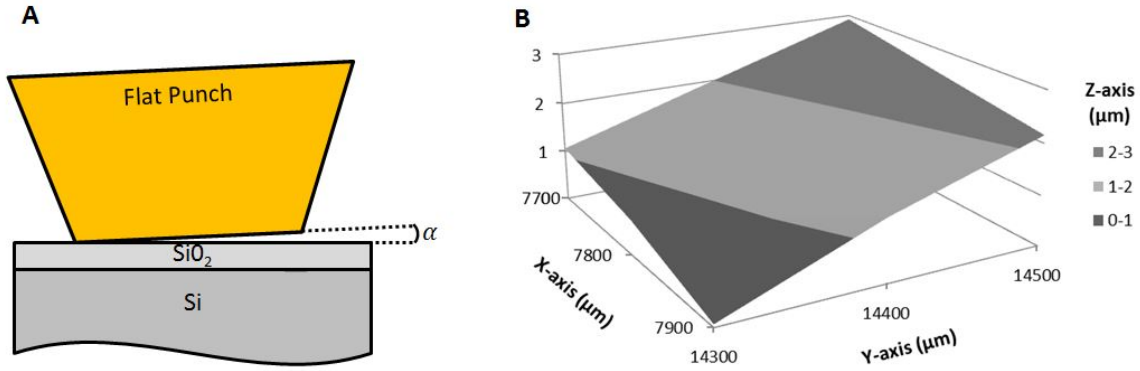

Figure 7.13: A: schematic of the misalignment between the flat punch and the surface and B: measured surface inclination.

7.4 Experimental results

7.4.1 C-V curves

Using the procedure described above, C-V curves have been extracted for the 49nm, 157nm, 184nm, 481nm and 974nm samples. An example of such curves is given in figure 7.12 C. The measured capacitance C_m ranges from 220 to 240 fF, depending on the tested sample. The phase ϕ of the measured signal was found to be around 89.6-89.8°, which ensures the leak

conductance to be negligible.

The value of the measured capacitance $C_{measured}$ does not only come from the MOS capacitance C_{MOS}, but is mainly due to a stray capacitance C_{stray}, which comes from various capacitive coupling on the experimental set-up. This stray capacitance is in parallel with the MOS capacitance, and thus $C_{measured} = C_{stray} + C_{MOS}$.

Figure 7.14 provides examples of results obtained on two different locations for each sample. For each curve, the minimal value of the capacitance C_{min} (inversion regime) has been subtracted to the measured capacitance.

This capacitance shift has been calculated for three different locations distant from 50 µm for each sample (table 7.3). The percentage corresponding to the stray capacitance C_{stray} can also be estimated, by considering that the stray capacitance equals the measured capacitance in the accumulation regime. This percentage is less than 0.1 % (except for the 974nm sample where it is $\sim$ 1 %), making negligible the shift capacitance between two locations. This result is promising, since it shows that in this set-up the measurement is not sensitive to the localisation on the sample. However, measurements have been performed in the center of large samples, and the influence of edge effects as not been investigated during this work.

Results from figure 7.14 are highly reproducible. All samples provide C-V curves with the three accumulation, depletion and inversion regimes, even though an increase in capacitance is found at high DC bias for the 481nm sample. As expected, the amplitude of the C-V curves strongly decreases with increasing oxide layer thickness, ranging from 3.5 fF to 200 aF for oxide thickness from 49 nm to 974 nm.

Samples are also characterized by almost no hysteresis between the decrease and the increase in voltage, except for the 49nm sample. This hysteresis is the signature of charged defects at the silica/silicon interface.

Sample name	$\delta \mathbf{C}^{\mathbf{acc}}_{\mathbf{measured}}$	**Percentage of $\mathbf{C_{stray}}$**
49nm	0.06 ± 0.02 fF	0.03 %
157nm	0.1 ± 0.08 fF	0.05 %
184nm	0.04 ± 0.02 fF	0.02 %
481nm	0.08 ± 0.04 fF	0.04 %
974nm	2 ± 0.5 fF	1 %

Table 7.3: Variation $\delta C^{acc}_{measured}$ of the capacitance between different locations spaced of $\sim$ 50 µm and corresponding variation of the stray capacitance C_{stray}.

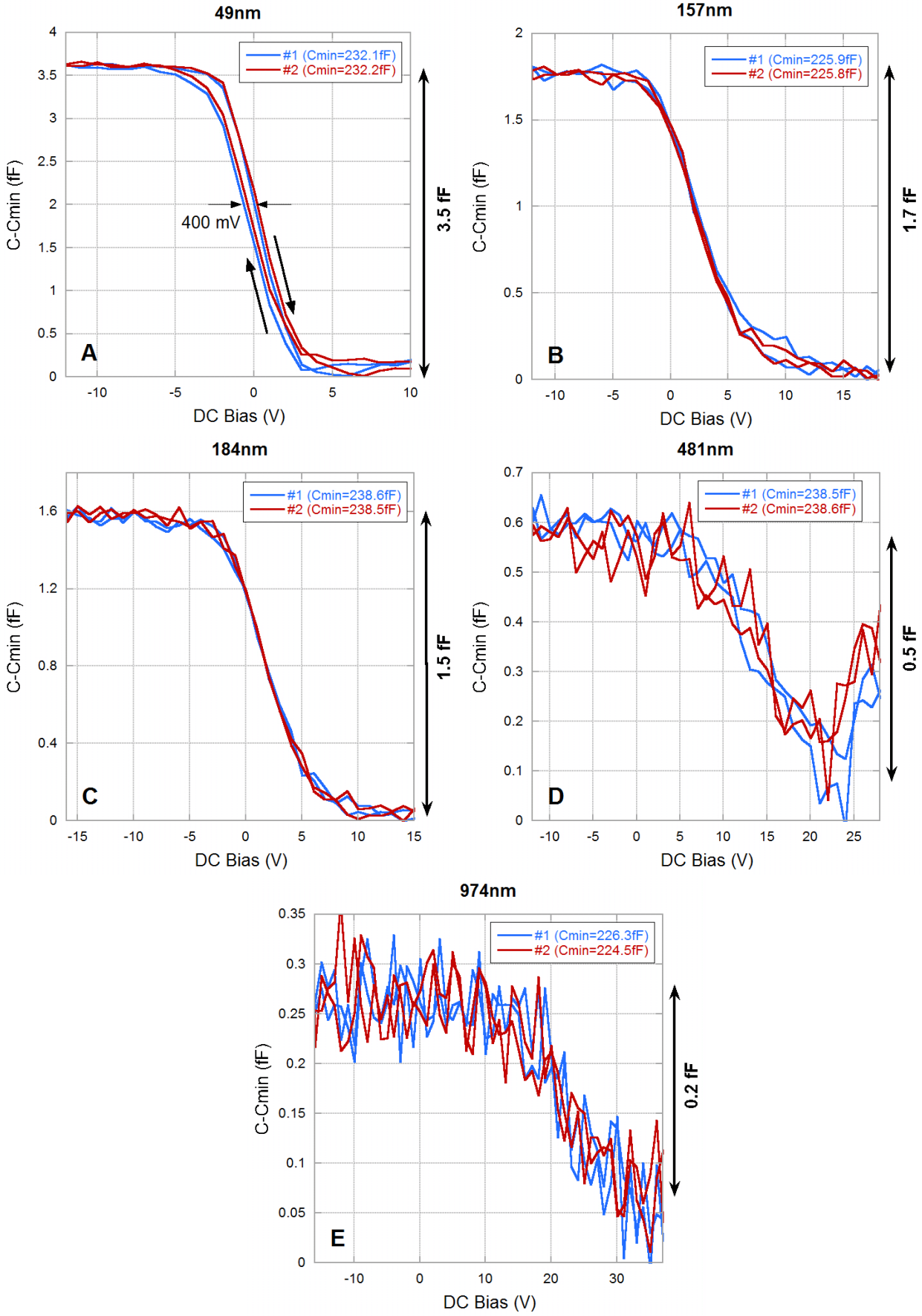

Figure 7.14: CV-curves at 2 MHz for 49nm (A), 157nm (B), 184nm (C), 481nm (D) and 935nm (E) samples.

7.4.2 Effect of dielectric degradation

During capacitive measurements, high electric fields are applied to the oxide layer. Table 7.4 gives the value of the maximal electric field applied to the oxide for each sample, and the corresponding percentage to the silica dielectric strength (~ 10 MV.cm^{-1}). For each sample, the applied dielectric field corresponds to an important fraction of the dielectric strength of silica. As a result, alteration of the oxide is supposed to occur during these capacitive measurements. Within the frame of this work, oxide alteration has been seen in the particular case where successive capacitive measurements are performed on the same location, especially for the 49nm sample, where the applied electric field is the highest. Figure 7.15 A provides an example of such an alteration during six successive measurements on the 49nm sample. The C-V curves are modified, with an increasing hysteresis, and with a decrease of the bias at which the depletion regime starts. During the last measurements, a dip is observed at the beginning of the inversion regime ($V_{DC} \sim 3$V). All these modifications come with an increase of the measured conductance during the successive tests (figure 7.15 B), which is the signature of dielectric degradation.

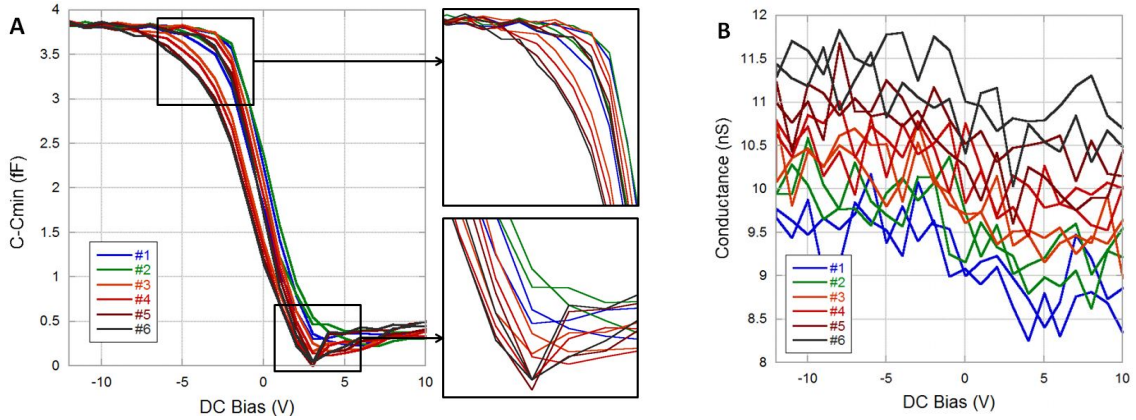

Figure 7.15: Evidence of oxide degradation on capacitance (A) and conductance (B) curves during successive capacitive measurements on the same location on 49nm sample.

Sample	Maximal electric field	Percentage of dielectric strength
49nm	2.45 MV.cm^{-1}	25 %
157nm	1.14 MV.cm^{-1}	11 %
184nm	0.87 MV.cm^{-1}	9 %
481nm	0.58 MV.cm^{-1}	6 %
974nm	0.38 MV.cm^{-1}	4 %

Table 7.4: Electric field applied to the oxide layer during capacitive measurements.

7.5 Analytical modelling of C-V curves

Since the stray capacitance C_{stray} is unknown, quantitative analysis cannot be directly performed on C-V curves. This issue can be overcome by analysing the amplitude of the measured C-V curves $\Delta C_{measured}$, which corresponds to the difference between the capacitance in accumulation and in inversion regimes (equation 7.7, figure 7.16). Table 7.5 gives the amplitudes obtained for each sample. The error bar corresponds to the noise of the measurement.

$$\Delta C_{measured} = C_{MOS}^{accumulation} - C_{MOS}^{inversion} \tag{7.7}$$

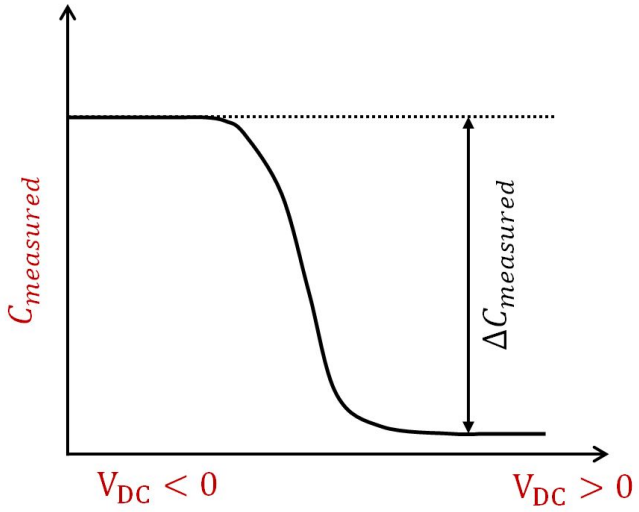

Figure 7.16: Schematic of C-V curve amplitude.

Sample	$\Delta C_{measured}$
49nm	3.5 ± 0.1 fF
157nm	1.7 ± 0.05 fF
184nm	1.5 ± 0.1 fF
481nm	0.5 ± 0.07 fF
974nm	0.2 ± 0.05 fF

Table 7.5: C-V amplitude measured for each sample.

In this section, efforts are made to relate this amplitude to magnitudes which depend only on sample properties. In that purpose, analytical models, which take as an input the sample properties, are derived in order to model the capacitance amplitude $\Delta C_{analytic}$.

7.5.1 Simple analytical model

As already discussed, in the accumulation regime, the MOS capacitance corresponds to the oxide capacitance C_{ox}. In the inversion regime it corresponds to the oxide capacitance C_{ox} in series with the capacitance of the depletion layer C_{dep}. This leads to equation 7.8. C_{ox} and C_{dep} are respectively described in equations (7.2) and (7.6), with the depletion layer width W_i given by equation (7.5). The theoretical value of the C-V amplitude can then be computed, using the tabulated values $\epsilon_{ox} = 3.9$ and $\epsilon_S = 11.68$ for the dielectric constants of silica and silicon and $n_i = 1 \cdot 10^{10}$ cm $^{-3}$ for the intrinsic carrier concentration in silicon at room temperature.

$$\Delta C_{analytic} = C_{ox} - \frac{C_{ox} C_{dep}}{C_{ox} + C_{dep}} \tag{7.8}$$

Analytical results are shown in figure 7.17 (red curve). They strongly differ from experimental $\Delta C_{measured}$ (blue curve): on the thinnest sample the amplitude values from the analytical expression are up to 3.5 times higher than the amplitude measured.
However, the analytical expression above does not take into account the slight misalignment between the flat punch and the sample surface (figure 7.18 A). This simple analytical model has then been extended in order to account for the air wedge between the flat punch and the sample surface, due to this misalignment.

7.5.2 Analytical model with a misalignment between the flat punch and the sample

Capacitance contributions

Let us consider a flat punch making an angle α with a flat oxide + semiconductor stack (figure 7.18 A). The total measured capacitance $C_{measured}$ is constituted of the stray capacitance C_{stray} in parallel with the tip-to-sample capacitance $C_{tip-sample}$ (figure 7.18 B). This tip-to-sample capacitance is constituted of elementary capacitances $dC_{air}(x)$ (coming from the air wedge) in series with the elementary capacitances $dC_{sample}(x)$ (coming from the sample) (figure 7.18 C). Each elementary capacitance $dC_{tip-sample}(x)$ is given by equation (7.9).

$$dC_{tip-sample}(x) = \left(\frac{1}{dC_{sample}(x)} + \frac{1}{dC_{air}(x)}\right)^{-1} \tag{7.9}$$

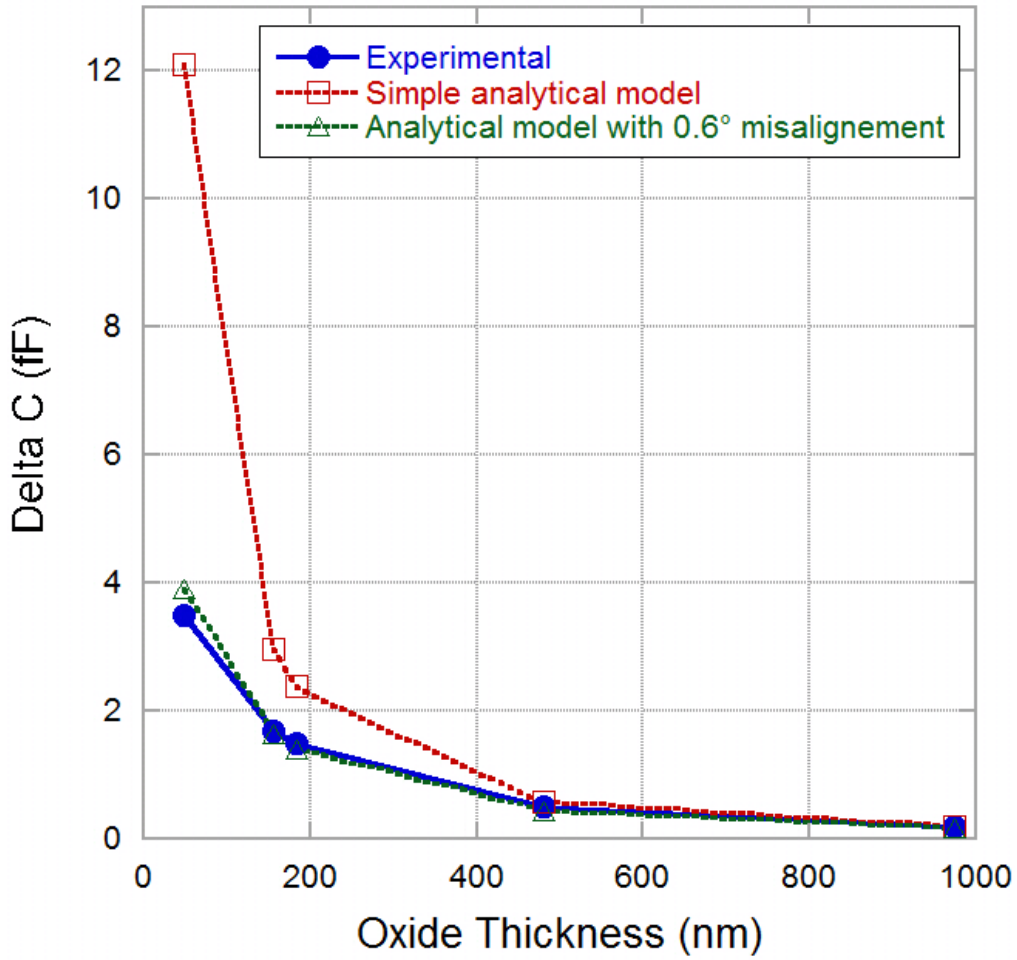

Figure 7.17: Capacitance amplitude from experimental C-V curves (blue) and analytical expressions with no angle (red) and a 0.6° angle (green) between the flat punch and the sample surface.

Elementary capacitance expression

Because α is small (~ 0.01 rad), the plate capacitor model can be applied to these elementary capacitances (the stray field at the open-end can be neglected). Within this hypothesis, these elementary capacitances can be expressed as follows:

- The elementary capacitance $dC_{sample}(x)$ is given by equation (7.10), with C^S_{sample} the sample capacitance per unit area and $dS(x)$ the elementary surface area, which will be detailed later on. At this stage, C^S_{sample} is generic and can either account for the sample capacitance in the accumulation regime ($C^{S,acc}_{sample}$) or in the inversion regime ($C^{S,inv}_{sample}$).

$$dC_{sample}(x) = dS(x) \cdot C^S_{sample} \tag{7.10}$$

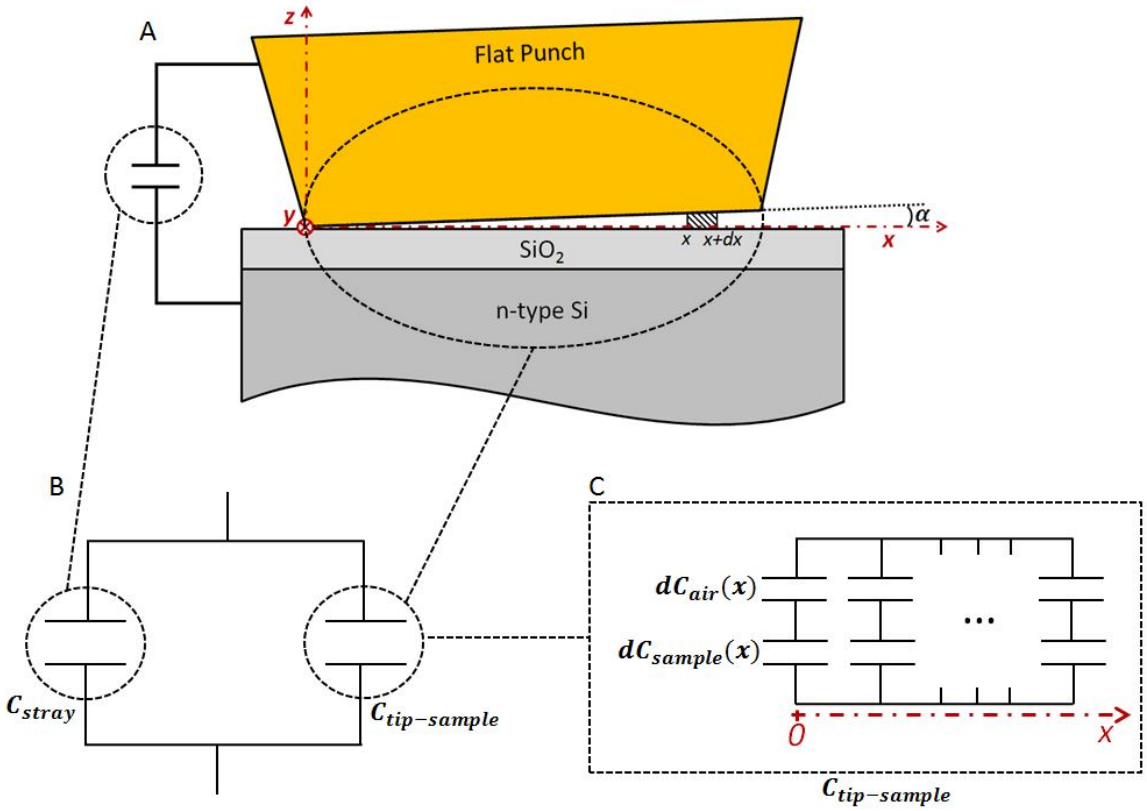

Figure 7.18: Schematic of the misalignment between the flat punch and the sample surface (A) and electrical diagram corresponding to the measured capacitance $C_{measured}$ (B) and the tip-to-sample capacitance $C_{tip-sample}$ (C).

- The elementary capacitance $dC_{air}(x)$ is given by equation (7.11), with $t(x)$ the height of the air wedge.

$$dC_{air}(x) = \frac{dS(x)\epsilon_0}{t(x)} \tag{7.11}$$

The surface element $dS(x)$ corresponds to the hatched sector in figure 7.19 A. In cylindrical coordinate, $dS(x)$ can be expressed by equation (7.12), with R the flat punch radius and θ the angle as defined in the figure. The height of the air wedge $t(x)$ corresponds to the height of the hatched sector in figure 7.19 B. In cylindrical coordinate, it can be expressed by equation (7.13).

$$dS(\theta) = R^2(1 - cos(2\theta))d\theta, \quad \theta \in [0; \pi] \tag{7.12}$$

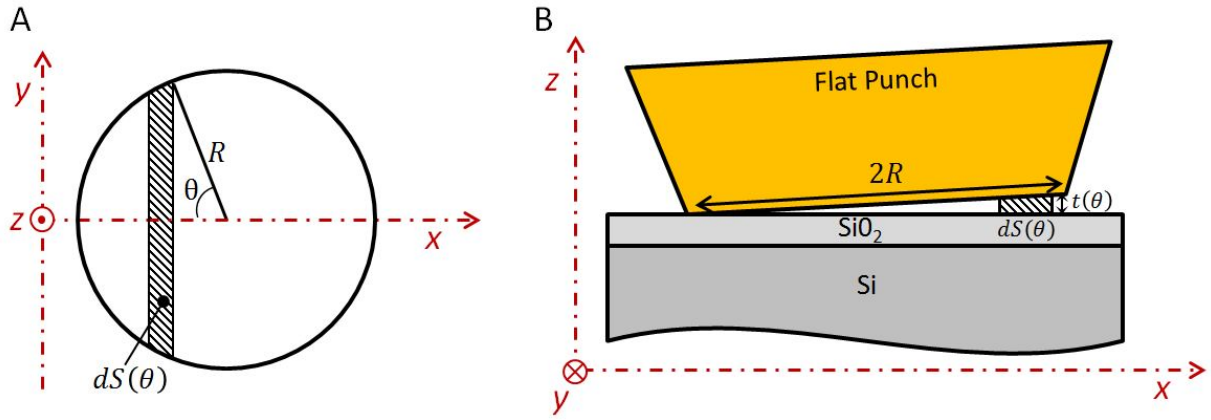

Figure 7.19: Representation of surface and height elements in both planes (y,x) (A) and (z,x) (B).

$$t(\theta) = R\tan(\alpha)(1 - cos(\theta)) \tag{7.13}$$

As a result, the elementary capacitance $dC_{tip-sample}$ is given by equation 7.14.

$$dC_{tip-sample}(\theta) = \frac{C^S_{sample} R^2 (1 - cos(2\theta)) d\theta}{1 + \frac{C^S_{sample}}{\epsilon_0} R\tan(\alpha)(1 - \cos(\theta))}, \quad \theta \in [0; \pi] \tag{7.14}$$

The tip-to-sample capacitance $C_{tip-sample}$ is obtained by integrating $dC_{tip-sample}$ over $\theta \in [0,\pi]$.

Analytical capacitance amplitude computation

Finally, the analytical capacitance $C_{analytic}$ is the sum of the tip-to-sample capacitance $C_{tip-sample}$ and the stray capacitance C_{stray}. When the MOS stack is in accumulation regime, $C^S_{sample} = C^{S,acc}_{sample}$, while $C^S_{sample} = C^{S,inv}_{sample}$ in the inversion regime (equation 7.15).

$$C_{analytic} = C_{stray} + \int_0^{\pi} \frac{C^S_{sample} R^2 (1 - \cos(2\theta))}{1 + \frac{C^S_{sample} R\tan(\alpha)}{\epsilon_0}(1 - \cos(\theta))} \tag{7.15}$$

As previously, the stray capacitance can be removed by calculating the analytical capacitance amplitude $\Delta C_{analytic}$, which is the difference between the analytical capacitance in the accumulation regime and the analytical capacitance in the inversion regime (equation 7.16). $\Delta C_{analytic}$ can then be expressed by equation (7.17).

$$\Delta C_{analytic} = C_{analytic}^{accumulation} - C_{analytic}^{inversion} \tag{7.16}$$

$$\Delta C_{measured} = \Delta_{inv \to acc} \int_0^{\pi} \frac{C_{sample}^{S} R^2 (1 - \cos(2\theta))}{1 + \frac{C_{sample}^{S} R \tan(\alpha)}{\epsilon_0} (1 - \cos(\theta))} d\theta \tag{7.17}$$

The misalignment angle α has been experimentally measured ($\alpha \sim 0.01$ rad), as described in paragraph 7.3.3 (page 254).

Analytical results coming from equation (7.17) are given in figure 7.17 (green curve) and show remarkable agreements with the experimental results.

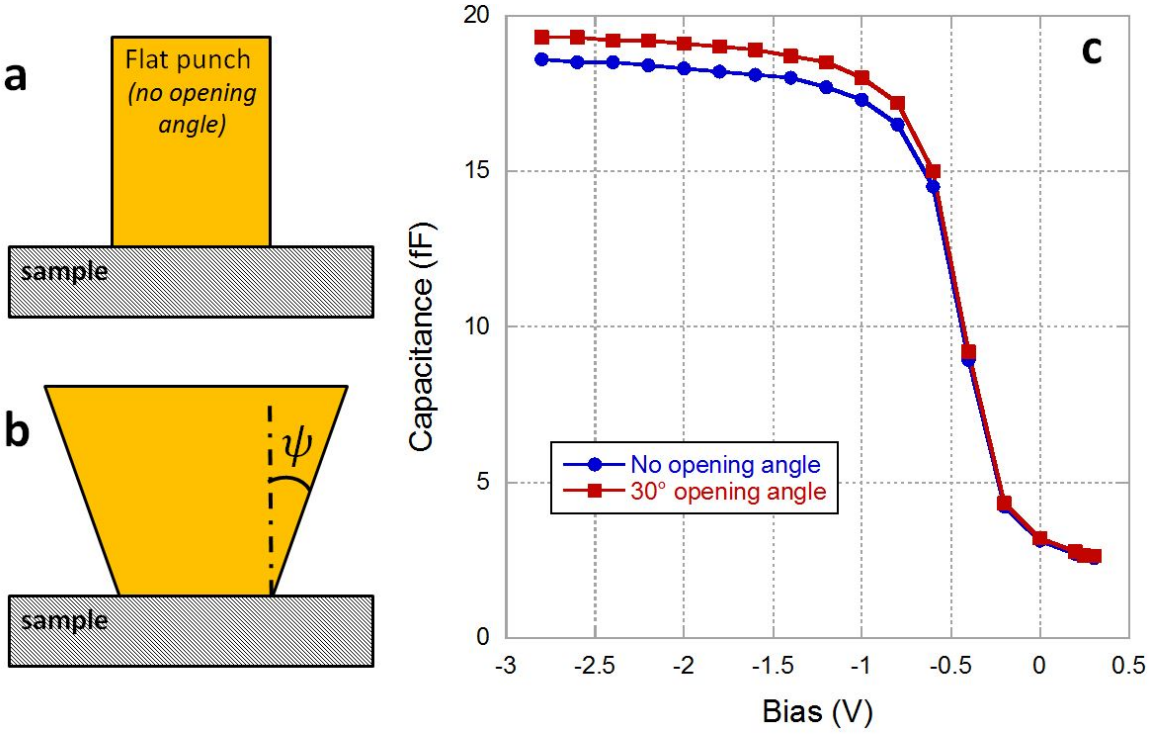

Figure 7.20: C-V curves from ATHENA simulations (c) for a cylinder flat punch (no opening angle, a) and a flat punch with an opening angle $\psi = 30°$.

In this analytical model, the flat punch is considered as a perfect cylinder (figure 7.20 A). In reality, it is a truncated cone with a 30° opening angle (figure 7.20 B). This opening angle is supposed to add a parallel capacitance to the total measured capacitance. However, numerical simulations with ATHENA software from SILVACO (performed at CIME Nanotech platform) have shown that the effect of this angle on the capacitance was less than 5 % compared to the same simulation with a cylinder flat punch (figure 7.20).

7.6 Conclusion and prospects for capacitive measurements with a nanoindenter

In this chapter, capacitive measurements have been successively performed with the experimental nanoindentation set-up described in chapter 3 (page 81). Measurements have been conducted on MOS structures with oxide size from 49 to 925 nm. Experimental results have shown very good agreements with analytical model.

In this study, experiments have been conducted at room atmosphere on bulk samples. However, the nanoindentation set-up developed within the frame of this thesis can be integrated within a FEG-SEM, which allows precise positioning on small scale objects. This opens up the prospect of being able to measure dielectric properties of small scale systems.

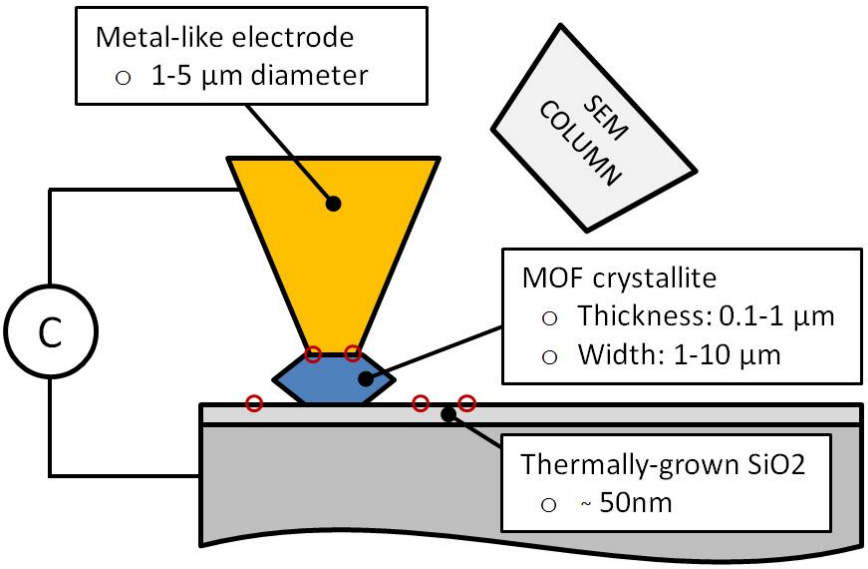

Figure 7.21: Principe of *in situ* SEM capacitance measurements of MOF crystallite. Red circles corresponds to different measurement locations, which allows the deconvolution of the capacitance signal and the crystallite geometry.

In particular, this ability could be used for dielectric characterisation of Metal Organic Framework (MOF) material, which corresponds to a research topic of our group. Because MOF materials are usually processed as powders, their accurate characterisation for dielectric applications is challenging due to the presence of porosity. Thanks to the *in situ* FEG-SEM nanoindentation set-up, the dielectric response of isolated MOF crystallites could be measured and deconvoluted from tip and crystallite geometries (figure 7.21).

Moreover, thanks to the nanoindenter, the load applied to the crystallite during capacitive measurements can be perfectly controlled. This is particularly useful to characterize Spin-Cross Over MOF (MOF-SCO). For these materials the spin crossover depends on physical stimuli (mechanical, thermal, optical, magnetic...). Reversible switching of their dielectric response under thermal cycles makes them excellent candidate for "molecular memory" applications [227]. Such reversible switching of the dielectric response is also expected for MOF-SCO under mechanical loading.

Conclusions and prospects

Within the frame of this thesis a nanoindenter *in situ* FEG-SEM coupled with electrical measurements has been developed and tested on various experimental case studies. The main results of this work can be summarized into five key points:

1. The first objective of this thesis was the development of the nanoindentation set-up. During the first year of this project, a nanoindenter *in situ* FEG-SEM coupled with electrical measurements has been successfully developed in SIMaP lab. Thanks to the SEM integration, this device allows indent positioning with a precision better than 100 nm. This enables the mechanical study of submicrometric systems. The electrical apparatus used for resistance measurements can measure resistance changes over 10 decades, with acquisition rate up to 1 kHz. This allows the monitoring of fast mechanical events. A special Blitz 3D nanoindentation method allows to perform large maps and profiles of mechanical properties across samples, with high throughput as compared to conventional indentation methods.

2. This *in situ* FEG-SEM nanoindenter has then been tested on a large variety of samples, from complex architectured materials (duplex stainless steel composite and AlN coated polymer scaffolds) to multiphase alloys with submicrometric phase (ferritic steel with cementite carbides), samples with composition gradients (dissimilar metal weld) and submicrometric crystallites. These studies have shown the convenience of *in situ* SEM Inforce nanoindenter to measure mechanical properties of small individual phases or 3D structures.

3. In particular, this *in situ* FEG-SEM nanoindenter has been used for nanoindentation and nanocompression of a large number of submicrometric gold islands on sapphire, obtained by solid state dewetting. The stochastic nature of the mechanical behavior of gold islands under mechanical testing has been underlined. However, despite this stochastic behavior,

deterministic mechanical laws have been extracted from a large set of nanocompression and nanoindentation experiments. This gives a methodology to obtain the lower-bound quantitative behavior for such small scale materials. BCDI experiments to investigate crystals state before and after mechanical loading have also been given. Data corresponding to these experiments are not fully analysed, but qualitative results are promising. In particular, we demonstrated that defects are nucleated prior to the displacement burst. Therefore, critical stresses of displacement bursts are the signature of intense plastic activity (softening) and not dislocation nucleation.

4. In parallel with the investigation of the mechanical properties of small scale systems thanks to *in situ* SEM nanoindentation, resistive-nanoindentations have been performed on various samples. Resistive electrical measurements have been performed during indentation of noble metal (Au) and natively oxidised metals (Cu, Al), either as bulk single crystals or as polycrystalline thin films. Both BDD and WC tips have been used. Different local environment have also been assessed (room atmosphere, intermediate and high vacuum). Qualitative results emphasise the importance of the oxide layer on the electrical response during indentation: In the presence of an oxide layer, strong electrochemical reactions seem to occur at the contact. When no oxide is involved at the tip-to-sample contact (Au/BDD), resistance values during indentation are found to continuously decrease with increasing contact depth. The measured resistance has been fully described by an analytical model, thus allowing quantitative analysis. A numerical model has also been derived. After a calibration on a bulk Au single crystal, contact area have been successfully computed from resistive-nanoindentation of a gold thin film. Thus, the main objective of this part has been reached.

5. The ability of the set-up to perform capacitive measurements have finally been assessed. Capacitive measurements have been performed on MOS structures with various oxide thicknesses. Experimental results have shown good agreements with analytical model. The main advantage of capacitive measurements with a nanoindenter is that the stray capacitance is expected to be roughly constant during measurements. It can then be more easily subtracted, compared to capacitive measurements with AFM. Moreover, due to the probe size, capacitive measurements can be performed with driven frequency around 1-2 MHz, without dedicated electronics. However, capacitive nanoindentation obviously comes with a loss in spatial resolution compared to capacitive AFM.

This work provides the potential for further developments and investigations:

- **In terms of instrumental development:** Due to a lack of time, the "5-axes" set-up described in chapter 3 (page 81) has not been fully implemented. However, it will be a major improvement compared to the "3-axes" system. Indeed, this set-up will allow the use of *in situ* SEM analytical facilities such as EDX or EBSD.

- **In terms of mechanical investigation of small scale systems:** The coupling of BCDI measurements with nanoindentation experiments is of considerable interest. In order to fully understand the relationship between crystal defects and mechanical properties, a sufficient statistic of BCDI data of crystallites before and after a mechanical loading is required.

- **In terms of resistive nanoindentation:** Main efforts must be done to understand the electrical contact between the tip and the sample. A serious investigation of the electrochemical mechanisms involved at the tip-to-sample contact in the presence of an oxide layer is required. One of the aim will be to optimize the bias applied at the contact in order to reduce the effects of electrochemical mechanisms. In order to improve the understanding of the resistance-versus-depth curves, the development of numerical models can also be beneficial. Finally, it can be interesting to test other materials for the indentation tip, such as other carbides tip (VC) or even BDD tip electrically functionalized by conductive coating.

- **In terms of capacitive measurements:** The integration *in situ* SEM of the set-up opens up the prospect of being able to measure dielectric properties of small scale systems. In particular, this ability can be used for dielectric characterisation of Metal-Organic-Framework (MOF) material, which corresponds to a research topic of our group. Since with this set-up the load applied to the sample can be controlled during capacitive measurements, the dependence of dielectric properties on mechanical loading could also be investigated.

Appendix A

Interface for "square head" monitoring

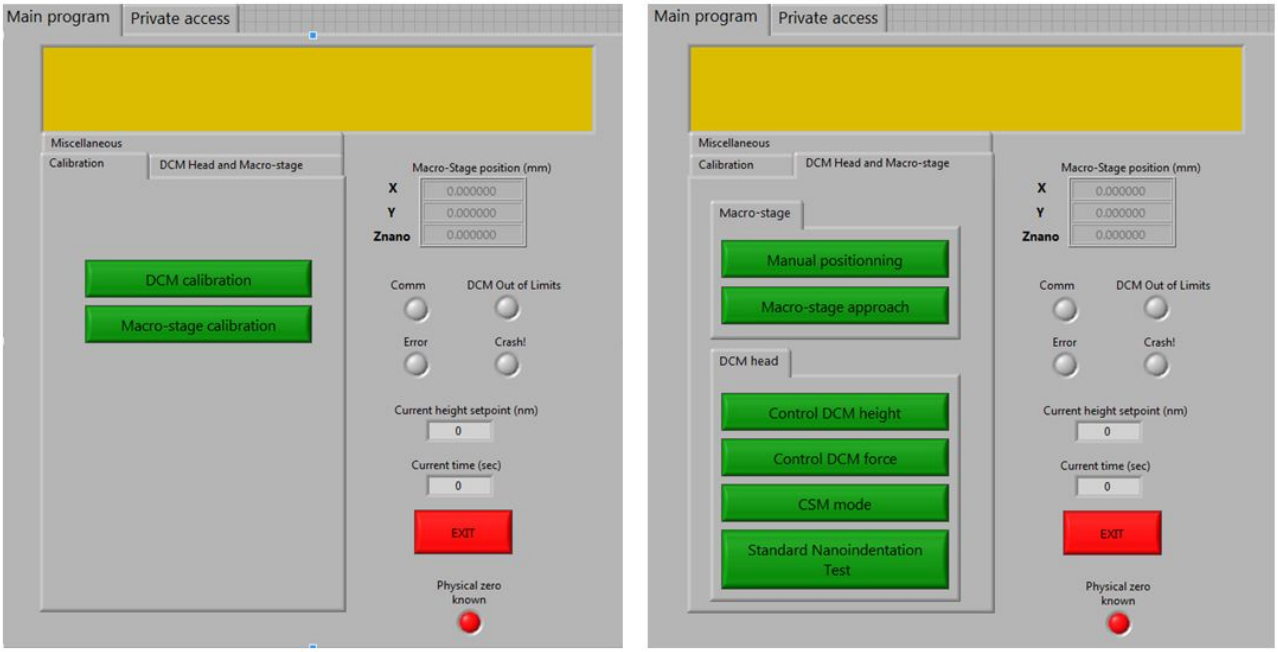

Figure A.1: Home-made labview interface for the square head monitoring (1)

The Labview program (figure A.1) for the square head monitoring is composed of:

- The DCM calibration: this corresponds to the scanning of the whole displacement range of the nanoindenter in order to obtain the column stiffness and to see eventual column damage (figure A.2 A).
- The macro-stage calibration: this corresponds to the initialisation of the SmarAct translators. After this step the physical zeros of translators are known (figure A.2 B).
- The manual positioning of the macro-stage: the SmarAct translators are moved toward the position set-point (figure A.3).

- The macro-stage approach: the Z axis is moved until the surface is reached (figure A.4).
- The control of the DCM height: the nanoindenter head is controlled in displacement (close loop) and is moved toward the displacement set-point (figure A.5 A).
- The control of the DCM force: the nanoindenter head is controlled in force (close loop) and is moved toward the force set-point (figure A.5 B).
- The control of the CSM mode: CSM frequency, CSM amplitude range and CSM force can be chosen (figure A.6).
- The standard nanoindentation test: A single indent as well as a matrix of indents can be performed (figure A.7 A). The test is constituted of a first thermal drift step (figure A.7 B). When the drift is below a target value (typically 0.05 nm.s^{-}1) the head goes to the first location of the matrix and a fine surface approach is performed (figure A.8 A). The loading is conducted either at constant strain rate or at constant loading rate (figure A.8 B). An holding step is then performed at maximal load (figure A.9 A), and then a first unloading down to 10 % of the maximal load is achieved. The drift is recorded for further post treatment, before final unloading. Then the head goes to the next location of the matrix, following the pattern of figure A.10. CSM mode is avalaible for both fine surface approach and nanoindentation (figure A.9 B).

Additional miscellaneous options allows to change the sample name, to add comments to the sample file, to change the acquisition rate for data recording, to set the last surface coordinates or to tare the labview time.
Safety limits for the head displacement range and the SmarAct translators displacement range are set at the opening of the program with the initial settings for the nanoindenter head (figure A.11).

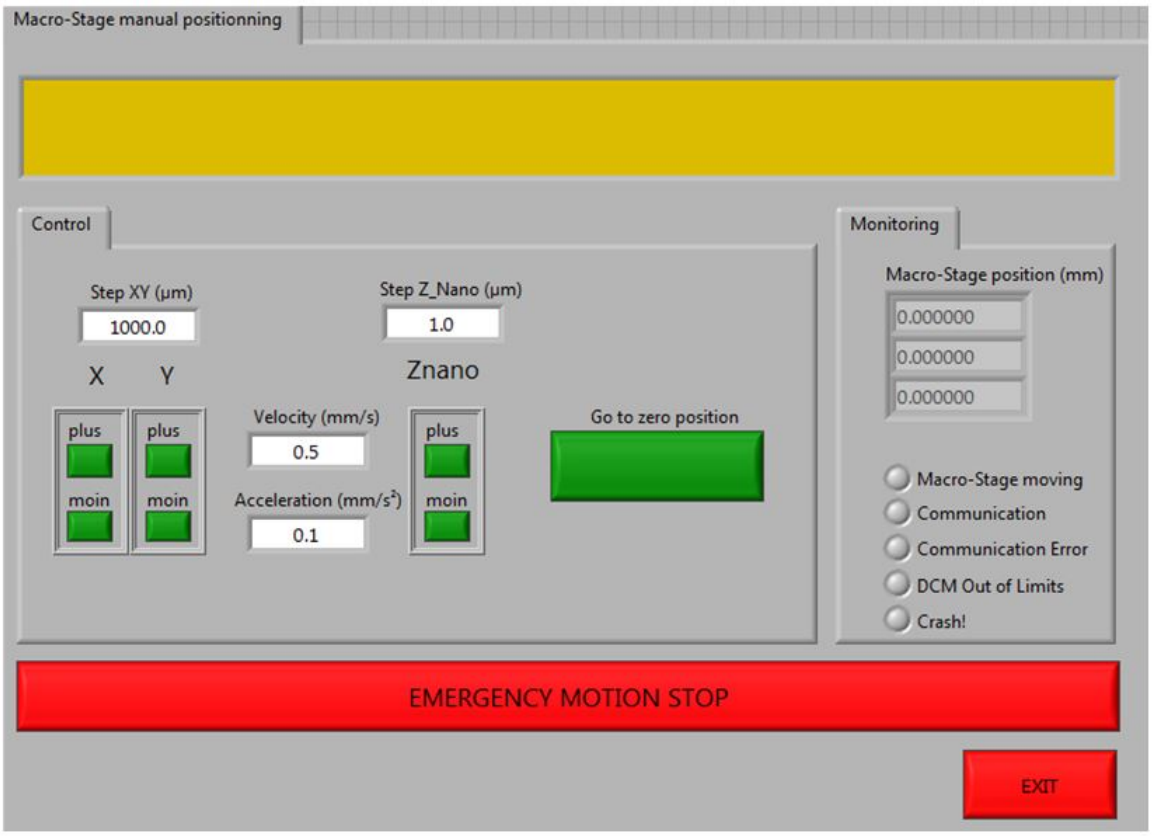

Figure A.2: Home-made labview interface for the square head monitoring (2)

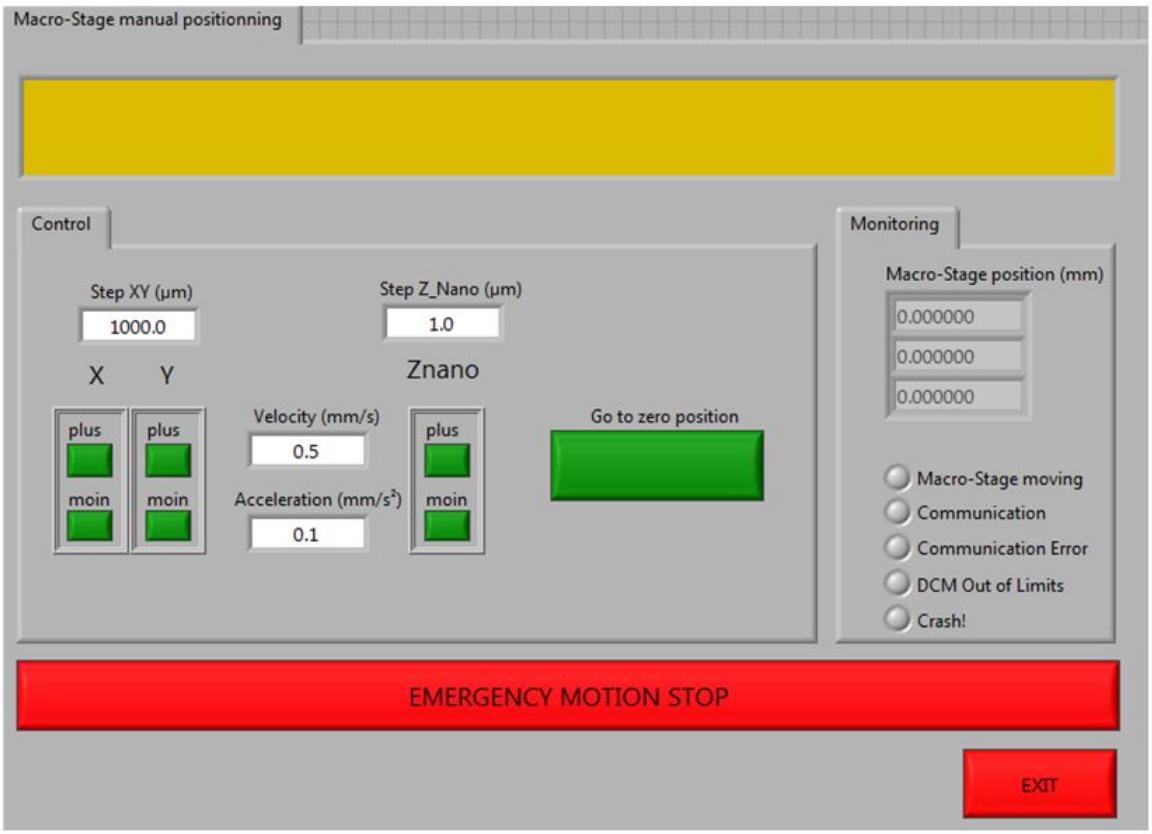

Figure A.3: Home-made labview interface for the square head monitoring (3)

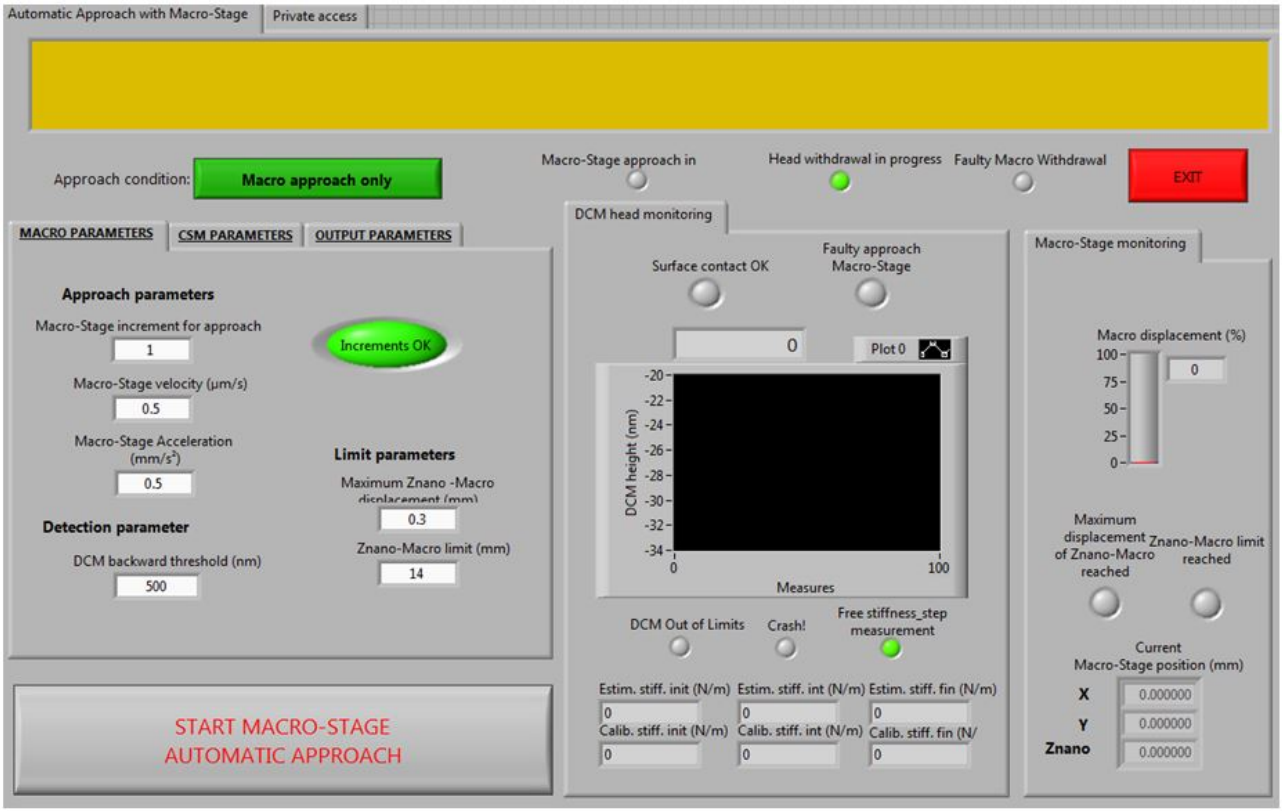

Figure A.4: Home-made labview interface for the square head monitoring (4)

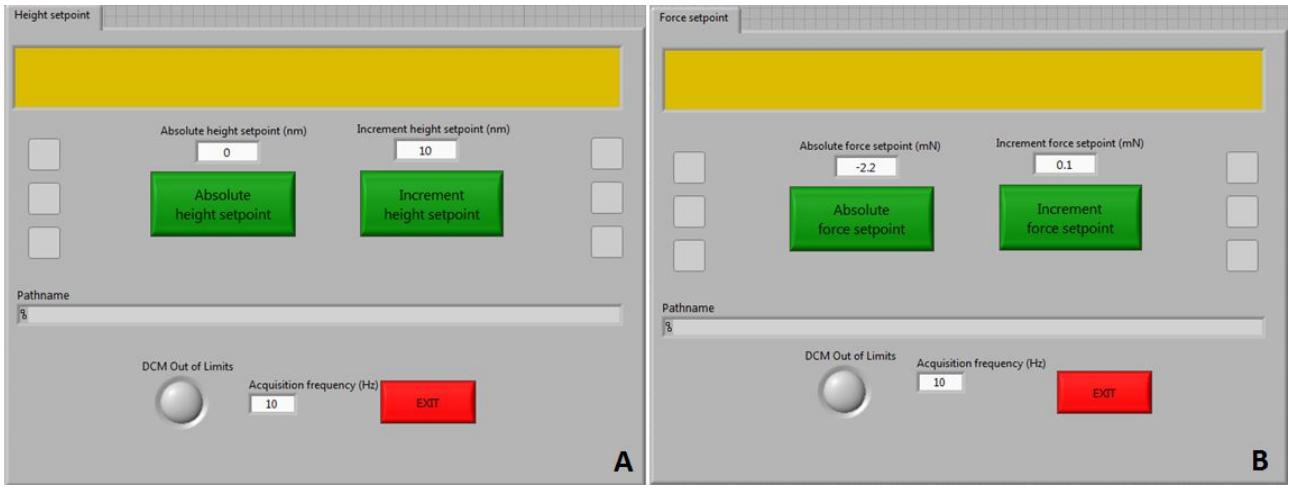

Figure A.5: Home-made labview interface for the square head monitoring (5)

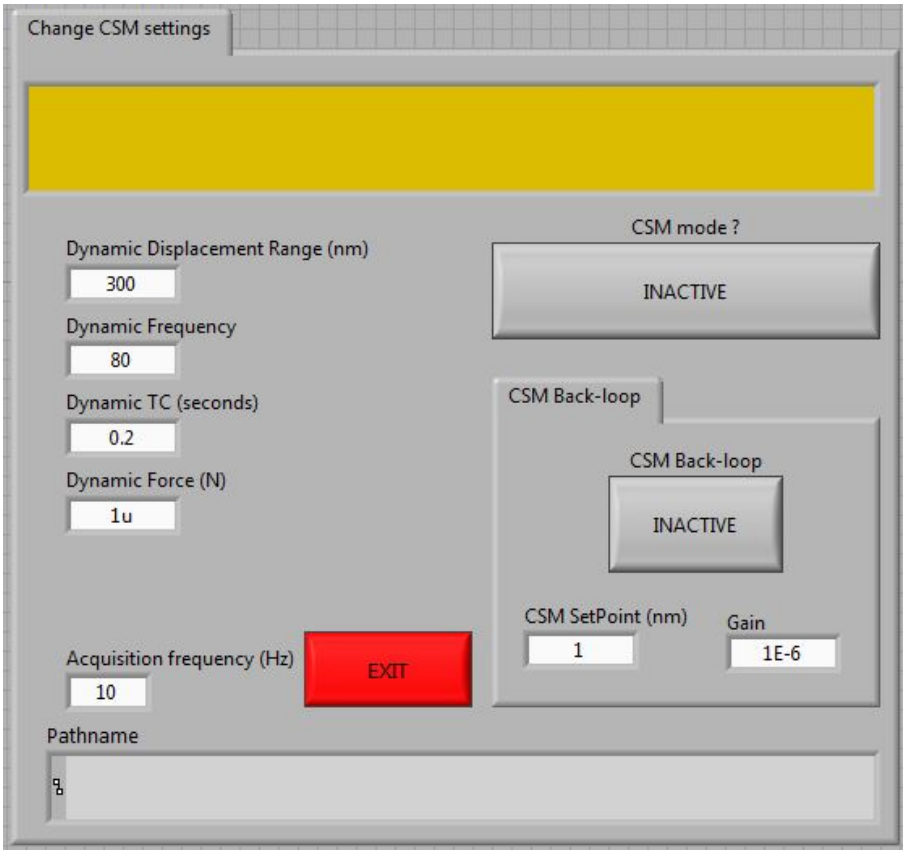

Figure A.6: Home-made labview interface for the square head monitoring (6)

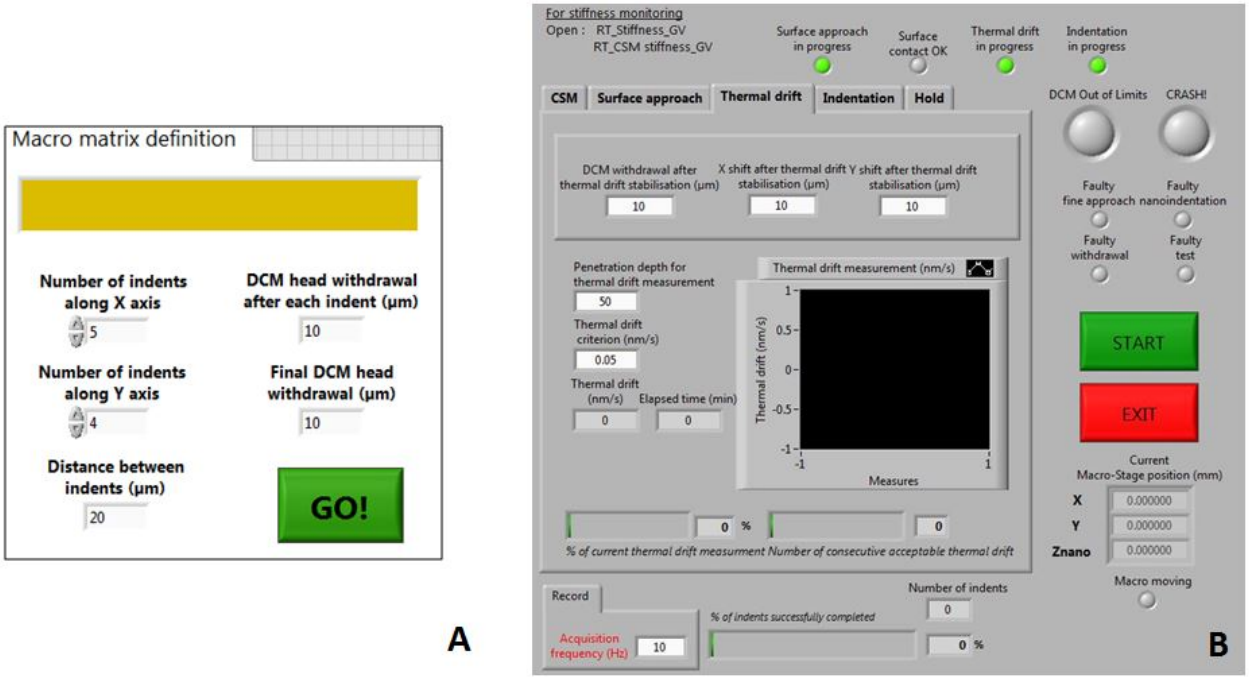

Figure A.7: Home-made labview interface for the square head monitoring (7)

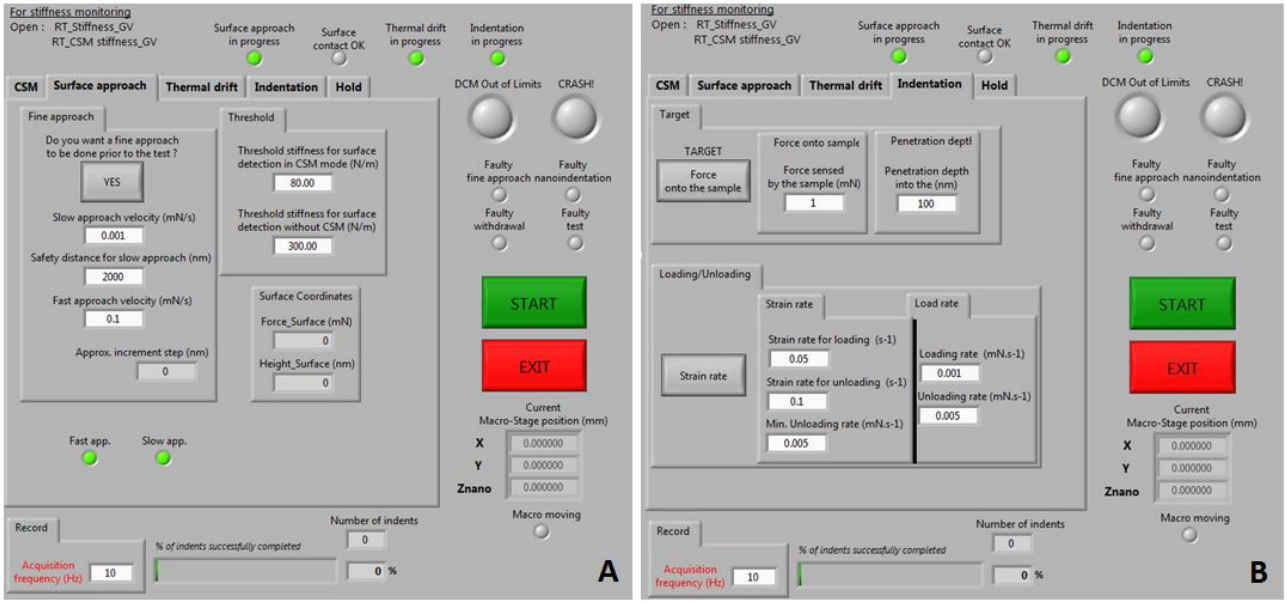

Figure A.8: Home-made labview interface for the square head monitoring (8)

Figure A.9: Home-made labview interface for the square head monitoring (10)

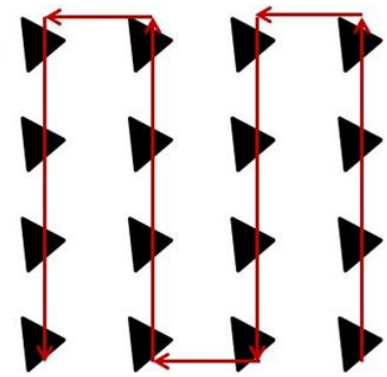

Figure A.10: Matrix pattern during standard nanoindentation test.

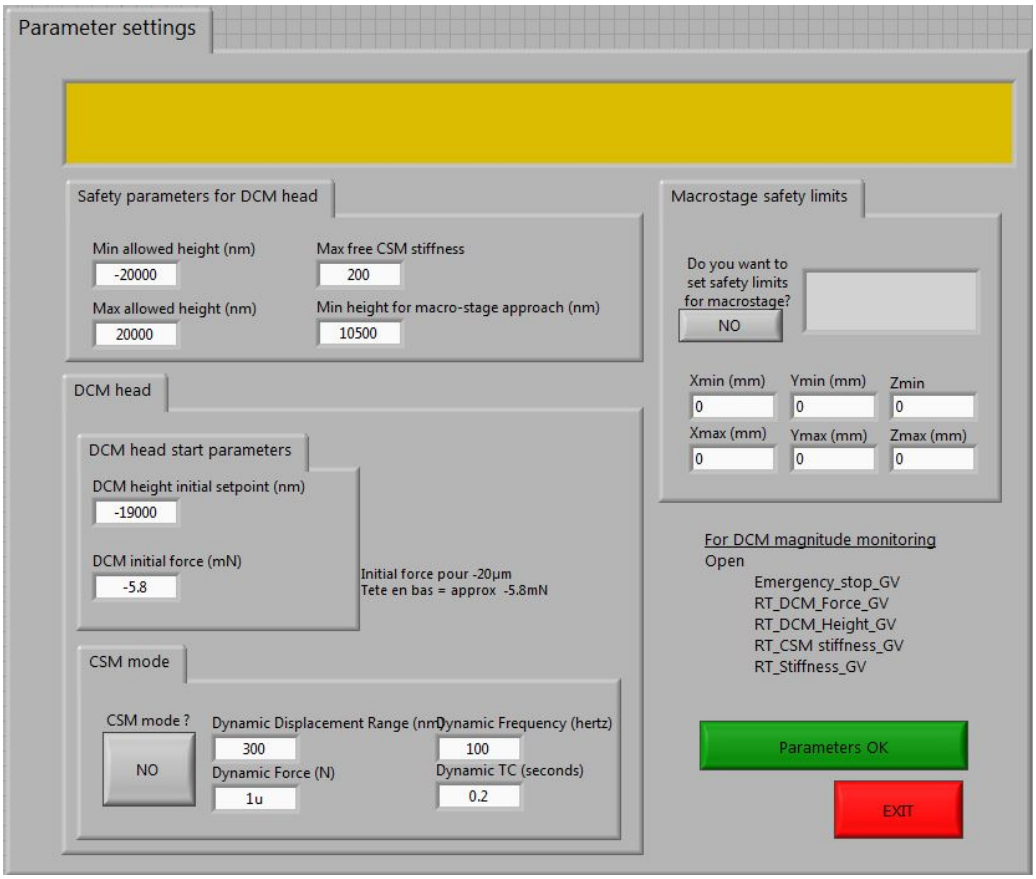

Figure A.11: Home-made labview interface for the square head monitoring (9)

Appendix B

Volume, cross sectional area and density computation of AlN coated polymer scaffolds

In this appendix, volume, cross sectional area and density computations of AlN coated polymer scaffolds from section 4.3 (page 137) are described.
The polymer scaffold is composed of 64 cubic cells of length $l = 10$ µm with four cube diagonals. The radius of each bare is $a = 0.287$ µm. The length of each cube diagonal is then equal to $l\sqrt{3}$ minus the length due to the two intersections with the cube lattice and minus the length due to the intersection with other cube diagonals (for three of the four diagonals). The average length of the cube diagonal $L_{diagonal}$ is then given by:

$$L_{diagonal} = l\sqrt{3} - 2 \cdot 2a\sqrt{3} - 3/4 \cdot 2a = 14.91\mu\text{m} \tag{B.1}$$

The volume $V1$ of the polymer due to the diagonals is then:

$$V1 = 64 \cdot 4\pi a^2 L_{diagonal} = 987\mu\text{m}^3 \tag{B.2}$$

The scaffold is also composed of 75 vertical and horizontal bares of lenght $4l$. Each of them have five intersection with the others. As a result the length of the two-thirds of the vertical and horizontal bares have been reduced due to these intersections. The volume $V2$ of the polymer due to these bars is then:

$$V2 = 75 \cdot \pi a^2(4l - 2/3 \cdot 5 \cdot 2a) = 739\mu\text{m}^3 \tag{B.3}$$

Coating thickness	**Volume of ceramic**	**Total volume**	**Cross-sectional area**	**Total mass**	**Density**
60 nm	686 μm^3	2326 μm^3	58.2 μm^2	$3.78 \cdot 10^{-9}$ g	88.8 $kg.m^{-}3$
120 nm	1372 μm^3	3012 μm^3	75.3 μm^2	$5.68 \cdot 10^{-9}$ g	59.0 $kg.m^{-}3$

Table B.1: Volume, cross-sectional area, mass and density of AlN coated polymer scaffold.

Assuming 5 % of shrinkage due to the high temperature during AlN deposition (250°C), the total volume of the polymer $V_{polymer}$ is then 1640 μm^3.
Since all the constituent of the scaffold are cylinders, the polymer surface of the scaffold can simply be computed as follows:

$$S_{polymer} = 2 \cdot V_{polymer}/a = 11429 \mu m^2 \tag{B.4}$$

For a thickness $t_{coating}$ of AlN, the volume of the ceramic part is then:

$$V_{ceramic} = S_{polymer} \cdot t_{coating} \tag{B.5}$$

Corresponding values for both 60 nm and 120 nm AlN coated scaffolds are given in table B.1.
Cross-sectional area is then computed by divided the total volume (ceramic and polymer) by the scaffold height (*i. e.* $4l = 40 \mu m$).
The mass of the scaffold is calculated using a AlN density of 2.78 $g.cm^{-3}$ and a polymer density of 1.89 $g.cm^{-3}$.
The density of the scaffold corresponds to the mass of the scaffold divided by the apparent volume of the scaffold (*i. e.* $(4l)^3 = 64000 \mu m^3$).

Appendix C

Coherent X-ray diffraction

C.1 X-ray diffraction

Diffraction is an interference effect between a wave and the crystallographic planes in a solid. X-ray diffraction allows the determination of the atomic structure of crystalline material. Information such as lattice spacing, strain or defect contents can be characterized. Moreover, the investigated material does not need any particular preparation, due to the weak interaction of the X-rays with the matter.

X-ray diffraction occurs in a crystal when the X-ray wavelength is lower than twice the distance between the crystallographic planes of the solid. In that case, X-rays interfere constructively between the crystallographic planes at the Bragg angle θ, resulting in a maximal intensity (figure C.1): this is the Bragg peak. In Bragg condition, the wavelength λ is related to the interplanar spacing d by the Bragg's law (C.1).

$$\lambda = 2d\sin(\theta) \tag{C.1}$$

X-ray diffraction gives information about the interplanar spacing d, and thus is sensitive to strain within the crystal.

Each series of crystallographic planes induces a series of Bragg reflections. Altogether, they form a periodic lattice (the reciprocal lattice of the crystal) in the reciprocal space. Mathematically, the reciprocal lattice is the Fourier transforms of the direct lattice.

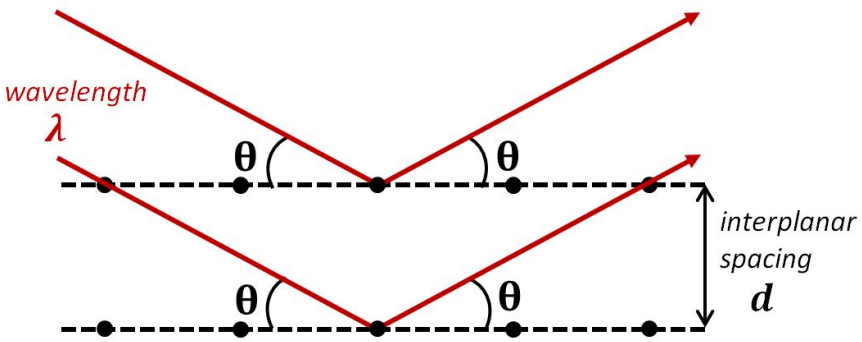

Figure C.1: Diffraction of a wavefront in Bragg condition.

C.2 Coherence

A crucial point in X-ray diffraction is the coherence of the beam, which means the ability to produce interference. In usual diffraction experiments, the coherence is limited to the crystallographic scale, allowing constructive interference between crystallographic planes, but the whole beam is mostly incoherent, *i. e.* no interference effect can occur between points separated by more than a few 100 nm. On the other hand, lasers (including X-ray free-electron lasers) provide fully coherent beams. Undulators in 3rd generation synchrotron facilities deliver poorly coherent beams, from whom a fully coherent beam can be extracted at the price of the flux (3 to 4 orders of magnitude are lost).

The beam coherence is anisotropic: the propagation direction of the beam has different coherence properties than those of the plane transverse to the propagation direction. The coherence properties of the beam can also be anisotropic within the transverse plane (horizontal versus vertical directions) if the emission source is anisotropic, as it is the case with synchrotron radiation.

A convenient way to describe the coherence properties of a beam is to define coherence lengths, which quantify the maximal distance between two points of the beam that can interfere together. Within the frame of the Gaussian beam approximation, a longitudinal coherence length (along the propagation direction) and transverse coherence lengths can be defined as respectively ξ_l (equation C.2)and ξ_t (equation C.3), with λ the wavelength of the beam, L the source distance and S the source size.

$$\xi_l = \frac{1}{2}\frac{\lambda}{\Delta\lambda}\lambda \tag{C.2}$$

$$\xi_l = \frac{\lambda L}{S} \tag{C.3}$$

∘ The longitudinal coherence length depends on the monochromaticity of the beam $\Delta\lambda/\lambda$, and thus can be optimized by using monochromators. Si(111) monochromators, which are by far the most used on hard X-ray beamlines, provide a longitudinal coherence length ξ_l of ~ 1 µm at 8 keV. Strong interference between two scatterers in the sample occurs when the optical path difference is smaller than ξ_l.

∘ The transverse coherence lengths are inversely proportional to the size of the source S (along the horizontal or the vertical direction), which is a motivation for the reduction of the horizontal spread of electrons bunches in storage rings. They also depend on the distance L from the source which is the reason why long beamlines are preferentially used for coherent X-ray diffraction.

A beam is generally qualified as incoherent if its size is larger than the transverse coherence lengths, and as coherent if they are at least of the same order of magnitude. Synchrotron sources are known to be poorly coherent sources. Indeed, each electrons of the beam acts as a coherent source, but they are mutually incoherent. A coherent beam is extracted from the full monochromatic beam by inserting slits open to the transverse coherence lengths [196].

C.3 Coherent X-ray diffraction

Information obtained from diffraction with an incoherent beam and from diffraction with a coherent beam strongly differ. An incoherent beam gives access to statistical informations deduced from the summed intensities of the incoherent waves scattered by different coherence domains of the material (figure C.2 a). On the contrary, with a coherence beam, there is a single coherence domain illuminating the sample, such that the intensity distribution is not blurred by statistical averaging. The scattering pattern is characterized by sharp intensity fluctuation (speckles) and is directly the result of the properties of the highlighted domain (figure C.2 b). In that case, the resulting intensity is the square of the sum of the waves modulus. This leads to equation (C.4), with $F(\vec{q})$ the Fourier transform of the scattering function $f(\vec{r})$.

$$I(\vec{q}) = |F(\vec{q})|^2 = |TF(f(\vec{r}))|^2 \tag{C.4}$$

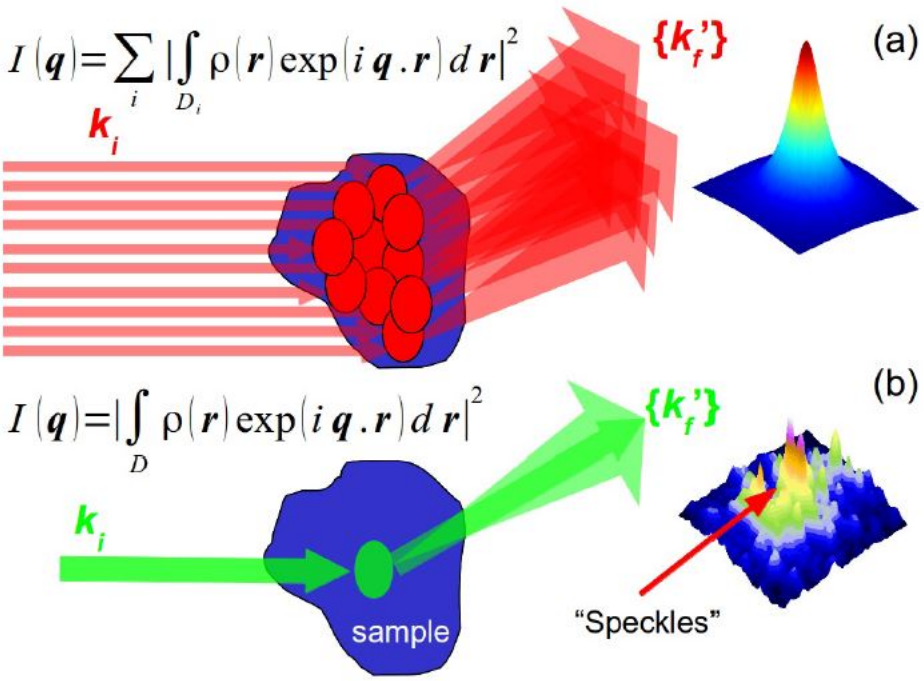

Figure C.2: Scattering from an incoherent beam (a) and a coherent beam (b), from Dupraz [189].

Thus, the phase of $F(\vec{q})$ is lost during coherent X-ray diffraction, and only the modulus is measured.

C.4 Bragg geometry

During Bragg Coherent Diffraction Imaging (BCDI), a single Bragg peak of the diffraction pattern is selected and imaged. In that case, the obtained diffraction pattern corresponds to this Bragg peak and its immediate vicinity.
In Bragg geometry, $f(\vec{r})$ can be defined by equation (C.5), with $\rho(\vec{r})$ the electronic density, $\vec{Q}$ the Bragg vector and $\vec{u}$ the displacement vector within the crystal lattice (related to the elastic field as well as the crystal defects).

$$f(\vec{r}) = \rho(\vec{r})e^{i\vec{Q}\cdot\vec{u}(\vec{r})}\vec{u}(\vec{r}) \tag{C.5}$$

The measured intensity corresponds directly to the square of the modulus of $F(\vec{q})$, and thus to the electronic density. However, the loss of the phase means the loss of the displacement field within the lattice. Since the last few years, methods based on iterative phase-retrieval

algorithms have been developed in order to retrieve phase information, and access to the 3D displacement field [196].

C.5 Reconstruction algorithm

Iterative phase-retrieval algorithms are based on the Stayre's oversampling principle, which established that the signal must be sampled at last at twice the Nyquist frequency in order to retrieve the entire signal. This leads to a data redundancy, which theoretically allows the retrieval of the phase.

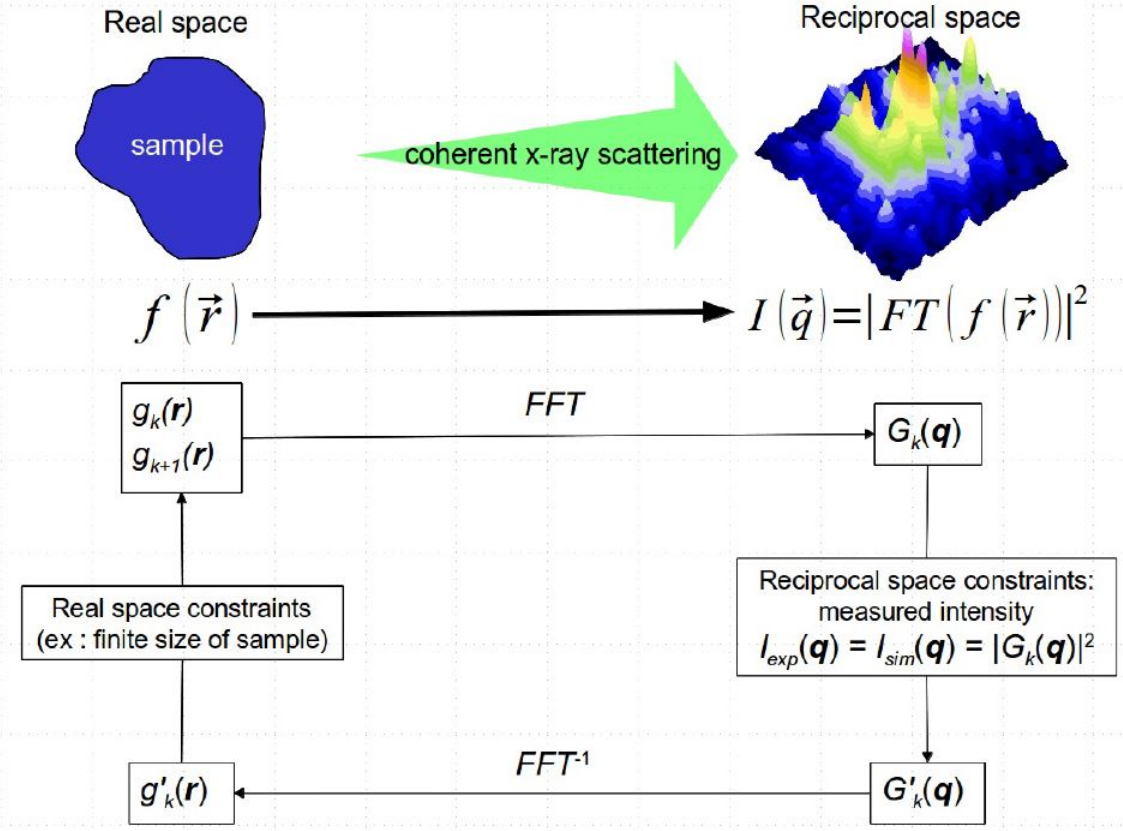

Figure C.3: Schematic of phase-retrieval algorithms, from Dupraz [189].

Iterative phase-retrieval algorithms consists in iteratively going back and forth between the real space and the reciprocal space, as schematized in figure C.3. During coherent X-ray diffraction measurements, a wave interact with the sample. This leads in the reciprocal space to a diffraction pattern with intensity $I(\vec{q})$, which corresponds to the square of the amplitude of the Fourier transform of the diffusion function $f(\vec{r})$ (as described in equation C.4). Phase-retrieval algorithms are then carried out in several steps, which are described in what follows

for our particular cases:

1. In the real space, a guess of the wave function $g_k(\vec{r})$ is chosen. In our case, for the first guess the amplitude of the wave function is defined as uniform in space and equal to the mean value of the intensity. The phase is chosen randomly in the space. This function is defined over a "support" S_k, which can be firstly computed if knowing roughly the size of the studied object or using a Patterson function, *i. e.* the Fourier transform of the measured intensity.

2. The Fast Fourier Transform (FFT) of $g_k(\vec{r})$ is computed, leading to $G_k(\vec{q})$ function in the reciprocal space (equation C.6).

$$G_k(\vec{q}) = FT(g_k(\vec{r})) = |G_k(\vec{q})|e^{\Phi(\vec{q})} \tag{C.6}$$

3. A reciprocal space constraint is applied: since the measured intensity must be equal to the simulated intensity (which corresponds to the square of the amplitude of $G_k(\vec{q})$), a new function $G'_k(\vec{q})$ is defined as $G'_k(\vec{q}) = \sqrt{|I(\vec{q})|}e^{i\Phi(\vec{q})}$, where $I(\vec{q}$ is the measured intensity and $\Phi(\vec{q}$ is the phase of the previous function $G_k(\vec{q})$.

4. In the real space, the function $g'_k(\vec{r})$ is defined as the inverse FFT of $G'_k(\vec{q})$ (equation C.7).

$$g'_k(\vec{r}) = FT^{-1}(G'_k(\vec{q})) \tag{C.7}$$

5. A real space constraints is applied: The new wave function $g_{k+1}(\vec{r})$ corresponds to $g'_k(\vec{r})$ which is adapted to fulfill this constraint. The support S_k can also be modified at this step, leading to a new support S_{k+1}. Several real space constraints can be applied, corresponding to specific algorithms:

   - The Error Reduction (ER) algorithm [228]:

$$\begin{cases} g_{k+1}(\vec{r}) = g'_k(\vec{r}) & if \quad \vec{r} \in S_k \\ g_{k+1}(\vec{r}) = 0 & if \quad \vec{r} \notin S_k \end{cases}$$

     In that case $S_k = S_{k+1}$. The issue of this algorithm is that it converge quickly towards a local minimum.

- The Hybride Input Output (HIO) algorithm [229]:

$$\begin{cases} g_{k+1}(\vec{r}) = g'_k(\vec{r}) \quad if \quad \vec{r} \in S_k \\ g_{k+1}(\vec{r}) = g_k(\vec{r}) - \beta \cdot g'_k(\vec{r}) \quad if \quad \vec{r} \notin S_k \end{cases}$$

  Here $S_k = S_{k+1}$, but the guess is not set to zero outside the support: a part of the information outside the support is kept and subtracted for the next iteration after being multiplied by a factor β. During this project $\beta = 0.9$ was chosen. This algorithm introduces a little perturbation compared to the ER algorithm, which allows to leave local minimums.

- The Shrink-Wrap (SW) algorithm [230]: it updates the support S_k, using the Patterson function applied to the simulated intensity. The support S_{k+1} is reduced to a domain with amplitude values above 10 % of the maximal resulting amplitude. The pixels which do not fulfill this conditions are removed from the support. During this project, a modified version of this algorithm has also been used, where only the pixels of the support surface could be removed.

These five steps are iteratively repeated using a combination of ER, HIO and SW algorithms. After all the iterations the best solution is selected, which correspond to the lowest $\chi^2 = (|G_k| - \sqrt{(I)})^2$ value.

Appendix D

Additional data regarding the simulations of islands compression by FEM

The goal of this numerical study is to identify the relationship between the experimental compression curves of faceted gold islands and the intrinsic elastic-plastic deformation laws used as input. We use the same apparent stress and strain variables as for the experiment, namely the stress is the force on the flat punch divided by the current area of contact $\frac{L}{A_c}$ (true stress), the strain is the relative height reduction $\frac{\Delta h}{h_0}$.

D.1 FEM model

D.1.1 Geometry

The simulations have been carried out using the finite element method (FEM) software ABAQUS. The three dimensional model is composed of 3 parts, displayed in figure D.1:

- The indenter is modelled as a rigid disk (top of figure D.1).
- The Au crystallite (island) is the polyhedron in the center part of figure D.1. The geometry has been generated automatically using a python script. Experimental 3D geometry data are taken from a typical gold island, reconstructed using BCDI [189]. The data consist, for each facet i, of the coordinates (x_i, y_i, z_i) of one point on the facet as well as the facet normal vector (n_x^i, n_y^i, n_z^i). The script then generates the final volume by making successive cuts in a large cube. The island is 280 nm high and about 600 nm wide. The material is taken as elastic isotropic ($E = 79$ GPa, $\nu = 0.4$) in most of the study since

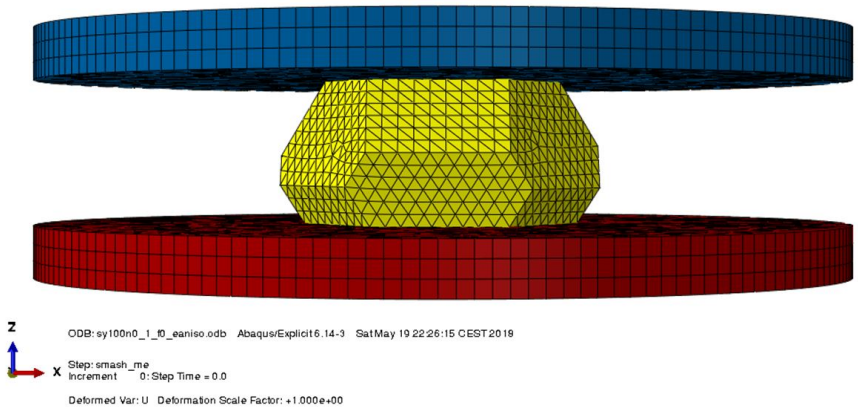

Figure D.1: Constitutive parts of the model: rigid indenter (blue), gold island (yellow), substrate (red).

elastic anisotropy appears to be of a second order effect, using anisotropic stiffness tensor [231]. Plastic behaviour is considered here as isotropic (see below for details).

- The substrate is modelled by a rigid plane (bottom of figure D.1).

D.1.2 Boundary conditions and interactions

The substrate is fixed. The indenter is translated downwards (decreasing z). There are two contact interactions: one between the indenter surface and the surface of the island, one between the substrate surface and the surface of the island. It is worth noting that all the surface of the island is involved in both interactions, as the surface coming into contact with both the indenter and the substrate is strongly increasing during the compression.

The normal contact is rigid. Two tangential contact cases have been considered in the simulation: a frictionless contact and a Coulomb type friction contact (with μ ratio normal to tangential force).

An additional case with an island pinned at its bottom surface have also been considered. As the real mechanical behavior at the island / substrate interface is not known, the frictionless contact and the pinning correspond to two extreme case: a weak island / substrate interaction and a very strong interaction, respectively.

The island height is reduced by 70 % of its initial height during compression.

D.1.3 Constitutive law for the island

An isotropic plasticity behavior has been implemented, with hardening following a Ludwik law (equation D.1).

$$\sigma_{eq} = \sigma_y + K(\epsilon^p_{eq})^n \tag{D.1}$$

with σ_{eq} the Von-Mises equivalent stress, ϵ^p_{eq} the equivalent plastic strain, σ_y the initial yield stress, K a constant and n the hardening exponent. The law has been implemented up to 100 % strain after what the hardening is kept constant. This saturation stress is used at very large strain as compared to bulk behavior where is appears around strain of 0.5 for FCC metals. We also used a simple elastic-perfect plastic model ($\sigma_{eq} = \sigma_y$) for one reference case.

D.1.4 Numerical integration

The explicit solver is used with mass scaling in order to make a quasi-static simulation. The usual precautions are taken to ensure the quasi-static character of the simulation (smooth loadings and negligible kinetic energy compared to strain energy). The elements chosen for the island are tetrahedrons, with quadratic interpolation. No re-meshing has been used, as the distortion of the tetrahedrons remains moderate on most of the model.

Deformed state of the system at several loading stages are displayed in two cases: figure D.2 for a frictionless contact between the island and the substrate and figure D.3 for island bottom pinned to the substrate. The compression is measured by axial compression strain $\epsilon = \frac{\Delta h}{h_0}$, *i. e.* the displacement Δh of the indenter divided by the island height h_0. A mapping of the equivalent plastic strain have been superimposed (the maximum value in the scale being fixed at 200 % deformation). It is interesting to see that the strain distribution is quite different in the two cases. The lateral spreading in the case of the frictionless contact is about 970 nm whereas it is 890 nm in the case of the pinned substrate.

The plastic strain is concentrated at the edges of the island. In the free-bottom case, only the edges of the upper surface are really concentrating strains, whereas both top and bottom edges show strong strain concentrations in the pinned-bottom case.

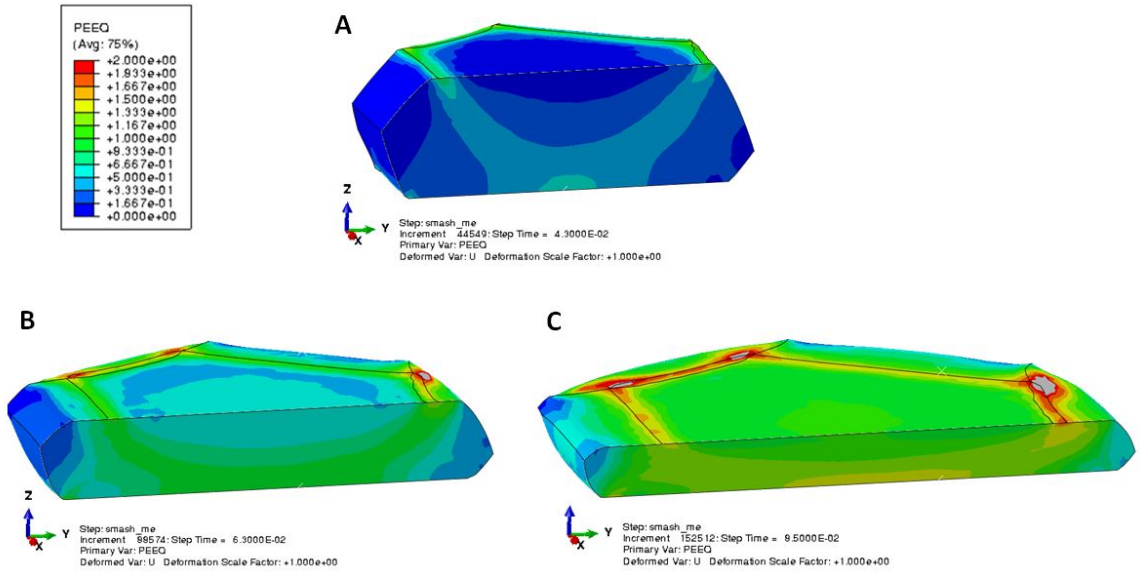

Figure D.2: Deformed shape of the island at increasing levels of compression $\epsilon = \frac{\Delta h}{h_0}$, in the case of a frictionless contact between the island and the substrate. A mapping of the equivalent plastic strain has been superimposed: (A) $\epsilon = 26.5$ %, (B) $\epsilon = 52.3$ % and (C) $\epsilon = 71.4$ %.

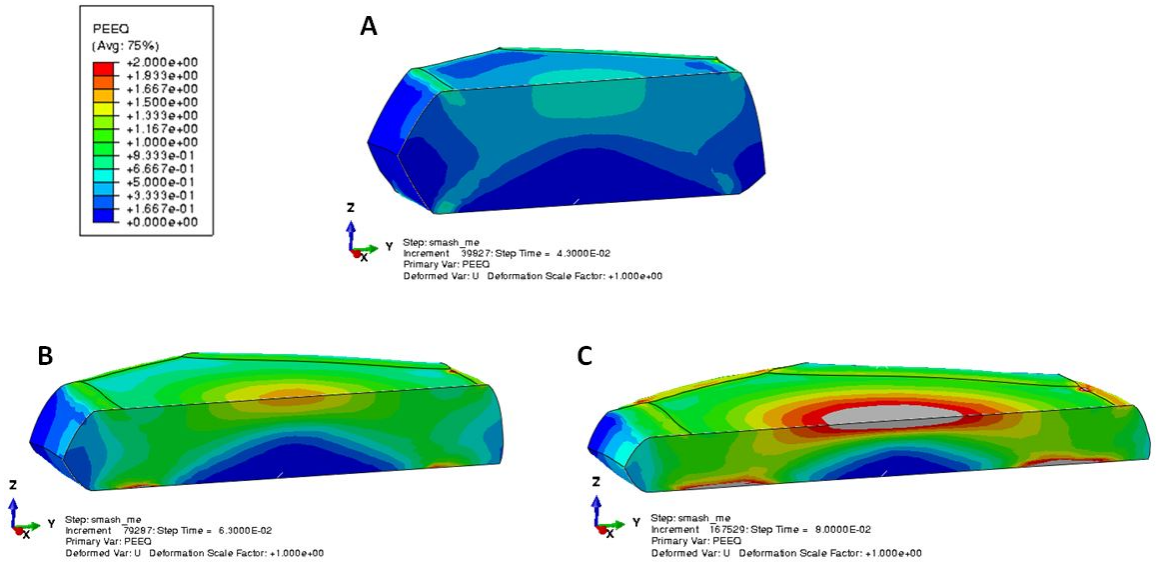

Figure D.3: Deformed shape of the island at increasing levels of compression $\epsilon = \frac{\Delta h}{h_0}$, in the case of a a island pinned at the bottom surface. A mapping of the equivalent plastic strain has been superimposed: (A) $\epsilon = 26.5$ %, (B) $\epsilon = 52.3$ % and (C) $\epsilon = 67.3$ %.

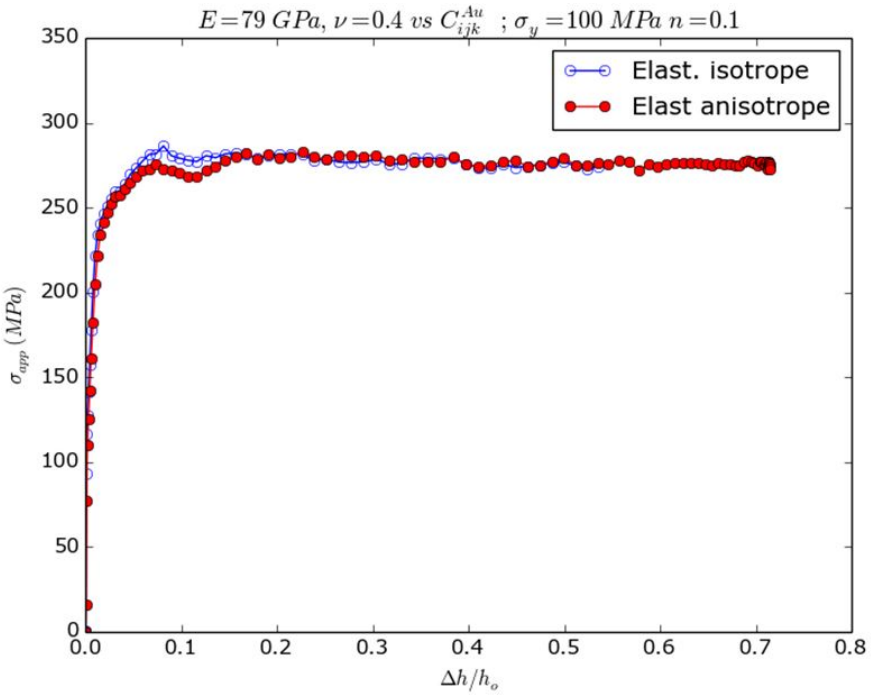

Figure D.4: Apparent stress-strain curves from FEM simulations using either isotropic elasticity or the anisotropic elastic stiffness tensor with a plastic power law ($n = 0.1$, $\sigma_y = 100$ MPa).

D.2 Global stress strain response from FEM simulations

D.2.1 Isotropic / Anisotropic elastic effect

No real distinction is observed using the two set of parameters for the elastic behavior, either isotropic (Young's modulus and Poisson's ratio fixed) or the complete standard Au elastic stiffness tensor [231]. This is shown in figure D.4, where the apparent response for an elastic-plastic power law (n=0.1 for work hardening power exponent) is used.
In the rest of this study, only isotropic elastic behavior will be considered.

D.2.2 Effect of friction

Since during the burst of deformation is rapid (less than 100 ms [184]) and the feedback loop is in force controlled mode, we ignore if the flat punch remains always in contact with the islands during the whole burst. Two extreme cases are then studied: a non friction case and a large Coulomb friction coefficient ($\mu = 0.3$).
Due to some convergence problem for the elastic-perfect plastic case without friction, only for this case a very small friction coefficient is used ($\mu = 0.05$, figure D.5 A). It appears that in this case the geometrical shape (cross section variation) of the island plays a little role on the

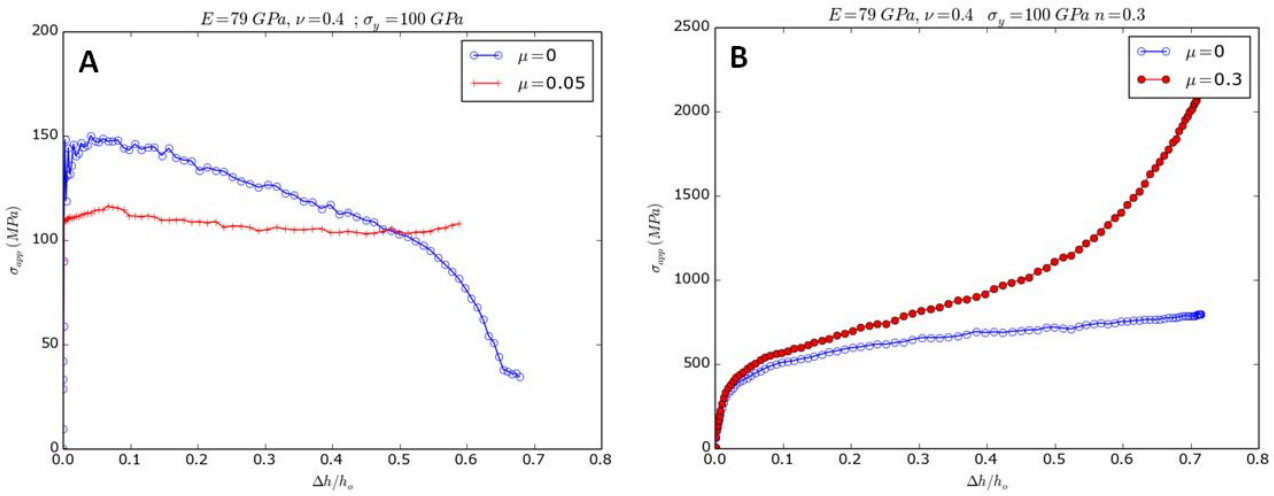

Figure D.5: A: Effect of addition of a tiny friction coefficient on the compression curves of an elastic-perfect plastic behavior, B: effect of friction ($\mu = 0.3$) for a elastic-plastic behavior ($n = 0.3$).

apparent compression curve. For the elastic-perfect plastic case, the compression curve appear globally to go through a maximum around a strain of 0.1 (150 MPa) followed by a small stress softening tending towards the chosen constant yield stress (100 MPa).

In the presence of work hardening, ($n = 0.3$, figure D.5 B) the friction leads to dissipative process and a constant increase of the resulting apparent stress with the compression strain above 0.15.

D.2.3 Effect of plastic behavior

Figure D.6 illustrates the various apparent response of compressed islands with various degree of work hardening, the power law exponent n varying between 0 and 0.3. It is shown together with the respective input constitutive law (true stress and strain) used. Remarkably, there is little difference between the 'input' and 'output' curves, the cross section geometry playing a second order effect.

This lead us to state that the compression of the faceted crystal is closed to the one of a cylinder. Small difference appear between the apparent flow stress and the constitutive input true stress. The extent in strain for the two behavior to superimpose increase with the work hardening coefficient n. The ratio between the two stress are less than 1.5 in all cases and the saturation stress (stress at large strain, greater than 0.3) is equivalent.

The chosen plastic power law strain hardening behaviors are phenomenological laws used to

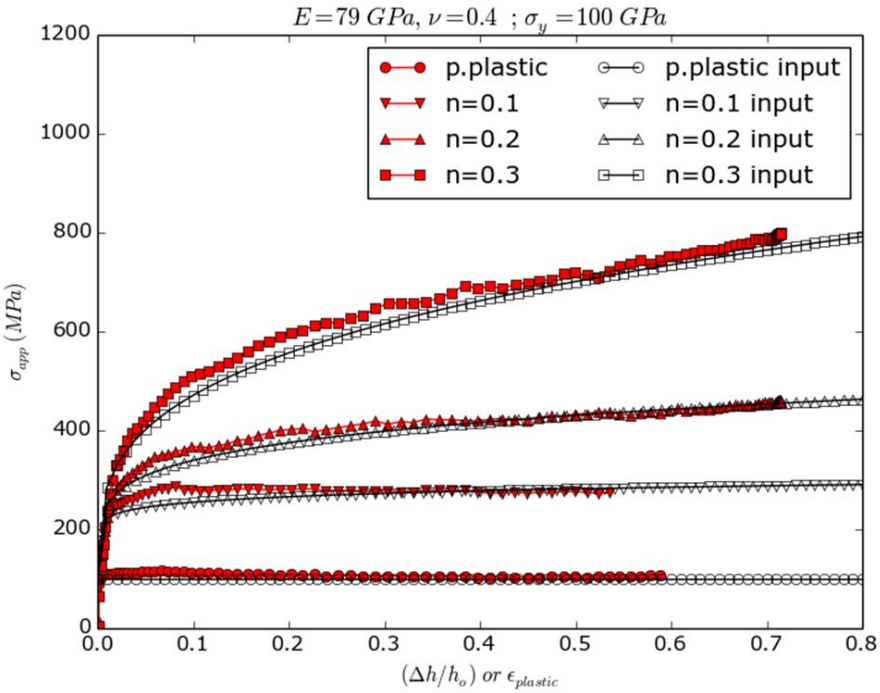

Figure D.6: Stress strain curves for various elastic-plastic behaviors (increasing work hardening coefficient): comparison between the apparent stress, strain curves and the constitutive law used as input.

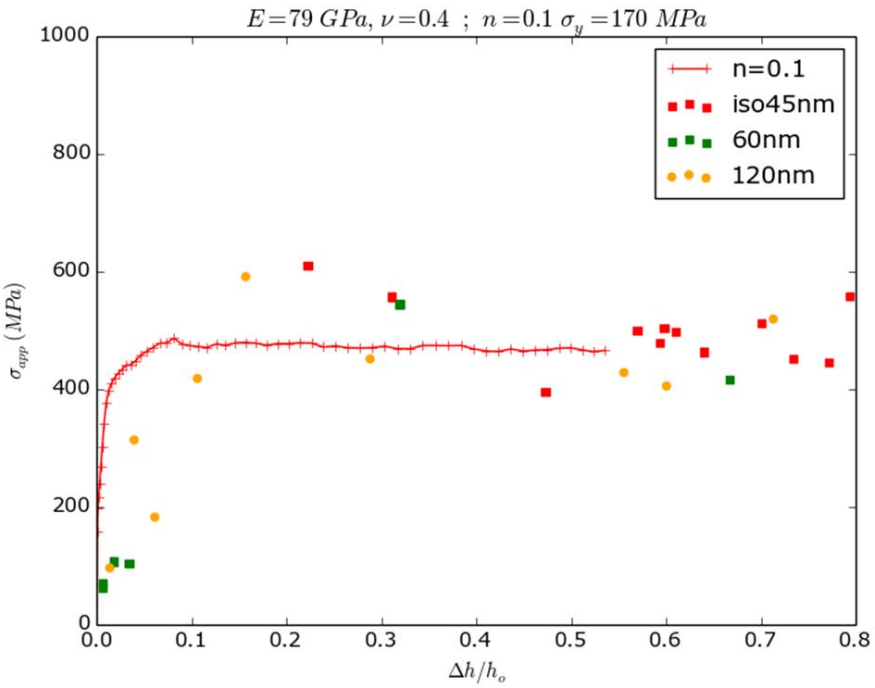

Figure D.7: Comparison of experimental stress strain curves with a set of simulation data: $\sigma_y = 170$ MPa [184], n=0.1.

explore the response of the crystallite. One major unknown is the strain for which hardening ceases (saturation stress at large deformation) which is not varied here (work hardening is maintained throughout large strain (0.8 true strain). Nevertheless a comparison of one set of behavior ($\sigma_y = 170$ MPa as obtained in [184], n=0.1) with the experimental data indicate that the hardening is less rapid in the experimental case in terms of strain and that a saturation stress close to 500 MPa is observed (figure D.7).

Indeed, gold micro-crystallites in compression exhibit linear work hardening, with a yield stress around 100 MPa, and an hardening of 400 MPa in 20 % strain reduction, reaching a saturation stress around 500 MPa. Figure D.8 shows both experimental results and results from FEM calculations for a linear hardening.

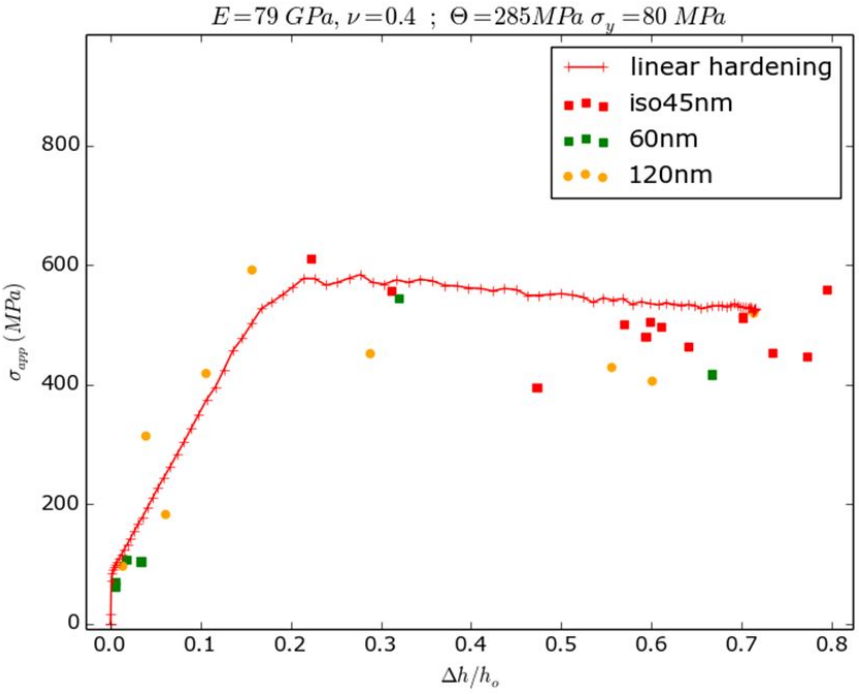

Figure D.8: Comparison of experimental stress strain curves with a set of simulation data with linear hardening: $E = 79$ GPa, $\nu = 0.4$, $\sigma_y = 80$ MPa, $\Theta = 285$ MPa.

No sharp increase in stress due to boundary conditions at large strain (friction and/or block bottom interface) is observed: either these effects are present and then the intrinsic behavior of the crystallites at large strain would be a counteracting softening, or they are negligible and the saturation stress is definitely present.

Appendix E

Cleaning and elaboration conditions of samples for capacitive measurements

Each sample for capacitive measurements of chapter 7 (page 239) has been prepared as follows:

- **Cleaning:** Silicon wafers have been cleaned with Piranha solution (H_2SO_4 + H_20_2).
- **Silica growth by dry oxidation:** Dry thermal oxidation has been performed to produce a first 49 nm silica layer on silicon. Conditions for dry thermal oxidation were a ramp of 25 min from 700°C to 1050°C under a 5000 $cm^3.min^{-1}$ flow of N_2, followed by a stabilisation step at 1050°C for 25 min under a 5000 $cm^3.min^{-1}$ flow of N_2. Then the dry oxidation is performed for 20 min at 1050°C under a 6000 $cm^3.min^{-1}$ flow of 0_2. The ramp down to 700°C is performed under a 5000 $cm^3.min^{-1}$ flow of N_2 for 30 min.
- **Silica deposition by PECVD:** An additional layer of silica with various thickness has then been deposited by Plasma-Enhanced Chemical Vapor Deposition (PECVD). Temperature condition for PECVD was 280°C, under a pressure of 1800 mT. Deposition has been performed under flows of SiH_4, N_2O and Ar, with the following conditions
  - For 157nm and 184nm samples: 9 $cm^3.min^{-1}$ flow of SiH_4, 250 $cm^3.min^{-1}$ flow of N_2O, 500 $cm^3.min^{-1}$ flow of Ar
  - For 481nm and 974nm samples: 35 $cm^3.min^{-1}$ flow of SiH_4, 1000 $cm^3.min^{-1}$ flow of N_2O, 500 $cm^3.min^{-1}$ flow of Ar

Bibliography

[1] http://cemam.grenoble-inp.fr.
(Cited on page 17)

[2] J. B. Pethica, R. Hutchings, and W. C. Oliver. Composition and hardness profiles in ion implanted metals. *Nuclear Instruments & Methods*, 209/210:995–1000, 1983.
(Cited on page 22)

[3] J. L. Loubet, J. M. Georges, J. M. Marchesini, and Meille G. Vickers indentation curves of magnesium oxide. *Journal of tribology*, 106:43–48, 1984.
(Cited on pages 22, 31, and 34)

[4] J. L. Loubet, J. M. Georges, and G. Meille. *Microindentation Techniques in Materials Science and Engineering: Vickers Indentation Curves of Elastoplastic Materials.* American society for Testing and materials, 1986.
(Cited on page 22)

[5] M. Oyen and R. F. Cook. A practical guide for analysis of nanoindentation data. *Journal of the mechanical behavior of biomedical materials*, 2:396–407, 2009.
(Cited on page 26)

[6] V. Maier, B. Merle, M. Göken, and K. Durst. An improved long-term nanoindentation creep testing approach for studying the local deformation processes in nanocrystalline metals at room and elevated temperatures. *Journal of Materials Research*, 28(9):1177–1188, 2013.
(Cited on page 27)

[7] K. Durst and C. Maier. Dynamic nanoindentation testing for studying ththermal activated processes from single to nanocrystalline metals. *Current Opinion in Solid State and*

Material Science, 19(6):340–353, 2015.
(Cited on page 27)

[8] V. Maier, A. Hohenwarter, R. Pippan, and D. Kiener. Thermal activated deformation processes in body-centered cr - how microstructures iinfluence strain rate sensitivity. *Scripta Materialia*, 106:42–45, 2015.
(Cited on page 27)

[9] H. Hertz. *Miscellaneous Papers- On the contact of elastic solids.* Macmillan and co., 1896. first published in 1881.
(Cited on page 28)

[10] H. Hertz. *Miscellaneous Papers-On the contact of rigid elastic solids and on Hardness.* Macmillan and co., 1896. first published in 1881.
(Cited on page 28)

[11] A. E. H. Love. Boussinesq's problem for a rigid cone. *Quaterly Journal of Mathematics*, 10:164–175, 1939.
(Cited on page 30)

[12] J. Boussinesq. *Application des potentiels à l'étude de l'équilibre et du mouvement des solides élastiques.* Gauthier Villard, 1885.
(Cited on page 30)

[13] A. E. H. Love. The stress produced in a semi-infinite solid by pressure on part of the boundary. *Philosophical Transactions of the Royal Society of London. Series A, Containing Papersof a Mathematical or Physical Character*, 228:377–420, 1929.
(Cited on pages 30 and 31)

[14] I. N. Sneddon. The relation between load and penetration in the axisymetric boussinesq problem for a punch of arbitrary profile. *Int. J. Engng Sci.*, 3:47–57, 1965.
(Cited on pages 31, 34, and 90)

[15] I. N. Sneddon. *Fourier transforms.* Dover publications, 1951.
(Cited on page 31)

[16] J. R. Willis. Hertzian contact of anisotropic bodies. *Journal of Mechanical Physics of Solids*, 14:163–176, 1966.
(Cited on page 31)

[17] C. M. Segedin. The relation between load and penetration for a spherical punch. *Mathematika*, 4:156–161, 1956.
(Cited on page 31)

[18] M. F. Doerner and W. D. Nix. A method for interpreting the data from depth-sensing indentation instruments. *Journal of Materials Research*, 1(4):601–609, 1986.
(Cited on pages 31, 33, 36, and 37)

[19] G. M. Pharr, W. C. oliver, and F. R. Brotzen. On the generality of the relarelation among contact stiffness, contact area and elastic modulus. *Journal of Materials Re*, 7(3):613–617, 1992.
(Cited on page 31)

[20] W. C. Oliver and G. M. Pharr. An improved technique for determining hardness and elastic modulus using load and displacement sensing indentation experiments. *Journal of Materials Research*, 7(6):1564–1582, 1992.
(Cited on pages 34, 36, 37, 50, 179, and 193)

[21] J. L. Loubet, M. Bauer, A. Tonck, S. Bec, and B. Gauthier-Manuel. *Mechanical Properties and Deformation Behavior of Materials Having Ultra-Fine Microstructures : Nanoexperiments with a surface force appartus*. Kluwer Academic Publisher, 1993.
(Cited on pages 35, 39, and 179)

[22] G. Hochstetter, A. Jimenez, and J. L. Loubet. Strain rate effect on hardness of glassy polymers in the nanoscale range. comparison between quasi-static and continous stiffness measurements. *Journal of Macromolecular Science, Part B: Physics*, 38(5-6):681–692, 1999.
(Cited on pages 35 and 39)

[23] J. L. Bucaille, E Felder, and G Hochstetter. Inanoindentation the viscoplastic behavior of a polycarbonate based on experiments and numeical modeling of the nano-indentation test. *Journal of Materials Science*, 37:3999–4011, 2002.
(Cited on pages 35 and 48)

[24] J. B. Pethica and W. C. Oliver. *Mechanical properties of nanometer volumes of material: use of elastic response of small area indentations. IN: Thin films: ststress and mechanical properties*, volume 130. Materials Research Society Symposium Proceedings, 1989.
(Cited on page 36)

[25] S. A. Syed Asif and J. B. Pethica. *Nanoscale creep and the role of defects. In: Thin films: ststress and mechanical properties.*, volume 436. Materials Research Society Symposium Proceedings, 1997.
(Cited on page 36)

[26] X. Li and B. Bhushan. A review of nanoindentation continuous stiffness measurement technique and its applications. *Materials Characterization*, 48:11–36, 2002.
(Cited on pages 36 and 37)

[27] E. G. Herbert, K. E. Johanns, R. S. Singleton, and G. M. Pharr. On the measurement of energy dissipation using nanoindentation and the continuous stiffness measurement technique. *Journal of Materials Research*, 28(21):3029–3042, 2013.
(Cited on page 36)

[28] W. C. Oliver and G. M. Pharr. Measurements of hardness and elastic modulus by instrumented indentation: Advances in understanding and refinements to methodology. *Journal of Materials Research*, 19(1):3–20, 2004.
(Cited on pages 37, 39, 117, 121, and 125)

[29] D. Tabor. A simple theory of static and dynamic hardness. *Proceedings of the royal society of london, Serie A*, 192:247–274, 1948.
(Cited on pages 40 and 42)

[30] D. Tabor. *The hardness of Metals*. Oxford University Press, 1951.
(Cited on pages 40, 42, and 48)

[31] H. Hencky. Über einige statisch bestimmte falle des gleichgewichts in plastischen korpern. *Journal of Applied Mathematics and Mechanics/Zeitschrift für Angewandte Mathematik und Mechanik*, 3(4):241–251, 1923.
(Cited on page 40)

[32] Ishlinsky. Axisymmectrical problem of plaplastic theory and brinel test. *Journal of Applied Mathematics and Mechanics*, 8(3):201–228, 1944.
(Cited on page 40)

[33] E. G. Herbert, G. M. Pharr, W. C. Oliver, B. N. Lucas, and J. L.s Hay. On the measurement of stress-strain curves by spherical indentation. *Thin Solid Films*, 398-399:331–335, 2001.
(Cited on page 42)

[34] K. L. Johnson. The correlation of indentation experiments. *Journal of Mechanical Physics of Solids*, 18:115–126, 1970.
(Cited on page 42)

[35] R. F. Bishop, R. Hill, and N. F. Mott. The theory of indentation and hardness tests. *The proceedings of the physical society*, 57(321):147–159, 1945.
(Cited on page 42)

[36] D. M. Marsh. Platest flow in glass. *Proceedings of the Royal Society of London. Series A, Mathematical and Physical Sciences*, 279(18):420–438, 1964.
(Cited on page 42)

[37] R. Hill. *Themathemmetals theory of plasticity.* Oxford University Press, 1950.
(Cited on pages 42 and 43)

[38] F. J. Lockett. Indentaton of a rigid/plastic material by conical indenter. *Journal of Mechanical Physics of Solids*, 11:347–355, 1963.
(Cited on page 42)

[39] G. Kermouche, J. L. Loubet, and J. M. Bergheau. An approximate solution to the problem of cone or wedge indentation of elastoplastic solids. *Comptes Rendus Mecanique*, 333:389–395, 2005.
(Cited on page 43)

[40] G. Kermouche. *Contribution à la modélisation théorique et numérique des essais d'indentation et de rayure.* PhD thesis, Ecole Centrale de Lyon, 2005.
(Cited on page 43)

[41] Y. T. Cheng and C. M. Cheng. Effect of 'sinking in' and 'piling up' on estimating the contact area under load in indentation. *Philosophical Magazine Letters*, 78(2):115–120, 1998.
(Cited on pages 44, 46, and 47)

[42] Y. T. Cheng and C. M. Cheng. Scalindentation to conical indentation in elastic-plastic solids with work hardening. *Jounral of Applied Physics*, 83(3):1284–1291, 1998.
(Cited on page 44)

[43] Y. T. Cheng and C. M. Cheng. Can stress-strain relatrelation be obtained from indentation curves using conical and pyramidal indenters? *Journal of Materials Research*, 14(9):3493–3496, 1999.
(Cited on page 44)

[44] M. Dao, N. Chollacoop, K. J. Van Vliet, T. A. Venkatesh, and S.. Suresh. Computational modeling of the forward and reverse pproblem in instrumented sharp indentation. *Acta Materialia*, 49:3899–3918, 2001.
(Cited on page 47)

[45] A. E. Giannakopoulos, P. Larsson, and R. V. Vestergaard. Analysis of vickers indentation. *International Journal of Solids Structures*, 31:2679–2708, 1994.
(Cited on page 47)

[46] O. Casals and J. Alcala. The duality in mechanical property extractions from vickers and berkovich instrumented indentation experiments. *Acta Materialia*, 53:3545–3561, 2005.
(Cited on page 48)

[47] J.L Bucaille, S Stauss, E Felder, and J Michler. Determination of plastic properties of metals by instrumented indentation using different sharp indenters. *Acta Materialia*, 51:1663–1678, 2003.
(Cited on page 48)

[48] S. R. Kalidindi and S. Pathak. Determination of the effective zero-point and the extraction of spherical nanoindentation stress-strain curves. *Acta Materialia*, 56:3523–3532, 2008.
(Cited on page 48)

[49] O. Casals, J. Ocenasek, and J. Alcala. Crystal plasticity finite element simulations of pyramidal indentation in copper single crystals. *Acta Materialia*, 55(1):55–68, 2007.
(Cited on page 48)

[50] O. Casals, J. Ocenasek, and J. Alcala. Micromechanics of pyramidal indentation in fcc metals: single crystal plasticity finite element analysis. *Journal of Mechanical Physics of Solids*, 56(11):3277–3303, 2008.
(Cited on page 48)

[51] Y. Liu, M. Yoshino, H. Lu, and R. Komanduri. Combined numerical simulation and nanoindentation for determining mechanical properties of single crystal copper at mesoscale. *International Journal of Plasticity*, 24:1990–2015, 2008.
(Cited on page 48)

[52] N. Zaafarani, D. Raabe, F. Dingh, N. andRoters, and S. Zaefferer. Three dimensional investigation of the texture and microstructure below a nanoindent in a cu single crystal using 3d ebsd and crystal plasticity finite element simulations. *Acta Materialia*, 54:1707–1994, 2006.
(Cited on page 48)

[53] M. Verdier, H. J. Chang, and M. Fivel. Effet de la densité initiale de dislocations en indentation de monocristaux de cuivre. *Materiaux et techniques*, 96:53–57, 2008.
(Cited on page 49)

[54] H. J. Chang, M. Fivel, D. Rodney, and M. Verdier. Multiscale modelling of indentation in fcc metals: From atomic to continuum. *Comptes Rendus Physique*, 11(3-4):285–292, 2010.
(Cited on pages 49, 146, and 165)

[55] H. J. Chang, M. Fivel, and M. Verdier. Indentation crystal plasticity: Experiments and multiscale simulations. *MRS Proceedings*, 1224, 2010.
(Cited on page 49)

[56] S. VuHoang. *Simulations numériques et mesure eexpérimentale du comportement mécanique de films minces*. PhD thesis, Université de Grenoble, 2006.
(Cited on page 49)

[57] S. VuHoang, G. Parry, and M. Verdier. Crystal plasticity of single crystal and film on substrate pprobe by nano-indentation: Simulations and experiments. *MRS Proceedings*, 1363, 2011.
(Cited on page 49)

[58] H. Nili, K. Kalentar-zadeh, M. Bhaskaran, and S. Sriram. In situ nanoindentation: Probing nanoscale multifunctionality. *Progress in Materials Science*, 58:1–29, 2013.
(Cited on pages 50 and 76)

[59] R. Rabe, J. M. Breguet, P. Schwaller, S. Stauss, F. J. Haug, and J. Patscheider. Observation of fracture and plastic deformation during indentation and scratching. *Thin Solid Films*, 206(13):469–470, 2004.
(Cited on page 50)

[60] K. A. Rzepiejewska-Malyska, G. Buerki, Michler J., R. C. Major, E. Cyrankowski, and S. A. S. Asif. In situ mechanical observation during nanoindentation inside a high-resolution scanning electron microscope. *Journal of Materials Research*, 23:1973–1979, 2008.
(Cited on page 50)

[61] B. Moser, J. Kuebler, H. Meinhard, W. Muster, and J. Michler. Observation of instabilities during plastic deformation by in-situ sem indentation experiments. *Advanced Engineering Materials*, 7:388–392, 2005.
(Cited on page 50)

[62] B. Moser, J. F. Löffler, and Michler J. Discrete deformation in amorphous metals: an in situ sem indentation study. *Philosophical Magazine*, 86:5715–5728, 2006.
(Cited on page 50)

[63] I. E. Khodasevych, C. M. Shah, S. Sriram, M. Bhaskaran, W. Withayachumnankul, and B. S. Y. Ung. Elastomeric silicone substrates for terahertz fishnet metamaterials. *Applied Physics Letters*, 100:061101–1–3, 2012.
(Cited on page 50)

[64] K. A. Rzepiejewska-Malyska, M. Parlinska-Wojtan, K. Wasmer, J. Hejduk, and Michler J. In-situ sem indentation studies of the deformation mmechanism in tin, crn and tin/crn.

Micron, 40:22–27, 2009.
(Cited on page 50)

[65] K. A. Rzepiejewska-Malyska, W. M. Mook, M. Parlinska-Wojtan, J. Hejduk, and Michler J. In situ scanning electron microscopy indentation studies on multilayer nitride films: Methodology and deformation mechanisms. *Journal of Materials Research*, 24:1208–1221, 2009.
(Cited on page 50)

[66] N. Vecchione, K. Wasmer, D. S. Balint, and K. Nikbin. Characterisation of eb-pvd yttrium-stabilised zirconia by nanoindentation. *Surface Coating Technology*, 203:1743–1747, 2009.
(Cited on page 50)

[67] E. A. Stach, T. Freeman, A.M. Minor, D. K. Owen, J. Cumings, and M. A. Wall. Development of a nanoindenter in situ transmission electron microscopy. *Microscopy and Microanalysis*, 7:507–517, 2001.
(Cited on page 51)

[68] A. Minor, E. T. Lilleodden, E. A. Stach, and Morris J. In-situ transmission electron microscopy study of nanoidnentation behavior of al. *Journal of Electronic Materials*, 31:958–964, 2002.
(Cited on page 51)

[69] A. M. Minor, E. T. Lilleodden, E. A. Stach, and Morris J. W. Direct oobservation of incipient plasticity during nanoindentation of al. *Journal of Materials Research*, 19:176–82, 2004.
(Cited on page 51)

[70] M. Jin, A. M. Minor, D. Ge, and Morris J. W. Study of deformation behavior of ultrafine-grained materials through in situ nanoindentation in a transmission electron microscope. *Journal of Materials Research*, 20:1735–40, 2005.
(Cited on page 51)

[71] T. Ohmura, A. M. Minor, E. A. Stach, and Morris J. W. Dislocations-grain boundary interactions in martensitic steel observed through in-situ nanoindentation in a transmis-

sion electron miscroscope. *Journal of Materials Research*, 19:3626–3623, 2004.
(Cited on page 51)

[72] L. Zhang, T. Ohmura, K. Seikido, K. Nakajima, T. Hara, and K. Tsuzaki. Direct observation of plastic deformation in iron-3crystal by in situ nanoindentation in transmission electron microscopy. *Scripta Materialia*, 64:919–922, 2011.
(Cited on page 51)

[73] E. Withey, M. Jin, A. Minor, S. Kuramoto, D. C. Chrzan, and J. W. Morris Jr. The deformation of "gum metal" in nanoindentation. *Materials Science & Engineering, A: Structural Materials: Properties, Microstructure and Processing*, 493:26–32, 2008.
(Cited on page 51)

[74] R. Holm. *Electrics Contacts, Theory and Applications*. Springer, 2000.
(Cited on pages 53, 55, 59, 61, 64, and 184)

[75] R. S. Timsit. *Electrical Contact Resistance: Fundamental Principles*. CRC Press, 1999.
(Cited on pages 53, 54, 56, 63, and 65)

[76] M. Braunovic, V. V. Konchits, and N. K. Myshkin. *Electrical Contacts, Fundamental, Applications and Technology*. CRC Press, 2007.
(Cited on pages 53, 55, 57, 61, and 233)

[77] H. Aichi and N. Tahara. Analysis on the constriction resistance of the electric contact by the model using electrolyte bath. *Proceedings of 7th International Conference on Electrical Contacts*, pages 1–10, 1994.
(Cited on page 55)

[78] M. Nakamura. Constriction resistance of conducting spots by the boudary element methode. *IEEE Transactions on Components Hy*, 16(3):339–343, 1993.
(Cited on pages 55, 198, and 200)

[79] M. G. Cooper, B. B. Mikic, and M. M. Yovanovich. Thermal contact conductance. *International Journal of Heat and Mass Transfer*, 12:279–300, 1969.
(Cited on page 56)

[80] Y. Sano. Effect of space angle on constriction resistance and contact resistance for a point contact. *Journal of applied physiscs*, 58(7):2651–2654, 1985.
(Cited on page 56)

[81] Y. Sharvin. A possible method for studying fermi surfaces. *Soviet Physics Jetp-Ussr*, 21(3):655–656, 1965.
(Cited on pages 57 and 197)

[82] G. Wexler. The size effect and the non-local boltzmann transport equation in orifice and disk geometry. *Proceedings of the Physical Society*, 89:927–941, 1966.
(Cited on page 57)

[83] R. S. Timsit. Electrical contact resistance: Properties of stationnary interfaces. *IEEE Transactions on Components and*, 22:85–98, 1999.
(Cited on pages 57, 59, and 66)

[84] A. Mikrajuddin, F. G. Shi, H. K. Kim, and K. Okuyama. Size-dependant electrical constriction resistance for contacts of arbitrary size: from sharvin to holm limits. *Materials Science in Semiconductor Processing 2*, pages 321–327, 1999.
(Cited on page 57)

[85] B. Nikolic and P. B. Allen. Electron transport through a circular constriction. *Physical Review B: Condensed Matter and Materials Physics*, 60(6):3963–3969, 1999.
(Cited on page 57)

[86] D. Erts, H. Olin, L. Ryen, E. Olsson, and A. Thölén. Maxwell and sharvin conductance in gold point contacts investigated using tem-stm. *Physical Review B*, 61(19):12 725–12 727, 2000.
(Cited on page 59)

[87] B. Ludolph, Devoret M. H., Esteve D., C. Urbina, and J. M. van Ruitenbeek. Evidence for saturation of channel transmission from conductance fluctuations in atomic-size point contacts. *Physical Review Letters*, 82(7):1530–1533, 1999.
(Cited on page 59)

[88] B. Ludolph and J. M. van Ruitenbeek. Thermopower of atomic-size metallic contacts. *Physical Review B*, 59(19):12 290 – 12 293, 1999.
(Cited on page 59)

[89] J. A. Greenwood. Constriction resistance and the real area of contact. *Journal of Applied Physics*, 17:1621–1631, 1966.
(Cited on pages 60 and 61)

[90] R. S. Timsit. Some fundamental properties of aluminum-aluminum electrical contacts. *IEEE Transactions on components, hybrids, and manufacturing technology*, 3(1):71–79, 1980.
(Cited on page 62)

[91] E. Crinon and J. T. Evans. The effect of surface roughness, oxide film thickness and interfacial sliding on electrical contact resistance of aluminium. *Materials Science and Engineering*, A242:121–128, 1998.
(Cited on pages 62 and 63)

[92] J. Aronstein. An updated view of the aluminum contact interface. *IEEE Holm conference on electrical contact*, pages 98–103, 2004.
(Cited on page 62)

[93] D. Mercier, V. Mandrillon, A. Holtz, F. Volpi, M. Verdier, and Y. Bréchet. Quantitative evolution of electrical contact resistance between aluminium thin films. *Proceedings of the 58th IEEE Holm Conference on elecrical contact*, pages 1–8, 2012.
(Cited on pages 62, 182, and 209)

[94] H. R. Le, M. P. F. Sutcliffe, P. Z. Wang, and G. T. Burstein. Surface oxide fracture in cold aluminium rolling. *Acta Materialia*, 52:911–920, 2004.
(Cited on pages 62, 63, and 214)

[95] H. R. Le, M. P. F. Sutcliffe, P. Wang, and G. T. Burstein. Surface generation and boundary lubrification in bulk forming of aluminium alloy. *Wear*, 258:1567–1576, 2005.
(Cited on pages 62, 63, and 214)

[96] H. A. Mohamed and J. Washburn. Mechanism of solid state pressure welding. *Welding Research Supplement*, 54(9):302–310, 1975.
(Cited on pages 62 and 214)

[97] J. G. Simmons. Generalized formula for the electric tunnel effect between similar electrodes separeted by a thin insulating film. *Journal of applied physiscs*, 34(6):1793–1803,

1963.
(Cited on page 62)

[98] I. C. Chen, S. E. Holland, and C. M. Hu. Electrical breakdown in thin gate and tuntunnel oxides. *IEEE Transactions on Electron*, 32(2):413–422, 1985.
(Cited on page 63)

[99] K. Gloos, P. J. Koppinen, and J. P. Pekola. Properties of native ultrathin aluminium oxide tunnel barriers. *Journal of Physics: Condensed Matter*, 15:1733–1746, 2003.
(Cited on page 63)

[100] A. Bouchoucha, H. Zaidi, E. K. Kadiri, and D. Paulmier. Influence of electric fields on tribological behaviour of electrodynamical copper/steel contacts. *Wear*, 203-204:434–441, 1997.
(Cited on pages 64, 218, and 219)

[101] W. C. Liu, S. W. Chen, and C. M. Chen. The al/ni interfacial reactions under the influence of electric current. *Journal of Electronic Materials*, 27(1):5–9, 1998.
(Cited on page 65)

[102] F. Kohlraush. Über den stationären temperatursustand eines elektrish geheizten leiters. *Annalen der Physik*, 306(1):132–158, 1900.
(Cited on pages 65 and 232)

[103] R. S. Timsit. On the evaluation of contact temperature from potential-drop measurements. *IEEE Transactions on components, hybrids, and manufacturing technology*, 6(1):115, 121 1983.
(Cited on page 66)

[104] V. V. Konchits and C. K. Kim. Electrical current passage and interface heating. *Wear*, 232:31–40, 1999.
(Cited on pages 66 and 67)

[105] H. Blok. Theoritical study of temperature rise at surfaces of actual contact under oilness lubricating conditions. *Proceedings of Institude of Mechanical Engineering*, 2:222–235, 1959.
(Cited on page 66)

[106] J. S. Jaeger. Moving sources of heat and the temperature at sliding surfaces. *Proceedings of the Royal Society of New South Wales*, 56:203–224, 1942.
(Cited on page 66)

[107] P. De Wolf, T. Clarysse, and W. Vandervorst. Quantification of nanospreading resistance profiling data. *Journal of Vacuum Science & Technology, B: Nanotechnology and Microelectronics*, 16(1):320–326, 1997.
(Cited on pages 68 and 69)

[108] W. Vandervorst and M. Meuris. European patent 466274, 1992.
(Cited on page 68)

[109] P. Eyben, W. Vandervorst, D. Alvarez, M. Xu, and M. Fouchier. *Probing Semiconducteurs Technology and Devices with Scanning Spreading Resistance Microscopy IN Scanning Probe Microscopy Electrical and Electromechanical Phenomena at the NaProbing.* Springer, 2007.
(Cited on pages 68 and 70)

[110] P. Eyben, S. Denis, T. Clarysse, and W. Vandervorst. Progress towards a physical contact model for scanning spreading resistance microscopy. *Materials Science & Engineering, B: Solid-State Materials for Advanced Technology*, 102:132–137, 2003.
(Cited on pages 69 and 70)

[111] T. Clarysse, P. Eyben, N. Duhayon, and M. W. Xu. Carrier spilling revisited: on-bevel junction behavior of different electrical depth profiling techniques. *Journal of Vacuum Science & Technology, B: Nanotechnology and Microelectronics*, 21(2):729–736, 2003.
(Cited on page 70)

[112] A. Olbrich, B. Ebersberger, and C. Boit. Conducting atomic force microscopy for nanoscale electrical characterization of thin si02. *Applied Physics Letters*, 73:3114–3116, 1998.
(Cited on pages 71, 72, and 74)

[113] A. Olbrich, B. Ebersberger, and C. Boit. Nanoscale electrical characterization of thin oxides with conducting atomic force microscopy. *36th annual IEEE*, pages 163–168, 1998.
(Cited on pages 71 and 74)

[114] M. Porti, M. Nafria, X. Aymerich, A. Olbrich, and B. Ebersberger. Nanometer-scale electrical characterization of ststress ultrathin si02 films using conducting atomic force microscopy. *Applied Physics Letters*, 78:4181–4183, 2001.
(Cited on page 71)

[115] W. Frammelsberger, G. Benstetter, J. Kiely, and R. Stamp. C-afm-based thickness determination of thin and ultra-thin si02 films by use of different conductive-coated probe tips. *Applied Surface Science*, 253:3615–3626, 2007.
(Cited on pages 71, 72, and 74)

[116] G. Benstetter, R. Biberger, and D. Liu. A review of advanced scanning probe microscope analysis of functional films and semiconductor devices. *Thin Solid Films*, 517:5100–5105, 2009.
(Cited on pages 71, 72, and 74)

[117] S. J. O'Shea, R. M. Atta, M. P. Murrel, and M. E. Welland. Conducting atomic force microscopy study of silicon dioxide breakdown. *Journal of Vacuum Science & Technology, B: Nanotechnology and microelectronics*, 13(5):1945–1952, 1995.
(Cited on pages 71 and 74)

[118] C. I. Pakes, S. Ramelow, S. Prawer, and D. N. Jamieson. Nanoscale electrical characterization of trap-assisted quasibreakdown fluctuations in si02. *Applied Physics Letters*, 84(16):3142–3144, 2004.
(Cited on pages 71 and 74)

[119] Z. G. Sun, H. Kuramochi, H. Akinaga, H. H. Yu, and E. D. Gu. Conductive atomic force microscopy study of silica nanotrench structure. *Applied Physics Letters*, 90:042106–1–3, 2007.
(Cited on pages 71, 72, 74, and 75)

[120] S. Gsell, M. Schreck, G. Benstetter, B. Lodermeier, and B. Stritzker. Combined afm-sem study of the diamond nucleation layer on ir(001). *Diamond & Related Materials*, 16:665–670, 2007.
(Cited on pages 71, 75, and 181)

[121] A. A. Pomarico, D. Huang, J. Dickinson, A. A. Baski, R. Cingolani, H. Morkoç, and R. Molnar. Current mapping of gan films by conductive atomic force microscopy. *Applied*

Physics Letters, 82(12):1890–1892, 2003.
(Cited on pages 71, 72, and 74)

[122] X. A. Cao, J. M. teetsov, M. P. D'Evelyn, D. W. Merfeld, and C. H. Yan. electrical characteristics of ingan/gan light emitting diodes grown on gan and sapphire substrates. *Applied Physics Letters*, 85(1):7–9, 2004.
(Cited on pages 71 and 74)

[123] H. N. Lin, H. L. Lin, S. S. Wang, L. S. Yu, G. Y. Perng, S. A. Chen, and S. H. Chen. Nanoscale charge transport in an electroluminescent polymer investigated by conducting atomic force microscopy. *Applied Physics Letters*, 81(14):2572–2574, 2002.
(Cited on pages 71 and 73)

[124] J. A. J. Steen, J. Hayakawa, T. Harada, K. Lee, F. Calame, G. Boero, A. J. Kulik, and J. Brugger. Elelectrical conducting probes with full tungsten cantilever and tip for scaning probe applications. *Nanotechnology*, 17:1464–1469, 2006.
(Cited on page 71)

[125] S. J. O'Shea, R. M. Atta, and M. E. Welland. Characterization of tips for conducting atomic microscopy. *Review of Scientific Instruments*, 66(3):2508–2512, 1995.
(Cited on page 71)

[126] E. Chery. *Fiabilité des diéléctriques low-k SiOCH poreux dans les interconnections CMOS avancées*. PhD thesis, Université de Grenoble, 2006.
(Cited on pages 71 and 73)

[127] E. W. Lim and R. Ismail. Conduction mechanism of valence change resistive switching memory: A survey. *Electronics*, 4(3):586–613, 2015.
(Cited on page 73)

[128] J. W. P. Hsu, M. J. Manfra, R. J. Molnar, B. Heying, and J. S. Speck. Direct imaging of reverse-bias leakage through pure screw dislocations in gan films grown by molecular beam epitaxy on gan templates. *Applied Physics Letters*, 81(1):79–81, 2002.
(Cited on page 74)

[129] M. Lanza, M. Porti, M. Nafria, X. Aymerich, E. Whittaker, and B. Hamilton. Electrical resolution during conductive atomic force microscopy measurements under different environmental conditions and contact forces. *Review of Scientific Instruments*, 81:106110–1–3,

2010.
(Cited on pages 75 and 181)

[130] M. Lanza, M. Porti, M. Nafria, X. Aymerich, E. Whittaker, and B. Hamilton. Uhv cafm characterisation of high-k dielectrics: Effect of the technique resolution on the pre- and post-breakdown electrical measurements. *Microelectronics Reliability*, 50:1312–1315, 2010.
(Cited on pages 75, 76, and 181)

[131] D. Stievenard and B. legrand. Silicon surface nano-oxidation using scanning probe microscopy. *Progress in Surface Science*, 81:112–140, 2006.
(Cited on pages 75 and 181)

[132] D. R. Clarke, M.C. Kroll, P. D. Kirchner, R. F. Cook, and B. J. Hockey. Amorphization and conductivity of silicon and germanium induced by indentation. *Physical Review Letters*, 60:2156–2159, 1988.
(Cited on page 76)

[133] G. M. Pharr, W. C. Oliver, R. F. Cook, P. D. Kirchner, M.. KrKroll, and T. R. Dinger. Electrical resistance of metallic contacts on silicon and germanium during indentation. *Journal of Materials Research*, 7:961–972, 1992.
(Cited on pages 76 and 180)

[134] A. B. Mann, D. van Heerden, J. B. Pethica, and T. P. Weihs. Size-dependent phase transformation during point loading of silicon. *Journal of Materials Research*, 15(8):1754–1758, 2000.
(Cited on pages 76, 78, 180, and 182)

[135] A. B. Mann, D. van Heerden, J. B. Pethica, Bowes P., and T. P. Weihs. Contact resistance and phase ttransformation during nanoindentation of silicon. *Philosophical Magazine A*, 82(10):1921–1929, 2002.
(Cited on pages 76, 78, 180, and 182)

[136] J. E Bradby, J. S. Williams, and M. V. Swain. In situ electrical characterisation of phase transformation in si during indentation. *Physical Review B: Condensed Matter and Materials Physics*, 67:085205, 2003.
(Cited on pages 76 and 180)

[137] S Ruffell, J. E Bradby, J. S. Williams, and Warren; O. L. An in situ electrical measurement technique via a conducting diamond tip for nanoindentation in silicon. *Journal of Materials Research*, 22(3):578–585, mars 2007.
(Cited on pages 76, 78, 180, and 181)

[138] S Ruffell, J. E Bradby, N. Fujisawa, and J. S. Williams. Identification of nanoindentation-induced phase changes in silicon by in situ electrical characterization. *Journal of Applied Physics*, 101:083531, april 2007.
(Cited on pages 76, 78, 180, and 181)

[139] D. D. Stauffer, R. C. Major, D. Vodnick, J. H. Thomas, Parkern J., M. Manno, C. Leighton, and W. W. Gerberich. Plastic response of the native oxide on cr and al thin films from in situ conductive nanoindentation. *Journal of Materials Research*, 27(4):685–693, 2012.
(Cited on pages 77 and 180)

[140] J. B. Pethica and D. Tabor. Contact of characterised metal surface at very low loads: deformation and adhesion. *Surface Science*, 89:189–190, 1979.
(Cited on pages 76 and 180)

[141] H. H. Nguyen, P. J. Wei, and J. F. Lin. Electrical contact resistance for monitoring nanoindentation-induced delamination. *Advanced Natural Sciences: nanoscience and nanotechnology*, 2:015007–1–4, 2011.
(Cited on pages 77 and 180)

[142] P. Y. Duvivier. *Etude expérimentale et modélisation du contact électrique et mécanique quasi statique entre surfaces rugueuses d'or: application aux micro-relais mems.* PhD thesis, Ecole nationale supérieure des mines de Saint Etienne, 2010.
(Cited on page 77)

[143] L. Fang, C. L. Muhlsteing, J. G. Collins, A. L. Romasco, and L. H. Friedman. Continuous electrical in situ contact area measurement during instrumented indentation. *Journal of Materials Research*, 23(9):2480–2485, 2008.
(Cited on pages 77, 78, 179, and 181)

[144] D. J. Sprouster, S Ruffel, J. E Bradby, D. D. Stauffer, R. C. Major, Warren; O. L., and J. S. Williams. Quantitative electromechanical characterization of materials using

conductive ceramic tips. *Acta Materialia*, 71:153–163, 2014.
(Cited on pages 77, 78, 179, and 182)

[145] D. J. Sprouster, S Ruffel, J. E. Bradby, J. S. Williams, M. N. Lockrey, M. R. Phillips, R. C. Major, and Warren; O. L. Structural characterization of b-doped diamond nanoindentation tips. *Journal of Materials Research*, 26(24):3051–3057, 2011.
(Cited on pages 78, 181, and 188)

[146] T. Yudate, J. Toyoizumi, M. Onuma, T. Kondo, T. Shimizu, S. Kawabata, N. Watanabe, and K. Mori. The investigation of the electrical contact resistance through thin oxide layer on a nanometer scale. *IEEE Holm conference on electrical contact*, pages 60–65, 2016.
(Cited on page 78)

[147] http://nanomechanicsinc.com/products/.
(Cited on pages 83 and 128)

[148] http://www.smaract.com/technology/.
(Cited on page 84)

[149] L. Maniguet, F. Roussel, R. Martin, E. Djurado, M. C. steil, E. Bichaud, A. Le Goff, M. Holzinger, S. Cosnier, J. M. Chaix, and C. Carry. Fuel cells and cceramic - characterizing real-world ssample with a fe-sem ready for challenges. *Microscopy and Analysis*, 21:4–7, 2015.
(Cited on page 93)

[150] http://www.csinstruments.eu/our-products/resiscopell-electrical-characterization/.
(Cited on pages 104 and 105)

[151] F. Houzé, R. Meyer, O. Schneegans, and L. Boyer. Imaging the local electrical properties of metal surfaces by atomic force microscopy with conducting probes. *Applied Physics Letters*, 69:1975–1977, 1996.
(Cited on pages 104, 180, and 181)

[152] C. Herrera, D. Ponge, and D. Raabe. Design of a novel mn-based 1gpa duplex stainless trip steel with 60ductility by a reduction of austenite stability. *Acta Materialia*, 59:4653–4664, 2011.
(Cited on page 116)

[153] A. Lechartier. *Influence de la transformation martensitique induite par la déformation sur le comportement mécanique d'aciers inoxydables duplex*. PhD thesis, Université Grenoble Alpes, 2016.
(Cited on pages 116 and 122)

[154] A. Lechartier, G. Martin, S. Comby, F. Roussel-Dherbey, A. Deschamps, M. Mantel, N. Meyer, M. Verdier, and M. Veron. Influene of the martensite transformation on the microscale plastic strain heterogeneities in a duplex stainless steel. *Metallurgical and Materials Transactions A: Physical Metallurgy and Materials Science*, 48(1):20–25, 2017.
(Cited on pages 116, 118, and 122)

[155] M. Asgari, R. Johnsen, and A. Barnoush. Nanomechanical characterization of the hydrogen effect on pulsed plasma nitrided super duplex stainless steel. *International Journal of Hydrogen Energy*, 38:15520–31, 2013.
(Cited on page 117)

[156] M. Delince, P. J. Jacques, and T. Pardoen. Separation of size-dependent strengthening contributions in fine-grained dual phase steels by nanoindentation. *Acta Materialia*, 54:3395–3404, 2006.
(Cited on page 118)

[157] H. Naser. *Development of architectured micro-composite duplex stainless ssteel: manufacturing, microstructure & mechanical behavior*. PhD thesis, Université Grenoble Alpes, 2016.
(Cited on pages 119, 120, 121, and 122)

[158] R. Saha and W. D. Nix. Effect of the substrate on the determination of thin film mechanical properties by nanoindentation. *Acta Materialia*, 50:23–38, 2002.
(Cited on page 126)

[159] R. Ouahab. *Comportement des aciers bainitiques à différentes temperature: étude de la cémentite aux grands instruments*. PhD thesis, Ecole nationale supérieure des arts et métiers, 2012.
(Cited on page 127)

[160] A. Fernandes-Vincente, M. Pellizzari, and J. L. Arias. Feasibility of laser surface treatment of pearlitic and bainitic ductile irons for hot rolls. *Journal of Materials Processing*

Technology, 212:989–1002, 2008.
(Cited on page 127)

[161] G. Constantinides, K. S. R. Chandran, F. J. Ulm, and K. J. Van Vliet. Grid indentation analysis of composite microstructure and mechanics: Principles and validation. *Materials Science & Engineering, A: Structural Materials: Properties, Microstructure and Processing*, 430:189–202, 2005.
(Cited on pages 128 and 130)

[162] F. Mas, C. Tassin, N. Valle, Robautn F., F. Charlot, M. Yescas, F. Roch, P. Todeschini, and Y. Bréchet. Metallurgical characterization of coupled carbon diffusion and precipitation in dissimilar steel welds. *Journal of Materials Science*, 51(10):4864–4879, 2016.
(Cited on page 133)

[163] J. D. Currey. *Bones: Structure and Mechanics*. Princeton Univ Press, 2002.
(Cited on page 137)

[164] C. E. Hamm, R. Merkel, O. Springer, P. Jurkojc, C. Maier, K. Prechtel, and V. Smetacek. Architecture and material properties of diatom shells provide effective mechanical protection. *Nature*, 421:841–843, 2003.
(Cited on page 137)

[165] J. C. Weaver, J. Aizenberg, G. E. Fantner, D. Kisailus, A. Woesz, P. Allen, K. Fields, M. J. Porter, F. W. Zok, P. Fratzl, and D. E. Morse. Hierarchical assembly of the siliceous skeletal lattice of the hexactinellid sponge euplectella aspergillum. *Journal of Structural Biology*, 158(1):93–106, 2007.
(Cited on page 137)

[166] M. Bauer, S. Hengsbach, I. Tesari, R. Schwaiger, and O. Kraft. High-strenght cellular ceramic ccomposite with 3d microarchitecture. *Proceedings of the National Academy of Sciences*, 111(7):2453–2458, 2014.
(Cited on pages 137, 139, and 140)

[167] L. R. Meza, S. Das, and J. R. Greer. Strong, lightwlight, and recoverable three-dimensional ceramic nanolattices. *Science*, 345(6202):1322–1326, 2014.
(Cited on pages 137 and 140)

[168] J. Bauer, A. Schroer, R. Schwaiger, and O. Kraft. Approching theoritical strength in glassy carbon nanolattices. *Nature Materials*, 15:438–444, 2016.
(Cited on pages 137, 140, and 141)

[169] I. Wang, M. Bouriau, and P. L. Baldeck. Three-dimensional microfabrication by two-photon initiated polymerpolymer with a low-cost microlaser. *Optics Letters*, 27(15):1348–1350s, 2002.
(Cited on page 137)

[170] M. F. Ashby, L. J. Gibson, U. Wegst, and R. Olive. The mechanical properties of natural materials. i. material property charts. *Proceedings of The Royal Society A: Mathematical, Physical and Engineering Sciences*, 450:123–140, 1995.
(Cited on page 140)

[171] S. S. Brenner. Plastic deformation of copper and silver whiskers. *Journal of Applied Physics*, 28:1023–1026, 1957.
(Cited on pages 143, 144, 160, and 168)

[172] B. Wu, A. Heidelber, and J. J. Boland. Mechanical properties of ultrahigh-strength gold nanowires. *Nature materials*, 4:525–529, 2005.
(Cited on page 143)

[173] G. Richter, K. Hillerich, D. S. Gianola, R. Mönig, O. Kraft, and A. Volkert. Ultrahigh strength single crystalline nanowhiskers grown by physical vapor deposition. *Nano Letters*, 9(8):3048–3052, 2009.
(Cited on pages 143 and 145)

[174] F. Östlund, K. A. Rzepiejewska-Malyska, K. Leifer, L. M. Hale, Y. Tang, R. Ballarini, W. W. Gerberich, and Michler J. Nanostructure fracturing: Brittle-to-ductile transition in uniaxial compression of silicon pillars at room temperature. *Advanced Functional Materials*, 19(15):2439–2444, 2009.
(Cited on page 144)

[175] S. G. Corcoran, R. J. Colton, E. T. Lilleodden, and W. W. Gerberich. Anomalous plastic deformation at surfaces: Nanoindentation of gold single crystals. *Physical Review B: Condensed Matter and Materials Physics*, 55(24):R16 057–060, 1997.
(Cited on pages 144 and 170)

[176] H. Bei, S. Shim, G. M. Pharr, and E. P. George. Effects of pre-strain on the compressive stress-strain response of mo-alloy single-crystal micropillars. *Acta Materialia*, 56(17):4762–4770, 2008.
(Cited on page 144)

[177] M. U. Uchic, D. M. Dimiduk, J. N. Florando, and W. D. Nix. Sample dimensions influence strength and crystal plasticity. *Science*, 50:986–989, 2004.
(Cited on pages 144 and 145)

[178] J. R. Greer, W. C. Oliver, and W. D. Nix. Size dependance of mechanical properties of gold at the micron scale in the abscence of strain gradient. *Acta Materialia*, 53:1821–1830, 2005.
(Cited on pages 144, 145, 161, 170, and 172)

[179] H. Bei, S. Shim, M. K. Miller, G. M. Pharr, and E. P. George. Effects of focused ion beam milling on the nanomechanical behavior of a molybdenum-alloy single crystal. *Journal of Applied Physics*, 91:111915–1–4, 2007.
(Cited on page 144)

[180] D Kiener, C. Motz, M. Rester, M. Jenko, and G. Dehm. Fib damage of cu possible consequences for miniaturized mechanical tests. *Materials Science & Engineering, A: Structural Materials: Properties, Microstructure and Processing*, 459:262–272, 2007.
(Cited on page 144)

[181] H. Bei, S. Shim, E. P. George, M. K. Miller, E. G. Herbert, and G. M. Pharr. Compressive sstrength of molybdenum alloy micro-pillars prepared using a new technique. *Scripta Materialia*, 57:397–400, 2007.
(Cited on page 145)

[182] D. Mordehai, M. Kazakevich, D. J. Srolovitz, and E. Rabkin. Nanoindentation size effect in single-crystal nanoparticles and thin films: a comparative experimental and simulation study. *Acta Materialia*, 59:2309–2321, 2011.
(Cited on pages 145, 146, 153, 165, and 170)

[183] D. Mordehai, S. K. Lee, B. Backes, D. J. Srolovitz, W. D. Nix, and E. Rabkin. Size effect in compression of single-crystal gold microparticles. *Acta Materialia*, 59:5202–5215,

2011.
(Cited on pages 145, 161, 164, and 172)

[184] W. M. Mook, C. Niederberger, M. Bechelany, Philippe L., and Michler J. Compression of freestanding gold nanostructures: from stochastic yield to predictable flow. *Nanotechnology*, 21:1–9, 2010.
(Cited on pages 145, 160, 165, 166, 167, 293, 295, and 296)

[185] W. D. Nix and Y. Gao. Indentation size effect in crystalline materials: a law for strain gradient plastictity. *Journal of Mechanics and Physics of Solids*, 46(3):411–425, 1998.
(Cited on pages 145, 165, and 170)

[186] A. H. W. Ngan, L. Zuo, and P. C. Wo. Size dependance and stochastic nature of yield strength of micron-sized crystals: a case study on ni3al. *Proceedings of the royal society of london, Serie A*, 462:1661–1681, 2006.
(Cited on pages 145 and 164)

[187] J. R. Greer and W. D. Nix. Nanoscale gold pillars strengthened throug dislocation starvation. *Physical Review B: Condensed Matter and Materials Physics*, 73:245410–1–6, 2006.
(Cited on page 145)

[188] Y. Feruz and D. Mordehai. Towards a universal size-dependant strength of face-centered cubic nanoparticles. *Acta Materialia*, 103:133–441, 2016.
(Cited on pages 145 and 172)

[189] M. Dupraz. *Coherent X-ray diffraction applied to metal physics*. PhD thesis, Université Grenoble Alpes, 2015.
(Cited on pages 146, 157, 158, 165, 284, 285, and 289)

[190] R. Rupp. Solid state dewetting of gold on sapphire for ptychography measurements of nano-indented crystals. Master's thesis, Institut Polytechnique de Grenoble, 2015.
(Cited on pages 147 and 153)

[191] G. Beutier, M. Verdier, G. Parry, B. Gilles, S. Labat, M. I. Richard, T. Cornelius, P. F. Lory, S. V. Hoang, F. Livet, O. Thomas, and M. De Boissieu. Strain inhomogeneity in copper islands probed by x-ray diffraction. *Thin Solid Films*, 530:120–124, 2013.
(Cited on page 147)

[192] G. Wulff. Zur frage der geschwindigkeit des wachstums und der auflösung der krystallflagen. *Zeitschrift für Krystallographie und Mineralogie*, 34(5/6):449–530, 1901.
(Cited on page 150)

[193] W. L. Winterbottom. Equilibrium shape of a small particle in contact with a foreign substrate. *Acta Metallurgica*, 15:303–309, 1967.
(Cited on pages 150 and 152)

[194] O. Malyi, L. Klinger, D. J. Srolovitz, and E. Rabkin. Size and shape evolution of faceted bicrystal nanoparticles of gold on sapphire. *Acta Materialia*, 59:2872–2881, 2011.
(Cited on page 153)

[195] O. Kovalenko and E. Rabkin. Mechano-stimulated equilibration of gold nanoparticles on sapphire. *Scripta Materialia*, 107:149–152, 2015.
(Cited on page 154)

[196] I. Robinson and R. Harder. Coherent x-ray diffraction imaging strain at the nanoscale. *Nature materials*, 8(291-298), 2009.
(Cited on pages 157, 283, and 285)

[197] M. Dupraz, G. Beutier, T. Cornelius, G. Parry, Z. Ren, S. Labat, M. I. Richard, G. A. Chahine, O. Kovalenko, M. De Boissieu, E. Rabkin, M. Verdier, and O. Thomas. 3d imaging of a dislocation loop at the onset of plasticity in an indented nanocrystal. *Nano Letters*, 17(11):6696–6701, 2017.
(Cited on page 157)

[198] J. Miao, P. Charalambous, J. Kirz, and D. Sayre. Extending the methodology of x-ray crystallography to allow imaging of micrometre-sized non-crystalline specimens. *Nature*, 400:342–344, 1999.
(Cited on page 157)

[199] M. C. Newton, S. J. Leake, R. Harder, and I. K. Robinson. Three-dimensional imaging of strain in a single zno nanorod. *Nature Materials*, 9(279):120–124, 2010.
(Cited on page 157)

[200] G. J. Williams, M. A. Pfeifer, I. A. Vartanyants, and I. K. Robinson. Three-dimensional imaging of microstructure in au nanocrystals. *Physical Review Letters*, 90(17):175501–1–

4, 2003.
(Cited on page 159)

[201] U. F. Kocks and H. Mecking. Physics and phenomenology of strain hardening: the fcc case. *Progress in Materials Science*, 48:177, 2003.
(Cited on page 168)

[202] M. Dupraz, G. Beutier, D. Rodney, D. Mordehai, and M. Verdier. Signature of dislocations and stacking faults of face-centred cubic nanocrystals in coherent x-ray diffraction patterns: a numerical study. *Journal of Applied Crystallography*, 48(3):1–34, 2015.
(Cited on page 174)

[203] D. Mercier, V. Mandrillon, G. Parry, M. Verdier, R. Estevez, Y. Bréchet, and T. Maindron. Investigation of the fracture of very thin amorphous alumina film durin spherical nanoindentation. *Thin Solid Films*, 638:34–47, 2017.
(Cited on pages 182 and 209)

[204] O. Schneegans, L. Boyer, F. Houzé, R Meyer, and P. Chrétien. Copper sample analysed with an n-doped silicon tip using conducting probe atomic force microscopy. *Journal of Vacuum Science & Technology, B: Nanotechnology and microelectronics*, 20(5):1929–1934, 2002.
(Cited on pages 190 and 191)

[205] J. Liening. Electromigration and its impact on physical design in future technology. *Proceedings of the 2013 ACM international symposium on physical design*, pages 33–40, 2013.
(Cited on page 233)

[206] M. Runde. Mass transport in stationary contact points. *IEEE Transactions on Components , Hybrids, and Manufacturing Technology*, CHMT-10(1):89–99, 1987.
(Cited on page 233)

[207] H. Gan, W. J. Choi, and K. N. Tu. Electromigration in solder joints and solder lines. *The Journal of The Minerals, Metals & Materials Society*, 54(6):34–37, 2002.
(Cited on page 233)

[208] J. Liening. Introduction to electromigration-aware physical design. *Proceeedings of SLIP*, pages 81–88, 2006.
(Cited on page 233)

[209] J. A. Slinkman, H. K. Wickramasinghe, and C. C. Williams. Scanning capacitance-voltage microscopy, 1991.
(Cited on page 239)

[210] J. J. Kopanski. *Scanning capacitance microsscopy for electrical characterization of semiconductors and dielectrics IN Scanning Probe Microscopy: Electrical and Electromechanical Phenomena at the Nanoscale*. Springer, 2007.
(Cited on pages 239, 240, and 241)

[211] H. P. Huber, I. humer, M. Hochleitner, M. fenner, M. Moertelmaier, C. Rankl, A. Imitiaz, T. M. Wallis, P. Tanbakuchi, P. Kabos, J. Smoliner, J. J. kopanski, and F. Kienberger. Calibrated nanoscale dopant profiling using a scanning microwave miscroscope. *Journal of Applied Physics*, 111:014301–1–9, 2012.
(Cited on page 240)

[212] L. S. C. Pingree and M. C. Hersam. Bridge-enhanced nanoscale impedance microscopy. *Applied Physics Letters*, 87:233117–1–4, 2005.
(Cited on pages 241 and 242)

[213] A. Layson, S. Gadad, and D. Teeters. Resistance measurements at the nanoscale: scanning probe ac impedance spectroscopy. *Electrochimica Acta*, 48:2207–2213, 2003.
(Cited on page 241)

[214] R. Shao, S. V. Kalinin, and D. A. Bonnell. Local impedance imaging and spectroscopy of polycrystalline zno using contact atomic force microscopy. *Applied Physics Letters*, 82(12):1869–1872, 2001.
(Cited on page 241)

[215] R. O'hayre, G. Feng, W. D. Nix, and F. B. Prinz. Quantitative impedance measurement using atomic force microscopy. *Journal of Applied Physics*, 96(6):3540–3549, 2004.
(Cited on page 241)

[216] O. Schneegans, P. Chrétien, F. Houzé, and R. Meyer. Capacitance measurements on small parallel plate capacitors using nanoscale impedance microscopy. *Applied Physics*

Letters, 90:043116–1–4, 2007.
(Cited on pages 241 and 243)

[217] I. Estevez, P. Chrétien, O. Schneegans, and F. Houzé. Specific methodology for capacitance imaging by atomic force microscopy: A breakthrough towards an elimination of parasite effects. *Applied Physics Letters*, 104:083108–1–4, 2014.
(Cited on pages 242 and 243)

[218] D. T. Lee, J. P. pelz, and B. Bushan. Instrumentation for direct, low frequency scanning capacitance microscopy and analysis of position dependent stray capacitance. *Review of scientific instruments*, 73(10):3525–3533, 2002.
(Cited on pages 241 and 242)

[219] L. Fumagalli, G. Farrari, M. Sampietro, I. Casuso, E. Martinez, J. Samitier, and G. Gomila. Nanoscale capacitance imaging with attofarad resolution using ac current sensing atomic force microscopy. *Nanotechnology*, 17:4581–4587, 2006.
(Cited on page 242)

[220] F. Houzé, P. Chrétien, O. Schneegans, R. Meyer, and L. Boyer. Simultaneous resistance and capacitance cartography by conducting probe atomic force microscopy in contact mode. *Applied Physics Letters*, 86:123103–1–3, 2005.
(Cited on page 243)

[221] T. Motoki, S. Kiyono, and T. Ono. A nanoindentation instrument for mechanical property measurement of 3d micro/nano-structured surfaces. *Measurement Science and Technology*, 17:495–499, 2006.
(Cited on page 243)

[222] B. K. Nowakowski, D. T. Smith, S. T. Smith, L. F. Correa, and R. F. Cook. Development of a precision nanoindentation platform. *Review of Scientific Instruments*, 84:075110–1–10, 2013.
(Cited on page 243)

[223] W. Kang, M. Merrill, and J. M. Wheeler. In situ thermomechanical testing methods for micro/nano-scale materials. *Nanoscale*, 9:2666–2688, 2017.
(Cited on page 243)

[224] Z. L. Zhang, H. Kristiansen, and J. Liu. A method for determining elastic properties of micron-sized polymer particles by using flat punch test. *Computational Materials Science*, 39:305–314, 2007.
(Cited on page 243)

[225] A. Koszewski, D. Levy, and F. Souchon. Study of mechanical properties of rf mems switches by nanoindentation: characterization and modeling of electro-mechanical behavior. *Sensors and Actuators, A: Physical*, 163:205–212, 2010.
(Cited on page 243)

[226] V. Koval, M. J. Reece, and A. J. Bushby. Relaxation processes in dielectrics and electromechanical response of pzt thin films under nanoindentation. *Ferroelectrics*, 318:55–61, 2005.
(Cited on page 243)

[227] G. Molnar, S. Rat, L. Salmon, W. Nicolazzi, and A. Boussekou. Spin crossover, nanomaterials: From fundamental concepts to devices. *Advanced Materials*, 30:17003862–1–23, 2018.
(Cited on page 265)

[228] J. R. Fienup. Reconstruction of an object from the modulus of its fourier transform. *Optics Letters*, 3(1):22–29, 1978.
(Cited on page 286)

[229] J. R. Fienup. Phase retrieval algorithms: a comparison. *Applied Optics*, 21(15):2758–2769, 1982.
(Cited on page 287)

[230] S. Marchesini, H. He, H. N. Chapman, S. P. Hau-Riege, A. Noy, M. R. Howells, U. Weierstall, and J. C. H. Spence. X-ray image reconstruction from a diffraction pattern alone. *Physical Review B: Condensed Matter and Materials Physics*, 68(14):140101–1–4, 2003.
(Cited on page 287)

[231] J. M. Zhang, Y. Zhang, K. W. Xu, and V. Ji. Young modulus surface and poisson ratio curves for cubic metals. *Journal of Physics and Chemistry of Solids*, 68:503–510, 2007.
(Cited on pages 290 and 293)

The increasing demand for multifunctional materials has become a recurrent challenge for a wide panel of application fields such as microelectronics and structural applications. Within the frame of this project, a multifunctional characterisation set-up has been developed at SIMaP lab, mainly based on the electrical / mechanical coupling. The heart of this device is an *in situ* FEG-SEM (Field Emission Gun Scanning Electron Microscope) nanoindenter coupled with an electrical measurement apparatus. This work has threefold objectives: (1) The investigation of mechanical behavior of small scale systems, (2) The input of electrical data to the quantitative analysis of mechanical behavior during indentation, in particular to obtain a better estimation of the contact area (3) The local study of electronic properties of thin film stacks. SEM integration of the device has been validated and indent positioning with a precision better than 100 nm is successfully obtained. This performance allows the studies of mechanical properties at submicrometric length scale, with a high throughput allowing statistical measurements. Various bulk composite materials have been characterized as well as submicrometric gold islands on sapphire. In the latter case, despite the stochastic nature of their mechanical behavior, a deterministic law has been extracted. 3D-BCDI (Bragg Coherent Diffraction Imaging) experiments have been performed on a few islands at synchrotron facility to investigate the crystal state before and after mechanical loading. These experiments reveal initial dislocation nucleation prior to large deformation bursts. In parallel to this study, electrical measurements have been performed during indentation on various cases. Resistive-nanoindentations have been performed on noble metals (Au) and natively oxidized metals (Cu, Al), either as bulk single crystals or as polycrystalline thin films. Qualitative results emphasize the importance of the oxide layer on the electrical response. In the presence of an oxide layer, strong electrochemical reactions seem to occur at the tip-to-sample interface. When no oxide is involved, the measured resistance can be fully described by an analytical model and the computed electrical contact area is successfully validated with residual areas measurements. Finally, capacitive measurements have been performed on MOS structures with various oxide thicknesses. Experimental results have been well described by analytical modelling, which paves the way for quantitative local dielectric permittivity measurements under mechanical loading.

L'essor de la demande actuelle pour des matériaux architecturés, en microélectronique par exemple, ou pour des matériaux de structure, nécessite le développement d'outils de caractérisation toujours plus performants. Dans cette optique, un instrument de caractérisation multifonctionnel basé sur un couplage mécanique / électrique, a été développé au laboratoire SIMaP. Le cœur de ce dispositif est un nanoindenteur *in situ* FEG-SEM (Field Emission Gun Scanning Electron Microscope) couplé à des mesures électriques. Ce travail est porté par trois principales motivations: (1) L'étude du comportement mécanique d'objets petites échelles, (2) L'apport des données électriques à l'analyse quantitative du comportement mécanique pendant l'indentation, en particulier pour obtenir une meilleur estimation de l'aire de contact, (3) L'étude locale des propriétés électroniques d'empilements de films minces. L'intégration *in situ* SEM a été validée et permet un positionnement des indents avec une précision meilleure que 100 nm, autorisant ainsi l'étude des propriétés mécaniques à l'échelle submicrométrique. La rapidité des essais permet également des mesures statistiques. Des caractérisations mécaniques ont été menées aussi bien sur des échantillons composites massifs que sur des ilots d'or submicrométriques. Pour ce dernier cas, malgré la nature stochastique de leur comportement mécanique, une loi déterministe a pu être extraite des données mécaniques. Des mesures 3D-BCDI (Bragg Coherent Diffraction Imaging) au synchrotron ont été réalisées sur certains ilots avant et après chargement mécanique, révélant une germination de dislocations avant l'avalanche de grandes déformations plastiques. En parallèle de cette étude, des mesures électriques ont été réalisées pendant l'indentation de divers échantillons. Des mesures de nanoindentation résistive ont ainsi été effectuées sur des métaux nobles (Au) ou recouverts de leur oxyde natif (Cu, Al), soit à l'état de monocristal massif ou de film polycristallin. Les résultats quantitatifs soulignent l'importance de la présence d'une couche d'oxyde sur la réponse électrique. En présence d'un oxyde, l'interface pointe / échantillon semble être le lieu d'importantes réactions électrochimiques. En l'absence d'oxyde, la résistance mesurée peut être entièrement décrite par un modèle analytique. Dans ce cas, l'aire de contact électrique peut être prédite à partir des mesures de résistance. Enfin, des mesures capacitives ont été réalisées sur des structures MOS avec différentes épaisseurs d'oxyde. Les résultats expérimentaux sont parfaitement décrits par un modèle analytique, ce qui ouvre la voie à des mesures locales de permittivité diélectrique sous contrainte mécanique.